

THÈSE

Présentée à

L'UNIVERSITÉ BORDEAUX 1

ÉCOLE DOCTORALE DES SCIENCES CHIMIQUES

Par **DARGIE HAILU DERIBEW**

Pour Obtenir le Grade de

DOCTEUR

SPÉCIALITÉ : **POLYMÈRES**

***STRUCTURE, MORPHOLOGY AND PERFORMANCE
RELATIONSHIPS OF ORGANIC PHOTOVOLTAIC DEVICES – THE
BLOCK COPOLYMER APPROACH***

Directeur de thèse: **Prof. Georges Hadziioannou**

Soutenue le: 14 Juin, 2013

Devant la commission d'examen formée de:

M. Stergios LOGOTHETIDIS	Professeur, Université Aristotle de Thessaloniki	Rapporteur
M. Yvan BONNASSIEUX	Directeur de recherche / École Polytechnique	Rapporteur
M. Lionel HIRSCH	Directeur de recherche/ IMS, Université de Bordeaux	Examineur
M. Bernard RATIER	Professeur/ XLIM, Université de Limoges	Examineur
M. Georges HADZIOANNOU	Professeur/ LCPO, Université de Bordeaux	Examineur
Mme Laurence VIGNAU	Professeur/IMS, Université de Bordeaux	Invité
M. Guillaume FLEURY	Maître de conférence/LCPO, Université de Bordeaux	Invité

To my beloved Mother - The late Tsehaynesk Yimam

Acknowledgements

This manuscript represents the culmination of a three years PhD research work. PhD thesis is not only a personal effort but also a contribution of ideas, suggestion, helps and encouragement of different people, to whom I would like to express my respect and acknowledgements.

First and foremost, my deepest gratitude goes to my supervisor, **Prof. Georges Hadziioannou**; for the opportunity he gave to me to work in his multidisciplinary research group and for his thoughtful guidance throughout my work. I have been amazingly fortunate to work under him who gave me the freedom to explore my research and give credits to all the wonderful things that happened. Without doubt, he's direction as well as his fatherly advices will have a big impact in my future life. I am highly grateful to my co-supervisor **Dr. Guillaume Fleury** for his brilliant guidance, encouragement, friendship and helps of all sorts. I have learnt a lot from all the discussions, for his tirelessly correcting my papers as well as this manuscript that has left me with tremendous experience. My sincere thanks goes to **Dr. Eric Cloutet** and **Dr. Cyril Brochon** (a.k.a. **Ras Cyril**) for their excellent support and thoughtful discussions they provide me during all my work. **Ras Cyril**, your knowledge about Ethiopian history is so great; and I highly appreciate that. I'm also very much grateful to **Prof. Mark Geoghegan** (University of Sheffield) for his valuable advice and discussions particularly for the basics of Neutron reflectivity.

This thesis was performed in collaboration with the Laboratory of IMS. I would like to express my deepest gratitude to **Prof. Laurence Vignau**, **Dr. Guillaume Wantz**, **Dr. Lionel Hirsch** and **Dr. Pascal Tardy** for allowing me to work at IMS without any obstacle and for their full consideration as an integral member of the ELORGA team. Their hospitality and support during my time at IMS was very much significant and I am extremely grateful for that.

I am grateful to acknowledge **Prof. Stergios Logothetidis** (Aristotle University of Thessaloniki, Greece), **Dr. Yvan Bonnassieux** (École Polytechnique Paris, France) for their thoughtful comments regarding the manuscript that enabled this work to be eligible for PhD award as well as accepting to participate in the examining committee. I also kindly acknowledge **Prof. Bernard Ratier** (University of Université de Limoges, France), **Dr. Lionel Hirsch** (University of Bordeaux, France) and **Prof. Georges Hadziioannou** (University of Bordeaux, France) who are the members of the examiners. I am thankful to **Prof. Laurence Vignau** (University of Bordeaux, France) and **Dr. Guillaume Fleury** (University of Bordeaux, France) for their accepting the invitation to be members of the jury.

I would like to thank all the people and colleagues who highly contributed to this work; **Celia** and **Jun** for their excellent cooperation in providing the novel materials for my research work. My research work wouldn't have gone smoothly without the help of **Eleni** (for the XRD and Neutron data analysis and explanations) and **Cedric** (for his magnificent help in the explanations about the devices physics and the device fabrication techniques particularly at the start of my work). Thank you very much for your excellent contribution for the realization of this work. I am also very much grateful to **Gilles** for his help in

the SFM measurements, to people at Bordeaux Imaging Center (BIC) for allowing me to carry out TEM measurements, to **Véronique** for the self-nucleation experiment and to **Sokha** for his tirelessly showing all the electronic equipments at IMS-ELORGA and for his help during the problems while doing my lab works. I would like to thank to all the members of LCPO, in particular, the current and past administrative personnel (**Catherine, Joanna, Audrey, and Aude**) for the different administrative helps that I got from the beginning to the end of my study.

I would like to acknowledge the **Arkema Corporation** and the **Aquitaine Council** for providing me a three year fund to accomplish my PhD thesis through the Chair of Excellency for Advanced Functional Materials for Energy, IT and Communication.

I am quite lucky to have so much of nice friends who made my life easier and enjoyable inside and outside the lab. **Mahfoudh, Sylvain, Mamatimin, Uyxing, Lionel (BG), Leo (BG), and Fredric (BG)**, thank you a lot. Apart from our scientific discussions, special thanks to **Wiljan** for all the sport activities that we did: the squash, the badminton and the discussions of various forms are unforgettable, you are a wonderful friend. **Carine and Katerina**, I wanted to thank you for being such a kind friend. You were always around when I need help, constantly willing to support. I want to thank all my Ethiopian friends in Bordeaux that made my time very enjoyable.

Last, but not least, my deepest gratitude goes to my lovely wife **Nigisti**, for your affectionate, caring and loving. Thank you for being on my-side during all my studies, you really sacrifice your precious-time for the sake of my studies, I owe you a lot! My brothers **Nuredin, Getch, and BKA** without your continuous help and encouragements, my life wouldn't have been so pleasant. **Nure**, your support is so exceptional. I love you all!

አመሰግናለሁ!

//Dargie H. DERIBEW

Table of Contents

<i>Acknowledgments</i>	<i>i</i>
<i>Resumé/Abstract</i>	<i>vii</i>
<i>List of symbols and abbreviations</i>	<i>xiii</i>
<i>General Introduction</i>	<i>1</i>
<i>Chapter – 1 Fundamentals of Organic Solar Cells</i>	<i>11</i>
<i>1.1. Introduction</i>	<i>13</i>
<i>1.2. The origin of semiconducting behavior in Organic Semiconductors</i>	<i>14</i>
<i>1.3. Operational Principles of Organic Solar Cells</i>	<i>20</i>
<i>1.4. Organic Photovoltaic Device Architectures</i>	<i>23</i>
<i>1.4.1. Introduction</i>	<i>23</i>
<i>1.4.2. The Bulk-Heterojunction (BHJ) Device Architecture</i>	<i>25</i>
<i>1.5. Morphology of the BHJ Systems (the P3HT:PCBM case)</i>	<i>34</i>
<i>1.6. Conclusion</i>	<i>43</i>
<i>1.7. Problem and Aim of the Project</i>	<i>44</i>
<i>1.8. References</i>	<i>45</i>
<i>Chapter -2 Block Copolymers and Their Application in Organic Photovoltaics</i>	<i>53</i>
<i>2.1. Introduction</i>	<i>55</i>
<i>2.2. Architecture, Phase Behavior and Morphology of Block copolymers</i>	<i>55</i>
<i>2.2.1. Phase behavior of Coil-Coil block copolymers</i>	<i>59</i>
<i>2.2.2. Phase Behavior of Rod-containing block copolymers systems</i>	<i>63</i>
<i>2.2.2.1. Phase behavior of rod-coil block copolymer systems</i>	<i>64</i>

2.2.2.2. Self-assembly properties of all-conjugated rod-rod block copolymers -----	73
2.3. Block copolymers for Photovoltaic Application -----	77
2.3.1. Block copolymers as Single Self-structured Active Layer in OPV -----	78
2.3.2. Block copolymers as main donor material in OPV Active Layer -----	82
2.3.3. Block copolymers as compatibilizers in OPV Active layers -----	88
2.4. Conclusion-----	93
2.5. References-----	94

Chapter -3 Microstructure and Photovoltaic Performance Optimizations in P3HT:PCBM Blends -----105

3.1. Introduction -----	107
3.2. Effect of Thermal Annealing on Morphology and Performance on P3HT:PCBM PV blends -- -----	108
3.3. Influence of P3HT Molecular Weight on the Thin Film Morphology and PV Characteristics-----	115
3.3.1. Influence of the P3HT Molecular Weight on Thin film Morphology -----	117
3.3.2. Influence of P3HT Molecular Weight on Device Performance -----	119
3.4. Study of the Phase Diagram of P3HT:PCBM blends -----	124
3.5. Vertical Stratification Studies of P3HT:PCBM blends by Neutron Reflectometry -----	130
3.6. Conclusion-----	138
3.7. References-----	139

Chapter -4 Semirigid Rod-coil Block Copolymers for Optimized Active layer Morphology and Device Performance in P3HT:PCBM Blends -----143

4.1. Introduction -----	145
4.2. Incorporation of Insulating Materials into P3HT:PCBM blends and its effect on Device Performance: the case of PS-b-PI block copolymer -----	147

4.3.	<i>P3HT-b-PI as P3HT Crystallization Agent and the Enhancement of Device Efficiency in P3HT:PCBM PV blends</i>	151
4.3.1.	<i>Effect of P3HT-b-PI on Morphology and Structural Properties of P3HT:PCBM BHJ PV Blends</i>	153
4.3.2.	<i>Effect of P3HT-b-PI on the performance of P3HT:PCBM BHJ PV Cells</i>	165
4.4.	<i>Diblock Copolymers as Interfacial compatibilizer and Nanostructuring agent - A Trend towards Fabricating Annealing-free Photovoltaic Devices</i>	170
4.4.1.	<i>P3HT-b-PS as Interfacial Compatibilizer in P3HT:PCBM blends</i>	171
4.4.2.	<i>P3HT-b-P4VP: A novel Nanostructuring Agent in Controlling the Macrophase Separation of P3HT:PCBM PV blends</i>	176
4.5.	<i>Conclusion</i>	185
4.6.	<i>References</i>	186

Chapter -5 Effect of semirigid Rod-coil Block Copolymers on Device Stability -----189

5.1.	<i>Introduction</i>	191
5.2.	<i>Reproducibility of fabrication processes</i>	194
5.3.	<i>Repeatability of device performance</i>	195
5.4.	<i>Effect Photodegradation on Device lifetime of P3HT:PCBM photovoltaic Devices – The Block Copolymer Approach</i>	200
5.4.1.	<i>Fresh device performance</i>	200
5.4.2.	<i>Stabilized device performance</i>	203
5.4.3.	<i>Device Ageing Mechanisms</i>	207
5.4.3.1.	<i>Photodegradation</i>	207
5.5.	<i>Conclusion</i>	215
5.6.	<i>References</i>	216

Chapter -6 Conclusions and Outlook	219
6.1. Conclusions	221
6.2. Outlook	223
Chapter -7 Experimental Method	225
7.1. Thin film and Device Fabrication Techniques	227
7.2. Device Characterizations	231
7.2.1. Quantum Efficiency Measurements	232
7.2.2. The Photovoltaic Parameters	233
7.2.3. The Real Cell Condition and the Equivalent Circuit diagram	234
7.3. Differential Scanning Calorimetry (DSC)	237
7.4. Morphology and Structural Characterizations	241
7.4.1. Optical Microscopy	241
7.4.2. Scanning Force Microscopy (SFM)	241
7.4.3. Transmission Electron Microscopy (TEM)	243
7.4.4. UV-vis Absorption Measurements	244
7.4.5. X-ray Diffraction and Neutron Reflectometry	245
7.5. References	248

Resumé

Ce travail se focalise sur l'étude de cellules solaires organiques modèles basées sur le mélange de poly(3-hexylthiophène) (P3HT) et de l'ester méthylique de l'acide [6,6]-phényl C61 butyrique (PCBM). La corrélation entre la morphologie de la couche active, les paramètres de mises en œuvre et le rendement photovoltaïque a été soigneusement étudiée afin d'obtenir l'optimisation de l'efficacité de tels dispositifs. Une méthode originale pour contrôler la séparation de phases dans ces mélanges a été proposée et consiste à l'intégration de copolymères blocs comme additifs. Trois copolymères séquencés ont été utilisés en tant qu'agents de nanostructuration et/ou d'agents de nucléation. Il a notamment été montré que l'incorporation de P3HT-*b*-PI permet l'augmentation du nombre de cristallites de P3HT tout en limitant l'agglomération du PCBM. D'autre part, l'incorporation de P3HT-*b*-P4VP dans les mélanges de P3HT:PCBM a permis de contrôler l'orientation des cristallites de P3HT, améliorant par ce fait le transport de charge dans les dispositifs.

Mot-clé: *Morphologie, séparation de phase, diagramme de phase, agent de nucléation, agent compatibilisant, L'efficacité de conversion de puissance, durée de vie de dispositif.*

Abstract

This work investigates organic solar cells made of a blend of polymeric materials based on poly(3-hexylthiophene) (P3HT) and [6,6]-phenyl-C61-butyric acid methyl ester (PCBM) as model system. The correlation between the photovoltaic active layer morphology and the performance of the solar cell has thoroughly investigated. The influence of P3HT macromolecular characteristics, the optimal ratios between P3HT and PCBM (by establishing the P3HT:PCBM phase diagram) as well as the vertical composition profile of the components has been considered in this investigation. The results showed that the P3HT macromolecular characteristics are the determining factors for the resulting morphologies of P3HT:PCBM blends. We have demonstrated that the maximum photovoltaic characteristics were obtained at eutectic or close to eutectic composition for the different Mn of P3HT under study. The other chosen method for controlling the phase separation in the polymeric blends was to incorporate block copolymers as additives. Three systematically selected block copolymers; P3HT-*b*-polyisoprene (P3HT-*b*-PI), P3HT-*b*-polystyrene (P3HT-*b*-PS) and P3HT-*b*-poly(4-vinylpyridine) (P3HT-*b*-P4VP) were used as nanostructuring and/or nucleating agents. Indeed, the incorporation of P3HT-*b*-PI induces the increase in the number of P3HT crystallites as well as suppresses the growth of PCBM aggregates. On the other hand, the incorporation of P3HT-*b*-P4VP into P3HT:PCBM decreases the crystallization of P3HT but increases its face-on orientation, a requirement for an enhanced charge transport in polymeric PV devices. In addition, the incorporation of P3HT-*b*-PS and P3HT-*b*-P4VP has contributed a lot to the improvement of the device performance, by decreasing the size of the PCBM domains and thus increases the interfaces available for exciton dissociation. Generally, the simplicity of adding a well-designed block copolymer into the archetypical P3HT:PCBM BHJ as crystallization agent or nano-structuring agent appears to be a valuable and efficient method to optimize the active layer morphology and improve device performance of polymer photovoltaic cells.

Keywords: Morphology, phase separation, phase diagram, nucleating agent, compatibilizing agent, power conversion efficiency (PCE), device life time.

Sommaire

Les prédictions en matière de demandes énergétiques globales envisagent un doublement de la consommation de 14 TW à 30 TW au cours de 50 prochaines années. A ce jour, la grande majorité de l'énergie est générée à partir de ressources fossiles non renouvelables, plus spécifiquement à partir de pétrole, gaz et charbon. C'est pourquoi le développement de ressources d'énergie renouvelables est aujourd'hui considéré comme un des challenges primordiaux dans le futur. Parmi les ressources renouvelables, l'énergie offerte par le soleil est encore grandement inexploitée alors qu'une heure d'énergie solaire serait suffisante pour subvenir aux besoins en énergie de notre société pour une année. Dans le but de récolter cette quantité impressionnante d'énergie, plusieurs types de dispositifs photovoltaïques ont été inventés. On peut nommer les cellules photovoltaïques à base de silicium cristallin ou amorphe, les cellules à pigment photosensible et les cellules photovoltaïques organiques à base de petites molécules et/ou polymères. Bien que chacune de ces technologies présentent leurs propres avantages et inconvénients, les cellules photovoltaïques organiques à base de polymère semi-conducteur offrent d'intéressantes perspectives que cela soit en terme de facilité de production (les procédés de fabrication sont nettement moins consommateurs d'énergie que ceux mis en œuvre pour les cellules à base de semi-conducteurs inorganiques) ou en terme d'applications puisque la flexibilité mécanique des matériaux employés permet une utilisation sur des formes non planaires. Cependant leur développement est à ce jour limité par deux facteurs reliés à l'efficacité photovoltaïque et à la stabilité des dispositifs inhérente à la dégradation des matériaux sous illumination prolongée. C'est pourquoi ce travail de thèse s'est focalisé sur la compréhension de relations structure / performance pour le système archétypal de P3HT:PCBM et sur une méthodologie permettant l'amélioration de l'efficacité et de la stabilité de ces dispositifs par l'ajout de copolymères à blocs dans le mélange P3HT:PCBM. Ces copolymères à blocs, de par leur nature amphiphilique, devraient modifier la mesostructure du mélange afin de promouvoir la séparation et le transport de charge tout en permettant une stabilité thermodynamique renforcée du mélange.

Premièrement nous nous sommes intéressés à l'optimisation du procédé de fabrication des dispositifs photovoltaïques à base de P3HT : PCBM. Une étude complète des paramètres de mise en œuvre (solvant de co-solvation, température et durée de recuit, etc.) a été menée sur un P3HT commercial de haute masse moléculaire afin d'obtenir des performances photovoltaïques optimisées. Ces paramètres ont par la suite été conservés afin d'étudier l'influence des paramètres macromoléculaires du polymère semi-conducteur P3HT (masse moléculaire M_n , indice de polydispersité I_p , régio-régularité et taux de cristallinité) sur les performances photovoltaïques. Une large gamme de P3HT avec différentes masses moléculaires (de 5,6 kg/mol à 60 kg/mol) a ainsi été synthétisée par métathèse de Grignard, méthodologie permettant une polymérisation contrôlée de l'hexyl de thiophène). Ces polymères et le PCBM ont alors été mélangés à différentes compositions afin d'étudier l'influence du ratio entre le donneur et l'accepteur sur les performances photovoltaïques dans les hétérojonctions en masse P3HT : PCBM. Parallèlement les diagrammes de phases en fonction de la température ont été étudiés afin de corréler les propriétés photovoltaïques à la mesostructure des mélanges P3HT : PCBM. Nous avons pu montrer que le système P3HT : PCBM est un système eutectique pour lequel la composition de l'eutectique est fortement dépendante de la masse moléculaire du P3HT. De plus le maximum des propriétés photovoltaïques correspond, pour chaque masse moléculaire, à la composition de l'eutectique entre le P3HT et le PCBM. En effet, cette composition particulière permet d'obtenir lors du refroidissement du liquidus P3HT : PCBM une mesostructure finement interpénétrée entre les domaines de P3HT et de PCBM comme cela a été démontrée par microscopie à force atomique (AFM). En conclusion le rapport entre les fractions de P3HT et de PCBM doit être impérativement optimisé en fonction de la masse moléculaire du P3HT afin d'obtenir des performances photovoltaïques optimales.

Suite à l'optimisation des propriétés photovoltaïques du mélange P3HT : PCBM en fonction des caractéristiques macromoléculaires du P3HT et de la méthodologie de fabrication, nous nous sommes intéressés aux effets de l'ajout de copolymères à blocs comprenant un bloc P3HT et un bloc permettant l'addition d'une nouvelle fonctionnalité. Deux types de fonctionnalités ont été visés : une

fonctionnalité de comptabilisation avec l'ajout d'un bloc de type poly(styrène) (PS) ou poly(4-vinyl pyridine) (P4VP) possédant une forte affinité avec le PCBM ou une fonctionnalité permettant une plus grande mobilité moléculaire du système avec l'ajout d'un bloc à faible température de transition vitreuse (poly(isoprène) (PI)). L'ajout d'une faible fraction massique de copolymères de type P3HT-*b*-PI au mélange P3HT : PCBM a tout d'abord montré une augmentation importante des performances photovoltaïques (d'un PCE de 3,5% à 4,6%). Ces résultats ont été corrélés aux changements de mesostructure observés par AFM et diffraction de rayons X (GIXD). Ainsi nous avons pu mettre en évidence un nombre de cristallites plus importantes dans les échantillons comprenant le copolymère à blocs. De plus l'augmentation de la proportion de cristaux de P3HT orientés « edge-on » est également à relier à l'augmentation des propriétés photovoltaïques et plus particulièrement de transport de charges. L'évolution des profils en composition selon la normale au substrat des différents hétérojonctions en masse avec ou sans copolymère a également été étudiée par réflectométrie de neutrons et nous avons pu montrer que l'ajout de copolymère à blocs n'influe pas le profil en composition. Une autre famille de copolymère à blocs a été envisagée afin d'augmenter la compatibilité entre le P3HT et le PCBM. Nous avons montré que l'ajout de P3HT-*b*-P4VP permet également d'augmenter les performances photovoltaïques mais selon un processus différent. En effet l'analyse par GIXD et par AFM a montré que ce copolymère permet d'éviter la formation d'agglomérats mesoscopiques de PCBM et ainsi de créer une mesostructure avec des domaines plus petits. Ce résultat prometteur a été confirmé en montrant que ce type de copolymère permet d'obtenir des cellules photovoltaïques organiques fonctionnelles sans l'étape de recuit thermique. Cette avancée ouvre la voie à la mise en œuvre de cellules photovoltaïques organiques par des procédés d'enduction sur des substrats flexibles.

Finalement nous avons étudié l'apport des copolymères à blocs sur la stabilité des cellules photovoltaïques organiques basées sur le système P3HT : PCBM. Nous avons tout d'abord testé la reproductibilité et répétabilité de nos processus de fabrication de dispositifs et de mesures de performances photovoltaïques. Nous avons ainsi montré une très bonne reproductibilité de nos

manipulations. Ensuite nous avons montré que lors de mesures de répétabilité, l'efficacité de nos dispositifs diminue très fortement lors d'une période de « burn-in » réversible lorsque le dispositif est de nouveau recuit thermiquement. Cette période de « burn-in » est suivie d'un plateau en efficacité se situant aux alentours de 80% de l'efficacité initiale. L'ajout de copolymères à blocs dans les dispositifs photovoltaïques ne permet pas d'éliminer cette zone de perte d'efficacité liée au « burn-in » mais permet d'améliorer sensiblement la valeur du plateau en efficacité. Par ailleurs une étude de stabilité sous illumination continue a montré que les dispositifs comprenant des copolymères à blocs permettaient d'augmenter de 50% le temps de demi-vie des dispositifs même si les mécanismes permettant ce gain de performances sont encore à élucider. Une étude préliminaire a cependant montré l'importance des modifications de la mesostructure des hétérojonctions en masse de P3HT : PCBM sous illumination prolongée.

En conclusion cette thèse a permis de mieux appréhender les mécanismes de formation de la mesostructure des hétérojonctions en masse de P3HT : PCBM. Nous avons montré qu'une optimisation des performances photovoltaïques est très fortement liée aux paramètres macromoléculaires du P3HT ainsi qu'aux procédés de fabrication des dispositifs photovoltaïques. De plus la méthodologie se basant sur l'ajout de copolymères à blocs afin de modifier et d'optimiser la structure des hétérojonctions en masse de P3HT : PCBM a montré son fort potentiel aussi bien en terme de performance que de stabilisation des propriétés. Cette méthodologie présente de nombreuses perspectives avec notamment sa transposition pour de nouveaux systèmes photovoltaïques organiques à base de polymères semi-conducteurs à faible largeur de bande interdite.

List of symbols and abbreviations

- AM 1.5G:** Air Mass 1.5 Global
- BCP:** Block copolymer
- BHJ:** Bulk Heterojunction
- CB:** Conduction Band
- C_e:** Eutectic Composition
- DSC:** Differential Scanning Calorimeter
- DSSCs:** Dye Sensitized Solar Cells
- E_a:** Activation Energy
- EA:** Electron Affinity
- ED:** Electron Diffraction
- E_g:** Band gap energy
- EQE:** External Quantum Efficiency
- ETL:** Electron Transporting Layer
- eV:** Electron volt
- FF:** Fill Factor
- HOMO:** Highest Occupied Molecular Orbital
- HTL:** Hole Transporting Layer
- IP:** Ionization Potential
- IPCE:** Incident Photon Conversion Efficiency
- J_{sc}:** Short-circuit Current
- k_{deg}:** Decay rate
- LBG:** Low Band-gap
- LED:** Light Emitting Diodes
- LUMO:** Lowest Unoccupied Molecular Orbital
- M_n:** Number Average Molecular Weight
- N:** Degree of polymerization
- N_A:** Avogadro's Number
- NE:** Nucleation Efficiency

NIST: *National Institute of Standards and Technology*

o-DCB: *ortho-Dichlorobenzene*

ODT: *Order-disorder Transition*

OLED: *Organic Light Emitting Diodes*

OPVs: *Organic Photovoltaics*

OSCs: *Organic Solar Cells*

OTFTs: *Organic thin Film Transistors*

PCE: *Power Conversion Efficiency*

PL: *Photoluminescence*

PV: *Photovoltaic*

RFIDs: *Radio Frequency Identification Tags*

SAXS: *Small-angle X-ray Scattering*

SFM: *Scanning Force Microscopy*

SLD: *Scattering Length Density*

T_c: *Crystallization Temperature*

TEM: *Transmission Electron Microscopy*

T_g: *Glass-transition Temperature*

T_M: *Melting Temperature*

T_S: *Nucleation Temperature*

TW: *Terawatt*

UV-vis: *Ultraviolet-visible*

VB: *Valence Band*

V_{oc}: *Open-circuit Voltage*

WAXS: *Wide-angle X-ray Scattering*

XPS: *X-ray Photoelectron Spectroscopy*

XRD: *X-ray Diffraction*

b: *Nuclear Scattering Vector*

μ: *Charge carrier mobility*

S.cm⁻¹: *Siemens per centimeter*

Ω/□: *Ohm per Square*

-
- χ :** Flory-Huggins interaction parameter
- ΔG_m :** Change in Gibbs' Free Energy of Mixing
- ΔH :** Change in Enthalpy
- ΔS :** Change in Entropy
- k_B :** The Boltzmann Constant
- δ :** Solubility parameter
- γ :** Surface Energy
- ρ :** Scattering Length Density
- k :** Extinction Coefficient
- λ :** Wavelength
- α :** Absorption Coefficient
- q :** Scattering Vector
- $R(q_z)$:** Absolute Reflectivity

General Introduction

General Introduction

It is expected that the global energy demand will double from the current yearly consumption of 14 TW towards 30 TW per year within the next 40-50 years as the result of population growth and economic developments.^[1] Currently, the vast portion of the global energy is generated from non-renewable sources, specifically oil, coal and gas.^[2] As can be seen from the chart in Figure 1.1, fossil fuels account for over 80% of the world's total energy supply. However, due to the predicted end of those sources and the harmful long-term effect of carbon dioxide on our planet, the search for other sources of energy is crucial. Renewable energy sources have been considered as the best alternatives to replace the conventional energy sources. Hence, developing an efficient and environmentally friendly energy source is one of the main challenges in the future. Renewable energy is generated from natural resources; such as sunlight, wind, hydroelectric, and geothermal heat, which have no significant harmful effects on our environment.^[3]

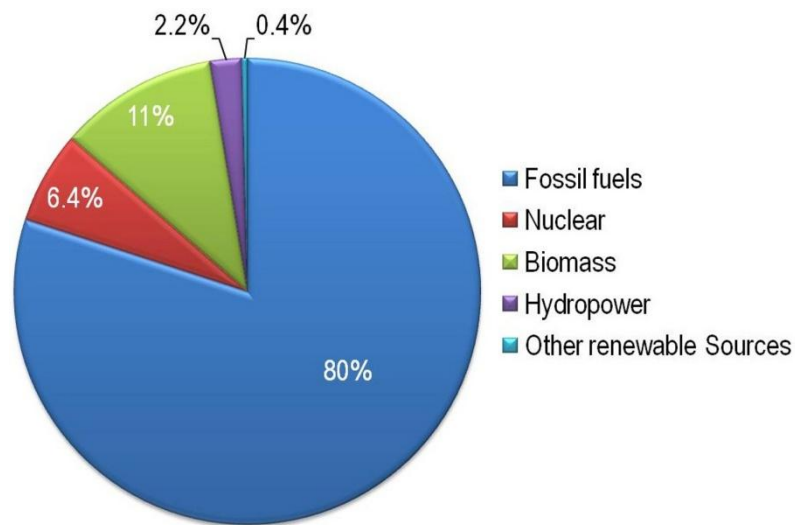


Figure 1.1: Global energy consumption by source.^[2]

Among the renewable energy sources, the most abundant, but not yet utilized at its full potential, is the solar energy: one hour of sunshine is more than enough to satisfy the worldwide energy needs for an entire year if it is correctly collected.^[4] This freely available solar energy can directly be converted into electricity by a photovoltaic device.^{[5][6]} The conversion process relies on the

General Introduction

principle established by the quantum theory. Light can be seen as packets of energy, called photons. The energy of the photons depends on the frequency (or wavelength) of the light (from the higher energy rays (ultra violet) to the relatively lower energy (infrared rays)). The photons in the UV and visible range have enough energy to excite electrons in solid semiconducting material, and this phenomenon can be effectively used for charge generation. But in most cases, when the absorbed photons excite the ground state electrons of a material to higher energy states, the excited electrons quickly relax to the ground state. However, in photovoltaic devices, some built-in potential (*i.e.* the excited electrons generates a potential difference) can pull the electrons and holes before they can relax, and thus, transports them to an external circuit to produce current (power). This effect is known as the photovoltaic effect. It was first discovered by Edmund Becquerel in 1839, who observed the production of a photocurrent in an electrolytic cell under light illumination.^[7, 8]

Some forty years later, Adams and Smith observed the photovoltaic effect in a sample of selenium that was placed between two metal electrodes.^{[9][10]} Some years later, Charles Fritts developed a first large-area photovoltaic (PV) device by using gold coated Selenium semiconductor materials.^[11] The resulting cells had a power conversion efficiency of less than 1% owing to the properties of selenium and the use of semitransparent thin metal electrode.

Since 1946 an intensive work has been carried out to develop highly efficient photovoltaic devices. In 1954, Bell Labs revealed the first high-power silicon PV cell, which used a p-n junction and reported a PCE of 6%.^[12] Other PV cells made of cadmium sulphide (CdS), gallium arsenide (GaAs), cadmium telluride (CdTe), and indium phosphide (InP) have been developed in parallel. Currently, the conversion efficiency has reached more than 25% for single crystal Si solar cells and more than 40% for group III-V compounds such as GaAs. The different technologies and its state of art power conversion efficiencies are presented in Figure 1.2. However, some of the inorganic PV devices contain hazardous elements; such as cadmium which exhibit a high toxicity. Besides the fabrication of inorganic solar cells requires costly technologies, as it requires extremely pure materials and sophisticated production tools

General Introduction

used for patterning and various coating processes.^[13] As a result, the inorganic photovoltaic devices are quite expensive for consumers in the market. For this reason, the use of those PV cells has been limited in some specific end-uses (e.g. remote communication equipments, weather monitoring stations, in satellites and vehicles in remote locations). Therefore, if the energy from the sun is to be considered as the major future global energy source, the PV devices should be fabricated at reasonably lower cost and it should also be suited for large-scale manufacturing process. Considerable efforts have been done in developing semiconducting materials that can be processed by using few steps and cheaper technologies. For example, solar cells based on multijunction polycrystalline or inorganic thin films based on amorphous Si have appeared as alternatives to the crystalline Si based solar cells.^[14] However, they are less efficient as compared to group III-V compounds or Si based solar cells. Consequently new concepts and strategies need to be envisioned to achieve competitive, cost effective and efficient photovoltaic devices.

In this context, an alternative solar cell based on a photo-electrochemical cell was proposed. One of the most successful cells of this type are the dye sensitized solar cells (DSSCs) developed by Grätzel and co-workers, which are now commonly referred as "Grätzel cells".^[15] The dye usually consists of a transition metal complex based on ruthenium or osmium. Power conversion efficiencies higher than 8.0% for cell area of 2.36 cm² and 4.7% for a sub-module area of 141.4 cm² were already reported. More recently, higher efficiencies (up to 12.1%) have been reported for smaller device areas (0.28 cm²).^{[16][17][18]} The current challenge in the DSSC design is that the electrolyte solution contains volatile organic compounds which need a carefully sealing technique as the solvents are hazardous to health and the environment. Replacing the liquid electrolyte with a solid hybrid material as well as with solvent free electrolyte solution has been a major ongoing field of research.^{[19][20]}

General Introduction

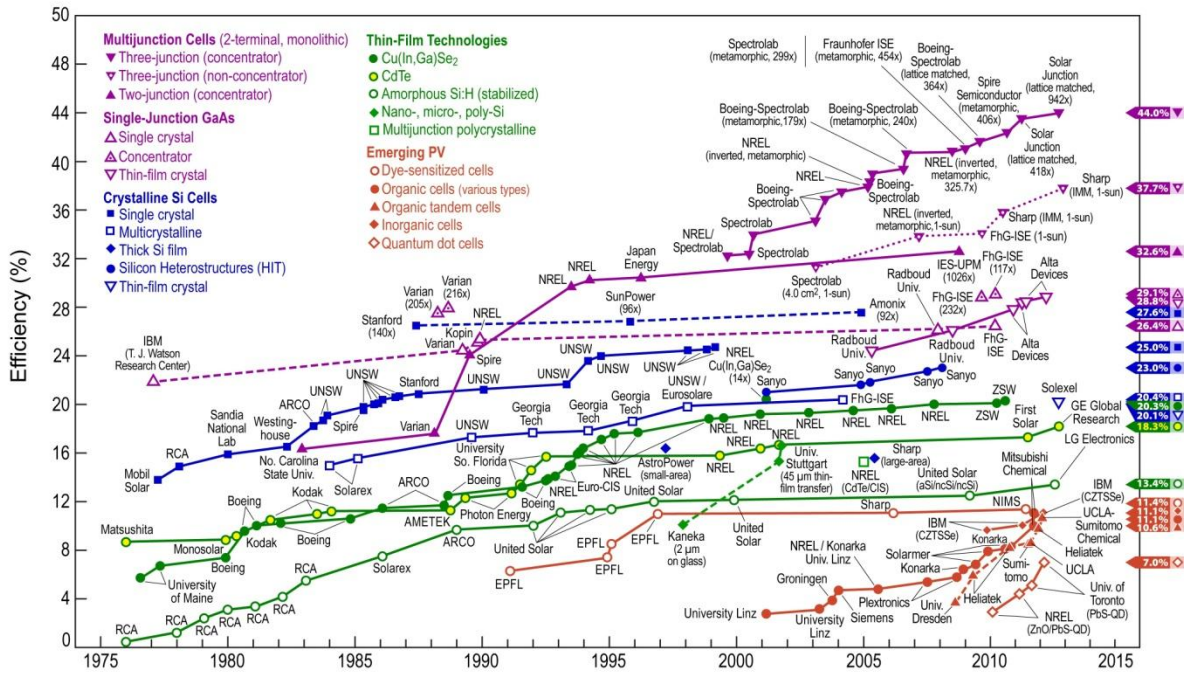


Figure 1.2: Best research cell-efficiencies for the different technologies. [21]

Conducting organic materials, in particular π -conjugated polymers have emerged as a new class of semiconductors. A first class of conducting polymers was discovered in 1977 when high conductivity was observed in doped polyacetylene by Heeger, MacDiarmid, and Shirakawa, who won the Nobel Prize for their contribution to the field. [22][23][24] Since then, active research on conjugated organic polymers have been ongoing and paved the path to electronic devices using organic semiconductors; the so-called "organic electronics". The Figure 1.3 shows the number of articles yearly published in the domains of organic electronics (organic light emitting diodes (OLED), organic thin film transistors (OTFTs), and organic photovoltaics (OPVs)). [25] Organic semiconductors can be processed from solutions by spin coating or printing techniques and hence are one of the best choices for the fabrication of large area and flexible electronic devices. Moreover these carbon-based materials are typically inexpensive and easily processable since they exhibit low process temperatures (usually, from RT to 200°C). [26] Consequently they could be included in broader applications (fashion, curtains, toys, etc...) in addition to the more technological applications (power generator, displays, electronic papers, memory devices, etc...). Furthermore the functionality of those conjugated polymers can be easily

tailored through macromolecular engineering, giving rise to various types of materials with specific optical and electrical properties.

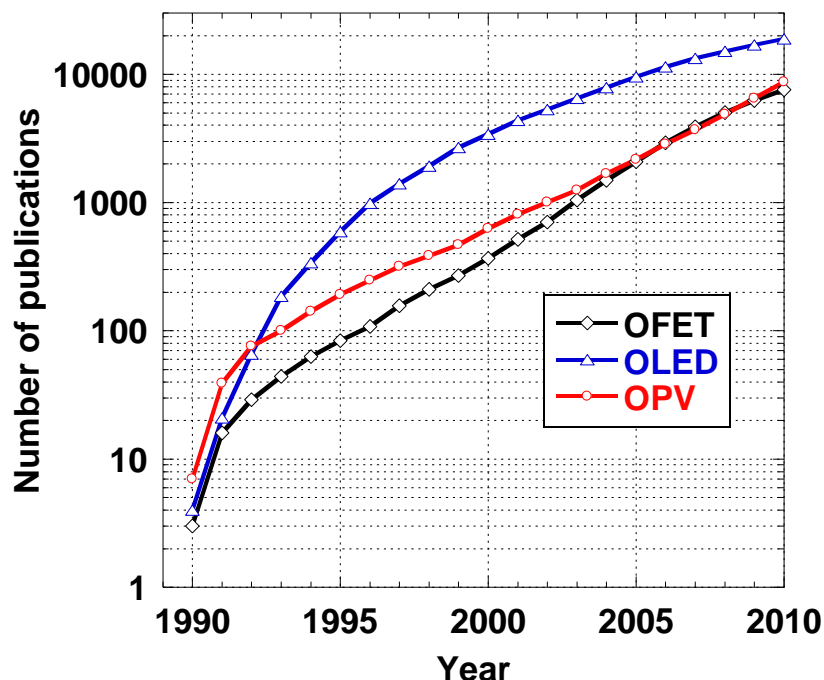


Figure 1.3: The annual production of publications in the field of organic electronics. Adapted from ISI Web of knowledge: key words; "Polymer Photovoltaic" or "Organic solar Cells", accessed on Sept. 2012.

Concerning the OPVs, organic thin-film solar cell using a double-layer device architecture was reported by Tang in 1986.^[27] In 1995, polymer-based bulk heterojunction (BHJ) PV devices were developed by Wudl & Heeger.^[28] Since then, great interest has been devoted both to the synthesis of new functional organic materials and to the optimization of the device fabrication techniques. A remarkable increase of PCEs, from about 5% in 2005 to 10% in 2012 has been already achieved in laboratories (Figure 1.2).^{[29][30][31]} Though those efficiencies can be compared to the ones of amorphous Si:H (hydrogenated amorphous silicon) cells, BHJ organic solar cells are still far from commercialization. That means further improvements in efficiency and stability are required to make OPV competitive as regard to their inorganic counterparts.^[32]

General Introduction

Keeping in mind these considerations, this dissertation focuses on PV cells that use organic semiconductors as active layer materials. In this thesis, several issues concerning the photovoltaic parameters for BHJ type device architecture are addressed. One of the main factors that affect the performance of BHJ PV cells is the way the donor and acceptor components organize. The morphology resulting of the blending of the donor and acceptor materials in a BHJ is a crucial parameter for the device performance. Ideally, to ensure efficient exciton dissociation, an acceptor domain should be within the exciton diffusion length (usually, in the range of 5-10 nm) from any donor domain, and vice versa.^{[28][33]} In addition, both the donor and the acceptor phases should form a continuous path with interpenetrating donor-acceptor domains to the respected electrodes in order to allow efficient charge transport. In principle, phase separation with an appropriate structuring may be achieved through different processing techniques.^{[34][35][36]} Block copolymers (BCPs) has recently emerged as a useful strategy to control the nanostructure of donor-acceptor components in organic photovoltaics.^{[37][38][39]} The microscopic properties of the devices; such as the exciton dissociation and charge transport was mainly improved by using block copolymer as nanostructuring agents (compatibilizer) as it minimizes the interfacial energy between the donor and acceptor domains. In this regard, different types of block copolymers were used in this work both as nanostructuring agent but as well as nucleation agents for improving the crystallinity of P3HT in P3HT:PCBM blends. Besides, obtaining a nanoscale bulk-heterojunction morphology which is stable in time and with temperature is one of the challenges that must be addressed before polymer photovoltaics can be successfully transferred to the industry. In this respect, it would be useful to test the stability of devices under different external conditions. With this in mind, this thesis is organized as follows. In Chapter 1, the general information about the molecular structure of semiconductors polymers, some example of semiconducting polymers, their application in organic photovoltaics (OPVs), device structures, device fabrication methods, device working principles, and the different factors affecting the morphology of the bulk heterojunction (BHJ) architecture are briefly presented. At the end of this chapter, strategies to improve the PCE of the BHJ PV cells are briefly introduced. Chapter 2 is mainly focused on the

General Introduction

literature review in relation to this work. Chapter 3 discusses the device fabrication optimization and the understanding of the phase segregation in P3HT:PCBM blends. The phase diagrams of the P3HT:PCBM blends as function of the composition and temperature for different molecular weight (M_n) of P3HT will be presented. The work on this chapter is the base for further experiments. In Chapter 4, the use of different block copolymers (P3HT-*b*-PI, P3HT-*b*-PS, PS-*b*-PI and P3HT-*b*-P4VP) and their effect on the P3HT:PCBM blend morphology and their subsequent effect on device performance are thoroughly investigated. In Chapter 5, the life time and degradation mechanisms of P3HT:PCBM PV devices and the influence of the different block copolymers incorporation are thoroughly discussed. The general conclusion, the lessons learned, and the outlooks for further research are presented on Chapter 6. Finally, the experimental methods and the different equipments used in this thesis work are presented in Chapter 7.

References

- [1] US Energy Information Administration, EIA, **2011**.
- [2] FAO, *Forests and Energy, Key Issues*, **2008**.
- [3] http://en.wikipedia.org/wiki/Renewable_Energy, Accessed on 28/12/ **2012**.
- [4] O. Morton, *Nature* **2006**, 443, 19–22.
- [5] S.S. Sun, N. S.Sariciftci, *Organic Photovoltaics: Mechanisms, Materials, and Devices*, Marcel Dekker Inc.**2005**.
- [6] V.D. C. Brabec, U. Scherf, *Organic Photovoltaics: Materials, Device Physics, and Manufacturing Technologies*, Wiley-Vch**2008**.
- [7] A.E.Becquerel, *Comptes Rendus* **1839**, 9, 561.
- [8] A.E. Becquerel, *Compt. Rend. Acad. Sci.* **1839**, 9, 145.
- [9] W. Smith, *Nature* **1873**, 7, 1873.
- [10] W.G.A.R.E. Day, *Proc. R. Soc. Lond* **1876**, 23, 113.
- [11] [Http://en.wikipedia.org/wiki/Charles_Fritts](http://en.wikipedia.org/wiki/Charles_Fritts), Accessed on 28/12/ **2012**.
- [12] D.M. Chapin, C.S. Fuller, G.L. Pearson, *Journal of Applied Physics* **1954**, 25, 676.

General Introduction

- [13] M. Tao, *Inorganic Photovoltaic Solar Cells: Silicon and Beyond* **2008**.
- [14] *Solar Server; Thin Film Technology to Make It Through*, **2008**.
- [15] M.G. Brian O'Regan, *Nature* **1991**, 737–740.
- [16] Y. Cao, Y. Bai, Q. Yu, Y. Cheng, S. Liu, D. Shi, F. Gao, P. Wang, *The Journal of Physical Chemistry C* **2009**, *113*, 6290–6297.
- [17] C. Chen, M. Wang, J. Li, N. Pootrakulchote, L. Alibabaei, J. Decoppet, J. Tsai, C. Gra, C. Wu, S.M. Zakeeruddin, M. Gra, *ACS Nano* **2009**, *3*, 3103–3109.
- [18] E. Dissociation, S. States, Q. Yu, Y. Wang, Z. Yi, N. Zu, J. Zhang, M. Zhang, P. Wang, *ACS Nano* **2010**, *4*, 6032–6038.
- [19] Y. Bai, Y. Cao, J. Zhang, M. Wang, R. Li, P. Wang, S.M. Zakeeruddin, M. Grätzel, *Nature Materials* **2008**, *7*, 626–30.
- [20] J. Bouclé, J. Ackermann, *Polymer International* **2012**, *61*, 355–373.
- [21] 2013 National Renewable Energy Laboratory (NREL); accessed on January, *National Renewable Energy Laboratory*, **n.d.**
- [22] C.K. Chiang, J. C. R. Fincher, Y.W. Park, A.J. Heeger, *Physical Review Letters* **1977**, *1101*, 1098–1101.
- [23] H.S. C. K. Chiang, M. A. Druy, S. C. Gau, A. J. Heeger, E. J. Louis, A. G. MacDiarmid, Y. W. Park, *Journal of American Chemical Society* **1978**, *100*, 1013–1015.
- [24] C.K. Chiang, Y.W. Park, a. J. Heeger, H. Shirakawa, E.J. Louis, A.G. MacDiarmid, *The Journal of Chemical Physics* **1978**, *69*, 5098.
- [25] "Polymer Photovoltaic" or "Organic Solar Cells", *ISI Web of Knowledge*, Accessed on Sept. **2012**.
- [26] G. Li, V. Shrotriya, J. Huang, Y. Yao, T. Moriarty, K. Emery, Y. Yang, *Nature Materials* **2005**, *4*, 864–868.
- [27] C.W. Tang, *Applied Physics Letters* **1986**, *48*, 183.
- [28] A.J. Yu, G.; Gao, J.; Hummelen, J. C.; Wudl, F.; Heeger, *Science* **1995**, *270*, 1789–1791.
- [29] W. Ma, C. Yang, X. Gong, K. Lee, A.J. Heeger, *Advanced Functional Materials* **2005**, *15*, 1617–1622.
- [30] M.A. Green, K. Emery, Y. Hishikawa, W. Warta, E.D. Dunlop, *Progress in Photovoltaics: Research and Applications* **2012**, *20*, 12–20.
- [31] W.Y. Huaxing Zhou, Liqiang Yang, *Macromolecules* **2012**, *45*, 607–632.
- [32] M. Jørgensen, K. Norrman, S. a Gevorgyan, T. Tromholt, B. Andreasen, F.C. Krebs, *Advanced Materials* **2012**, *24*, 580–612.

General Introduction

- [33] S.C.M.& A.B.H. J. J. M. Halls, C. A. Walsh, N. C. Greenham, E. A. Marseglia, R. H. Friend, *Nature* **1995**, 376, 498–500.
- [34] G. Li, Y. Yao, H. Yang, V. Shrotriya, G. Yang, Y. Yang, *Advanced Functional Materials* **2007**, 17, 1636–1644.
- [35] T.J. Savenije, J.E. Kroeze, X. Yang, J. Loos, *Advanced Functional Materials* **2005**, 15, 1260–1266.
- [36] Y. Kim, S.A. Choulis, J. Nelson, D.D.C. Bradley, *Journal of Materials Science* **2005**, 40, 1371 – 1376.
- [37] E.L. Muthukumar, M.; Ober, C. K.; Thomas, *Science* **1997**, 277, 1225–1232.
- [38] M.H. Van Der Veen, B. De Boer, U. Stalmach, K.I. Van De Wetering, G. Hadziioannou, *Macromolecules* **2004**, 37, 3673–3684.
- [39] K. Sivula, Z.T. Ball, N. Watanabe, J.M.J. Fréchet, *Advanced Materials* **2006**, 18, 206–210.

Chapter - I
Fundamentals of Organic Solar Cells

1.1. Introduction

Organic semiconductors can be categorized into two major classes, namely small molecules and macromolecules (or polymers).^[1] Both are conjugated systems consisting of a delocalized p-electron system along their backbones, but different in the overall size. Polymers are molecules made up of repeating structural units, or monomers and are referred to macromolecules because of their large in size.^[2] When all the repeating units along a chain are of the same chemical type, the resulting polymer is called a homopolymer while polymerization of more than one type of monomers results into a copolymer (*i.e.* when chains contain two or more different repeating units). In each of the polymer molecules, the atoms are bound together by covalent inter-atomic bonds and can form chemical structures that are linear, cyclic or branched. Some polymers have semiconducting properties due to their unique macromolecular structure characterized by the formation of alternating single and double bonds between the adjacent carbon atoms. These polymers are known as π -conjugated polymers. The processing technique to form thin films is another source of difference between the two classes of materials.^[3] Vacuum gas-phase sublimation or evaporation are used for deposition of small molecules, while conjugated polymers are processed from solution, e. g., by spin-coating or printing techniques. The semiconducting polymers, due to their unique physical properties, have attracted considerable attention in organic electronics domains, mainly; in light emitting diodes (OLED), electronic papers, radio frequency identification tags (RFID) and in photovoltaics (OPVs). The work reported in this thesis is mainly based on conjugated semiconductor polymers. In this chapter, the origin of the basic electronic properties of π -conjugated polymers, their application in organic photovoltaics (OPV), the type of device structures and the different factors affecting the morphology of the bulk heterojunction (BHJ) device architecture and its relation to its performance are briefly presented.

1.2. The origin of semiconducting behavior in Organic Semiconductors

Carbon atom (C-atom) is the main element constituting polymer materials. The type of bonds between two adjacent C-atom formed by their valence electrons determines the overall electronic properties of a given polymer. Those chemical bonds could be either saturated or unsaturated bonds. Saturated polymers are insulators since all the four valence electrons of C-atom are used for the formation of covalent bonds (i.e. sp^3 hybridization orbitals), while most conductive polymers have unsaturated conjugated structure. The electronic configuration of π -conjugated polymers stems from their alternated single and double carbon-carbon bonds. Therefore, the fundamental source of the semiconducting property of conjugated polymers originates from the overlapping between the molecular orbitals formed by the valence electrons of chemically bonded C-atoms. It is arisen from the π -delocalization of single $2p_z$ valence electrons along the polymer backbone. This phenomenon is occurring when one $2s$ orbital in C-atom is mixed with two of the $2p$ orbitals of C-atom to forms 3 sp^2 hybrid orbitals, leaving one p orbital in C-atom unhybridized (See Figure 1.1a). The sp^2 carbon hybrid orbitals are known to form a different bond length, strength and geometry when compared to other hybridized molecular orbitals. The sp^2 hybridization has one unpaired electron (π -electron) per C-atom. The three sp^2 hybrid orbitals of a C-atom arrange themselves in three-dimensional space to attain stable configuration. Their geometry is trigonal planar geometry, where the bond angle between the sp^2 hybrid orbitals is 120° . The unmixed pure p_z orbital lies perpendicular to the plane of the three sp^2 hybrid orbitals (See Figure 1.1b).

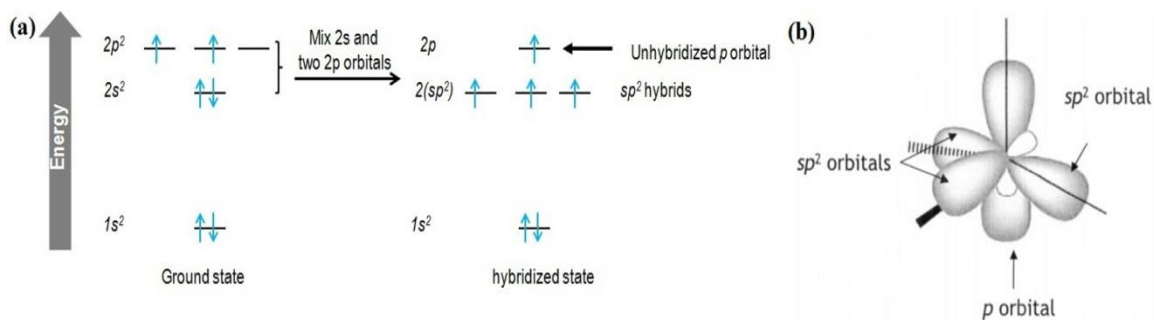


Figure 1.1: (a) The sp^2 hybridization of the valence shell electrons of a carbon atom. (b) Spatial distribution of orbitals on an sp^2 hybridized carbon atom.^[4]

For example, the carbon-carbon double bond in ethene consists of one σ -bond, formed by the overlap of two sp^2 orbitals, and a π -bond, which is formed by the *side-by-side* overlap of the two unhybridized $2p_z$ orbitals from each carbon (Figure 1.2a). If the numbers of carbon atoms are increased as in the case of conjugated polymers (e.g. polyacetylene, Figure 1.2b), it forms a continuous band-like (π -band) behavior. The wave function of each $2p_z$ electron overlaps together and gives a delocalized π -band that stretches over a segment of the polymer backbone. The π -bonds are, thus, considered as the basic source of charge transport band in the conjugated systems.^{[5][6]}

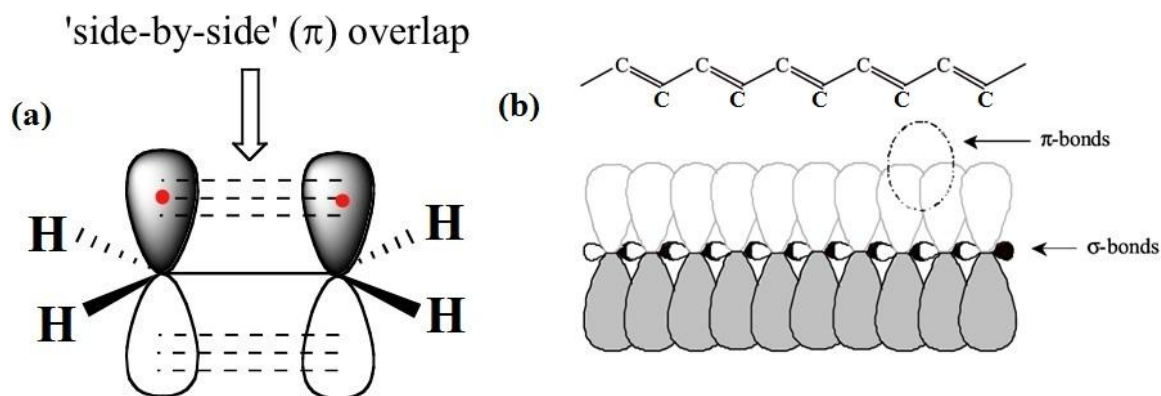


Figure 1.2: (a) The side-by-side overlaps of the two unhybridized $2p_z$ orbitals in ethane. (b) The molecular structure of polyacetylene (top), for clarity hydrogen atoms are not shown. The alternating double and single bonds indicate that the polymer is conjugated. The schematic representation of the

electronic bonds in polyacetylene is depicted in the bottom panel. The p_z -orbitals overlap to form π -bonds.

In terms of an energy-band description, the σ -bonds form completely filled bands, while π -bonds would correspond to half-filled states (Figure 1.3a).^[7] The filled bonding states in the delocalized orbitals form π -bands and the empty anti-bonding states form π^* -bands. Because of this reason, the molecular orbitals of a polymer form an energy band that lies within a certain energy range. For example, the anti-bonding π^* orbitals located higher in energy form a conduction band (CB) while the lower energy lying bonding orbitals form the valence band (VB). The full VB is separated from the upper empty CB by a discrete amount of energy. This gap is the base for the semiconducting properties of conjugated polymers. The gap between the VB and CB is commonly called the band-gap (E_g) and is, in first approximation, related to the chemical structure of the polymer. The VB and CB are characterized by their ionization potential and electron affinity, respectively (Figure 1.3b). The ionization potential (IP) refers to the upper state of the valence band (π -state; the energy required to pull an electron from the highest point) and corresponds to the highest occupied molecular orbital (HOMO). Similarly, the electron affinity (EA) of a semiconducting polymer corresponds to the lowest state of the conduction band (π^* state; the energy required to inject an electron) or the lowest unoccupied molecular orbital (LUMO).

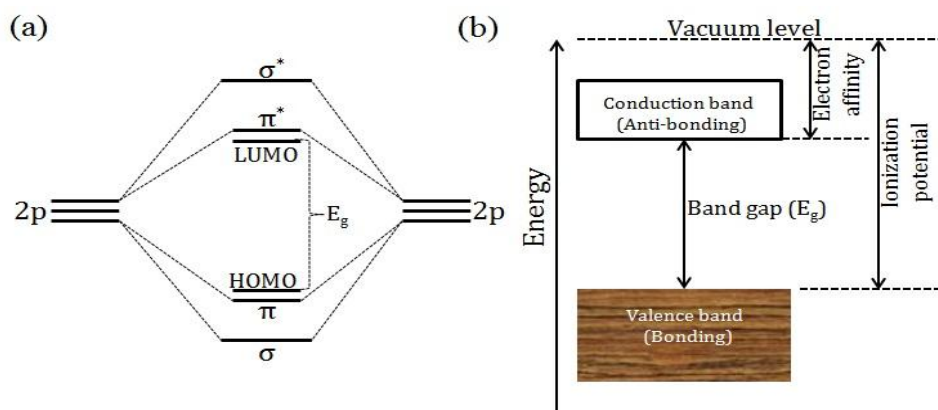


Figure 1.3: (a) Energy level splitting of orbitals in a conjugated polymer according to a molecular orbital theory. (b) HOMO, and LUMO refer to highest occupied molecular orbital and lowest unoccupied molecular orbital, respectively. It shows the molecular orbitals form bands separated by an energy gap.^[8]

The energy levels of these bands are reliant on the length of the conjugated segments. Figure 1.4 indicates how the band-gap of organic materials varies with respect to the number of carbon atoms participating to the conjugation length. Nevertheless, parameters such as; chain defects, metallic impurities, the structure of the polymer, etc ... affect the energy levels or the value of the band-gap of a given polymer. Depending on the structure, the type and amount of impurities, the band-gap of semiconducting polymers varies from 0.8 up to 4 eV.^[9] If the band gap of a polymer is much greater than 4 eV, the polymer is considered as insulator and therefore electron transfer between the bands are very limited.

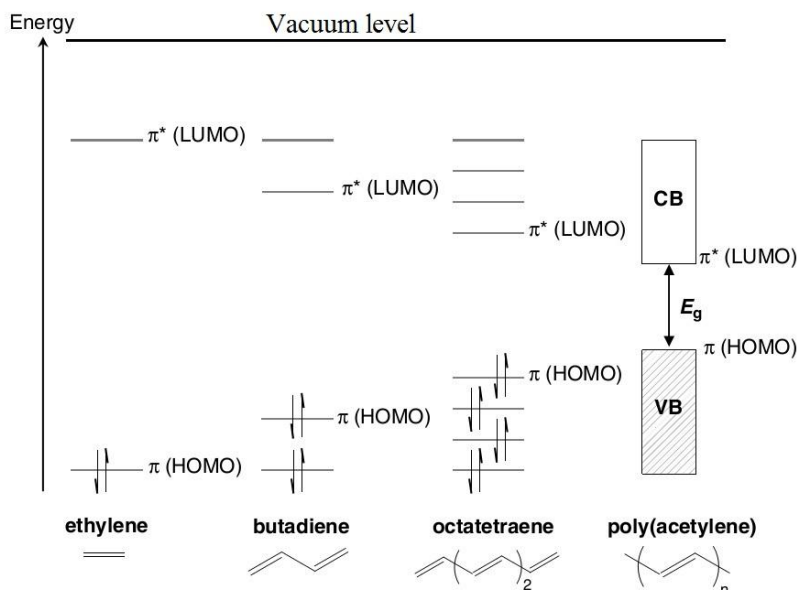


Figure 1.4: The evolution of the molecular orbital diagram (π -levels) with the number of monomer units.^{[10][11]}

The energy gap of conjugated polymers can be determined from optical, electrochemical and other spectroscopic measurements.^[5] Most semiconducting conjugated polymers have band gaps of the order of those detailed in Table 1. The band gaps indicated in Table 1 are well correlated for absorption of visible light. This means that the electrons can interact with light, and it is this property that is exploited in many optoelectronic applications, particularly in OPVs.

Polymer	Band gap (eV)
<i>Trans</i> -polyacetylene	1.4 – 1.5
Polythiophene	2.0 – 2.1
Poly(<i>p</i> -phenylene)	2.7
Poly(<i>p</i> -phenylenevinylene)	2.5
Polypyrrole	3.2
Poly[3,4-(ethylenedioxy)thiophene]	1.6

Table 1: The band gap of some conjugated polymers.^[12]

As previously mentioned, the conductivity in conjugated polymers arises from the π -electron delocalization along the carbon chains. The charge transport in conjugated polymers can involve the following processes: conduction along the polymer backbone (like band transport), hopping across chains due to inter-chain interactions or tunneling between conducting segments.^[9] For totally disordered polymer films, charge mobilities are small, in the range $10^{-6} - 10^{-3} \text{ cm}^2.\text{V}^{-1}.\text{s}^{-1}$. However, the mobilities can be significantly increased by order of magnitudes for ordered structures.^[13] Generally, the charge carrier mobilities (μ) of pure conjugated polymers are typically in the region of 10^{-6} to $10^2 \text{ cm}^2.\text{V}^{-1}.\text{s}^{-1}$ and their conductivity usually ranges from 10^{-14} to 10^2 S.cm^{-1} .^[9] As a comparison, inorganic materials such as polycrystalline silicon exhibit mobilities of the order of $10^2 \text{ cm}^2.\text{V}^{-1}.\text{s}^{-1}$. The mobility of semiconducting conjugated polymers as compared with that of other semiconductors is shown in Figure 1.5. More details on this and the transport of charges in polymers can be found in the work of Jaiswal and Menon^[9] and others.^{[14][15][16][17]}

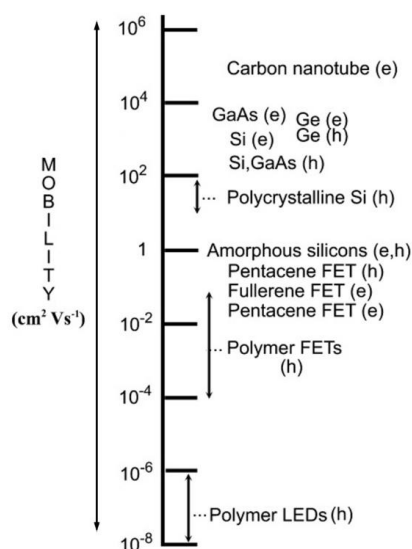


Figure 1.5: Mobility of semiconducting polymers compared with that of other semiconductors. The electron mobility is denoted as 'e' and the hole mobility is denoted as 'h'.^[9]

1.3. Operational Principles of Organic Solar Cells (Photovoltaic Device Physics)

Charge generation in organic semiconductors can take place by different means other than thermal excitation across the band-gap. Charges can be generated by either of the following mechanisms: (i) impurity excitation *i.e.* by introducing p-type and n-type dopants that create sub gap levels from which thermal excitation can be efficient; this is happening in conducting polymers and organic sensors; (ii) through injection from electrodes *e.g.* this charge carrier generation is mainly observed in OLEDs and OTFTs; (iii) or through photo-excitation *i.e.* excitons can be photo-induced and get dissociated into free *electrons* and *holes* either through electron transfer-induced dissociation or electric field-induced dissociation, this mechanism is mainly occurring in OPVs and photoconductors.^{[3][18][19]}

Efficient photovoltaic operation, whether organic or inorganic based devices, relies upon the efficient separation of charges and their collection at the device electrodes. Unlike inorganic based PV devices where an electron and a hole are generated by an immediate light absorption (oppositely charged carriers are only weakly bound due to an efficient electrostatic screening), the charge generation (separation) in organic photovoltaic devices is a multistep process. The steps involved in the conversion of incident light to electricity are shown in the flow chart depicted in Figure 1.6. As shown in Figure 1.6, semiconducting photo-sensitive material in an OPV cell absorbs irradiated light, which excites electron from its highest occupied molecular orbital to its lowest unoccupied molecular orbital (*i.e.* π to π^* transition). After light absorption, organic semiconductors generate bound electron-hole pairs named excitons. They diffuse in the semiconductor until they either decay radiatively (as in the case of LED) or dissociate into separate electrons and holes. This splitting can occur at a defect or trap site, or as it is usually intended, at the interface with a different organic semiconductor. The separate charges are then transported to the contacts under the influence of the built-in electric field which arises from the difference in the work function of the two electrodes. Finally the charges are collected at the contacts, and a photocurrent is extracted. This current can then be

used to do work (as in a solar cell) or used as a signal to detect and quantify light radiation (as in photodetector). A more detailed representation is also given in section 1.4.2 below.

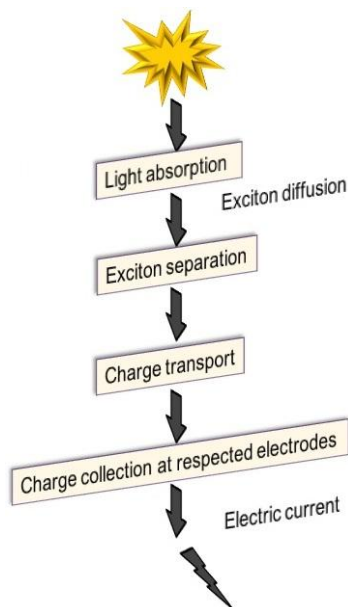


Figure 1.6: A flow chart showing the steps involved in the conversion of light to an electric current.

All of the steps in the flow diagram of Figure 1.6 are influenced by a large number of factors such as the optical properties of the semiconductor polymer (*i.e.* how much of the solar spectrum is absorbed by the conjugated polymer or the mismatch with respect to the light spectrum), the organization of the photoactive material in solid state (or film), the device structure, the type of electrodes, etc.^[20] As no material can absorb across the whole solar spectrum, there will always be wasted photons. Therefore, the first prerequisite for an efficient solar cell is to capture a large fraction of the incoming sun light by the conjugated polymer in the active layer. Hence, the semiconducting polymer is expected to have an optimum band-gap to absorb enough photons from the solar spectrum. However, most solution processable semiconducting polymers have band gaps larger than 1.9 eV, meaning that most conjugated polymers absorb in the green or blue regions of the spectrum (*i.e.* absorption at higher wavelength; in the red or infrared regions is harder to achieve). We can observe this variation in Figure 1.7, where the most studied conjugated polymer - poly(3-hexylthiophene) (P3HT) – only absorbs a fraction of the light spectrum of the standard Air Mass 1.5

global (AM 1.5G) solar spectrum. Additionally, the low charge carrier mobilities in conjugated polymers limit the useful thickness of devices to approximately 100 nm, which in turn leads to the absorption of only about 60 % of the incident light at the absorption maximum.^[20] This indicates that performance of an organic PV device is highly dependent on the absorption efficiency of the conjugated semiconductor polymer. To harvest the wasted photons, a number of researches are ongoing through the development of new donor conjugated polymers with tailored energy levels and good processability (such as the “low band gap” conjugated polymers). As such, internal quantum efficiency nearly reaches ~100% for a single bulk-heterojunction (OPVs) using *poly[N-9''-hepta-decanyl-2,7-carbazole-alt-5,5-(4',7'-di-2-thienyl-2',1',3'-benzothiadiazole)* (PCDTBT) low band gap alternating copolymer as donor and fullerene derivative as an acceptor under AM 1.5G irradiation of 100 mW.cm^{-2} illumination intensity.^[21]

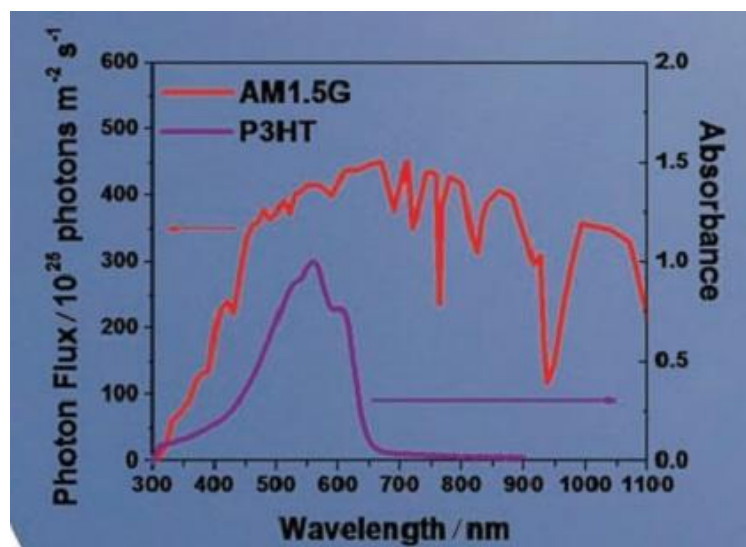


Figure 1.7: The typical P3HT absorption as compared to the solar emission spectrum (AM 1.5) of the sun.^[22]

In addition, researchers also focus on new processing techniques to obtain optimal mesostructures in the active layer as well as on the design of new device architectures with enhanced interfacial layers in order to induce efficient charge generation, transport and collection within a given semiconducting polymer. For example, Yang *et al.* have employed a multijunction (tandem) device architecture with a

low band-gap conjugated polymer to achieve a PCE of 8.62% from previously reported PCE of ~ 6.0%.^[23] This clearly shows the influence of device architectures on either exciton dissociation or efficient charge collection mechanisms or both.

1.4. Organic Photovoltaic Device Architectures

1.4.1. Introduction

The exciton dissociation can be improved by rectifying the energy level misalignments at the donor/acceptor interface or by using a proper type of device configurations. For example; if we go back to the early developments of organic photovoltaics, the power conversion efficiency was greatly improved by using double layer device architectures than single layer device models. The single-junction PV device consists of a layer of organic semiconductor sandwiched between two different metallic contacts, typically indium tin oxide (ITO) and a low work function metal such as Al, Ca or Mg (Figure 1.8a). The model was first reported 1959, where an organic material (*i.e.* anthracene crystal) was sandwiched between two dissimilar electrodes to fabricate organic solar cells.^[24] Since exciton creation and dissociation are taking place in a single material (mostly at the interface between the semiconducting organic layer and the cathode metal), exciton and charge loss through recombination is generally high. However; this problem was partially overcome by using a double layer device architecture (Figure 1.8b) which was developed by Tang in 1986.^[25] Additional organic material with high electron affinity (*i.e.* an acceptor material) was deposited on top of the donor material from orthogonal solvents or through evaporation to break-up the Coulomb force that bounds the electron-hole pairs. Sariciftci *et al.* applied this model to fabricate a double layer conjugated polymer PV cell by evaporating C₆₀ on top of a spin-coated poly[2-methoxy-5-(2'-ethylhexyloxy)-p-phenylene vinylene] (MEH-PPV) layer.^[26] The device structure consisted of indium tin oxide (ITO)/MEH-PPV/C₆₀/Al (Au). The C₆₀, with an electron affinity about 0.7 eV greater than that of MEH-PPV, was used to accept electrons from the conjugated polymer and transport them to the top electrode (aluminum or gold). The PCE improvement could be ascribed to the enhanced exciton diffusion and dissociation efficiencies

because the bilayer device allows interfaces between the polymer and another semiconductor which will allow efficient exciton dissociation as compared to single layer devices. The performance of a bilayer conjugated polymer PV cells, however, still has limitations as regards to external quantum efficiency (generally less than 10%) when compared to conventional organic or inorganic PV devices since only the excitons created at the bilayer interface are participating to charge generation.

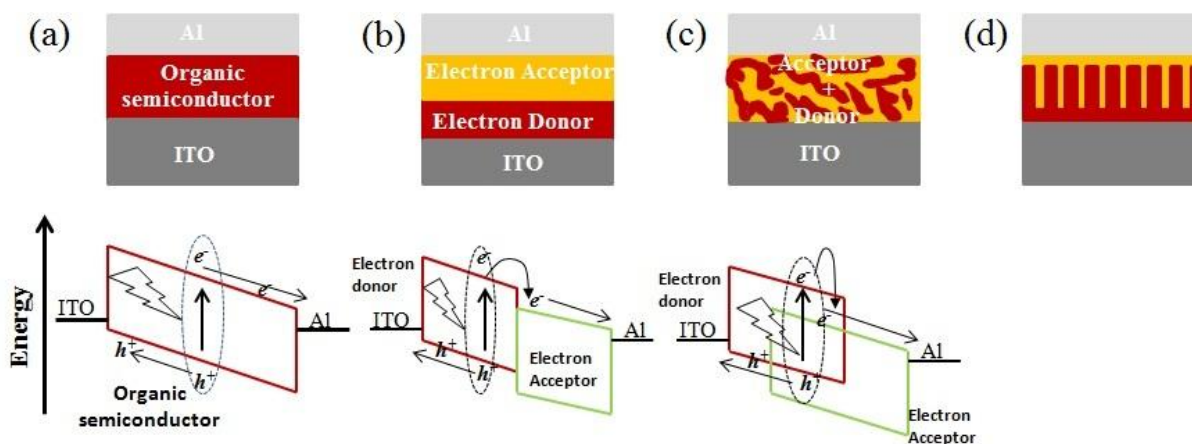


Figure 1.8: The different architectures of organic photovoltaic cells: (a) single-layer PV cell; (b) bilayer PV cell; (c) conventional bulk heterojunction; (d) Ideal bulk heterojunction.

So far, the most efficient and useful architecture used in organic photovoltaics is the bulk heterojunction (BHJ) device (Figure 1.8c). The active layer of BHJ organic solar cells is processed through the blending of two organic semiconductors, acting as electron donor and acceptor, sandwiched between two electrodes with different work functions. Since the work on this thesis is mainly focused on this class of device architecture, a detailed description on the device architecture and the type of semiconducting polymers used as donors and fullerene derivative as acceptors is briefly presented below.

1.4.2. The Bulk-Heterojunction (BHJ) Device Architecture

The current best polymer-based organic solar cells (OSCs) are made up of a blend of two semiconducting materials, an electron donor (like polymer or small molecule) and an electron acceptor (usually fullerene and its derivatives, polymer or small molecule) sandwiched between two metals (anode and cathode) as shown in Figure 1.9a. One of the electrodes is transparent in order to let the light in. The protective substrate can be glass or an inert polymer, such as poly(ethylene terephthalate) (PET) or poly(ethylene naphthalate) (PEN). In the dominant physical process, the photo-active material absorbs light and an electron is excited from its lower energy level (from its HOMO level) to higher energy level (LUMO) resulting in the formation of an electron-hole pair, termed as exciton (Figure 1.9b). If the exciton is perturbed by an interface in the composite between the donor and the acceptor, energy can be transferred across the physical boundary to yield to an electron in the acceptor phase and leave a hole in the donor phase. For this physical process to happen, a large number of donor-acceptor interfaces throughout the composite layer formed by the mixture of the donor and acceptor components in the single layer is highly favorable (Figure 1.9a).

It was initially reported in the early 1990s, that a conjugated semiconducting polymer - MEH-PPV - mixed with fullerene (C_{60}) forms a percolated network between the donor and acceptor.^[27] The concept of BHJ was initiated from previous work in which photoinduced electron transfer with a sub-picoseconds transfer rate has been observed in composites of polymer and C_{60} .^[28] The transfer of energy would occur if the exciton is exposed to an acceptor interface within 5 – 10 nm from its point of formation.^{[29][30][31][32]} Once the excitons are dissociated, the charges percolate along the respected phase towards the electrodes through an electric field induced by the different work functions of the cathode and the anode, as shown in Figure 1.9b.^{[21][22][33][34][35][36]}

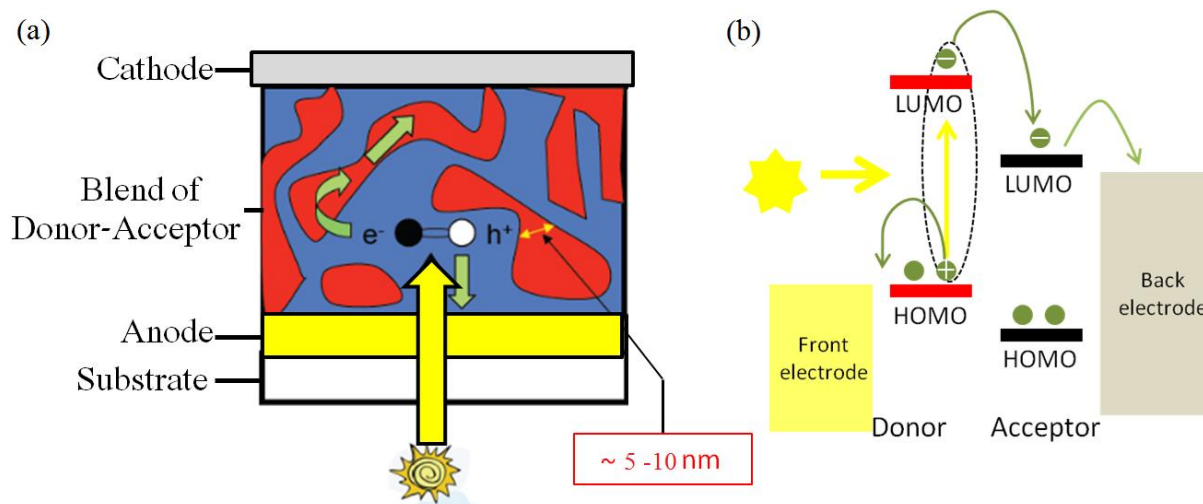


Figure 1.9: Basic principles of organic photovoltaics cells.

A typical BHJ solar cell consists of an ITO transparent electrode sputtered on glass, while the second electrode (cathode) is made by a thin layer of a low work-function metal (e.g., aluminum or silver), deposited on the active layer by evaporation. ITO is chosen thanks to its relatively good electrical conductivity (lower resistivity, 10 to 20 Ω/\square) and its high optical transparency in the visible range of the spectrum. Other organic and/or inorganic buffer layers (e.g., poly(3,4-ethylenedioxy thiophene):polystyrene-sulfonate, PEDOT:PSS) is also incorporated at the interfaces to improve the matching between the work functions of the anode or the cathode with respect to the active layer components so that charge collection process is facilitated.^{[37][38]} Therefore, the conventional configuration consists of glass/ITO/ PEDOT:PSS/active layer/cathode interlayer (e.g., Ca or LiF/Al). Low-work-function electrodes (e.g., Al) are easily oxidized and make the device unstable in air. To avoid the need of sophisticated encapsulation techniques, another type of device configuration was developed. The inverted configuration comprises glass/ITO/electron transporting metal oxide layer/active layer/hole transporting interfacial layer/Ag; where Ag with its high work function is stable in air and is used as the top electrode. An oxide hole transporting layer (e.g., MoO₃) is introduced between the active layer and the top electrode to facilitate hole transport.^[39] To fulfill the goal of using solution processing technique in each steps, either zinc oxide (ZnO) nanoparticle^{[40][41][42][43]} or titanium sub-

oxide (TiO_x)^{[44][45][46]} electron transporting layer are usually spin-coated on top of ITO. Figure 1.10(a) and (b) display the conventional and inverted organic solar cells, respectively.

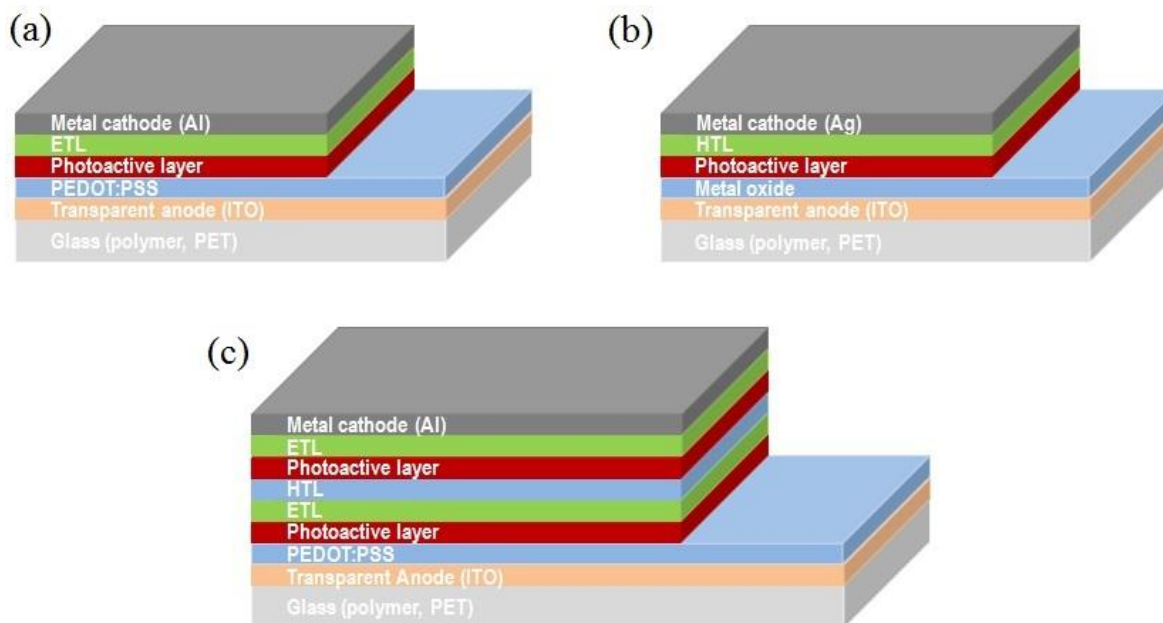


Figure 1.10: Device architectures of organic photovoltaics (a) conventional single-junction BHJ cell, (b) inverted single-junction BHJ cell, and (c) conventional (direct) multi-junction BHJ tandem cells.

The performance of PV devices are expressed through the open circuit voltage (V_{OC}), the short circuit current (J_{SC}) and the fill factor (FF). All these parameters are material characteristic (depends highly on type of conjugated polymer used). They are also very much reliant on the microstructure of the donor-acceptor components and the processing conditions. More detailed information about the PV parameters is presented in chapter 7. In theory, the PCE of a single-junction cell can be pushed toward 15% if low-band-gap polymers are introduced within BHJ configurations.^[47] But due to some processing constraints the PCE is lower than the theoretical predictions. To overcome this limitation, the concept of multi-junction (tandem) cells^[48] was proposed. Applying multi-junction device architecture increases the PV parameters; mainly the V_{OC} . Figure 1.10c presents a schematic representation of a multi-junction tandem cell having the conventional configuration. Two sub-cells are stacked and separated by the electron-transporting layer (ETL) and the hole-transporting layer

(HTL), which can collect electrons from the front cell and holes from the rear cell, respectively. The V_{OC} of a multi-junction cell can be estimated by summing the V_{OC} of the front and rear cells. To broaden the light absorption range, a low band gap polymer is employed for the rear cell to absorb the residual light from the front cell.^[49] However, fabricating the multi-junction BHJ solar cells are not that simple and complex procedural techniques are needed through the fabrication steps. In addition to the ITO-based electrode, other types of electrodes that are highly suitable for solution-processable and roll-to-roll fabrication techniques are emerging. Silver nanowires^{[50][51]}, modified PEDOT:PSS layer^{[52][53]} functionalized carbon nanotubes and graphene^{[54][55]} are some of the examples developed for photovoltaic applications. However, the solution-processable transparent electrodes should have an optimum transparency and electrical resistance before they are fully utilized as a substitute electrode to ITO.

Currently, conjugated polymer and fullerene derivatives BHJ solar cells represent the state-of-the-art organic photovoltaics. Fullerenes and its derivatives are found to out-perform all the other electron-accepting materials (e.g. phthalocyanine, perylenes) in photovoltaic devices due to their high electron affinity, superior capability to transport charges and its solution processability.^{[22][56]} Some of the most widely investigated conjugated polymers as electron donor, fullerene derivatives and poly[(9,9-dioctylfluorenyl-2,7-diyl)-alt-(4,7-bis(3-hexylthiophen-5-yl)-2,1,3-benzothiadiazole)-2',2''-diyl] (F8TBT) conjugated polymer as electron acceptor in OPVs are illustrated in Figure 1.11 and Figure 1.12, respectively.

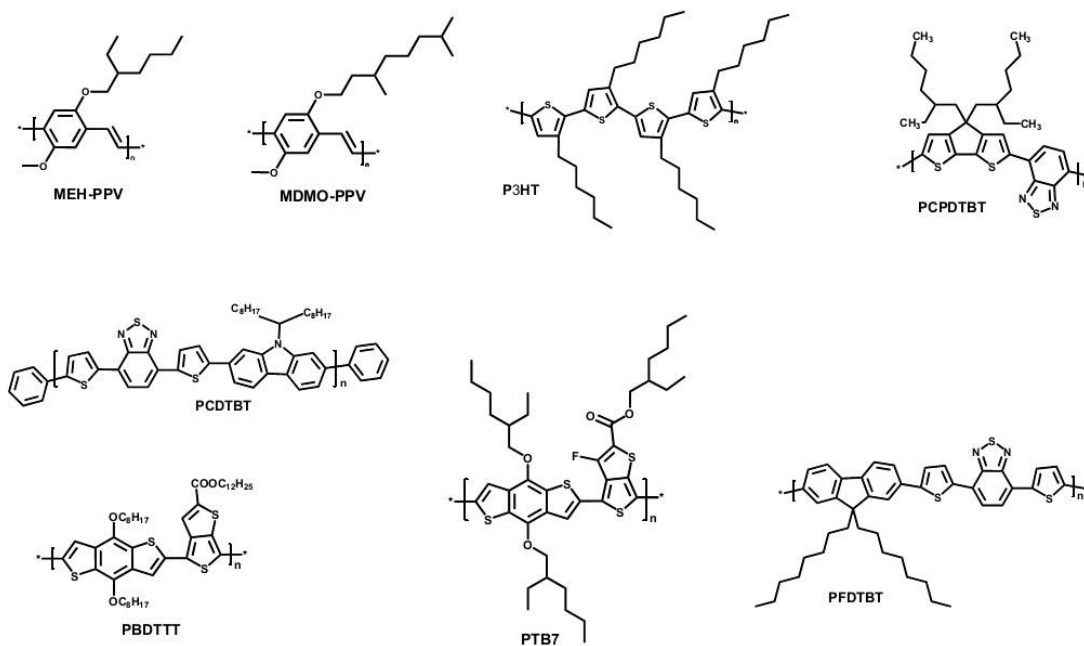


Figure 1.11: Chemical structures of some conducting π -conjugated polymers used in BHJ OPVs.

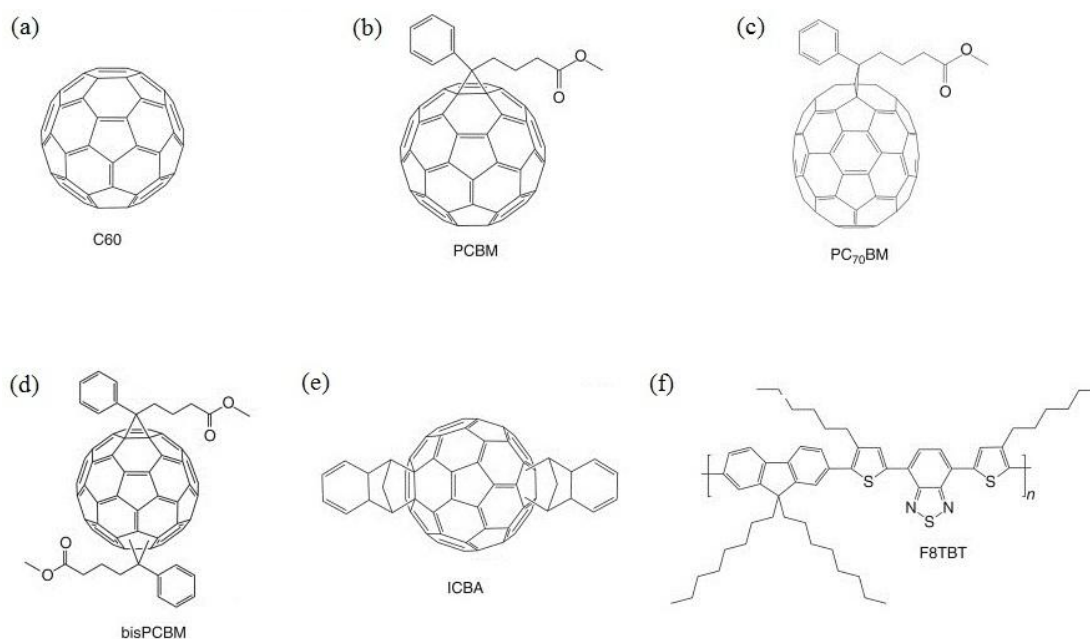


Figure 1.12: Chemical structures of representative acceptors, C_{60} and its derivatives, in OPVs

The regioregular alkyl-substituted polythiophenes currently display a reasonably high hole mobility in the range of $10^{-3} \text{ cm}^2 \cdot \text{V}^{-1} \cdot \text{s}^{-1}$ ^[57] and a field effect mobility which can be as high as 0.1–0.2 $\text{cm}^2 \cdot \text{V}^{-1} \cdot \text{s}^{-1}$ in high quality samples.^{[13][58][59]} The ease to synthesize predetermined molecular

weights,^{[60][61][62][63]} the simplicity of further chemical modification,^{[64][65][66][67][68][69]} its high solubility in organic solvents,^[70] and its semi-crystallinity which facilitates charge transfer through crystalline domains^{[71][72][73][74][75]} have made the regioregular poly(3-hexylthiophene) (P3HT) to become among the most widely studied conjugated polymer in the field of organic electronics, particularly in the OPV devices. The P3HT is generally combined with a modified fullerene (C₆₀), the archetypal product of [6,6]-phenyl C₆₁-butyric acid methyl ester (PCBM) to form a BHJ PV device.^{[76][77][78]} PV efficiency as high as 5% was reported for this class of conjugated polymer in direct type device configurations.^{[79][80]} The improvement in device performance for this class of polymer is due to the fact that rr-P3HT exhibits strong crystallinity and forms, when blends with PCBM, a bicontinuous morphology that significantly facilitates light absorption and charge transport in the composite film. Other macromolecular characteristics of P3HT (molecular weights and dispersity) and pre- and post-processing parameters (solvent type, ratio of the components, thermal and solvent annealing, thickness of the active layer, etc) have also shown to affect the performance of P3HT:PCBM BHJ devices. The review recently published by Dang *et al.* has shown how these mentioned factors effectively affect the performance of P3HT:PCBM BHJ devices (Figure 1.13).^[81] Although the prototypical BHJ solar cells based on P3HT and PCBM has achieved a significant device efficiencies,^{[80][82]} the performance of P3HT:PCBM cells is limited by the absorption range of P3HT. P3HT absorbs visible light until 650 nm (Figure 1.7), meaning that most of the red portion of the visible spectrum and all infrared photons cannot be harvested by P3HT-based photovoltaic cells. Therefore, other conjugated polymers (low band-gap polymers) were designed to solve this problem.

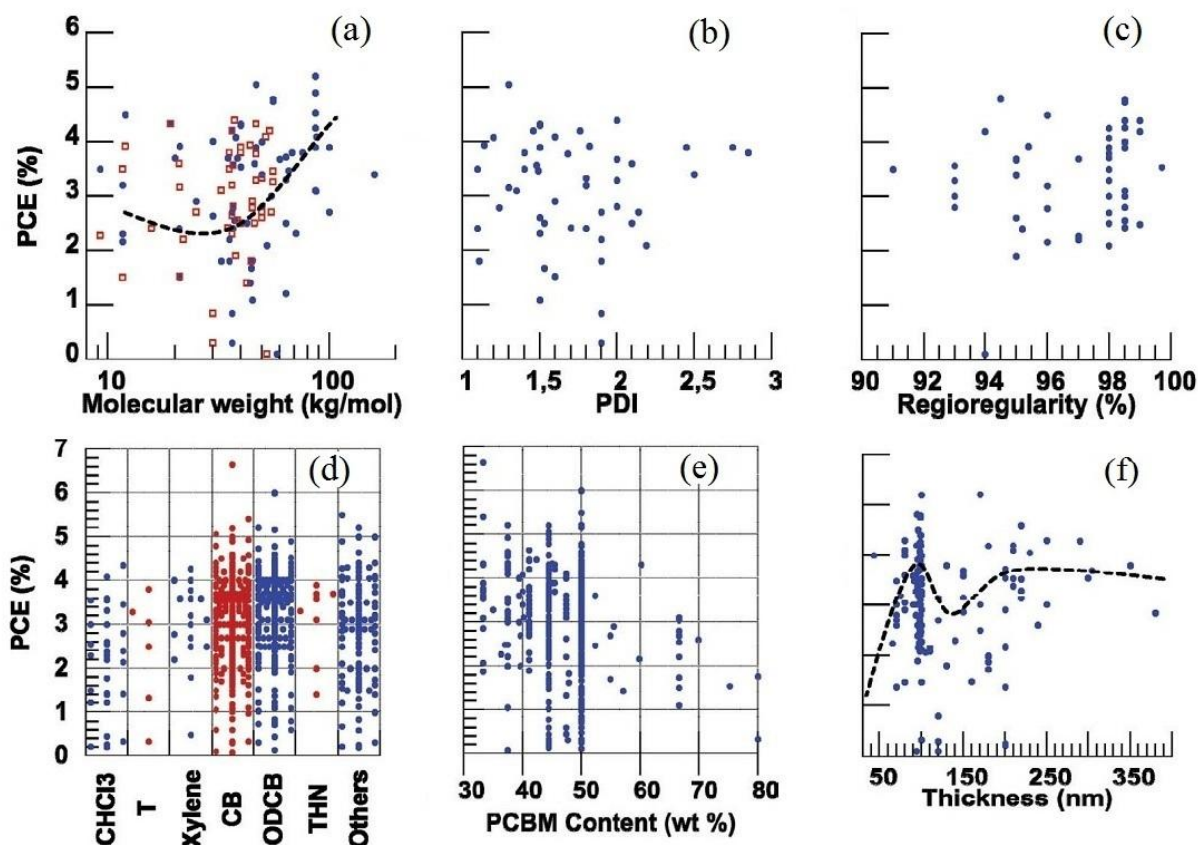


Figure 1.13: PCE of P3HT:PCBM as reported in the literature from 2002 to 2010 with the corresponding parameters: (a) P3HT molecular weights M_w (full-circle) and M_n (empty squares), (b) P3HT Dispersity, (c) P3HT regioregularity, (d) Effect of common solvents used: chloroform (CHCl_3), toluene (T), xylene, chlorobenzene (CB), o-dichlorobenzene (ODCB), and tetrahydronaphthalene (THN), (e) Effect of blend composition and (f) thickness of P3HT:PCBM active layer. The dashed lines are guidelines for the eye.^[81]

In terms of polymer-based photovoltaic systems, any polymer with a band-gap less than that of P3HT (i.e., less than 1.9 eV) is often referred to a low band-gap (LBG) polymers.^[22] LBG conjugated polymers, such as poly(2,7-carbazole) derivatives, have recently shown promising avenues as donor materials because of their air stability and tunable optical and electrochemical properties.^{[83][84][85]} The LBG polymers are commonly synthesized in a donor-acceptor approach, in which the alternating electron donating (benzothiadiazole or analogues) and electron accepting moieties are incorporated along the polymer backbone.^[86] Figure 1.11 includes a few of the successful LBG polymers explored so

far. Among them, poly[2,6-(4,4-bis-(2-ethylhexyl)-4H-cyclopenta[2,1-b;3,4-b]dithiophene)-alt-4,7-(2,1,3-benzothiadiazole)] (PCPDTBT), with a measured optical band-gap of about 1.45 eV, have shown an efficiency of 5.5% by using processing additives to optimize the film morphology.^[87] Luping Yu *et al.* developed novel LBG polymers containing thieno[3, 4-b]thiophene and benzodithiophene units. The first example was poly[4,8-bis-substituted-benzo[1,2-b:4,5-b']dithiophene-2,6-diyl-alt-4-substituted-thieno[3,4-b]thiophene-2,6-diyl] (PBDTTT), which presented an efficiency of 5.6% in conventional photovoltaic devices.^[88] The alteration of the HOMO of PBDTTT by adding the electron-withdrawing functional group results in a polymer (PBDTTT-CF) with a higher efficiency of 6.77% in direct device configuration.^[89] Park *et al.* has reported the power conversion efficiency of poly[N-9"-hepta-decanyl-2,7-carbazole-alt-5,5-(4',7'-di-2-thienyl-2',1',3'-benzothiadiazole)] (PCDTBT) and the fullerene derivative (PC₇₁BM) with an overall conversion efficiency of 6.1% on conventional devices architecture prepared by spin coating from dichlorobenzene solution.^[21] Further structural optimization gave the birth to a new LBG copolymer thieno[3,4-b]thiophene/benzodithiophene (PTB7) which presented an astonishing device efficiency of 7.4% in the field of polymer solar cells with direct device architecture.^[90] The maximum power conversion efficiency so far reported in literatures for single junction polymer solar cells is 9.2%.^[91] He *et al.* used inverted device structure, where an alcohol-/water-soluble conjugated polymer, poly[(9,9-bis(3'-(N,N-dimethylamino)propyl)-2,7-fluorene)-alt-2,7-(9,9-dioctylfluorene)] (PFN) is used as the ITO surface modifier, and a blend of LBG semiconducting polymer PTB7 with PC₇₁BM used as photoactive layer (see Figure 1.11 for chemical and Figure 1.14 for device structure).

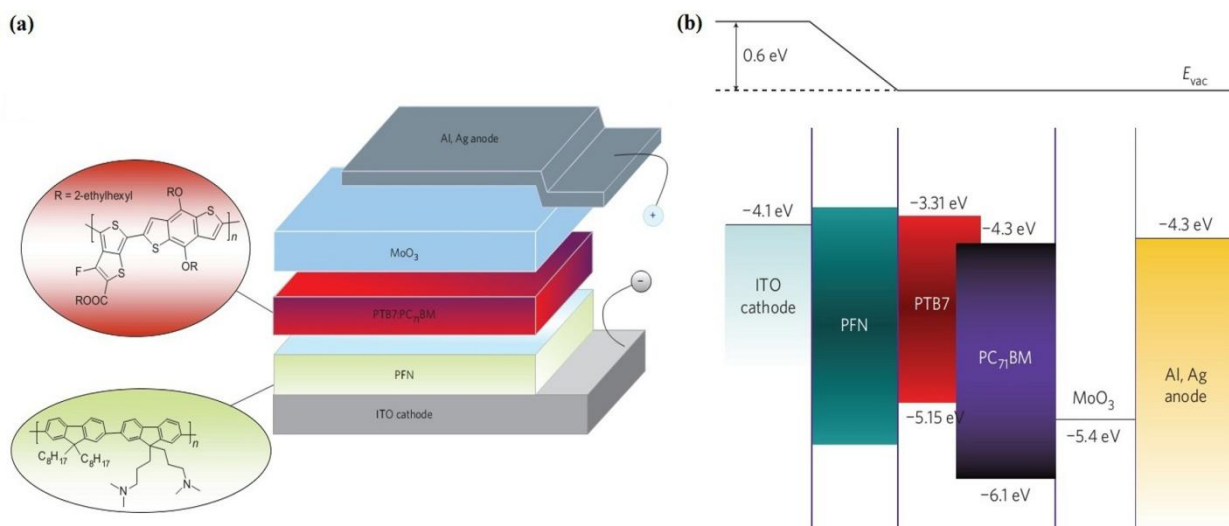


Figure 1.14: Device structure (a) and energy levels (b) of the inverted-type polymer solar cells. The inset shows the chemical structures of the water-/alcohol-soluble conjugated polymer and electron donor materials. The formation of a positive interfacial dipole moment (directed outwards) due to the PFN is shown in (b).^[91]

A certified PCE as high as 8.6% was also reported by Dou *et al* using a blend of polymer (P3HT, PBDTT-DPP):fullerene (IC₇₁BA) using multi-junction solar cells in inverted device configurations.^[23] The device configuration and the energy levels of the tandem solar cell device are presented in Figure 1.15. In the mean time, UCLA-Sumitomo claimed certified device efficiency as high as 10.6% in a multijunction device configuration.^[92] Polymer-polymer^{[93][94]} and polymer-small molecule^{[95][96]} donor-acceptor blends have also been employed in OPV technologies; though the maximum PCE from these blends are still far from the conventional polymer/fullerene derivative devices.

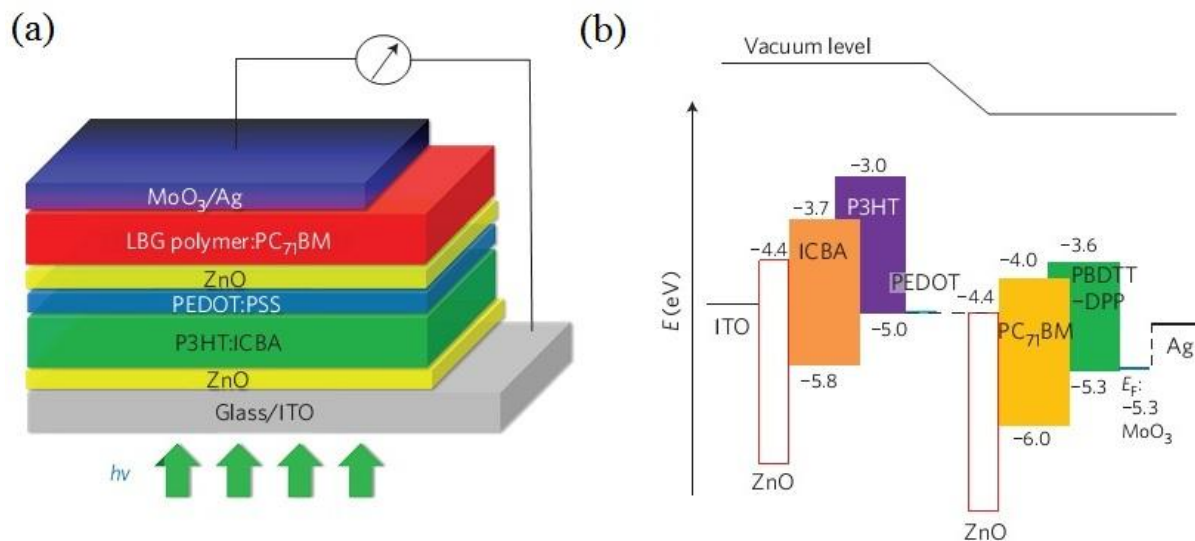


Figure 1.15: Device structure and energy diagram of the inverted tandem solar cell.^[23]

In all of the bulk heterojunction devices that were described to this point, the conjugated polymer and fullerene derivatives forms some organization throughout the film. The microstructure of the donor and acceptor components in BHJ blends has shown to play a significant role on charge photogeneration and transfer properties PV devices. For example, in poorly organized composite films, the isolated domains and randomly distributed interfaces may trap charges leading to high photoluminescence (PL) quenching, thus reducing the PCE. The following section discusses the microstructure of a blend of conjugated polymers with fullerene derivatives and its relation with respect to device performances, mainly taking P3HT:PCBM blend as an example. In the discussion, the factors affecting the morphology of these binary blends are highlighted.

1.5. Morphology of BHJ systems (the P3HT:PCBM case)

Exciton dissociation (charge generation) and charge transport of organic photovoltaics are strongly dependent on the phase behavior of the donor and acceptor blends.^[97] An unfavorable microstructure of donor–acceptor blend limits the PV characteristics (V_{OC} , J_{SC} and FF), thus the PCE. Controlling the morphology at the optimum scale (*i.e.* nanoscale) is the key challenge for the

development of efficient organic solar cell devices. The morphology of the donor:acceptor components in the PV active layer should fulfill the following criteria:

- (i) The components should phase-segregate in domains with the highest interfacial area for an optimized exciton dissociation;
- (ii) The phase separation should not either be too large or too fine (it should be in order of the exciton diffusion length ~ 10 nm), to avoid geminate and/or bimolecular recombination;
- (iii) It should fully form an interpenetrated and a continuous pathway to the electrodes to ensure an effective charge transport (*i.e.* no formation of isolated donor or acceptor domains so as to avoid charge trapping).^{[98][99]}

However, the real mesostructure of polymer:fullerene blends contains cluster of morphologies ranging from several nanometers (crystallites) to micro-scale aggregates. This formation of a hierarchical type mesostructure in thin films is governed by thermodynamics, and the final structure contains phases with a distribution of sizes (due to coarsening and nucleation effects as well as due to surface wetting and segregations).^[100] Previously, intensive morphological studies have been performed in analyzing the influence of the type of solvent and solution concentration, the ratio between the two components (*i.e.* composition of donor:acceptor), the molecular weight of the polymer, the use of additives, and the temperature and the duration of thermal annealing.^[97] These pre-and post-treatments conditions have a significant effect on the phase separation and crystallization behavior of the donor-acceptor components.^{[80][101][102]} For example, a number of groups have shown correlations between processing parameters and P3HT crystallinity.^{[103][104]} The common structural features of P3HT can be seen either from a crystallography point of view or from its preferred orientations. Due to the coplanar aromatic rings on thiophene and the conjugation through the chain, P3HTs adopts a plane structure.^{[13][105][106][107]} Brinkmann et al. suggested that,^[108] the lattice in P3HT unit cell arranges in a “monoclinic” (or possibly “triclinic”) crystal structure system, as opposed to the “orthorhombic” structure previously suggested by Prosa et al.^[105] The features are created by the

polythiophene chains along the conjugation, along the π -stacking and along the alkyl side chains, where the alkyl side chains act as spacers between polythiophene chains as shown in Figure 1.16. This was confirmed by Electron Diffraction (ED) technique. The study showed that the “monoclinic” structure has two chains per cell ($a = 16.0 \text{ \AA}$, $b = 7.8 \text{ \AA}$, $c = 7.8 \text{ \AA}$, and $\theta = 86.5^\circ$) and that the P3HT stacked planes are distant by 3.4 \AA . The P3HT side chains could be packed into one of the following forms: non-interdigitated (non-tilted), interdigitated (non-tilted) or non-interdigitated (tilted).^[109] Mena-Osteritz et al. performed in-situ scanning tunneling microscopy and found the interdigitation of P3HT side chains in lamellar structures.^[110]

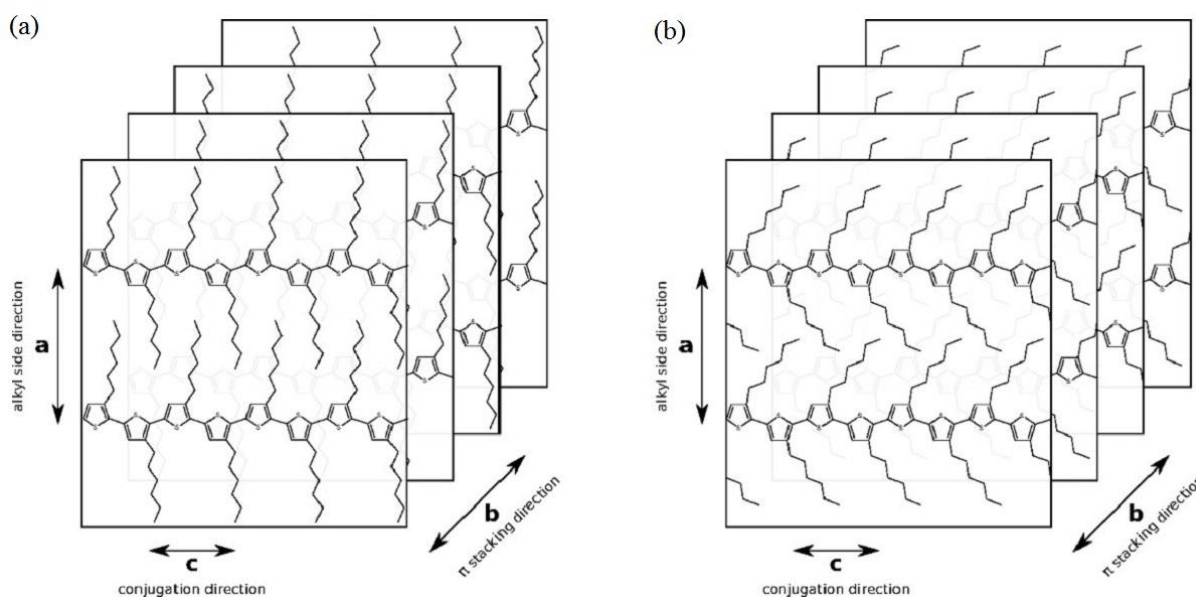


Figure 1.16: The schematic arrangements of rr-HT-P3HT polymer chains characterized by different amount of interdigitation of the alkyl side chains: *a*, *b*, and *c* are the edges of the “monoclinic” cell containing two strands of P3HT chains stacked along the *b*-edge and mutually shifted along the *c*-edge. (a) Comb-like arrangement (significant interdigitation). (b) Fishbone-like arrangement (minimal interdigitation).^[111]

In term of orientation or π -stacking alignment, P3HT chains are thus organized in lamellae which may be perpendicular (out-of-plan / edge-on) or parallel (in-plane orientation) to the substrate depending on the deposition conditions (Figure 1.17).^[112] For example, the orientation of P3HT with

their side chains parallel to the substrate (i.e. the flat-on configuration, shown in Figure 1.17c) was first identified by Fell *et al.* when P3HT solution was deposited by spin coating from chloroform on glass slides.^[113] Later on, Sirringhaus *et al.* discovered two more orientations of microcrystalline P3HT domains using grazing-incidence X-ray diffraction (GIXD) on films deposited in field-effect transistor (FET) configuration: the “edge-on” arrangement in which the side chains are normal to the substrate surface (Figure 1.17b) and an “in-plane” orientation in which the side chains are parallel to the substrate (Figure 1.17a).^[13] However, these orientations are dependent on macromolecular characteristic (i.e. they are dependent on P3HT regioregularity and molecular weight). It was also possible to control the orientation and the alignment of the polymer by tuning the surface properties of the substrate. For example, molecules of P3HT drop-cast on thin films of cross-linked poly(4-vinylphenol) are preferentially oriented edge-on, whereas monolayers of P3HT on Au (111) adopt a plane-on orientation.^[114]

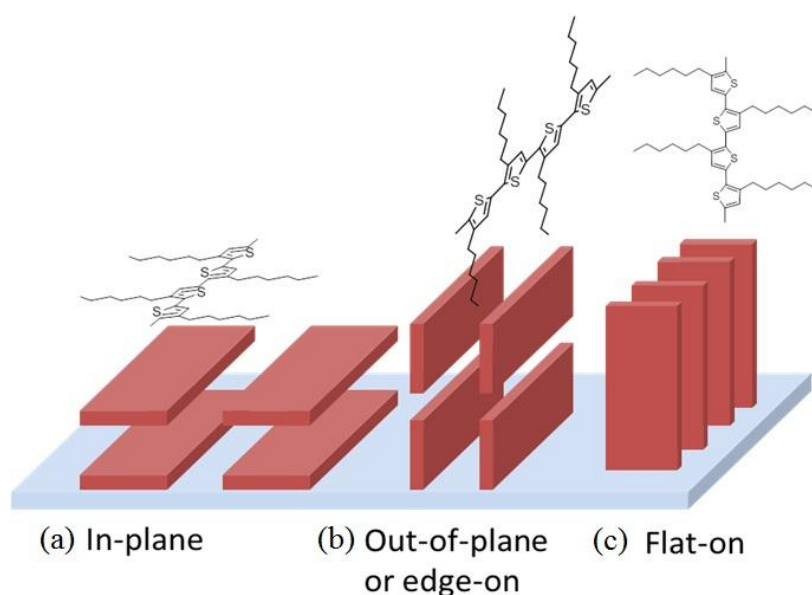


Figure 1.17: The different orientations of the P3HT lamellae.

Charge mobility (hole) in P3HT is highly orientational dependent. Sirringhaus *et al.* showed that the highest hole mobility in molecular field-effect transistors (OFETs) is achieved in P3HT films with an edge-on orientation.^[13] In organic solar cells, charge transport is perpendicular to the

electrodes. Since P3HT has a preferential orientation (*i.e.* the insulating side-chain are usually oriented perpendicular to the substrate), the “edge-on” orientation is unlikely to help charge transport in organic solar cells. However, for the “in-plane” P3HT orientation, interchain transport along the π -stacking direction is an efficient pathway to transport holes (Figure 1.18).^{[115][116]}

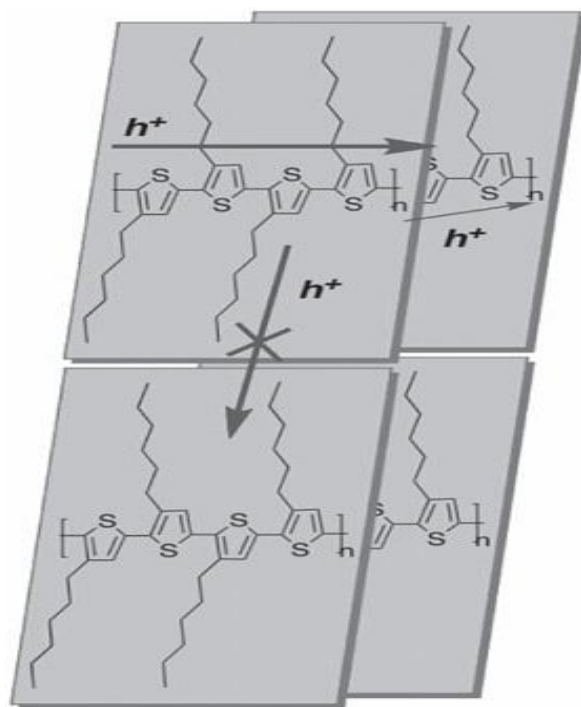


Figure 1.18: Schematic representation of hole (h^+) transport in P3HT.

The P3HT orientation depends on solvent evaporation rate and boiling point as well. Fast deposition techniques, like spin coating, which induce rapid solvent evaporation and/or low boiling point solvents lead preferentially to in-plane whereas edge-on orientation is favored by slow deposition methods and/or high boiling point solvents.^{[115][116][117][118][119]} Film thickness is also a parameter to consider for orientation. Joshi *et al.* and Kline *et al.* found out that in thick films, P3HT is randomly oriented whereas in thinner film, due to the interface influence, the P3HT crystals are orientated in-plane or out-of-plane.^{[120][121][122]} At the mesoscopic scale, P3HT lamellae may be organized in nano-rod or fibrillar structure with variable fibril length up to several microns depending on the P3HT solubility in solvent, the solvent boiling point and the deposition/evaporation

techniques.^{[123][124]} Fibrils are more easily formed when P3HT is deposited from poor solvents like cyclohexanone or xylene.^{[125][126][127]} Besides, the degree of crystallinity increases with the molecular weight of the P3HT. The hole mobility and photovoltaic performance increase with the molecular weight due to the increase of the intermolecular ordering (or π -stacking) of the P3HT phase^[128] while short molecular-weight fractions were shown to have inferior hole mobility, most likely because of main-chain defects.^{[71][129]} It has been suggested that "ideal" morphology of P3HT for OPV application is possible to obtain with an average M_w in the range 30 – 70 Kg/mol, and a rather high dispersity of around 2, as it gives a good mix of highly crystalline regions formed by low- M_w P3HT interconnected by a high- M_w P3HT matrix upon thermal annealing.^[130]

Thermal and solvent annealing are some of the standard tools that are usually employed to improve phase separation and crystallinity of the polymer phase.^{[80][131]} Figure 1.19 illustrates the phenomenon in P3HT:PCBM blends before and after thermal annealing. Different studies have shown that the blend of P3HT and PCBM is composed of three different phases: crystalline P3HT, aggregates of PCBM and an intermixed phase containing PCBM moieties in the amorphous P3HT regions.^{[132][133][134]} The intermixed areas enable improved exciton dissociation because of the proximity between P3HT and PCBM and the crystalline and aggregated areas provide an efficient charge transport to the electrodes.^[135] Crystallization in P3HT:PCBM blend film upon thermal annealing is a two-step process. First, local P3HT organization in fibers occurs, then, for longer annealing time, PCBM clusters are formed.^{[72][136]} Several studies showed that the addition of PCBM may disrupt or change the P3HT lamellae orientation or crystallization properties.^{[137][138]} This is demonstrated when a decrease in melting point of P3HT is observed upon PCBM addition.^[139] PCBM restricts the P3HT crystallization and limits the P3HT crystal size upon blending with PCBM.^[140] The degree of disruption depends on the amount of PCBM added into P3HT. However, in another study, Treat *et al.* used a bilayer of P3HT and PCBM model system to develop a more complete understanding of the miscibility and diffusion of PCBM within P3HT during thermal annealing.^[141] In this study, they report that PCBM

aggregates and/or molecular species are miscible and mobile in disordered P3HT, without disrupting the orientation of P3HT (ordered lamellar stacking of P3HT chains), as well as the crystal size and structure even at an equal P3HT:PCBM weight ratio.

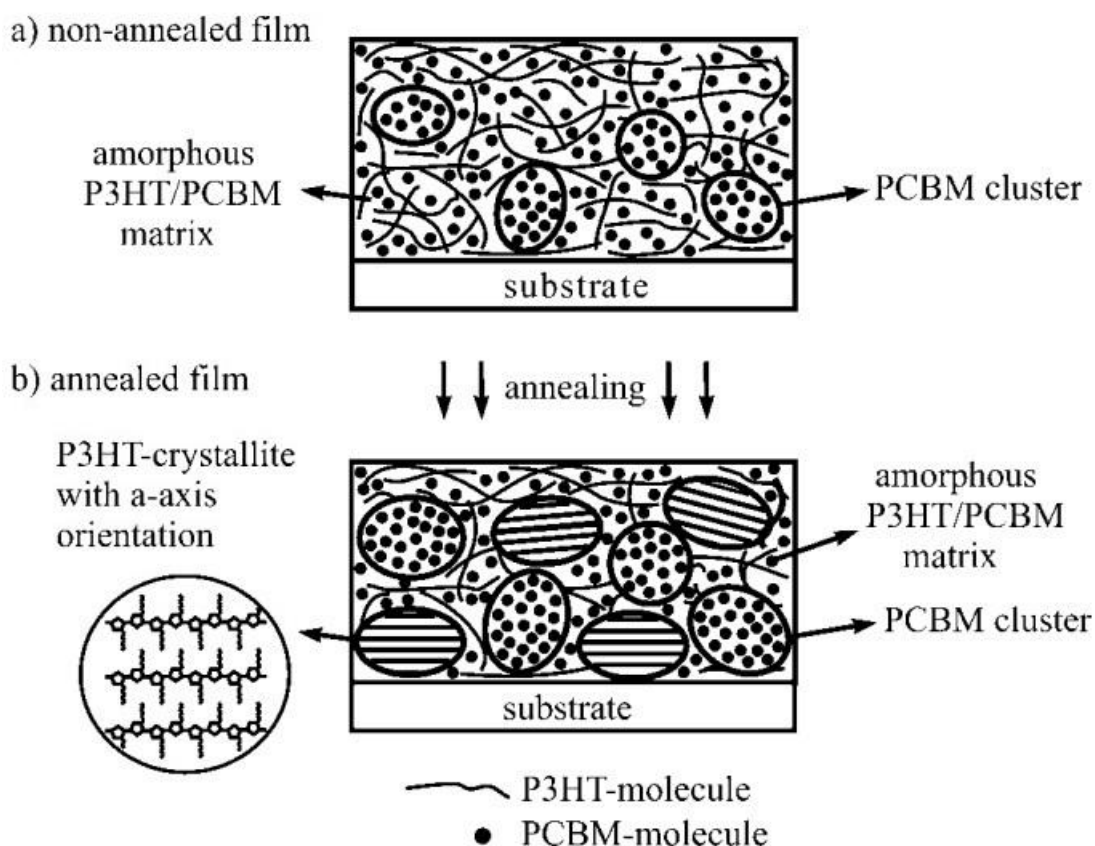


Figure 1.19: Schematic representation of the structural changes in P3HT:PCBM blends upon thermal annealing.^[134]

The formation of PCBM clusters through PCBM crystallization firstly occurs in the form of nanocrystals and then grows into needle-like micrometric aggregates as a function of annealing time at high temperature. This mechanism is similar to the Ostwald ripening process; upon thermal annealing the size of the aggregates increases significantly while their number density decreases simultaneously.^{[142][143]} As explained earlier, the P3HT crystallization and the formation of PCBM clusters during annealing may have two different behaviors depending on the annealing conditions.^{[144][145]} Under mild annealing conditions (5 min, 100 °C), only P3HT starts to crystallize. However, increasing

the annealing time and temperature leads to the formation of PCBM aggregates with size up to 100 μm . The formation of micrometric PCBM aggregates indicates the high degree of phase separation in P3HT:PCBM blends. This macrophase separation between P3HT and PCBM is usually associated with the lower efficiency obtained in P3HT:PCBM based PV devices as these agglomerates act like traps for charge carriers.^{[144][146]} However, the morphological relationships with device properties are not always straightforward to interpret. Experimental results revealed that increased P3HT crystallinity promoted through thermal or solvent annealing, increases device performance but also increases the intensity of photoluminescence (PL).^[147] This is a counterintuitive phenomenon. Kiel et al. demonstrated that the as cast film provides less PL indicating a high degree of exciton separation as compared to the annealed sample. However, the annealed sample is a substantially better solar cell device with an improved short circuit current and device efficiency as clearly shown in the Figure 1.20b. This phenomenon is either due to the coarsening effect of PCBM domains upon annealing so that efficient charge transport will be more dominant or due to the accumulation of PCBM components at the film-air interface creating an improved pathway for electrons to leave the device towards the metal electrode.^[148]

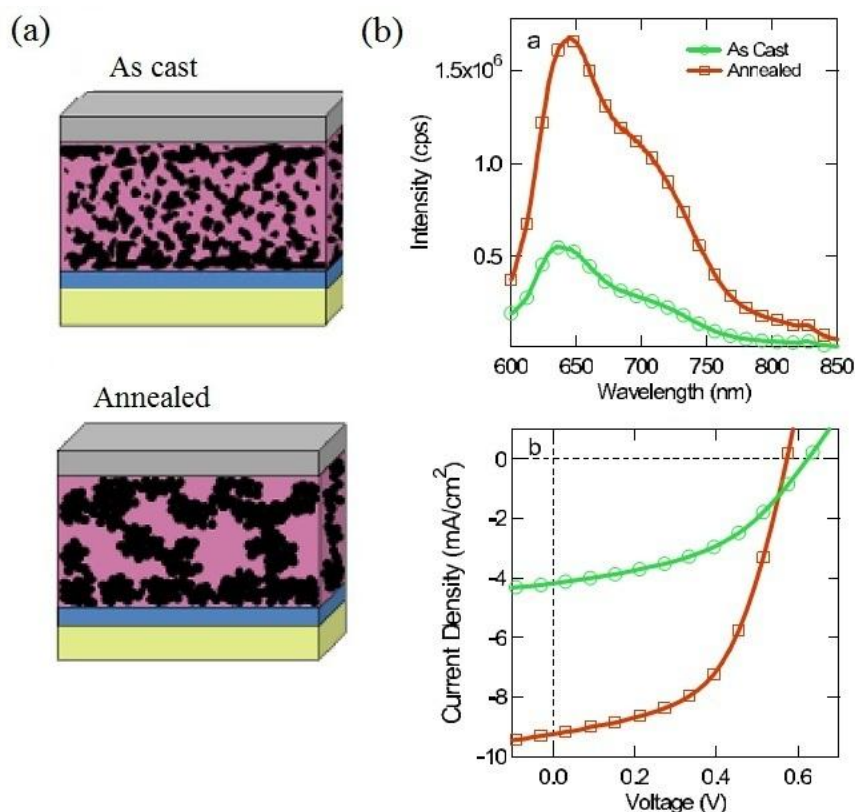


Figure 1.20: (a) Schematic representations of the morphological changes before and after thermal annealing. (b) Comparison of thermal annealing effects on photoluminescence and solar cell performance. Thermal annealing P3HT:PCBM (1:1 w/w) solar cell at 140 °C for 20 min increases the total amount of photoluminescence, indicating a much higher degree of recombination. However, this annealing also produces much improved device efficiency, increasing from 1.2% to 2.9%. ^[148]

The effect of other parameters, such as the ratio between P3HT and PCBM or the casting solvent have shown an important influence on the morphology of the active layer and therefore on device performance.^[149] In most studies the ratio of P3HT and PCBM to make PV devices lies between 1:0.8 and 1:1 both in w/w. The influence of the PCBM composition on the P3HT crystallization has been studied previously.^{[138][150]} As the amount of PCBM content increases (> 67% w/w), a blue-shift is observed along with the disappearance of the vibronic band, showing the disruption of P3HT π - π stacking. This observation was confirmed by XRD.^[151] As the PCBM content increases, edge-on crystal orientation is more dominant which shows the disruption of the P3HT π - π stacking. The origin of this

disruption may be due to the presence of disordered P3HT:PCBM mixed domains intercalated between the P3HT main chains. The poor light absorption at high wavelength and the disruption of the π - π packing lead to poor photovoltaic performance at higher PCBM content.^[152] In another development, regarding the influence of the casting solvent, the active layer made from toluene gave a PCE of about 0.9%, while using chlorobenzene increased the efficiency to 2.5%.^{[149][153]} Morphological studies revealed that a microscale phase segregation in the toluene-cast films with a micrometer-sized PCBM clusters, while in the chlorobenzene-cast films the size of the domains was reduced to a few tens of nanometers.^[154] All these results confirm and highlight the importance of macromolecular characteristics, annealing steps, type of solvent used for organizing the polymeric blends in order to achieve better device performance.

1.6. Conclusions

So far, we have seen the mechanisms of charge generation in organic semiconductors and the relation to organic photovoltaics. The charge generation, separation and charge transport in OPV devices are dependent on numerous parameters. One of the main parameters is the mesostructure of the photovoltaic active blend. In P3HT:PCBM blends, the device performance is highly dependent on P3HT crystallinity and the length scale of PCBM aggregates. Besides, the degree of phase separation is affected by material characteristic and process parameters. The macromolecular characteristics of P3HT (molecular weights and dispersity) and pre- and post-processing parameters (solvent type, ratio of the components, thermal and solvent annealing, thickness of the active layer, etc) have shown to affect the morphology, as the result the PCE of the BHJ device. For example, annealing treatment leads to the increase of the phase separation between P3HT and PCBM components while it increases the crystallinity of the P3HT phase which generally improves the absorption and the charge transport properties.

1.7. Problem and Aim of the Project

The PCE of solar cells made of a photo-active conjugated polymer as the electron donor and a soluble fullerene derivative as the electron acceptor in the form of BHJ have shown a significant stride within the last decade. However, there are several factors that have to be addressed in OPV technology before polymer solar cells become efficient enough for commercialization. For example, the active layer microstructure in BHJ organic solar cells which plays a key role on the properties of charge transfer, transport and consequently on the PCE of the PV devices have to be tuned in order to provide the optimal structure for photovoltaic applications. Ideally a crystalline and an interpenetrating donor-acceptor network with a size scale comparable to the exciton diffusion length is required within the active layer in order to achieve higher PCE. To obtain an optimized micro-structured in the BHJ active layer, a number of post-processing techniques such as annealing (thermal and/or solvent) is commonly performed. However, the formation of micro- and nano-scale mesostructures in the BHJs begins with spontaneous phase separation between the donor and the acceptor components during solvent evaporation. Although phase separation in those films is governed by thermodynamics, it is difficult to control experimentally, and the final structure results in uneven domain size distribution due to coarsening and nucleation effects. This implies that the factors affecting the development of specific thin film structures on those blends are not yet fully understood. The work in this thesis mainly aims to understand the interplay between morphology and performance relationships of OPV blends. In order to achieve the objective, a novel approach based on block copolymers as nucleation agents or as nano-structuring agents for enhancing crystallinity of the donor polymer or to enhance the compatibility between donor-acceptor components, mainly in P3HT:PCBM blends are employed. An integrated structural study of the P3HT:PCBM blend upon addition of different block copolymers using different structural characterization techniques, such as; optical microscopy, scanning force microscopy (SFM), grazing-incidence X-ray diffraction (GIXD), neutron reflectivity (NR), and UV-vis spectroscopy have been utilized besides to the electrical properties investigations.

References

- [1] M. Schwoerer, H.C. Wolf, *Organic Molecular Solids*, Wiley -VCH, Weinheim **2007**.
- [2] W.D. Callister, D.G. Rethwisch, *Materials Science and Engineering: An Introduction*, **2006**.
- [3] W. Brütting, *Physics of Organic Semiconductors*, WILEY-VCH Verlag GmbH & Co. KGaA, Weinheim **2005**.
- [4] G.M. Loudon, *Organic Chemistry*, The Benjamin Cummings Publishing Company, Inc. **1995**.
- [5] W.R. Salaneck, R.H. Friend, J.L. Bredas, *Physcs Reports* **1999**, 319, 231–251.
- [6] A.J. Heeger, *Reviews of Modern Physics* **2001**, 73, 681–700.
- [7] R. Hoffmann, C. Janiak, C. Kollmar, *Macromolecules* **1991**, 24.
- [8] A.J. Heeger, *Chemical Society Reviews* **2010**, 39, 2354–71.
- [9] M. Jaiswal, R. Menon, *Polymer International* **2006**, 55, 1371–1384.
- [10] A.-J. Attias, *Techniques De L'ingénieur* **2002**, E1862–20.
- [11] U. Salzner, J.B. Lagowski, P.G. Pickup, R.A. Poirier, *Synthetic Metals* **1998**, 96, 177–189.
- [12] A. de Cuendias, R.C. Hiorns, E. Cloutet, L. Vignau, H. Cramail, *Polymer International* **2010**, 59, 1452–1476.
- [13] D.M. Siringhaus, H.; Brown, P. J.; Friend, R. H.; Nielsen, M. M.; Bechgaard, K.; Langeveld-Voss, B. M. W.; Spiering, A. J. H.; Janssen, R. A. J.; Meijer, E. W.; Herwig, P. & de Leeuw, *Nature* **1999**, 401, 685–688.
- [14] N. Kirova, *Polymer International* **2008**, 688, 678–688.
- [15] A. Moliton, R.C. Hiorns, *Polymer International* **2004**, 53, 1397–1412.
- [16] J. Roncali, *Chemical Reviews* **1992**, 92, 711–738.
- [17] M. Kertesz, C.H. Choi, S. Yang, *Chemical Reviews* **2005**, 105, 3448–3481.
- [18] J. Hirsch, *J. Phys. C: Solid State Phys.*, **1979**, 12, 321–335.
- [19] P. Stallinga, *Advanced Materials* **2011**, 23, 3356–62.
- [20] J. Nelson, *Current Opinion in Solid State and Materials Science* **2002**, 6, 87–95.
- [21] K.L. and A.J.H. Sung Heum Park, Anshuman Roy, Serge Beaupre, Shinuk Cho Nelson Coates, Ji Sun Moob, Daniel Moses, mario Leclerc, *Nature Photonics* **2009**, 3, 297–303.

Chapter – 1: Fundamental of Organic Solar Cells

- [22] B.C. Thompson, J.M.J. Fréchet, *Angewandte Chemie (International Ed.)* **2008**, *47*, 58–77.
- [23] L. Dou, J. You, J. Yang, C. Chen, Y. He, S. Murase, T. Moriarty, K. Emery, G. Li, Y. Yang, *Nature Photonics* **2012**, *6*, 180–185.
- [24] H. Kallmann, M. Pope, *The Journal of Chemical Physics* **1959**, *30*, 585.
- [25] W. Tang, *Applied Physics Letters* **1986**, *48*, 1986.
- [26] N.S. Sariciftci, D. Braun, C. Zhang, V.I. Srdanov, a. J. Heeger, G. Stucky, F. Wudl, *Applied Physics Letters* **1993**, *62*, 585.
- [27] A.J. Yu, G.; Gao, J.; Hummelen, J. C.; Wudl, F.; Heeger, *Science* **1995**, *270*, 1789–1791.
- [28] N.S. Sariciftci, L. Smilowitz, A.J. Heeger, F. Wudl, *Science* **1992**, *258*, 1474–6.
- [29] A. Haugeneder, M. Neges, C. Kallinger, W. Spiro, U. Lemmer, J. Feldmann, U. Scherf, E. Harth, A. Gugel, K. Mullen, *Physical Review B* **1999**, *59*, 15346–15351.
- [30] M.. Theander, A.. Yartsev, D.. Zigmantas, V.. Sundstrom, W.. Mammo, M.R.. Andersson, O. Inganäs, *Physical Review B* **2000**, *61*, 12957.
- [31] T. Stübinger, W. Brütting, *Journal of Applied Physics* **2001**, *90*, 3632.
- [32] J. Nunzi, *C. R. Physique* **2002**, *3*, 523–542.
- [33] N.S. Gunes, S.; Neugebauer, H.; and Sariciftci, *Chemical Reviews* **2007**, *107*, 1324–1338.
- [34] M. Campoy-Quiles, T. Ferenczi, T. Agostinelli, P.G. Etchegoin, Y. Kim, T.D. Anthopoulos, P.N. Stavrinou, D.D.C. Bradley, J. Nelson, *Nature Materials* **2008**, *7*, 158–64.
- [35] D. Moses, A. Dogariu, A.J. Heeger, *Chemical Physics Letters* **2000**, *316*, 356–360.
- [36] C.J. Brabec, G. Zerza, G. Cerullo, S. De Silvestri, S. Luzzati, J.C. Hummelen, S. Sariciftci, *Chemical Physics Letters* **2001**, *340*, 232–236.
- [37] G. Dennler, M.C. Scharber, C.J. Brabec, *Advanced Materials* **2009**, *21*, 1323–1338.
- [38] H.-L. Yip, A.K.-Y. Jen, *Energy & Environmental Science* **2012**, *5*, 5994.
- [39] a. K.K. Kyaw, X.W. Sun, C.Y. Jiang, G.Q. Lo, D.W. Zhao, D.L. Kwong, *Applied Physics Letters* **2008**, *93*, 221107.
- [40] M.S. White, D.C. Olson, S.E. Shaheen, N. Kopidakis, D.S. Ginley, *Applied Physics Letters* **2006**, *89*, 143517.
- [41] S.K. Hau, H.-L. Yip, N.S. Baek, J. Zou, K. O'Malley, A.K.-Y. Jen, *Applied Physics Letters* **2008**, *92*, 253301.

Chapter – 1: Fundamental of Organic Solar Cells

- [42] T. Stubhan, H. Oh, L. Pinna, J. Krantz, I. Litzov, C.J. Brabec, *Organic Electronics* **2011**, *12*, 1539–1543.
- [43] Y. Sun, J.H. Seo, C.J. Takacs, J. Seifert, A.J. Heeger, *Advanced Materials* **2011**, *23*, 1679–83.
- [44] C. Waldauf, M. Morana, P. Denk, P. Schilinsky, K. Coakley, S. a. Choulis, C.J. Brabec, *Applied Physics Letters* **2006**, *89*, 233517.
- [45] R. Steim, S.A. Choulis, P. Schilinsky, C.J. Brabec, *Applied Physics Letters* **2008**, *92*, 093303.
- [46] W.E.B. Shepherd, A.D. Platt, D. Hofer, O. Ostroverkhova, M. Loth, J.E. Anthony, *Applied Physics Letters* **2010**, *97*, 163303.
- [47] G. Dennler, M.C. Scharber, T. Ameri, P. Denk, K. Forberich, C. Waldauf, C.J. Brabec, *Advanced Materials* **2008**, *20*, 579–583.
- [48] J. Gilot, M.M. Wienk, R. a. J. Janssen, *Applied Physics Letters* **2007**, *90*, 143512.
- [49] A. Hadipour, B. de Boer, P.W.M. Blom, *Advanced Functional Materials* **2008**, *18*, 169–181.
- [50] C. Chen, L. Dou, R. Zhu, C. Chung, T. Song, Y.B. Zheng, C.E.T. Al, *ACS Nano* **2012**, *6*, 7185–7190.
- [51] L. Yang, T. Zhang, H. Zhou, S.C. Price, B.J. Wiley, W. You, *ACS Applied Materials & Interfaces* **2011**, *3*, 4075–84.
- [52] Y.H. Kim, C. Sachse, M.L. Machala, C. May, L. Müller-Meskamp, K. Leo, *Advanced Functional Materials* **2011**, *21*, 1076–1081.
- [53] D. Alemu, H.-Y. Wei, K.-C. Ho, C.-W. Chu, *Energy & Environmental Science* **2012**, *5*, 9662.
- [54] R. V. Salvatierra, C.E. Cava, L.S. Roman, A.J.G. Zarbin, *Advanced Functional Materials* **2012**, 10.1002/adfm.201201878.
- [55] C.-L. Hsu, C.-T. Lin, J.-H. Huang, C.-W. Chu, K.-H. Wei, L.-J. Li, *ACS Nano* **2012**, *6*, 5031–9.
- [56] V. Coropceanu, J. Cornil, Y.O. Demetrio A. da Silva Filho, R. Silbey, J.-L. Brédas, *Chemical Reviews* **2007**, *107*, 926–952.
- [57] S.S. Pandey, W. Takashima, S. Nagamatsu, T. Endo, M. Rikukawa, K. chi Kaneto, *Japanese Journal of Applied Physics* **2000**, *39*, L94–L97.
- [58] Z. Bao, A. Dodabalapur, A.J. Lovinger, *Applied Physics Letters* **1996**, *69*, 4108.
- [59] H. Sirringhaus, *Science* **1998**, *280*, 1741–1744.
- [60] A. Yokoyama, R. Miyakoshi, Y. Tsutomu, *Macromolecules* **2004**, *37*, 1169–1171.
- [61] E.E. Sheina, J. Liu, M.C. Iovu, D.W. Laird, R.D. McCullough, *Macromolecules* **2004**, *37*, 3526–3528.
- [62] T. Yokozawa, A. Yokoyama, *Chemical Reviews* **2009**, *109*, 5595–619.

Chapter – 1: Fundamental of Organic Solar Cells

- [63] R.C. Hiorns, R. de Bettignies, J. Leroy, S. Bailly, M. Firon, C. Sentein, a. Khoukh, H. Preud'homme, C. Dagron-Lartigau, *Advanced Functional Materials* **2006**, *16*, 2263–2273.
- [64] J. Liu, R.S. Loewe, R.D. McCullough, *Macromolecules* **1999**, *32*, 5777–5785.
- [65] J. Liu, R.D. McCullough, *Macromolecules* **2002**, *35*, 9882–9889.
- [66] M. Jeffries-El, G. Sauvé, R.D. McCullough, *Macromolecules* **2005**, *38*, 10346–10352.
- [67] M. Urien, H. Erothu, E. Cloutet, R.C. Hiorns, L. Vignau, H. Cramail, *Macromolecules* **2008**, *41*, 7033–7040.
- [68] E. Kaul, V. Senkovskyy, R. Tkachov, V. Bocharova, H. Komber, M. Stamm, A. Kiriy, *Macromolecules* **2010**, *43*, 77–81.
- [69] H.A. Bronstein, C.K. Luscombe, *Journal of American Chemical Society* **2009**, *131*, 12894–12895.
- [70] Y.-K. Lan, C.H. Yang, H.-C. Yang, *Polymer International* **2010**, *59*, 16–21.
- [71] R.J. Kline, M.D. McGehee, E.N. Kadnikova, J. Liu, J.M.J. Fre, M.F. Toney, *Macromolecules* **2005**, *38*, 3312–3319.
- [72] A. Zen, M. Saphiannikova, I.D. Neher, S. Grigorian, U. Pietsch, U. Asawapirom, S. Janietz, U. Scherf, I. Lieberwirth, G. Wegner, *Macromolecules* **2006**, *39*, 2162–2171.
- [73] M. Brinkmann, P. Rannou, *Macromolecules* **2009**, *42*, 1125–1130.
- [74] D. Chirvase, J. Parisi, J.C. Hummelen, V. Dyakonov, *Nanotechnology* **2004**, *15*, 1317–1323.
- [75] X. Yang, J. Loos, S.C. Veenstra, W.J.H. Verhees, M.M. Wienk, J.M. Kroon, M.A.J. Michels, R.A.J. Janssen, *Nano Letters* **2005**, *5*, 579–83.
- [76] R.C. Haddon, A.S. Perel, R.C. Morris, T.T.M. Palstra, a. F. Hebard, R.M. Fleming, *Applied Physics Letters* **1995**, *67*, 121.
- [77] C.J. Brabec, N.S. Sariciftci, J.C. Hummelen, *Advanced Functional Materials* **2001**, *11*, 15–26.
- [78] P. Schilinsky, C. Waldauf, C.J. Brabec, *Applied Physics Letters* **2002**, *81*, 3885.
- [79] W. Ma, C. Yang, X. Gong, K. Lee, A.J. Heeger, *Advanced Functional Materials* **2005**, *15*, 1617–1622.
- [80] G. Li, V. Shrotriya, J. Huang, Y. Yao, T. Moriarty, K. Emery, Y. Yang, *Nature Materials* **2005**, *4*, 864–868.
- [81] M.T. Dang, L. Hirsch, G. Wantz, *Advanced Materials* **2011**, *23*, 3597–3602.
- [82] M. Reyes-Reyes, K. Kim, D.L. Carroll, *Applied Physics Letters* **2005**, *87*, 083506.

Chapter – 1: Fundamental of Organic Solar Cells

- [83] N. Blouin, A. Michaud, D. Gendron, S. Wakim, E. Blair, R. Neagu-Plesu, M. Belletête, G. Durocher, Y. Tao, M. Leclerc, *Journal of the American Chemical Society* **2008**, *130*, 732–42.
- [84] S. Wakim, B. Aïch, Y. Tao, M. Leclerc, *Polymer Review* **2008**, *48*, 432.
- [85] S. Wakim, S. Beaupré, N. Blouin, B.-R. Aich, S. Rodman, R. Gaudiana, Y. Tao, M. Leclerc, *Journal of Materials Chemistry* **2009**, *19*, 5351.
- [86] H. van Mullekom, J.A. Vekemans, E. Havinga, E. Meijer, *Materials Science and Engineering* **2001**, *32*, 1–40.
- [87] J. Peet, J.Y. Kim, N.E. Coates, W.L. Ma, D. Moses, A.J. Heeger, G.C. Bazan, *Nature Materials* **2007**, *6*, 497–500.
- [88] Y. Liang, Y. Wu, D. Feng, S.-T. Tsai, H.-J. Son, G. Li, L. Yu, *Journal of the American Chemical Society* **2009**, *131*, 56–7.
- [89] H. Chen, J. Hou, S. Zhang, Y. Liang, G. Yang, Y. Yang, *Nature Photonics* **2009**, *3*, 649–653.
- [90] Y. Liang, Z. Xu, J. Xia, S.-T. Tsai, Y. Wu, G. Li, C. Ray, L. Yu, *Advanced Materials (Deerfield Beach, Fla.)* **2010**, *22*, E135–8.
- [91] Z. He, C. Zhong, S. Su, M. Xu, H. Wu, Y. Cao, *Nature Photonics* **2012**, *6*, 591–595.
- [92] [Http://www.nrel.gov/news/press/2012/1801.html](http://www.nrel.gov/news/press/2012/1801.html); Accessed December **2012**.
- [93] J.J.M. Halls, C.A. Walsh, N.C. Greenham, E.A. Marseglia, R.H. Friend, S.C. Moratti, A.B. Holmes, *Nature* **1995**, *376*, 498–500.
- [94] C.R. McNeill, A. Abrusci, J. Zaumseil, R. Wilson, M.J. McKiernan, J.H. Burroughes, J.J.M. Halls, N.C. Greenham, R.H. Friend, *Applied Physics Letters* **2007**, *90*, 193506.
- [95] F.G. Brunetti, X. Gong, M. Tong, A.J. Heeger, F. Wudl, *Angewandte Chemie (International Ed. in English)* **2010**, *49*, 532–6.
- [96] W.S. Shin, H.-H. Jeong, M.-K. Kim, S.-H. Jin, M.-R. Kim, J.-K. Lee, J.W. Lee, Y.-S. Gal, *Journal of Materials Chemistry* **2006**, *16*, 384.
- [97] H. Hoppe, N.S. Sariciftci, *Journal of Materials Chemistry* **2006**, *16*, 45.
- [98] A.C. Arias, J.D. Mackenzie, R. Stevenson, J.J.M. Halls, M. Inbasekaran, E.P. Woo, D. Richards, R.H. Friend, *Macromolecules* **2001**, *34*, 6005–6013.
- [99] Y. Kim, S. Cook, S.A. Choulis, J. Nelson, J.R. Durrant, D.D.C. Bradley, *Chemistry of Materials* **2004**, *16*, 4812–4818.
- [100] M. Geoghegan, G. Krausch, *Progress in Polymer Science* **2003**, *28*, 261–302.
- [101] F. Zhang, K.G. Jespersen, C. Björström, M. Svensson, M.R. Andersson, V. Sundström, K. Magnusson, E. Moons, A. Yartsev, O. Inganäs, *Advanced Functional Materials* **2006**, *16*, 667–674.

Chapter – 1: Fundamental of Organic Solar Cells

- [102] J.K. Lee, W.L. Ma, C.J. Brabec, J. Yuen, J.S. Moon, J.Y. Kim, K. Lee, G.C. Bazan, A.J. Heeger, *Journal of the American Chemical Society* **2008**, *130*, 3619–23.
- [103] G. Li, Y. Yao, H. Yang, V. Shrotriya, G. Yang, Y. Yang, *Advanced Functional Materials* **2007**, *17*, 1636–1644.
- [104] M. Chiu, U. Jeng, C. Su, K.S. Liang, K. Wei, *Advanced Materials* **2008**, *20*, 2573–2578.
- [105] T.J. Prosa, M.J. Winokur, J. Moulton, P. Smith, A.J. Heeger, *Macromolecules* **1992**, *25*, 4364–4372.
- [106] R.D. Mccullough, S. Tristram-nagle, S.P. Williams, R.D. Lowevt, *Journal of American Chemical Society* **1993**, *115*, 4910–4911.
- [107] T. Chen, X. Wu, R.D. Rieke, *Journal of American Chemical Society* **1995**, *117*, 233–244.
- [108] M. Brinkmann, P. Rannou, *Advanced Functional Materials* **2007**, *17*, 101–108.
- [109] Z. Wu, A. Petzold, T. Henze, T. Thurn-Albrecht, R.H. Lohwasser, M. Sommer, M. Thelakkat, *Macromolecules* **2010**, *43*, 4646–4653.
- [110] E. Mena-osteritz, A. Meyer, B.M.W. Langeveld-voss, R.A.J. Janssen, E.W. Meijer, P. Bäuerle, *Angewandte Chemie (International Ed.)* **2000**, *39*, 2679–2684.
- [111] R. Colle, G. Grosso, A. Ronzani, C.M. Zicovich-Wilson, *Physica Status Solidi (B)* **2011**, *248*, 1360–1368.
- [112] A. Salleo, *Materials Today* **2007**, *10*, 38–45.
- [113] H.J. Fell, E.J. Samuelsen, J. Als-Nielsen, G. Grubel, J. Mardalen, *Solid State Communications* **1995**, *94*, 843–846.
- [114] K. Yamamoto, S. Ochiai, X. Wang, Y. Uchida, K. Kojima, A. Ohashi, T. Mizutani, *Thin Solid Films* **2008**, *516*, 2695–2699.
- [115] H. Sirringhaus, P.J. Brown, R.H. Friend, M.M. Nielsen, K. Bechgaard, B.M.W. Langeveld-Voss, A.J.H. Spiering, R.A.J. Janssen, E.W. Meijer, *Synthetic Metals* **2000**, *111-112*, 129–132.
- [116] J.-F. Chang, B. Sun, D.W. Breiby, M.M. Nielsen, T.I. Sölling, M. Giles, I. McCulloch, H. Sirringhaus, *Chemistry of Materials* **2004**, *16*, 4772–4776.
- [117] J. Chang, J. Clark, N. Zhao, H. Sirringhaus, D.W. Breiby, J.W. Andreasen, M. Nielsen, M. Giles, M. Heeney, I. Mcculloch, *Physical Review B* **2006**, *74*, 115318.
- [118] K.E. Aasmundtveit, E.J. Samuelsen, M. Guldstein, C. Steinsland, O. Flornes, C. Fagermo, T.M. Seeberg, L.A.A. Pettersson, O. Ingana, R. Feidnhans, S. Ferrer, *Macromolecules* **2000**, *33*, 3120–3127.
- [119] S. Speed, D.M. Delongchamp, B.M. Vogel, Y. Jung, M.C. Gurau, C.A. Richter, O.A. Kirillov, J. Obrzut, D.A. Fischer, S. Sambasivan, L.J. Richter, E.K. Lin, *Chemistry of Materials* **2005**, *17*, 5610–5612.

Chapter – 1: Fundamental of Organic Solar Cells

- [120] S. Joshi, S. Grigorian, U. Pietsch, P. Pingel, A. Zen, D. Neher, U. Scherf, *Macromolecules* **2008**, *41*, 6800–6808.
- [121] S. Joshi, P. Pingel, S. Grigorian, T. Panzner, U. Pietsch, D. Neher, M. Forster, U. Scherf, *Macromolecules* **2009**, *42*, 4651–4660.
- [122] R. Joseph Kline, M.D. McGehee, M.F. Toney, *Nature Materials* **2006**, *5*, 222–228.
- [123] H. Yang, T.J. Shin, L. Yang, K. Cho, C.Y. Ryu, Z. Bao, *Advanced Functional Materials* **2005**, *15*, 671–676.
- [124] D.H. Kim, J.T. Han, Y.D. Park, Y. Jang, J.H. Cho, M. Hwang, K. Cho, *Advanced Materials* **2006**, *18*, 719–723.
- [125] K.J. Ihn, J. Moulton, P. Smith, *Journal of Polymer Science Part B: Polymer Physics* **1993**, *31*, 735–742.
- [126] S. Berson, R. de Bettignies, S. Bailly, S. Guillerez, B. Jusselme, *Advanced Functional Materials* **2007**, *17*, 3363–3370.
- [127] S. Samitsu, T. Shimomura, S. Heike, T. Hashizume, *Macromolecules* **2008**, *41*, 8000–8010.
- [128] P. Schilinsky, U. Asawapirom, U. Scherf, M. Biele, C.J. Brabec, *Chemistry of Materials* **2005**, *17*, 2175–2180.
- [129] R.J. Kline, M.D. McGehee, E.N. Kadnikova, J. Liu, J.M.J. Fréchet, *Advanced Materials* **2003**, *15*, 1519–1522.
- [130] W. Ma, J.Y. Kim, K. Lee, A.J. Heeger, *Macromolecular Rapid Communications* **2007**, *28*, 1776–1780.
- [131] B.F. Padinger, R.S. Rittberger, N.S. Sariciftci, *Advanced Functional Materials* **2003**, *13*, 85–88.
- [132] A.J. Parnell, A.J. Cadby, O.O. Mykhaylyk, A.D.F. Dunbar, P.E. Hopkinson, A.M. Donald, R. a. L. Jones, *Macromolecules* **2011**, *44*, 6503–6508.
- [133] W. Yin, M. Dadmun, *ACS Nano* **2011**, 4756–4768.
- [134] T. Erb, U. Zhokhavets, G. Gobsch, S. Raleva, B. Stühn, P. Schilinsky, C. Waldauf, C.J. Brabec, *Advanced Functional Materials* **2005**, *15*, 1193–1196.
- [135] V.D. Mihailetschi, H.X. Xie, B. de Boer, L.J. a. Koster, P.W.M. Blom, *Advanced Functional Materials* **2006**, *16*, 699–708.
- [136] A. Zen, J. Pflaum, S. Hirschmann, W. Zhuang, F. Jaiser, U. Asawapirom, J.P. Rabe, U. Scherf, D. Neher, *Advanced Functional Materials* **2004**, *14*, 757–764.
- [137] M. Urien, L. Vignau, E. Cloutet, A. De Cuendias, G. Wantz, H. Cramail, L. Hirsch, J. Parneix, *Polymer International* **2008**, *769*, 764–769.

Chapter – 1: Fundamental of Organic Solar Cells

- [138] M. Sanyal, B. Schmidt-Hansberg, M.F.G. Klein, C. Munuera, A. Vorobiev, A. Colsmann, P. Scharfer, U. Lemmer, W. Schabel, H. Dosch, E. Barrena, *Macromolecules* **2011**, *44*, 3795–3800.
- [139] M. Shin, H. Kim, J. Park, S. Nam, K. Heo, M. Ree, C.-S. Ha, Y. Kim, *Advanced Functional Materials* **2010**, *20*, 748–754.
- [140] E. Verploegen, R. Mondal, C.J. Bettinger, S. Sok, M.F. Toney, Z. Bao, *Advanced Functional Materials* **2010**, *20*, 3519–3529.
- [141] N.D. Treat, M.A. Brady, G. Smith, M.F. Toney, E.J. Kramer, C.J. Hawker, M.L. Chabynyc, *Advanced Energy Materials* **2011**, *1*, 82–89.
- [142] H.-C. Liao, C.-S. Tsao, T.-H. Lin, C.-M. Chuang, C.-Y. Chen, U.-S. Jeng, C.-H. Su, Y.-F. Chen, W.-F. Su, *Journal of the American Chemical Society* **2011**, *133*, 13064–73.
- [143] V. Gernigon, P. Lévêque, C. Brochon, J. Audinot, R. Bechara, F. Richard, T. Heiser, G. Hadziioannou, *Eur. Phys. J. Appl. Phys.* **2011**, *56*, 34107.
- [144] A. Swinnen, I. Haeldermans, M. vande Ven, J. D’Haen, G. Vanhoyland, S. Aresu, M. D’Olieslaeger, J. Manca, *Advanced Functional Materials* **2006**, *16*, 760–765.
- [145] A. Swinnen, I. Haeldermans, P. Vanlaeke, J. D’Haen, J. Poortmans, M. D’Olieslaeger, J. V. Manca, *Eur. Phys. J. Appl. Phys.* **2006**, *36*, 251–256.
- [146] S. Bertho, G. Janssen, T.J. Cleij, B. Conings, W. Moons, *Solar Energy Materials & Solar Cells* **2008**, *92*, 753–760.
- [147] S.S. van Bavel, M. Bärenklau, G. de With, H. Hoppe, J. Loos, *Advanced Functional Materials* **2010**, *20*, 1458–1463.
- [148] J. Kiel, A. Eberle, M. Mackay, *Physical Review Letters* **2010**, *105*, 168701.
- [149] S.E. Shaheen, C.J. Brabec, N.S. Sariciftci, F. Padinger, T. Fromherz, J.C. Hummelen, *Applied Physics Letters* **2001**, *78*, 841.
- [150] J. Huang, G. Li, Y. Yang, *Applied Physics Letters* **2005**, *87*, 112105.
- [151] R.M. Beal, A. Stavrinadis, J.H. Warner, J.M. Smith, H.E. Assender, A.A.R. Watt, *Macromolecules* **2010**, *43*, 2343–2348.
- [152] G. Kalita, M. Masahiro, W. Koichi, M. Umeno, *Solid State Electronics* **2010**, *54*, 447–451.
- [153] H. Hoppe, M. Niggemann, C. Winder, J. Kraut, R. Hiesgen, a. Hinsch, D. Meissner, N.S. Sariciftci, *Advanced Functional Materials* **2004**, *14*, 1005–1011.
- [154] H. Hoppe, T. Glatzel, M. Niggemann, W. Schwinger, F. Schaeffler, A. Hinsch, M.C. Lux-Steiner, N.S. Sariciftci, *Thin Solid Films* **2006**, *511-512*, 587–592.

Chapter - II

*Block Copolymers and Their Application in
Organic Photovoltaics*

2.1. Introduction

In the previous section the motivation of the work as well as the factors affecting the morphological properties of the BHJ active layer were thoroughly discussed. Herein, we will review both the theoretical as well as the experimental works on block copolymers self-assembly with a focus on systems with applications in photovoltaics. First, the basic physical principals governing the phase behavior of block copolymer systems will be highlighted in order to better apprehend the potential of block copolymer systems for the tailoring of the BHJ active layer properties. Following, the specific applications of the different block copolymer architectures (*i.e.* chemical structure, architecture, physical properties of the blocks) in photovoltaics will be presented.

2.2. Architecture, Phase Behavior and Morphology of Block copolymers

Chemically different polymers usually macrophase separate from melt state due to the resulting balance between the entropic and enthalpic contributions inherent to their mixing.^{[1][2]} The entropic contribution for a binary polymer blend is proportionally associated to the number of molecules, whereas the enthalpic contribution is related to the number of monomers (or repeat units). Because of the large number of monomers in a polymer chain, even the weak interactions between chemically different monomers are magnified. Consequently the unfavorable enthalpic interactions generally dominate the stretching of polymer chains inherent to a macrophase-separated system (*i.e.* the entropic contribution), thus resulting in macrophase separations at the macro-scale level. However, when two chemically distinct polymers are covalently linked together to form the so-called block copolymer (BCP) architecture, they cannot separate on a macroscopic scale.^[3] They only separate on a local nanometer scale. Depending of the balance between the entropic and enthalpic contributions, the blocks of the copolymer either segregate into nanodomains or remain homogeneously mixed. Following decades of macromolecular engineering, block copolymers can be designed with various architectures due to large progresses in controlled and/or living polymerization techniques.^{[3][4]} Some of the typical block copolymer molecular architectures are presented in Figure 2.1. These block

copolymers have shown great diversity in morphology, depending on the composition of block copolymer as well as the molecular architectures. The simplest architecture is the linear AB diblock copolymer which is the result of the covalent linkage of two homopolymers. In this review, more emphasis will be given to this class of block copolymer architecture.

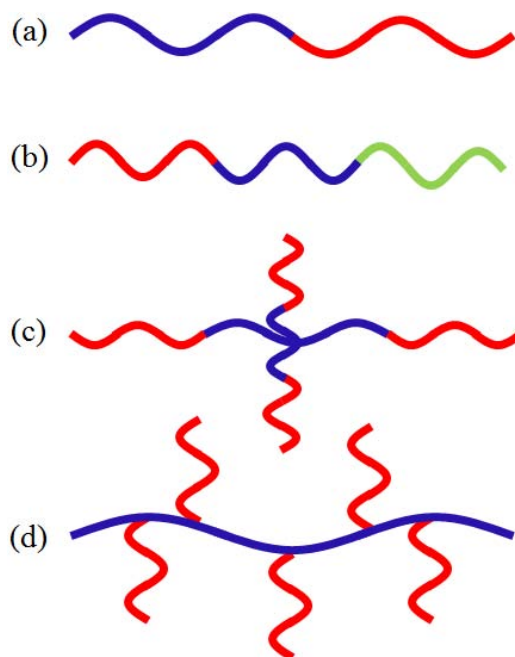


Figure 2.1: Various architectures of block copolymers: a) diblock copolymer, b) triblock copolymer, c) star shaped block copolymer, d) graft (brush) block copolymer. The color represents a polymer block composed of a linear sequence of same-type monomers.

As previously described, the phase separation (or miscibility) of polymer systems is thermodynamically driven and can be described by the enthalpic and entropic contributions.^{[1][2][5][6]} More appropriately for block copolymers, the product χN (where χ is the temperature-dependent Flory–Huggins interaction parameter and N is the total degree of polymerization or the total number of segments), controls the state of microphase separation as it represents the segregation strength of the two chemically distinct polymer constituents. The value of χ is an indicator of the incompatibility of two polymers. The value increases for more incompatible polymers, and depends mainly on the chosen monomers. Since different types of polymer units are usually chemically incompatible, *i.e.* have

repulsive interactions, there is a strong tendency for χ to be positive, as the result demixing occurs among the components. It is also known that the Flory-Huggins parameter, χ , is inversely proportional to the temperature (Equation 2.4), *i.e.* the lower the temperature the higher the χ value. Upon reducing the temperature the repulsive interactions start to dominate and microphase separation takes place leading to the formation of nanostructures. As opposed, a negative value of χ indicates favorable mixing. For example, at elevated temperatures (where χ become smaller or even negative) the entropy dominates and the block copolymer chains are in a disordered melt state indicating favorable mixing.^[7] Therefore, phase segregation only takes place when the product χN exceeds some critical value, the order-disorder transition (ODT).^{[8][9][10][11]} When $\chi N \leq 10.5$, the entropy contribution dominates the enthalpy, as the result mixing occurs between A and B segments, resulting in disordered phase. However, when $\chi N > 10.5$, the A and B blocks become immiscible and leading the unlike blocks to separate.^{[12][10][13]} The type of microstructure formed depends on the block copolymer composition (volume fraction).^{[7][14]} The way in which the diblock copolymers self-assemble into various nanostructures, was first theoretically described by Leibler.^[6] For example, in the case of a symmetric diblock copolymer - *i.e.* with A- and B-blocks of equal volume fractions - the stretching free energy of the A- and the B-block is equal in first approximation. This results into a morphology exhibiting a flat interface, *i.e.* a lamellar structure (L). However, if the polymers are asymmetric (*i.e.* A- and B-blocks have different volume fractions), the formation of curved interfaces are energetically favored. The interfaces will curve towards the minority domain resulting in morphologies with curved interfaces.^[15] As a result body-centered cubic sphere (S), hexagonal packed cylinder and gyroid structures are formed for diblock copolymer systems depending on the asymmetry of the structure. The schematic illustrations of the different block copolymer nanostructures are presented in figure 2.2. The lamellar, hexagonal, cubic and gyroid structures correspond to the stable phases.^{[10][16][17]}

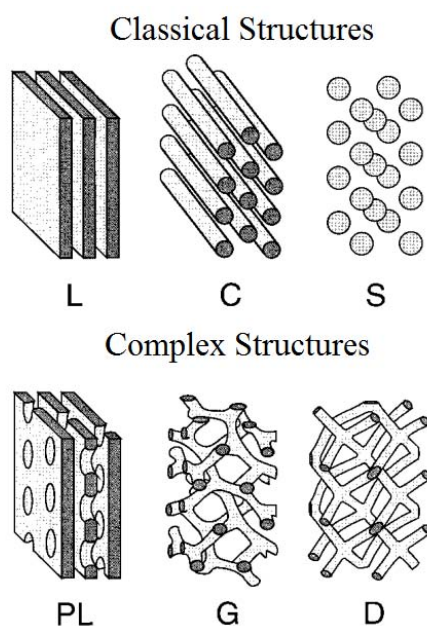


Figure 2.2: Schematic representations of block copolymer microstructures showing the domains occupied by the minority component blocks. Lamellar (L), Cylinder (C), Sphere (S), Perforated Lamellar (PL), Gyroid (G) and bicontinuous double Diamond (D). The majority component blocks fill the remaining space within the structure. Reproduced from Ref.^[7]

These interesting self-assembling properties of block copolymers leads to perfectly ordered structures with nanometrically defined periodicity which offer promising opportunities in various applications (for example; in lithography for patterning and templating as well as in nanostructuring of organic photovoltaic active layers).^{[18][19][20][21][22]} Besides the length-scale of the periodic structures can be easily tuned through macromolecular engineering in order to coincide with the length scale of typical photovoltaic process such as the exciton diffusion length. Consequently block copolymers have been envisioned as a provider of idealized nanostructures in OPVs in order to enhance each of the basic steps of photovoltaic energy conversions processes.^{[16][23]}

Depending on the degree of flexibility, block copolymers contain two major types of polymer segments: coils and/or rods. A coil describes a flexible polymer chain while a conjugated polymer in BCPs is often described as a rod-like block because of its rigidity (arise from the overlapping of π -orbitals).^{[24][25]} The variation in segment flexibility is one of the reasons to observe differences in self-

assembly behavior among coil-coil, rod-coil and rod-rod block copolymers. For example, the difference in stiffness among the rod and the coil blocks in rod-coil copolymers leads to a selective aggregation of the rod-like block with high structural order while the flexible coil acts as separator between the ordered phases.^[26] Therefore, understanding the self-assembly behavior of the different forms of block copolymers and controlling the molecular and structural parameters that dictate the formation of their ordered nanostructures are very much important in order for block copolymers to be used for different form of applications.

2.2.1. Phase behavior of coil-coil block copolymers

BCPs directly used in optoelectronic application usually carry at least one semiconductor conjugated polymer block which will complexify the phase behavior of the BCP.^{[25][27]} However, at a fundamental level, coil-coil copolymers have served as a model system to examine both theoretical and experimental questions relating to the self-assembly and phase behavior of block copolymer systems^{[13][28][29][30][31]} and can be used to apprehend, in first approximation, some fundamental aspects of the rod-containing counterparts. The phase behavior (miscibility) of coil-like polymer blends was first described by Flory and Huggins and is directly related to regular solution theory.^{[32][33]} The theory starts from the Gibbs' free energy of mixing (ΔG_m) for a blend of polymers 1 and 2 and follows Equation 2.1.

$$\Delta G = \Delta H - T\Delta S \quad (2.1)$$

Where; ΔH is the change in enthalpy and ΔS in the change in entropy upon mixing. The miscibility of polymer mixtures can roughly be estimated using the lattice theory developed by Flory and Huggins for polymer solutions. For molecules in a liquid with mixing entropy purely configurational, having identical lattices for the two polymer mixtures, with perfect mixing of segments and with interaction considered only between direct neighbors; the change in entropy and change in enthalpy of mixing at equilibrium will be:

$$\Delta S = -k_B N_S \left[\frac{\phi_1}{X_1} \ln(\phi_1) + \frac{\phi_2}{X_2} \ln(\phi_2) \right] \quad (2.2)$$

$$\Delta H = V(\delta_1 - \delta_2)^2 \phi_1 \phi_2 \quad (2.3)$$

Here; k_B is the Boltzmann constant, T is the temperature, N_S is the number of sites. ϕ_i is the volume fraction of polymer i and X_i is the degree of polymerization of polymer i . V is the total volume. The total volume is the product of the number of sites (N_S) with the volume of the lattice site (V_s). δ_i is the solubility parameter of polymer i . The solubility parameter is directly dependent on the non-specific interaction of the similar molecules but inversely proportional to the volume of the lattice site.

From equation 2.1, 2.2 and 2.3, the total free energy of mixing will be:

$$\frac{\Delta G_m}{N_S k_B T} = \chi_{12} \phi_1 \phi_2 + \frac{\phi_1}{X_1} \ln(\phi_1) + \frac{\phi_2}{X_2} \ln(\phi_2) \quad (2.4)$$

with $\chi_{12} = \frac{V_s(\delta_1 - \delta_2)^2}{k_B T}$; represents the polymer-polymer interaction (i.e. Flory-Huggins parameter).

The right hand side of Equation 2.4 represents the enthalpy of mixing (first term, which is usually greater than zero) and the entropy of mixing (the final two terms which are always negative, representing a favorable free energy change upon mixing). Since the entropic terms scale with the inverse of the degree of polymerization (for which this value is usually very large for polymers), the values are usually very small. Therefore, enthalpy overcomes entropy and phase separation is promoted in the majority of cases. This property is the cornerstone of the block copolymer self-assembling properties since the phase separation will be limited to nanoscopic level due to the covalent binding of the blocks.

As briefly comment in the previous paragraph, the phase diagrams of a linear A-B diblock copolymer system are fully characterized by three parameters: the total number of repeat units ($N = N_A + N_B$), the segment-segment (Flory-Huggins) interaction parameter (χ_{AB}), and the volume fraction of one of the blocks (f).^[34] Periodically ordered morphologies in coil-coil block copolymer are the result of the balance between the enthalpic terms driving the phase separation and the interfacial tension and

entropic stretching terms. Therefore, the precise equilibrium nanostructure that will be adopted by a specific coil-coil block copolymer will be dictated by the product χN and f . The theoretical phase diagram of A-B coil-coil block copolymers in this formalism has been described in numerous studies.^{[6][35]} A comprehensible representation taking into account the segmental profile of the blocks has been provided by Matsen and Bates as shown in Figure 2.3a.^{[3][7][29]} Above a critical χN value, phase separated morphologies develop while below this value the system is disordered (mixed). As the volume fraction of the B block is changed, the predicted morphology can also change for a given value of χN . The schematic representation of the most common morphologies adopted by coil-coil diblock copolymers are shown in Figure 2.3b.

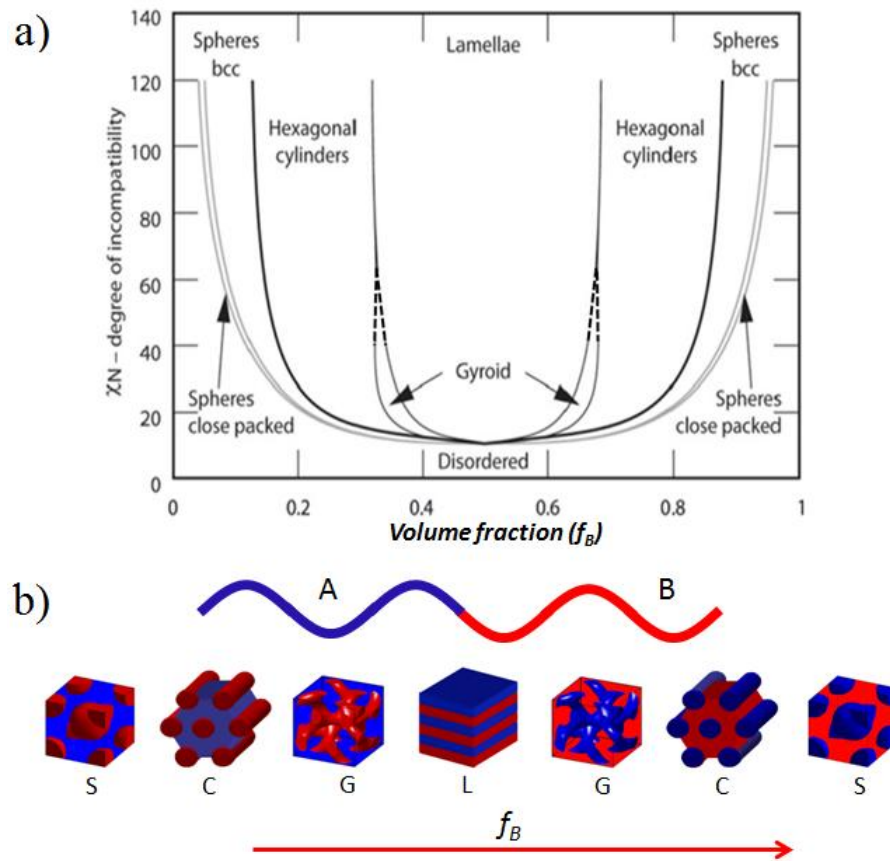


Figure 2.3: (a) Theoretical phase diagram of coil-coil A-B (blue-red) diblock copolymers. The ordered morphologies include: close-packed (face-centered cubic) spheres (CPS), body-centered cubic spheres (S), hexagonal packed cylinders (C), a bicontinuous gyroid network (G), and a lamellar phase (L). (b)

Schematic representations of the S, C, G, and L morphologies with the B block as both the minority (left) and majority (right) phase. Reproduced from Ref.^{[31][29]}

Those theoretical visualized microstructures of coil-coil A-B diblock copolymers have also been experimentally observed.^{[13][31][36][37][38]} For example; in classical styrene-*b*-butadiene (S-B) coil-coil diblock copolymer systems, the ordered mesostructures has been clearly observed. Electron microscopy of stained S-B copolymers (Figure 2.4) has shown that phase separation occurring in this system is in good agreement with the theoretically predicted one.^[39] The non-classical ordered morphologies (perforated lamellar or other complex geometries) have also been experimentally observed in polystyrene-*b*-polyisoprene block copolymers for particular volume fractions and molecular weights.^{[13][40][41]}

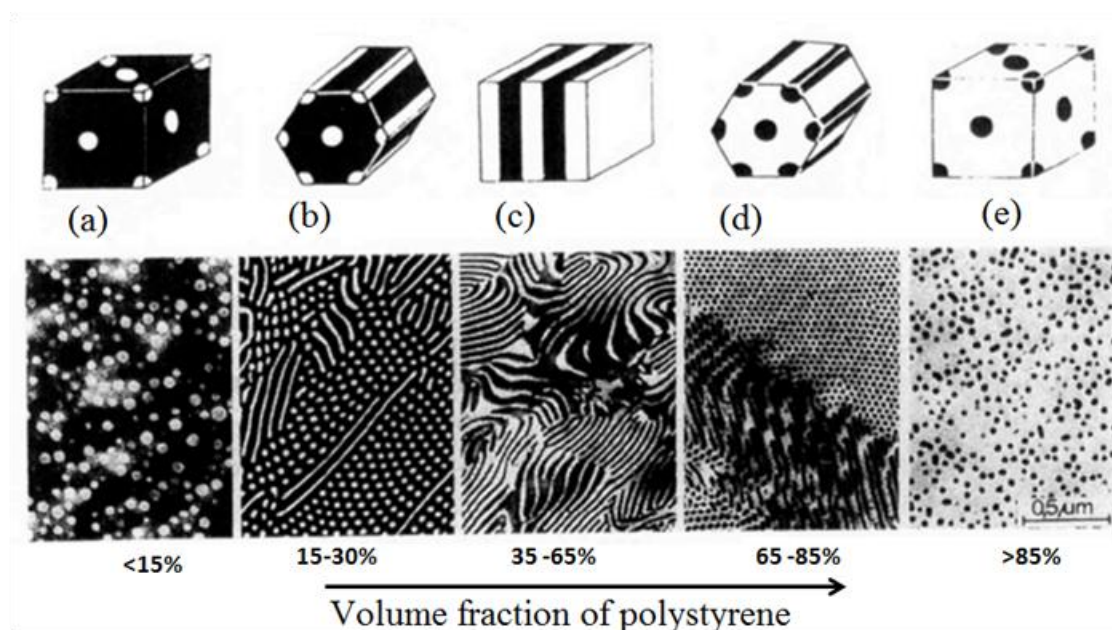


Figure 2.4: Schematic and observed morphologies of poly(styrene-*b*-butadiene) coil-coil block copolymer. (a) close-packed (face-centered cubic) spheres of PS in PB, (b) hexagonal packed cylinders of PS in PB, (c) Lamellar phase of PS and PB, (d) hexagonal packed cylinders of PB in PS and (e) close-packed (face-centered cubic) spheres of PB in PS. Reproduced from Ref.^[39]

The theoretical and experimental findings on the classical coil-coil diblock copolymer system have paved the way to the understanding of more complex systems such as the rod-coil block copolymers. Those classes of diblock copolymers have more complicated self-assembling behavior due to the intrinsic characteristics of the repeating units; the repeating unit contains rod-like liquid crystalline molecules in addition to the coil-like molecules. The difference in chain rigidity between the stiff rod block (arising from its liquid crystalline properties or $\pi - \pi$ interactions) and the flexible coil block is one of the factors influencing the formation of ordered and stable nanostructures in rod-coil block copolymers. Diblock copolymers in this category are interesting from the point of view of the additional complications of morphology that the rod-like part brings about. Their phase behavior and its potential applications of these types of copolymer are now under intense investigations.

2.2.2. Phase Behavior of Rod-containing Block Copolymer Systems

One of the most potent advantages of the block copolymer configuration is to purvey an addition of functionalities in a unique macromolecule. When we are thinking of an organic material designed for electronic applications, the material should contain an inherent electronic functionality. Consequently block copolymers are of particular interest for organic electronics since they can provide a combination of self-structuration abilities with electronic functionalities. As previously described, the coil-coil block copolymers have excellent properties in formation of periodic nanostructures, but possess extremely low charge carrier mobility due to the absence of overlapping π -orbitals.^[42] However, in addition to their rich morphological phase behavior (arising from the interplay between the liquid crystalline ordering of the rod-like units and the microphase segregation behavior between the unlike blocks), rod-containing block copolymers show promising opportunities in organic electronic field due to their excellent electrical conductivity (that arises from the strong $\pi - \pi$ interactions in the rigid phase of the block copolymer).^{[43][26][44][45]} There are two forms of block copolymer architectures of this category: (i) rod-coil block copolymers, where one part of the copolymer consists in a conductive rigid block while the second block is a flexible (coil) part; and (ii)

rod-rod block copolymers, in which both blocks show a high stiffness with a low conformational flexibility.

2.2.2.1. Phase Behavior of Rod-coil Block Copolymers

Rod-coil block copolymers have both a rigid rod and a coil blocks in the same macromolecular backbone. The rigid part of the rod-coil block copolymers can be based on different molecular configurations leading to a high stiffness of the macromolecular segment: helical, mesogenic and conjugated rods (semiconducting polymers).^{[26][46][47]} Here, more emphasis will be given to copolymers that contain conjugated structures. Though conjugated rod-coil copolymers form well-ordered mesostructures, their self-assembly and phase behavior are not as easy to explain as compared to the coil-coil system due to the interplay between the rod-rod organizational behavior and the rod/coil phase segregation. Indeed, the rigid part of the conjugated rod-coil copolymers leads to completely different self-assembly properties than the more classical coil-coil type counterparts.^{[48][49][50]} A rod block is characterized by a lower conformational entropy than a coil block, which restricts its ability to stretch in order to accommodate packing within self-assembled structures.^[17] The π - π stacking of the conjugated part of such block copolymers can also induce self-organization not only through incompatibility of the two blocks, but also through attraction of similar blocks.^[51] This anisotropic property of the rod-like chains leads to preferential interactions between the blocks, resulting in an extended chain crystalline phases or high-ordered smectics liquid crystalline phases.^{[26][52]} Due to these factors, it is difficult to predict the self-organization properties of conjugated rod-coil block copolymers despite the fact that the initial report on rod-coil block copolymers dates from 1969.^[53]

Semenov and Vasilenko performed theoretical studies on the phase behavior of rod-coil diblock copolymers in the 1980s.^[54] In their study, they consider a set of factors, such as; the steric interactions between rigid blocks, the stretching of the flexible coil blocks and the undesirable interactions between the blocks. From this theoretical study, two phases were established: a nematic phase and a smectic A phase. In both cases, the rods are aligned perpendicular to the lamellar

organization of the domains (See Figure 2.5). Later on, the smectic C phase was introduced, wherein the rigid blocks take up positions parallel to each other, but tilted at an angle with the domain interface.^{[54][55]} They also established a theoretical phase diagram describing second-order transitions between the nematic phase and the smectic A phase and between the smectic A and C phases (“hockey pucks”). The transition between a smectic A and a smectic C structures was explained by Halperin.^[56] The “hockey pucks” structures were also confirmed in the works of Williams and Fredrickson for high volume fraction of the coil block.^[57]

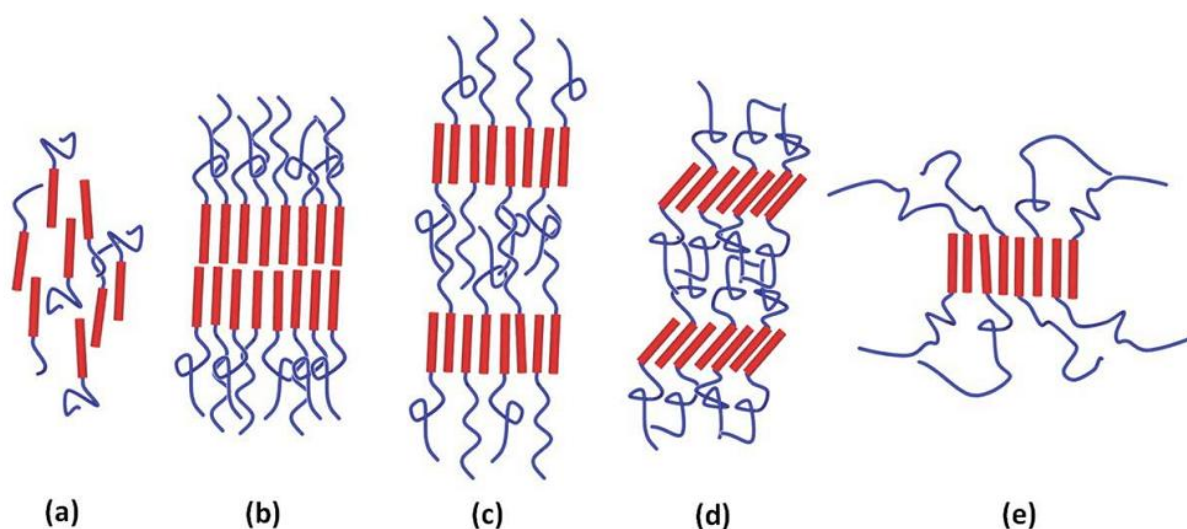


Figure 2.5: Illustrations of rod-coil block copolymer self-assembly into (a) nematic, (b) bilayer smectic A, (c) monolayer smectic A, (d) monolayer smectic C and (e) “hockey pucks.” Reproduced from Ref.^[24]

Further studies have been carried out in order to build the phase diagram of rod-coil block copolymers by considering two additional driving forces that arises from the interaction and/or crystallization of the rod-blocks. One is the Maier–Saupe interaction strength, μN , characterizing the aligning interaction between the rod-blocks, and the other is the geometrical asymmetry, ν , defined as the ratio between the coil radius of gyration and the rod length.^{[48][52][58]} Thus, in rod-coil BCPs, the equilibrium phase segregation is governed by a more complex set of parameters. The most dominant are: the Flory–Huggins interaction parameter (χ), the relative volume fractions of the coil block (f), the Maier–Saupe interaction parameter, and the geometrical asymmetry, leading to completely different

mesostructures as regards to the conventional coil-coil BCPs (Figure 2.4).^[59] Moreover, it is generally accepted that the χ parameter for such block copolymers is much larger than for coil-coil block copolymers^{[60][61]} and therefore the microphase separation can take place at much lower degrees of polymerization (lower molecular weights).

In order to explore the phase behavior and self-assembly mechanisms of rod-coil BCPs, the synthesis of BCPs with well-defined structures is required. A good synthetic strategy is vital to incorporate a proper choice of flexible coil blocks into rigid conjugated rod-like blocks, thereby facilitating the nanoscale phase separation.^{[62][63][64][65]} Some of the typical rod and coil blocks used to carry out these studies are indicated in Figure 2.6.

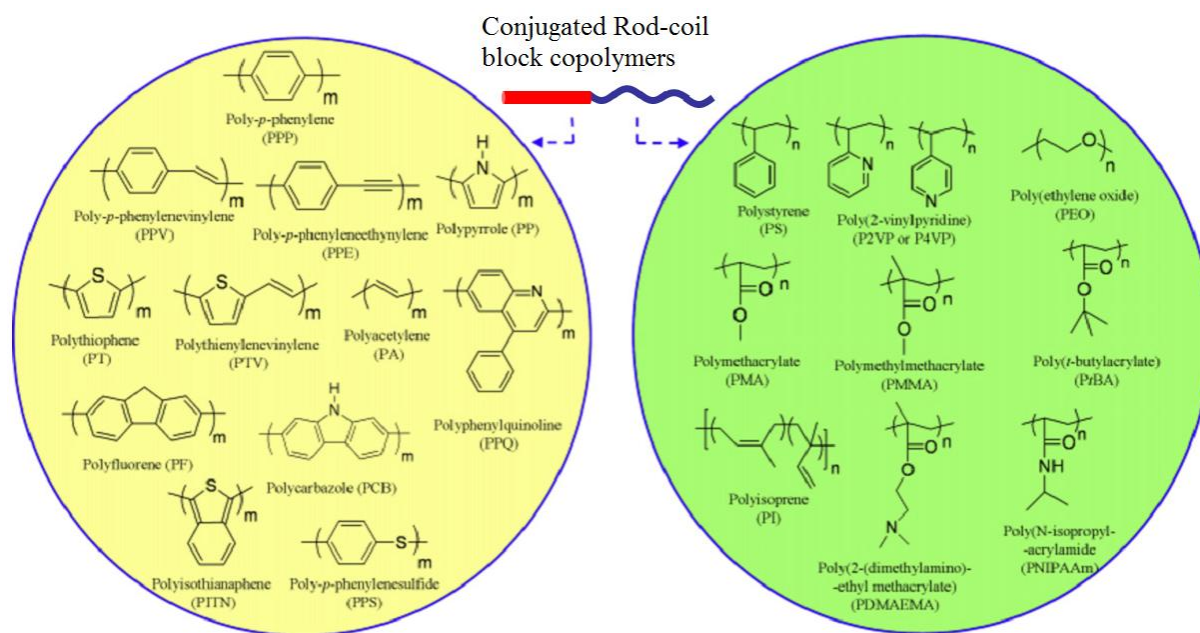


Figure 2.6: Several examples of polymer structures of conjugated rod-coil block copolymers. Reproduced from Ref.^[4]

In 1996, Chen *et al.* reported the mesostructure of rod-coil diblock copolymers consisting of a poly(hexylisocyanate) as the rod block and a polystyrene as the coil block (PHIC-*b*-PS) (synthesized through anionic polymerization).^{[48][66]} TEM images of the block copolymers revealed two new mesostructures which are nonexistent in the conventional coil-coil systems: the zigzag (Figure 2.7a)

and arrowhead (Figure 2.7b) structures were observed. Both of these structures have lamellae-like morphology in which the rod segments are organized into tilted layers, analogously to those observed in smectic phases. Radzilowski *et al.* have studied low dispersity rod-coil copolymers (mostly with a high volume fraction of the coil segments), and have observed unique structural transitions from lamellae to cylindrical phases to hexagonally packed micellar phases.^{[67][68]} Some other type of fibrillar structures were also observed where the conjugated segments aggregate to form ribbons, surrounded by the coil block.^{[69][70]}

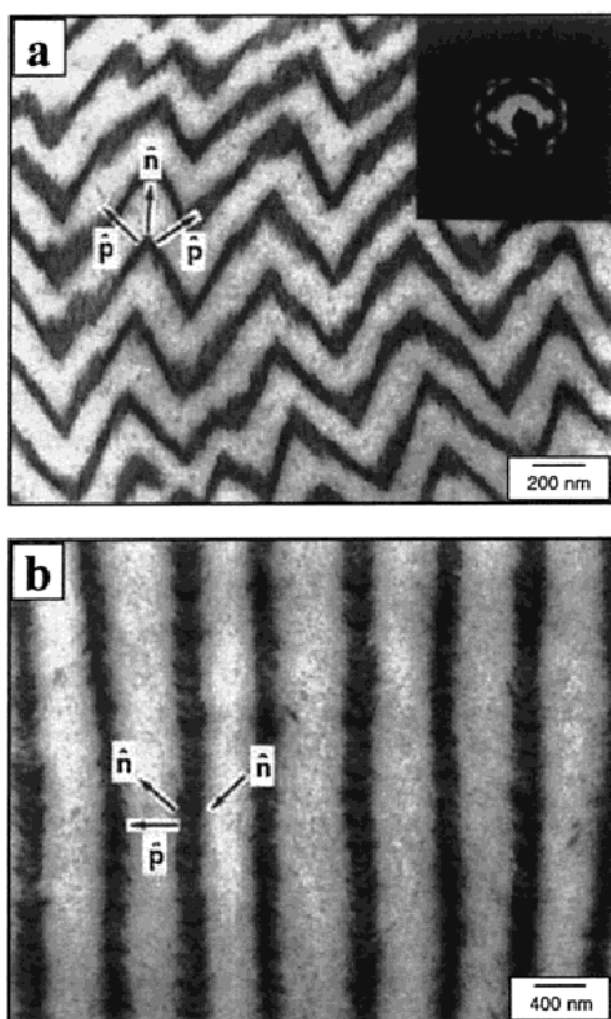


Figure 2.7: Transmission electron microscopy (TEM) images of poly(hexylisocyanate)-block-polystyrene (PHIC-*b*-PS) showing (a) zigzag lamellar ($f_{PS} = 0.10$) and (b) arrowhead ($f_{PS} = 0.02$) microstructures. In all of the figures, the dark regions correspond to the PS domains, which have been preferentially stained

with ruthenium tetroxide (RuO_4), whereas the relatively white regions correspond to the PHIC domains. The inset in (a) shows representative of PHIC selected-area electron diffraction (SAED) patterns. The PHIC chain axis and lamellar normals are denoted by n and p , respectively. Reproduced from Ref.^[48]

In the quest for a suitable architecture for photovoltaic applications, researchers have been forced to look at new class of rod-coil copolymers that fulfills both the structural and the electronic properties. Because of its high crystallinity and good electrical conductivity properties, poly(*p*-phenylenevinylene) (PPV) and its soluble derivatives remain one of the most widely studied conjugated polymers for optoelectronic applications.^{[43][44][71][72]} One of the earliest study on PPV-based rod-coil block copolymer systems was through the synthesis of alkoxy-substituted PPV (MEH-PPV) coupled with PS.^{[27][45]} Sary *et al.* investigated the self-assembly behavior of poly(diethylhexyl-*p*-phenylenevinylene-*block*-styrene) (PPV-*b*-PS) and poly(DEH-*p*-phenylenevinylene-*block*-4-vinylpyridine) (PPV-*b*-P4VP) rod-coil copolymers (their molecular structures are indicated in Figure 2.8) as a function of the coil volume fraction for weakly and moderately segregated regimes, respectively. X-ray diffractograms of the PPV-*b*-PS showed the existence of π - π stacking of the PPV blocks (related to strong Maier-Saupe interactions) resulting in a thermodynamically stable lamella clusters of the conjugated blocks within a matrix of PS.^[73]

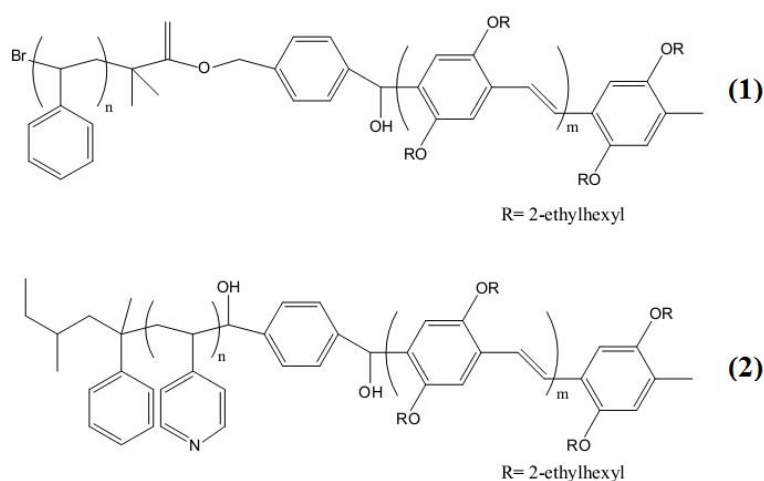


Figure 2.8: Molecular structure of poly(diethylhexyloxy-*p*-phenylene vinylene)-*block*-poly(styrene) (PPV-*b*-PS) **(1)** and poly(diethylhexyloxy-*p*-phenylene vinylene)-*block*-poly(4-vinylpyridine) (PPV-*b*-P4VP) **(2)**.

This group have further compared the theoretically predicted phase diagram of PPV-*b*-PS with the experimentally observed one using the model developed previously by Reenders and ten Brinke for monodisperse rod-coil diblock copolymers.^[52] Interestingly, this result confirmed that rod-coil block copolymers containing conjugated segments tend to form lamella-based morphologies due to the low conformational entropy of the rod, thus limiting curved interfaces in the self-assembled mesostructures.

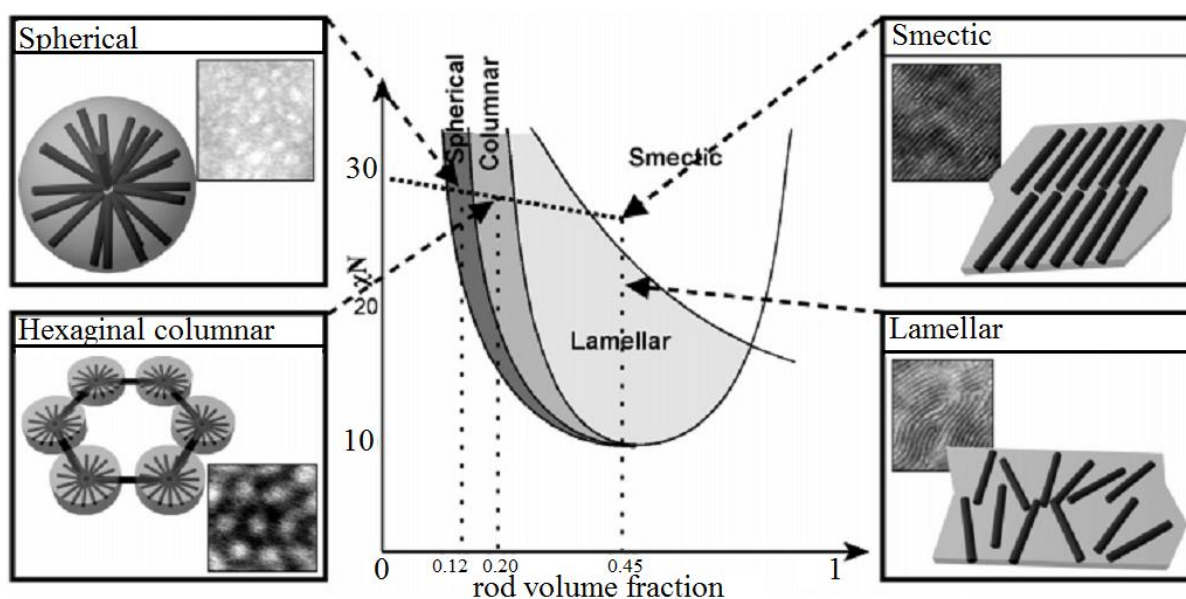


Figure 2.9: Representation of the schematic and observed morphologies as well as the phase diagram of PPV-*b*-P4VP rod-coil block copolymer. Reproduced from Ref.^[74]

Furthermore, the same group has extensively studied the phase diagram of PPV-*b*-P4VP rod coil block copolymers.^{[73][74]} Although the lamellar phase does dominate over a wide range of volume fractions (as expected due to the liquid-crystalline nature of the rod-blocks), it was found that hexagonal and spherical microphase-separated morphologies were accessible at high volume fractions of P4VP (Figure 2.9). Results from scattering characterizations have also shown that the block copolymers in the lamellar structure are organized in a smectic C double layer with a tilt angle of 52°, while the hexagonal phases self-organize in a homeotropic arrangements (with the PPV rods radially oriented and perpendicular to cylinder axis, while the P4VP coils form the dispersed continuous phase).

Aside from photovoltaic applications, other PPV based rod-coil block copolymers have also been investigated in several studies. For example, Yu and *coll.* reported the synthesis of alkyl substituted PPV coupled with polyisoprene (PI),^[75] poly(ethylene oxide) (PEO)^[76] and poly(propylene oxide) (PPO)^[77] at various volume fractions. Lamellar morphologies with a bilayer arrangement were confirmed using transmission electron microscopy and small-angle X-ray scattering techniques. For weakly segregated copolymers, such as poly(diethylhexyl-oxy)-p-phenylenevinylene)-*block*-polyisoprene (DEH-PPV-*b*-PI), the rod-coil block copolymer self-assembly as well as the resulted morphologies have also been investigated by other groups.^{[62][78][79]} Characterizations including SEM and grazing-incidence small-angle X-ray scattering have revealed that thermally annealed DEH-PPV-*b*-PI films self-assemble into lamellar phases with both parallel and perpendicular orientations relative to the substrate depending on film thickness and surface energy differences at confinements. Lamellar microdomains are oriented primarily parallel to the film in the case of thinner films, while the orientation of these lamellae domains at vacuum interface changes from parallel into perpendicular in the case of thicker films.

Other system of particular interest are the systems containing poly(alkyl-thiophene), particularly the poly(3-hexylthiophene) (P3HT). P3HT has become a subject of interest due to its superior charge carrier mobility, stability and processability as well as the possibility to control the chemistry inherent to its synthesis.^{[80][81][82]} McCullough and *coll.* studied the self-assembly of P3HT-based block copolymers that include PS, poly(methyl acrylate) (PMA) or polyurethane as the flexible coil block.^[64] They were able to establish the formation of crystalline P3HT lamellae ("nano-fibrils") embedded in a matrix of amorphous PS ($f_{PS} = 0.63$) for films casted from toluene. The formation of these "nanowires" structures is undoubtedly dictated by the immiscibility of the rod and coil segments. Even if many other P3HT-based A-B diblock and A-B-A triblock copolymer systems have been synthesized, most of them present the most commonly detected morphology for rod-coil block copolymer systems; *i.e.* a crystalline lamellae structure. Some rod-coil block copolymers of poly(3-hexylthiophene)-*block*-poly(2-vinyl pyridine) (P3HT-*b*-P2VP) have shown a nano-fibril structure at low volume fraction of P2VP, but with increasing volume fraction of the P2VP block, lamellar and cylindrical

mesostructures were observed.^{[65][83]} For example, in the recent work of Dai *et al* (Figure 2.10), the P3HT-*b*-P2VP displays a nanowire structure for $f_{P2VP} = 0.30$, indicating a strong rod-rod interaction between the P3HT blocks while, for $f_{P2VP} = 0.59$, the P3HT-*b*-P2VP shows a highly ordered structures with the P3HT block exhibiting lamellar domains. By further increasing the volume fraction of P2VP block to $f_{P2VP} = 0.75$ and $f_{P2VP} = 0.86$, the π -conjugated block copolymers display self-assembling nanostructures of hexagonal close packed cylinders and spheres, respectively, indicating that the P3HT chain adopts a coil-like structure allowing interfacial curvatures. This remarkable phase separation behavior observed in these P3HT-based block copolymers is inherent to the low molecular weight of the P3HT blocks as well as the large Flory-Huggins parameter between the thiophene and vinyl pyridine blocks. Besides, various P3HT-based block copolymers (P3HT-*b*-PS, P3HT-*b*-P4VP, P3HT-*b*-PMMA, and P3HT-*b*-poly(L-lactic acid) (P3HT-*b*-PLLA)) have been synthesized and their self-assembly properties were investigated while the block copolymers were used in photovoltaic and patterning applications.^{[22][84][85][86]} In all these investigations, fibrillar like P3HT nanostructures with poorly oriented (low degree of order) domains were observed. The degree of order in P3HT-*b*-PMMA was improved when small amounts of homopolymers were added to the block copolymer solution (for example, adding PMMA to P3HT-*b*-PMMA (9:1 w/w)). Highly ordered nano-fibril structure was produced, and the fibril length was extended over tens of micrometers.

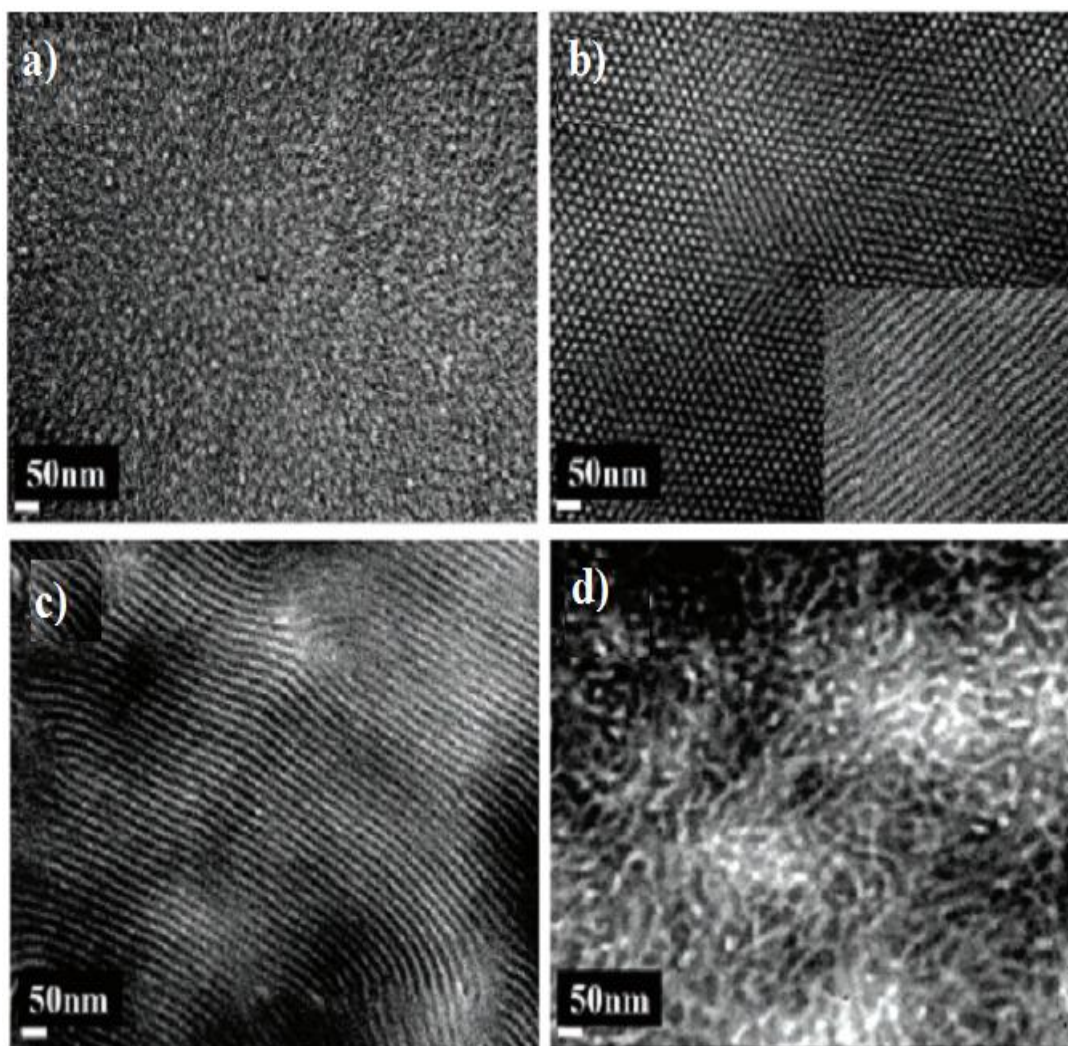


Figure 2.10: Transmission electron microscopy (TEM) images of poly(3-hexylthiophene)-block-poly(2-vinyl pyridine) (P3HT-P2VP) that contain (a) spherical ($f_{P2VP} = 0.86$), (b) cylindrical ($f_{P2VP} = 0.75$), (c) lamellar ($f_{P2VP} = 0.59$), and (d) nano-fibril-like ($f_{P2VP} = 0.30$) morphologies. The inset of (b) shows the cross-sectional view of the P3HT cylinders. The P2VP block is selectively stained black with iodine. Reproduced from Ref.^[65]

To sum up, a number of theoretical efforts have been devoted in order to capture and understand the self-assembly behavior of rod-coil block copolymers. These theories have demonstrated that rod-coil systems exhibit a complex self-assembly behavior which strongly differs from the one governing conventional coil-coil block copolymer systems. The models that have been developed at the early stages using the Landau expansion theory^{[52][60][87]} and the self-consistent-field

theory^{[49][88][89]} have helped researchers to elucidate the phase behavior of rod-coil block copolymers with good agreement with experimental studies.

2.2.2.2. Self-assembly Properties of all-Conjugated Rod-Rod Block Copolymers

In the previous part we examined the self-assembly and phase behavior of diblock copolymers containing a conjugated block (as rigid-rod) linked with a flexible coil block. Herein, some of the morphological and phase separation behaviors of all-conjugated rod-rod diblock copolymers will be presented. Due to the rigid nature of rod-like polymer chains, the physical properties and self-assembly mechanisms of these rod-rod diblock copolymers are more complex and far less understood than those of widely studied coil-coil and rod-coil diblock copolymers.^[59] However, conjugated rod-rod diblock copolymers possess both self-assembling and fascinating electronic properties (due to their continuous conjugation along the polymer chain) that provide comprehensive opportunities for developing high-performance organic electronics.^[25] In this regard, all-conjugated rod-rod BCPs have recently received attention from the organic electronic community, particularly for applications in polymer BHJ solar cells.^{[90][91][92][93]} Many of these researches emphasize on the highly crystalline poly(3-alkylthiophene)s rod-rod BCPs, due to the synthetic versatility obtained through their macromolecular engineering.^{[94][95][96][97]} Because of the large rod-rod interactions, conjugated rod-rod copolymers preferred to self-assemble in form of lamellar stacks.^{[98][99]} Ge *et al.* synthesized poly-(3-butylthiophene)-*block*-poly(3-hexylthiophene) (P3BT-*b*-P3HT) crystalline-crystalline all-conjugated diblock copolymer with well-controlled molecular weights and block ratios as well as narrow dispersities. The obtained diblock copolymer co-crystallizes into a uniform crystal domain, with the mutual interpenetration of the different side chains of the two blocks into a common interchain lamella.^[100] Following their pioneering work, this group has demonstrated that the co-crystallization and orientation of the block copolymer was possible to achieve through the control of the volume fractions of P3BT and P3HT blocks (shown in Figure 2.11a), leading to completely different solubilities and stacking of the polymer chains as regards to their homopolymer counterparts.^{[25][99][101]} The

crystalline packing of the different P3BT-*b*-P3HT rod-rod diblock copolymer with various volume fractions (Figure 2. 12b) was determined using X-ray diffraction (XRD). The films prepared from the block copolymers exhibiting different compositions (P3BHT21 (P3BT:P3HT = 2 : 1, mol/mol), P3BHT11 (P3BT:P3HT = 1 : 1, mol/mol) and P3BHT12 (P3BT:P3HT = 1 : 2, mol/mol)) show a unique [100] peak at $2\theta = 6.5^\circ$, 6.1° , and 5.8° , respectively, indicating that there was only one type of crystalline domain present in the system. These results were compared with respect of the XRD profiles of the P3BT and P3HT homopolymers, which showed a single [100] peak at $2\theta = 7.2^\circ$ and 5.7° , respectively.^{[101][102]}

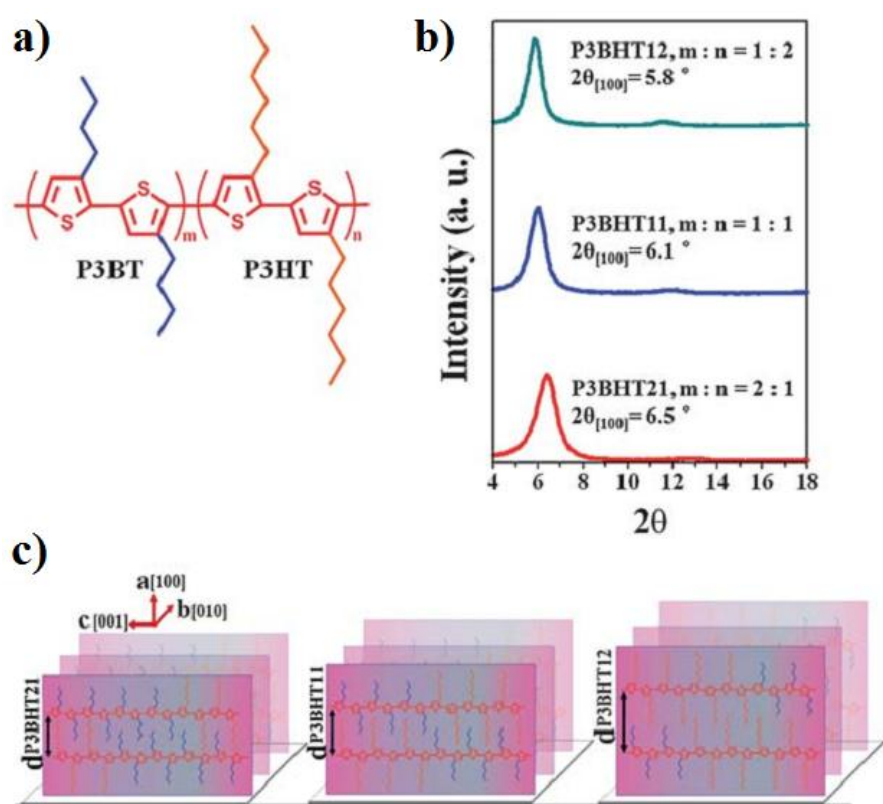


Figure 2.11: Chemical structure of poly(3-butylthiophene)-*b*-poly(3-hexylthiophene) (P3BHT) diblock copolymer. (b) XRD profiles of P3BT-*b*-P3HT films prepared from the *o*-dichlorobenzene solution. (c) Schematic representation of P3BHT21 (left panel), P3BHT11 (central panel), and P3BHT12 (right panel) lamella packing with the edge-on orientation. P3BT-*b*-P3HT diblock copolymers with different alkyl chain lengths tend to co-crystallize forming a crystalline lamellar structure by interpenetration of the two

different side chains, each with tunable interchain distance along the (100) axis (i.e., side-chain direction).^[99]

The XRD result clearly demonstrated that P3BT-*b*-P3HT diblock copolymers co-crystallized in the thin film configuration. The P3BT and P3HT blocks co-crystallize into a lamellar packing crystal structure with the interpenetration of the butyl and hexyl side chains, and adopt an edge-on orientation with the thienyl backbone aligned parallel to the substrate as depicted in Figure 2.11c.^{[99][103]} In their study they also notice that with an increased composition of P3BT, the interchain distance, d_{100} , progressively decreases from $d_{100, P3BHT12} = 15.0 \text{ \AA}$ to $d_{100, P3BHT11} = 14.1 \text{ \AA}$, to $d_{100, P3BHT21} = 13.2 \text{ \AA}$ indicating that the incorporation of higher quantity of P3BT in the diblock copolymer facilitates a closer packing of the thienyl backbones. This effect could be favorable in order to increase the charge mobility due to the lower intermolecular hopping distance along the [100] direction.^[104]

In a similar study, Wu *et al.* have thoroughly investigated the synthesis and the self-assembly of poly(3-butylthiophene)-*block*-poly(3-octylthiophene), P3BT-*b*-P3OT, crystalline-crystalline diblock copolymer.^[105] The P3BT-*b*-P3OT copolymers were found to self-assemble into crystalline nanowires (NWs) in solution. The P3BT-*b*-P3OT NWs observed through AFM and TEM techniques are similar to the ones obtained from the assembly of NWs from P3BT^[106] and P3OT^[107] homopolymers, implying that the π -stacking interactions are dominant relative to interactions of the side chains. However, the microphase-separation characterized by wide-angle X-ray scattering (WAXS) and small-angle X-ray scattering (SAXS) obtained from the melt indicated two distinct crystalline domains with a lamellar structure which is in opposition with the P3BT-*b*-P3HT diblock copolymers described previously. The two distinct crystalline domains observed in P3BT-*b*-P3OT copolymer melt were related to two distinct reflections in the WAXD spectrum inherent to the formation of P3BT- and P3OT-rich domains. Further SAXS characterization on these samples suggests a melt-phase assembly of the P3BT-*b*-P3OT diblock copolymer in the melt into a microphase-separated lamellar structure with two crystalline domains characteristic of the two different side chains.

Other conjugated rod-rod diblock copolymers have also been investigated. These copolymers were examined with the aim to improve the PV performance of organic solar cells through the nanostructuring of the diblock copolymer into ordered arrays with a length scale of the exciton diffusion length order (typically *ca.* 10 nm). In this regard, poly(3-hexylthiophene)-*block*-poly(3-dodecylthiophene), P3HT-*b*-P3DDT,^[108] poly(3-hexylthiophene)-*block*-poly(perylene diimide acrylate), P3HT-*b*-PPDA,^[59] poly(thiophene-*block*-perylene diimide)^[109] and Poly(3-hexylthiophene)-*block*-poly(perylene bisimide acrylate), P3HT-*b*-PPerAcr,^[110] were used as donor-acceptor materials to form single self structured organic solar cells. Those diblock copolymers were found to self-organize into controlled microphase-separated lamellar or sheet-like morphologies. Various microphase-separated morphologies were observed for different compositions; with the size and orientations of the mesostructures were related to the volume fraction of one of the rigid-rod block. This indicates that the fibrillar morphology obtained in thin films of those classes of diblock copolymers is encouraging, considering that both blocks are crystalline. However, understanding the microphase-separation mechanism and finding the right fabrication method to achieve the desired morphology for proper application have yet to be explored.

Generally, all conjugated diblock copolymers self-assemble in the solution or melt states into microphase-separated lamellar structures due to their highly crystalline character. Nevertheless, further studies are still needed to fully understand the molecular packing of the crystalline-crystalline diblock copolymers and their potential regarding to applications. For example, one of the potential applications of these functional conjugated diblock copolymers is to use them in the field of organic electronics. Usually, the block copolymers used in organic electronic applications should have an electronic property in addition to the capability of forming well-controlled nanostructures. The wide variety and the versatility of the synthetic tools available for the design of BCPs have motivated the development of functional BCPs for electronic applications. Among the potential applications of BCPs in organic electronics are (i) light-emitting devices, (ii) field effect transistors, and (iii) photovoltaic

devices. In the next paragraph, emphasis will be given to the application of BCPs in organic photovoltaics.

2.3. Block copolymers for Photovoltaic Application

Due to the promise of the low-cost fabrication of photovoltaic devices via solution processing methodology; a substantial research effort has been devoted to the field of organic photovoltaic over the past decade. Currently, power conversion efficiencies are surpassed the 10 % mark (the possible target for large-scale commercialization) in laboratories and PCEs of 7-8% are already foreseen in single junction BHJ organic solar cell devices.^{[111][112][113][114][115][116]} In such devices, the active layer morphology has been shown to be of crucial importance as regards to the device performance.^{[117][118][119]} As shown in previous sub-chapters, there has been a growing interest in the synthesis of conjugated block copolymers hoping that the block copolymers will offer a new strategy for synergistic device performance enhancement by controlling the phase separation.^{[20][27][45][120-123]} Controlling the phase separation using block copolymers has been demonstrated to be a promising approach for tuning micro-phase separations of the donor and acceptor materials in photovoltaic active layers.^{[22][124]} The ability of block copolymers to self-assemble^{[23][74][125][126][127]} into highly ordered and thermodynamically stable mesostructures as well as their amphiphilic nature^[76], renders them attractive for tailoring BHJ morphologies. Block copolymers used for this purpose comprise a rod-like block – usually a conjugated semiconducting polymer – and a coil-like block which brings additional functionalities (*i.e.* solubility, processability and self assembling properties) to the system. Block copolymers with rod-rod architectures can also lead to well defined p–n junctions, however their use in photovoltaic applications has been limited so far due to the modest processability they exhibit owing to the strong rod-rod interactions.^{[97][99]}

There are a number of ways to incorporate those rod-coil or coil-coil block copolymers in organic photovoltaic BHJ systems. First of all, a donor-*b*-acceptor copolymer can be used alone to form a single, self-structured active layer upon self-assembly. In a second approach, a copolymer that

contains a donor block can be blended with fullerene moieties or its derivatives to form BHJ architecture. An alternative and promising approach is to use block copolymer as additives in organic photovoltaics, mostly to control the microstructure of polymer:fullerene blends. For example, in the compatibilizing approach; the block copolymer is confined at domain interfaces between the donor and the acceptor, and lowers the interfacial tension of the A/B polymer blends, thus suppressing the coalescence and limiting domain sizes. Consequently an extended macro-phase segregation of the polymer:fullerene blend is bypassed and a more stable morphology can be promoted.^{[128][129]} In another way, the incorporation of the copolymer into polymer:fullerene blends could promote crystallization by acting as a nucleating agent for the donor polymer. It is generally considered that the addition of nucleating agents gives rise to increase the crystallinity of polymers.^[130] The additives exert an influence on the rate of the crystallization process and the morphology of final product.

2.3.1. Block copolymers as Single Self-structured Active Layer in OPV

In order to meet the specific requirement for an efficient photon to charge conversion, different device architectures have been developed. The first attempt to create an organic solar cell was made by sandwiching a single layer of an organic material (anthracene crystal) between two dissimilar electrodes.^[131] This type of device structure is very simple to fabricate but since both positive and negative photo-excited charges are transported through the same material recombination losses are generally high. In 1986, a major breakthrough was achieved by Tang, who introduced a double-layer structure in which the acceptor material was deposited on top of the donor material.^[132] The two-layer device was fabricated using copper phthalocyanine as the electron donor, and a perylene tetracarboxylic derivative as the electron acceptor. However, the performance of this type of device architecture was still severely limited by large excitonic losses (only excitons created at the bilayer interface participate in charge generation). Typical modern organic solar cells involve a blended donor-acceptor active layer known as a bulk heterojunction (BHJ).^[133-136] Significant progresses have been made in obtaining decent device efficiency using the BHJ device architectures model.

Nevertheless, the efficiency of a bulk-heterojunction OPV cell is highly correlated with the morphology of the electron donor/electron acceptor domains in the blend film. Such blends exhibit significant structural disorder since they rely on uncontrolled phase separation mechanisms. The domains formed through this spontaneous organization are either too large (excitonic loss), too small (charge recombination), or discontinuous (poor carrier mobility).^[16] So, researchers investigate novel materials that can microphase separate through controlled self-assembly, thus exhibiting better morphological stability while simultaneously keeping excellent electrical properties. One of the first configurations of BHJ following this concept was realized through the design of a block copolymer in which the A block contains a p-type electron donor and the B block contains an n-type electron acceptor sandwiched between two electrodes in order to form a single self-structured donor/acceptor active layer. The immiscibility of the blocks and the presence of a covalent bond between them lead to the spontaneous formation of ordered nanodomains, providing a larger interface for charge separation and improving the formation of a co-continuous (interpenetrated) pathway for charge transport.^[137]

Some early studies have shown the efficient energy transfer from the donor blocks to the acceptors blocks both within a single copolymer chain and between neighboring chains in particular for BCPs used in OLEDs applications.^[138–140] The first application of this methodology to OPV was related to the pioneering works of the Hazdiiannou's research group^{[20][23][27][45]} through the design of a rod-coil of PPV-*b*-P(S-stat-C₆₀MS) in which the poly(p-phenylenevinylene), PPV, and the C₆₀-functionalized polystyrene act as the donor and acceptor materials, respectively (Figure 2.12a). An efficient photoluminescence quenching and even enhanced photovoltaic performance were demonstrated through the design of such donor-*b*-acceptor BCP. Even though, the BCP BHJ of PPV and a grafted C₆₀ PS had shown some promises in using BCPs as single material in OPVs, the performance was still relatively poor due to a low resulting π -stacking hindered by the growth of fullerene nanocrystals.^[141] Consequently, the improvement of OPV performance following this methodology still requires additional research efforts into molecular design and processing techniques. To enhance the π -stacking in rod-coil copolymers, more efficient donor-acceptor systems have been

targeted. Regioregular P3HT (*rr*-P3HT) is well-known for its strong π -stacking interactions, responsible of its high charge carrier mobility.^[94] Holdcroft *et al.* have synthesized P3HT-*b*-P(S-*stat*-C₆₀MS) (Figure 2.12b) in a similar manner to that described by Hadziioannou *et coll.*^[142] These materials have been tested as active materials in BHJ solar cells but they exhibit low device performance related to a poor charge mobility and carrier losses due to the intrinsic non-conductive coil phase.^[143] Similar approaches have been reported by Hadziioannou *et coll.* and others (Figure 2.12c)^{[144][145][146]} using *rr*-P3HT as the rod block but the same limitations were observed as well. Optical properties indicate that these materials present suitable characteristics for photovoltaic applications; however, the analysis of photovoltaic performance was not reported. Hiorns *et al.* synthesized and studied poly(3-hexylthiophene)-*alt*-C₆₀ (Figure 2.12d) in order to enhance the photo-physical interactions between the conjugated p-type polymer block and the C₆₀ moieties by fusing the C₆₀ moieties directly into the polymer backbone.^[147] Due to the low molecular weight of the macromolecules, the obtained power conversion efficiency could not go higher than 0.05%.

Other rod-coil block copolymer systems with a different acceptor than the common C₆₀ moieties have also been studied. Due to its large molar absorption coefficients and good electron accepting properties^{[148][149][150][151]}, several groups have investigated BCPs comprised of poly(3-alkylthiophene) and a polyacrylate with perylene diimide pendant groups (Figure 2.12e) for photovoltaic applications.^{[109][152][153]} These copolymers showed efficient photoluminescence quenching in the solid state, indicative of charge separation, and were used to produce solar cells with power conversion efficiency as high as 0.49%.^[109] The low PV performance of these cells was related to poorly organized and mis-oriented nanostructures. In another development, functional rod-coil block copolymers of (poly(3-hexylthiophene)-*block*-poly(*n*-butyl acrylate-*stat*-acrylate perylene)) (Figure 2.12f) were synthesized as electron donor-acceptor moieties.^[154] These materials, which form highly crystalline domains favorable for charge carrier mobility, exhibit near total photoluminescence quenching and PV cells have been fabricated with efficiencies of 0.5%. However, this obtained efficiency still an order of

magnitude lower than efficiencies achieved with conventional blends of donor:acceptor BHJ organic solar cells.

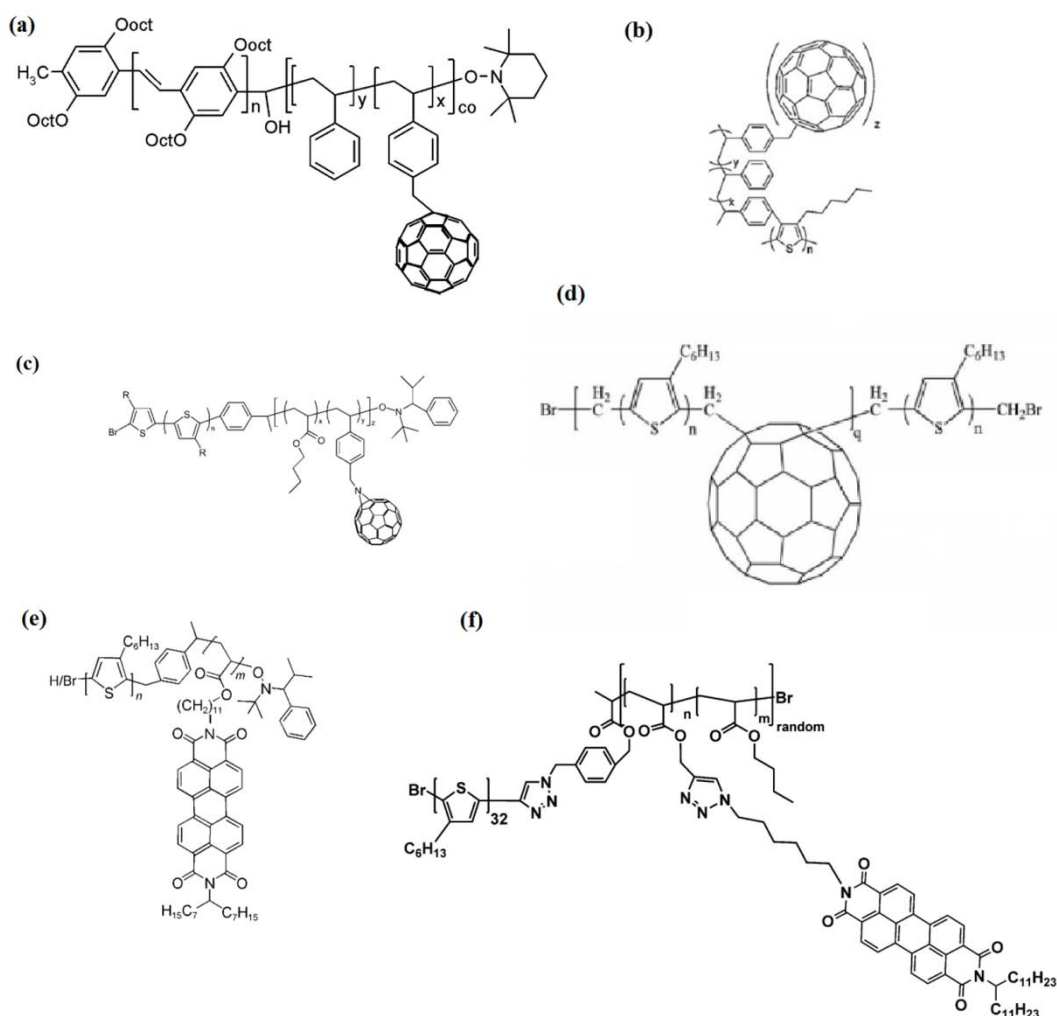


Figure 2.12: Chemical structures of donor-acceptor rod-coil BCPs. (a) PPV-*b*-P(S-stat-C₆₀MS), (b) P3HT-*b*-P(S-stat-C₆₀MS), (c) P3HT-*b*-P(BA-stat-N₃MSC₆₀), (d) P(P3HT-*b*-CH₂C₆₀), (e) P3HT-*b*-PPerAcr and (f) P3HT-*b*-P(BA-stat-PerAcr).

The photovoltaic performance obtained from the single self-structured donor-acceptor active layer was shown to be generally poor due to several reasons: (i) higher charge recombination because both electron and hole are transported within the same material, (ii) domain misorientation and (iii) poor charge mobility and carrier losses in the non-semiconducting segment (*i.e.* coil phase), such as in the polystyrene phase for example. Therefore, optimizations of the design of BCPs for OPVs as well as

a better control of the self-assembly properties are needed to alleviate the aforementioned problems. One methodology to bypass these limitations is to use the block copolymer as the donor material and to blend it with a known acceptor material (like, the phenyl-C₆₁-butyric acid methyl ester (PC₆₁BM)) rather than to use it as single self structured active layer.

2.3.2. Block copolymers as a main donor material in OPV Active Layer

The design and synthesis of well-defined BCPs consisting of a donor polymer and a coil block with some added functionality is expected to yield more preferable nanostructures when blended with fullerene derivatives than the randomly mixed semiconducting polymer with PCBM. In this regard, Sary *et al.*^[22] proposed a new approach to design bicontinuous donor-acceptor networks based on rod-coil P3HT-*block*-polyvinylpyridine, P3HT-*b*-P4VP, (Figure 2.13a) blended with PC₆₁BM promoted via weak supramolecular interactions between the P4VP and the PC₆₁BM. In this approach, each PC₆₁BM molecule is expected to form non-covalent bonds with multiple P4VP chains.^[155] TEM results indicate the ability of P3HT-*b*-P4VP to self-assemble into thermally stable nanostructured with PC₆₁BM enriched domains (Figure 2.14c, d) as compared to the classical P3HT:PCBM blends (Figure 2.14a, b). The preferential positioning of PC₆₁BM molecules within the coil domains was further assessed through the characterization of the PV device performance. PV devices both in the standard and inverted configurations were investigated. The PCE measured on devices with a standard architecture turned out to be extremely low, 0.03%, regardless of the PC₆₁BM content. These poor results were attributed to the presence of the P4VP-rich layer between the active layer and the PEDOT:PSS interface, whose existence was supported by TEM cross-sectional analysis. Indeed, the latter would lead to PC₆₁BM accumulation near the device anode and thereby introduce a hole collection barrier. However, with inverted device structure, the performance was improved and PCE as high as 1.2% was obtained.

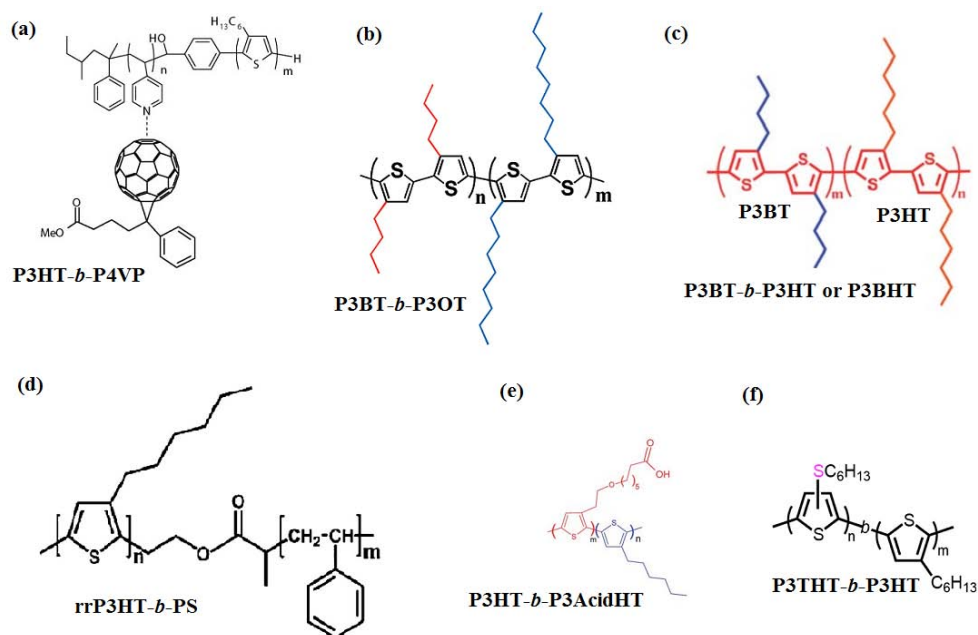


Figure 2.13: Chemical structures of rod-coil block copolymers used as donor materials in BHJ devices.

The structure in Figure 2.15a shows the non-covalent interaction between PC₆₁BM and P4VP blocks.

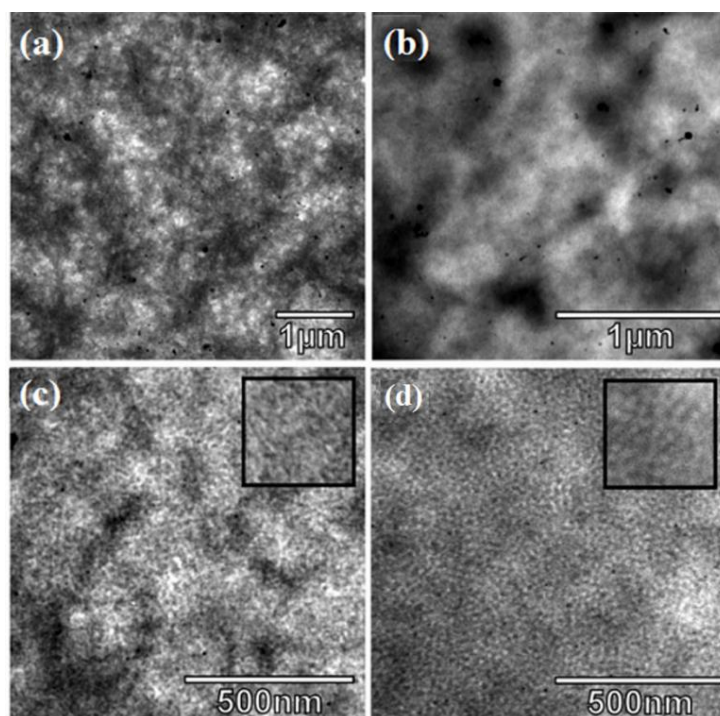


Figure 2.14: TEM images of P3HT:PCBM (1:1) and P3HT-*b*-P4VP:PCBM (36:64 v/v) thin films after iodine staining of the P4VP and various annealing times at 150°C: (a) and (c) Reference P3HT:PCBM and P3HT-*b*-P4VP:PCBM films after 30 min annealing, respectively. (b) and (d) reference P3HT:PCBM and P3HT-*b*-P4VP:PCBM films after 30 min annealing, respectively.

*P4VP:PCBM films after 24 h annealing; respectively. Macrophase separation is observed only in the reference film (b), whereas the block copolymer nanostructure improves upon long-term annealing (d). The inset shows the nanostructures of pure block copolymer P3HT-*b*-P4VP after 30 min (c, inset) and 24h (d, inset) annealing over a 200 nm × 200 nm surface area.*

Ren *et al.* investigated the photovoltaic properties, charge transport, and morphology of a series of diblock conjugated copolymers based on poly(3-butylthiophene)-*block*-poly(3-octylthiophene), P3BT-*b*-P3OT, (Figure 2.13b) as a function of block composition and found a photovoltaic performance as high as 3.0% when the block copolymer is blended with PC₇₁BM, which was much higher than the corresponding homopolymer-based PV devices.^[97] Surface force microscopy and transmission electron microscopy images of the P3BT-*b*-P3OT:PC₇₁BM blends (Figure 2.15a to f) in combination with XRD analysis have revealed the existence of a well-defined nanoscale phase separation consisting of a co-continuous network of polymer domains with small crystallites with a size of 11-18 nm. The largely improved photovoltaic efficiency was then related to the enhanced carrier mobility of holes in the BHJ devices, while the P3BT block with the short butyl side chains was responsible of enhanced self-assembly.

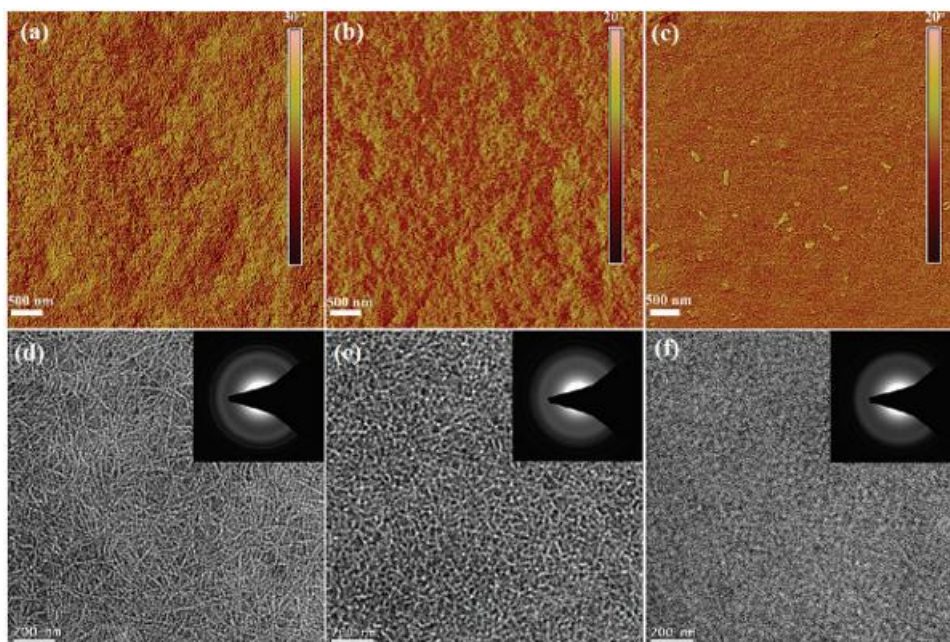


Figure 2.15: AFM phase images of (a) P3OT/PC₇₁BM (b) P3BT-*b*-P3OT(1:1)/PC₇₁BM (c) P3BT/PC₇₁BM blend thin films and their corresponding TEM images (d-f) (inset: Selected Area Electron Diffraction (SAED) pattern). The thin films were prepared by 5 min film aging in a Petri dish and 5 min thermal annealing at 110°C.

In a similarly study, He *et al.* have compared the device efficiency and morphological properties of poly(3-butylthiophene)-*block*-poly(3-hexylthiophene), P3BT-*b*-P3HT, (Figure 2.13c) to their poly(3-alkylthiophene)s (P3AT) homopolymer counterparts.^{[99][103]} The photovoltaic performance of the homopolymer blends of P3BT:PC₇₁BM and P3HT:PC₇₁BM were found to be 1.08% and 3.54%, respectively. However, PCE as high as 4.02% was achieved in a P3BHT:PC₇₁BM BHJ device. The ratio between the P3BT and P3HT blocks had a noticeable influence on the molecular organization of P3BT-*b*-P3HT, the film morphology of P3BT-*b*-P3HT:PC₇₁BM blends, and the final performance of P3BHT:PC₇₁BM photovoltaic devices (Figure 2.16). The size of crystalline domains of P3BT-*b*-P3HT:PC₇₁BM blend extracted from the full width at half-maximum (FWHM) of the diffraction peak was 10.4 nm. However, the size of P3BT crystals and P3HT domains were about 22.7 and 14.4 nm, respectively. Such larger size prevented efficient exciton diffusion in the P3BT:PC₇₁BM and P3HT:PC₇₁BM blends, thereby accounting for the low photogenerated charge density in those devices.

However, the crystal size in P3BT-*b*-P3HT:PC₇₁BM blend is comparable to the exciton diffusion length in P3ATs. The PCE obtained is therefore a direct consequence of the finer phase separation with a homogeneous donor–acceptor interface that maximizes charge generation, and percolating networks. With this, hole mobility as high as $2.0 \times 10^{-4} \text{ cm}^2 \text{ V}^{-1} \text{ s}^{-1}$ for P3BT-*b*-P3HT:PC₇₁BM blend was obtained.

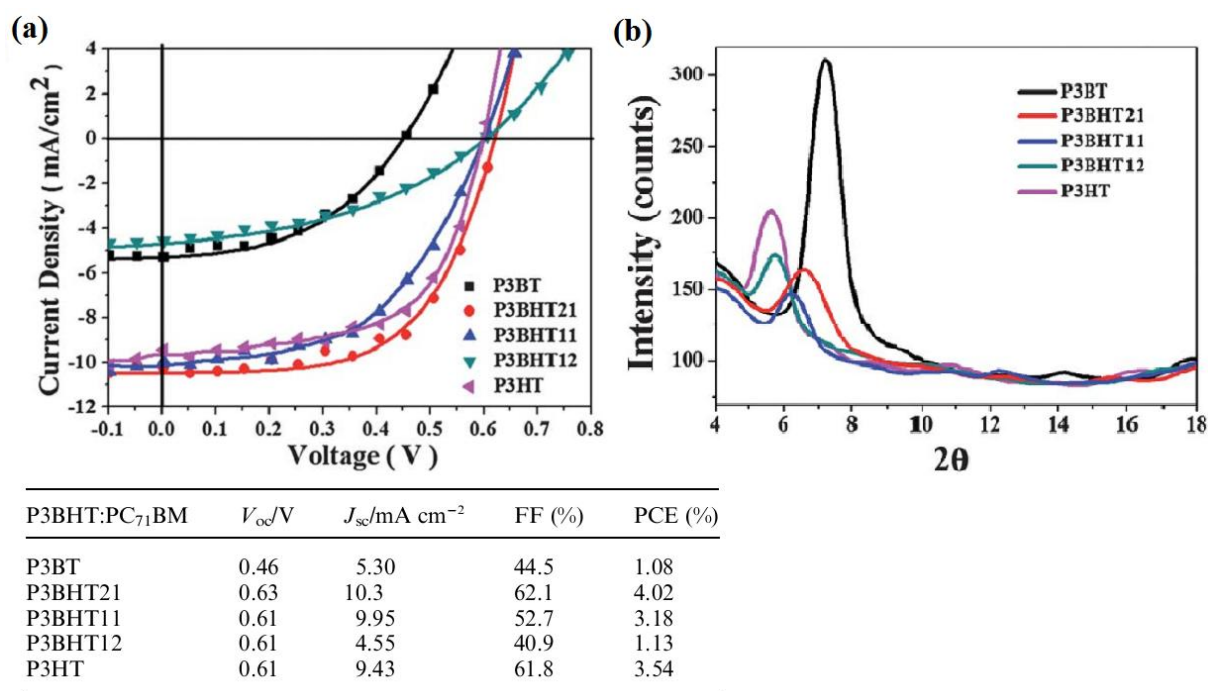


Figure 2.16: (a) *J*–*V* curves of bulk heterojunction solar cells fabricated from P3BT:PC₇₁BM, P3BT-*b*-P3HT:PC₇₁BM, and P3HT:PC₇₁BM solar cells under AM 1.5G illumination at 100 mW.cm⁻². The P3BT-*b*-P3HT diblock copolymers used have compositions of P3BHT21: P3BT:P3HT = 2:1, mol/mol), P3BHT11: P3BT:P3HT = 1:1, mol/mol), and P3BHT12: P3BT:P3HT = 1:2, mol/mol). Table shows summary of the different photovoltaic characteristics for different compositions. (b) XRD profiles of P3BT:PC₇₁BM, P3BT-*b*-P3HT:PC₇₁BM, and P3HT:PC₇₁BM blend films prepared by following the fabrication procedures of photovoltaic devices, but without depositing the Ca/Al layers on the top.

Poly(3-butylthiophene)-*block*-poly(styrene), P3BT-*b*-PS, (Figure 2.13d) block copolymer was synthesized and tested in photovoltaics by fixing the length of the semiconductor-block but varying the length of the insulator-block.^[156] These copolymers were blended with PC₆₁BM for the formation of bulk heterojunction photoactive layers. With appropriate insulator-block length and donor–acceptor

ratio, the power conversion efficiency and hole mobility increased by one order of magnitude compared with reference devices of the homopolymer blend (*i.e.* P3BT:PC₆₁BM). PS blocks improve the miscibility of the active layer blends remarkably. The P3BT-*b*-PS crystallizes as nanorods with the P3BT core covered with the PS-block, which creates a nanoscale tunneling barrier between donor and acceptor leading to more efficient transportation of charge carriers in the semiconductors. Other fully conjugated diblock copolymer, poly(3-thiohexylthiophene)-*block*-(3-hexylthiophene), P3THT-*b*-P3HT, (Figure 2.13f), which is composed of two equally proportioned donor-donor blocks that have distinct electronic structure were also tested in organic BHJ solar cells.^[157] In the solid state, X-ray diffraction and atomic force microscopy show that the polymer is semi-crystalline and has a structure related to the block copolymer composition, both with and without a fullerene-derivative. When tested in a device configuration (P3THT-*b*-P3HT:PC₇₁BM), the deep HOMO level of the P3THT block increases the open circuit voltage to a value that is equal to a P3THT:PC₇₁BM control device (0.66 V). This shows that the V_{oc} of an equally proportioned ternary organic solar cell can reach the upper limit of the corresponding binary devices. The study shows that donor–donor block copolymers are excellent materials for organic solar cells and that a high V_{oc} can be obtained even when the HOMO level of one of the blocks is high. More recently, Yassar *et al.* synthesized an amphiphilic conjugated block copolymer, denoted as P3HT-*b*-P3AcidHT (Figure 2.13e) for PV application to form BHJ devices with PC₆₁BM.^[158] The amphiphilic block copolymer showed the best performance so far when block copolymers were used as donor material with V_{oc} 0.60 V, J_{sc} 13.0 mA.cm⁻², fill factor (*FF*) 0.60 and PCE 4.2%, while its control device (P3HT:PC₆₁BM) exhibited V_{oc} 0.62 V, J_{sc} 12.66 mA cm⁻², *FF* 0.45, and PCE 3.24%. As a result, the efficiency of the best performing device showed a 30% improvement compared to the control device.

The photovoltaic and charge transport properties as well as morphology of bulk heterojunction solar cells based on a series of diblock copolymers as a donor material in polymer:fullerene blends have been presented. Some of the findings have shown that the increase in crystallinity through the design of block copolymers have substantially enhanced the photovoltaic

properties compared to the parent homopolymers or the self-structured donor-acceptor block copolymers. The observed enhancement of the carrier mobility of holes in the BHJ devices largely accounts for the large improvement in photovoltaic efficiency. The increase in performance is also based on weak, non-covalent interactions between one of the block and the acceptor or the fullerene derivatives. These demonstrate that conjugated block copolymers could be more effective if they are used as additives for nanostructuring the donor-acceptor blends, as detailed in the next section.

2.3.3. Block copolymers as compatibilizers in OPV Active Layers

To obtain high device performance, it is necessary to carefully optimize the morphology of the active layer. Different approaches have been applied to control the film morphology of BHJ solar cells, including adjusting the film-forming processes,^[159] solvent annealing,^{[160][161][162]} microwave annealing,^{[163][164]} and thermal annealing techniques.^{[165][166][167][168][169]} Although, higher local ordering and crystallinity with bicontinuous structure were obtained,^{[170][171]} it is challenging to apply these methods to practical fabrications. For example; high temperature annealing is not compatible with the use of flexible substrates because of the low melting and/or glassy transition temperatures and the solvent vapor annealing may not be suitable for real roll-to-roll process due to the dangers of solvent vapor.^{[172][173]} Therefore, it is necessary to create new procedure for the development of flexible low-cost organic solar cell with high performance. Since the addition of Silver (Ag) and Gold (Au) nanoparticles into poly(3-octylthiophene):C₆₀ bulk heterojunction blends were reported by Carroll *et al.*,^[174] the concept of incorporation of some other additives like; solvents^[175-177], high-boiling-point additives such as octanedithiol^[178, 179], n-dodecylthiol^[180] or small molecules^[181, 182] into the donor-acceptor blend system has been developed. Generally, they have a positive influence on device performance. However, some low volatile additives which still remain in the film after the film-forming process can also disrupt the stability of the morphology over time and influence the device performance as a result.^[183] One of the most promising approaches as an additive methodology is the utilization of block copolymer as compatibilizer or as nanostructuring agent in organic photovoltaic

blends. The methodology is inspired by the improved compatibility obtained in common A:B polymer blends when a block copolymer that comprises a block that is miscible with a polymer A, while the other block is miscible with a polymer B.^[128] Depending on the type and property of the block copolymer used, it may have different effects on the final organization of the donor-acceptor components. For example, amphiphilic diblock copolymers additives, used as compatibilizers, can reduce the interfacial energy and limit coalescence, thereby tuning the size of donor and acceptor domains and improving the phase stability between immiscible components (or adjusting the interaction between donor and acceptor to control the scale of phase separation due to the non-specific interaction that exists between the photovoltaic blend components and the copolymer).^{[184][185]} Another important effect of block copolymer additives is related to their potential as nucleating agent to increase the crystallization or planarity of conjugated molecule. As a case for P3HT:PCBM blend system, the crystallinity of P3HT is crucial to the device performance, as it affects the photons absorption and charge transport. The crystallization of P3HT is inherent to the interchain π - π stacking in P3HT main chains which is driven by a single chain conformational changes.^{[186][187]} However, its crystallization process (its coil-to-rod or folded-to-aligned transformations) could be hindered by chain entanglements. Adding a proper nucleating agent into P3HT:PCBM blend will reduce the polymer chain entanglements and favors its self-organization and crystallinity of the P3HT (*i.e.* the rigid conformation of P3HT could be induced by incorporating additives, which results in an enhanced crystallinity).^[180] Those copolymer additives acting as nucleating agent usually have a strong chemical affinity towards the polymer in the blend.^[183] To sum up, block copolymers used as additives can play different roles in optimizing the morphology of the P3HT:PCBM BHJ blends.

When block copolymers are introduced as compatibilizers or nucleating agents in photovoltaic active layers, the rod block is commonly of the same nature as the donor semiconducting polymer while the coil block can vary depending on the extra functionalities that are desirable. Several coil blocks (*e.g.* polyacrylates, polystyrene, poly(acrylonitrile), poly(4-vinylpyridine), perylene diimides (PDI), poly(methyl methacrylate), polyisoprene, poly(*tert*-butyl acrylate), poly(L-lactic acid)) have been

covalently attached to a P3HT block to form a rod-coil copolymer and used as compatibilizers in P3HT:PCBM blends.^[17] In this regard, Fréchet *and coll.* have reported the use of a diblock copolymer containing a P3HT-based block and a fullerene-containing block as a compatibilizer (Figure 2.17a) in order to lower the interfacial energy between the polymer and fullerene components in photovoltaic blends and, thus, to improve the stability of the thin film morphology upon thermal annealing. The addition of an optimized amount of diblock material (17 wt%) to a blend of P3HT:PC₆₁BM shows a comparable device performance to the control P3HT:PC₆₁BM device.^[188] In another report, Wudl *and coll.* used 5% of a P3HT-*b*-poly(styrene-*co*-acrylate) (Figure 2.17b) rod-coil copolymer with fullerenes chemically linked to the acrylate unit into a P3HT:PCBM blend and observed an improvement in *PCE* from 2.6% for the pristine device to 3.5%. AFM images have showed an improved co-continuity (interpenetrating networks) of the BHJ composite upon the copolymer addition, and thus greatly affects the short-circuit current.^[189] Lee *et al.* has synthesized C₆₀-end capped poly(3-hexylthiophene), P3HT-C₆₀, (Figure 2.17c) and used as a compatibilizer for the purpose of controlling the morphology of P3HT:PCBM blend films.^[190] In another study, the same group has synthesized and used a similar block copolymer architecture based on P3HT and side-chain fullerenes (Figure 2.17d) for compatibilizing of P3HT:PC₆₁BM blends.^[191] The addition of a small amount of the block copolymer into P3HT:PC₆₁BM blend has showed an improved stability in device performance over long-term thermal treatments. This is attributed to the reduction of domain size in the P3HT:PC₆₁BM blend and the limitation of the macrophase separation in the composite films, owing to the preferential location of the block copolymers at the interface between the P3HT and PC₆₁BM phases. The incorporation of poly(3-hexylthiophene)-*block*-poly(ethylene oxide), P3HT-*b*-PEO, in pure P3HT and P3HT:PCBM blends has also been reported^[192] and a change of the P3HT domain size with respect to copolymer concentration was observed. A rod-coil BCP based on a regioregular P3HT rod block and poly(butylacrylate-*stat*-C₆₀-methylstyrene), P3HT-*b*-P(BAC₆₀MS), (Figure 2.17e), was also used as compatibilizer for a P3HT:PC₆₁BM based BHJ solar cells.^[193] The addition of 2% (wt.) of the copolymer into the blend significantly improves all the photovoltaic parameters and leads to a 3.2% *PCE*, higher than the reference device

(the reference device has shown a PCE of 2.5%). This improvement was attributed due to changes in the morphology, improving charge generation and transport (higher J_{sc} and higher FF). However, higher copolymer amounts lead to a worsening of the device performances. These results were confirmed by AFM analysis of the film morphology. In the sample with 2% copolymer the presence of P3HT lamellae is preserved, while in a 5 wt% film a more disordered network of elongated structures was found. The rapid decline in the photovoltaic performances observed for higher percentage block copolymer incorporation (10%) was likely due to increased nucleation of PC₆₁BM micrometer crystals.

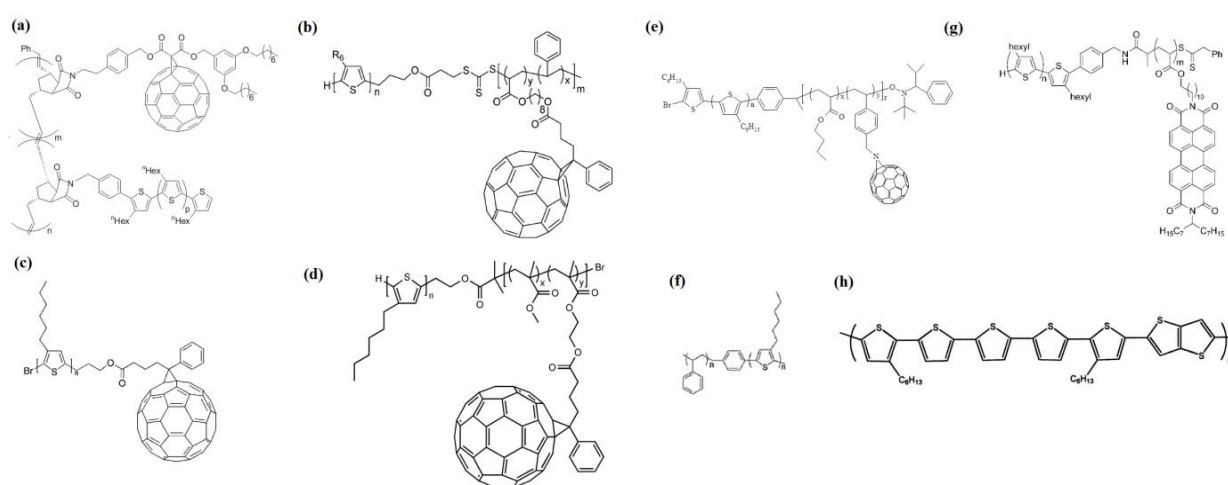


Figure 2.17: Chemical structures of rod-coil block copolymers used as compatibilizer in BHJ organic solar cells.

More recently, Xiao *et al.* presented an integrated study of the effect of a poly(3-hexylthiophene)-*block*-polystyrene, P3HT-*b*-PS, (Figure 2.17f) copolymer as interfacial compatibilizer in the P3HT:PCBM blend.^[194] Their work revealed that adding an optimized weight fraction of P3HT-*b*-PS copolymer (5 wt%) increases the crystallinity of P3HT (as shown from X-ray scattering (GIXS)) and homogenizes the vertical distribution of P3HT and PCBM (as shown from Neutron reflectivity (NR) measurements) in the active layer thereby increase the device performance (Figure 2.18). They attributed these outcomes to the favorable interactions of the P3HT block with the P3HT homopolymer and the strong affinity of PS block towards PCBM leading to enhanced hole transport and charge extraction. However, at higher concentrations of the copolymer additive, the device

performance started to degrade due to the appearance of discontinuous aggregates on the surface of the film. Higher carrier mobility in P3HT-*b*-PS (with 15 wt% PS block) has been indicated in another study as compared to the homopolymer P3HT, due to the increased crystallinity obtained through the addition of the copolymer.^[195] In another study, Rajaram *et al.* used a diblock copolymer (Figure 2.17g) to compatibilize a P3HT and perylene tetracarboxydiimide derivative (PDI) donor-acceptor blend and they achieved a three-fold improvement in *PCE* compared to previously reported P3HT:PDI BHJ devices.^[196] TEM images have shown the formation of smaller domains of the blend components resulting in a partial quenching of the PDI emission in the PL spectra upon the copolymer incorporation.

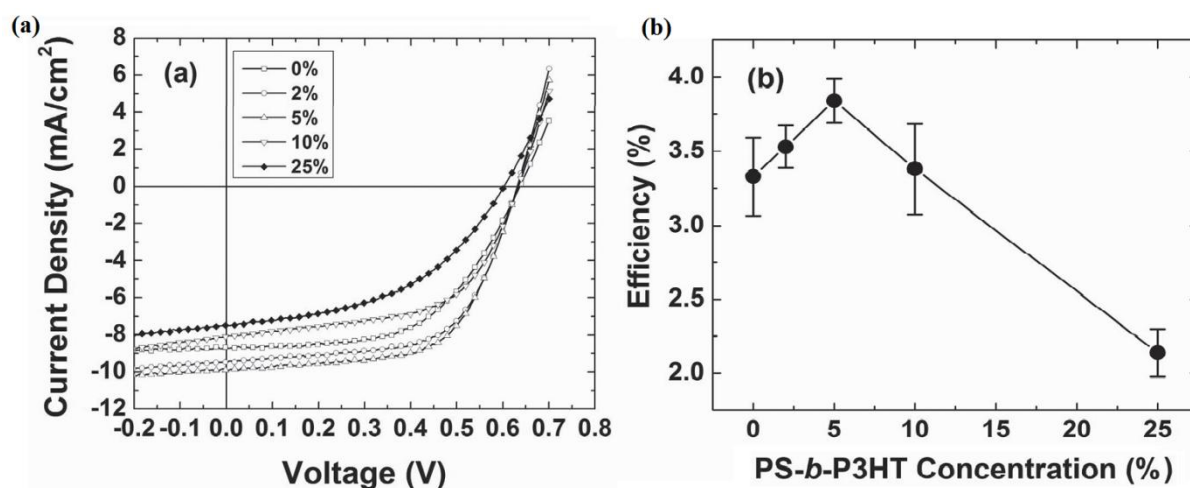


Figure 2.18: (a) *J-V* characteristics of selected devices (b) power-conversion efficiency P3HT:PCBM:P3HT-*b*-PS BHJ polymer solar cells (Error bars from standard deviation were based on 6-10 device samples).

So far, the block copolymers were mainly utilized as compatibilizers in P3HT:PCBM blends to reduce larger microphase separation by increasing the donor-acceptor interactions. However, other studies have showed that the incorporation of block copolymers based on thieno[3,2-*b*]thiophene and pentathiophene units, DHPT3, (Figure 2.17h)^[197] into P3HT:PCBM BHJ photovoltaic devices leads to enhancement of the crystallization. Due to the pronounced molecular planarity of thieno-thiophenes and/or the strong chemical affinity of pentathiophene towards P3HT, the copolymer acts as nucleating agent in the blend system to promote crystallization of P3HT. As observed by UV-vis spectroscopy, the

interactions between the copolymer and P3HT macromolecules induce a pronounced structural ordering (improvement of the crystallinity) of the polythiophene phase. However, the use of block copolymers as nucleating agents to promote the crystallization of the donor polymer have not yet fully investigated.

2.4. Conclusion

In conclusion, incorporation of additives to tune the interactions between electron donor and acceptor is an effective approach to control the degree of phase separation. The use of rod-coil BCPs in BHJ solar cells as compatibilizers and/or as nucleating agents has a beneficial effect either in term of improved miscibility between the donor:acceptor phases or in term of enhancing the crystallinity of the polymer. From the reports collected here, a clear trend has been indicated that thermodynamically stable nanoscale morphologies are accessible if the amphiphilic diblock copolymer contains a small insulating group to minimize unfavorable enthalpic contacts between the electron donor and acceptor. On the other hand, to improve the polymer crystallinity by enhancing the coplanar conformation of polymer chains, the copolymer additive which can act as nucleating agent must show a strong chemical affinity and strong interaction towards the polymer. Below, the effect of different P3HT based diblock copolymers on the morphology and device performance will be thoroughly investigated when they are utilized as compatibilizers and/or nucleating agents in P3HT:PCBM blends. However; before the block copolymer methodology was applied, the optimization of P3HT:PCBM blend is needed and has been systematically studied as well.

References

- [1] D. Bower, *An Introduction to Polymer Physics*, Cambridge University Press, London **2002**.
- [2] R.A. Pethrick, *Polymer Structure Characterization: From Nano to Macro Organization*, Royal Society Of Chemistry **2007**.
- [3] F.S. Bates, G.H. Fredrickson, *Physics Today* **1999**, 52, 32.
- [4] C.-L. Liu, C.-H. Lin, C.-C. Kuo, S.-T. Lin, W.-C. Chen, *Progress in Polymer Science* **2011**, 36, 603–637.
- [5] I.W. Hamley, *Physics of Block Copolymers*, Oxford University Press, Oxford, England **1999**.
- [6] L. Leibler, *Macromolecules* **1980**, 13, 1602–1617.
- [7] M.W. Matsen, F.S. Bates, *Journal of Polymer Science Part B: Polymer Physics* **1996**, 35, 945–952.
- [8] C.D. Han, J. Kim, J.K. Kim, *Macromolecules* **1989**, 22, 383–394.
- [9] C.D. Han, D.M. Baek, J.K. Kim, *Macromolecules* **1990**, 23, 561–570.
- [10] S. Forster, A.K. Khandpur, J. Zhao, F.S. Bates, I.W. Hamley, A.J. Ryan, W. Bras, *Macromolecules* **1994**, 27, 6922–6935.
- [11] J.K. Kim, H.H. Lee, Q. Gu, T. Chang, Y.H. Jeong, *Macromolecular Symposia* **1998**, 31, 4045–4048.
- [12] D.-C. Kim, H.-K. Lee, B.-H. Sohn, W.-C. Zin, *Macromolecules* **2001**, 34, 7767–7772.
- [13] A.K. Khandpurj, S. Farster, F.S. Bates, I.W. Hamley, A.J. Ryan, W. Bras, K. Almdal, K. Mortensen, *Macromolecules* **1995**, 28, 8796–8806.
- [14] G. Hadziioannout, A. Skoulios, *Macromolecules* **1982**, 15, 271–273.
- [15] Y. Matshuhita, *Structure and Properties of Multiphase Polymeric Materials*, Marcel Dekker Inc., New York **1998**.
- [16] S.B. Darling, *Energy & Environmental Science* **2009**, 2, 1266–1273.
- [17] J.K. Kim, S.Y. Yang, Y. Lee, Y. Kim, *Progress in Polymer Science* **2010**, 35, 1325–1349.
- [18] J.I. Lee, S.H. Cho, S.-M. Park, J.K. Kim, J.K. Kim, J.-W. Yu, Y.C. Kim, T.P. Russell, *Nano Letters* **2008**, 8, 2315–20.
- [19] D.A. Rider, K.A. Cavicchi, L. Vanderark, T.P. Russell, I. Manners, *Macromolecules* **2007**, 40, 3790–3796.
- [20] M.H. Van Der Veen, B. De Boer, U. Stalmach, K.I. Van De Wetering, G. Hadziioannou, *Macromolecules* **2004**, 37, 3673–3684.
- [21] N. Sary, R. Mezzenga, C. Brochon, G. Hadziioannou, *Macromolecules* **2007**, 40, 3277–3286.

- [22] N. Sary, F. Richard, C. Brochon, N. Leclerc, P. L  v  que, J.-N. Audinot, S. Berson, T. Heiser, G. Hadziioannou, R. Mezzenga, *Advanced Materials* **2010**, *22*, 763–768.
- [23] N. Sary, L. Rubatat, C. Brochon, G. Hadziioannou, R. Mezzenga, *Macromolecular Symposia* **2008**, *268*, 28–32.
- [24] P.D. Topham, A.J. Parnell, R.C. Hiorns, *Journal of Polymer Science Part B: Polymer Physics* **2011**, *49*, 1131–1156.
- [25] M. He, F. Qiu, Z. Lin, *Journal of Materials Chemistry* **2011**, *21*, 17039.
- [26] M. Lee, B.-K. Cho, W.-C. Zin, *Chemical Reviews* **2001**, *101*, 3869–3892.
- [27] B. de Boer, U. Stalmach, P.F. van Hutten, C. Melzer, V. V. Krasnikov, G. Hadziioannou, *Polymer* **2001**, *42*, 9097–9109.
- [28] M.W. Matsen, *J. Phys.: Condens. Matter* **2002**, *21*, R21–R47.
- [29] M.W. Matsen, F.S. Bates, *Macromolecules* **1996**, *29*, 1091–1098.
- [30] E.W. Cochran, C.J. Garcia-cervera, G.H. Fredrickson, *Macromolecules* **2006**, *39*, 2449–2451.
- [31] W. Zheng, Z. Wang, *Macromolecules* **1996**, *28*, 7215–7223.
- [32] P.J. Flory, *The Journal of Chemical Physics* **1949**, *17*, 303.
- [33] M.L. Huggins, *Journal of American Chemical Society* **1942**, *64*.
- [34] F.S. Bates, *Science* **1991**, *251*, 898–905.
- [35] M.W. Matsen, M. Schick, *Physical Review Letters* **1994**, *72*, 2660–2663.
- [36] D.S. Herman, D.J. Kinning, E.L. Thomas, L.J. Fetters, *Macromolecules* **1987**, *20*, 2940–2942.
- [37] M.F. Schulz, A.K. Khandpur, F.S. Bates, K. Almdal, K. Mortensen, D. a. Hajduk, S.M. Gruner, *Macromolecules* **1996**, *29*, 2857–2867.
- [38] G. Floudas, B. Vazaiou, F. Schipper, R. Ulrich, U. Wiesner, H. Iatrou, N. Hadjichristidis, *Macromolecules* **2001**, *34*, 2947–2957.
- [39] J.M.G. Cowie, *Developments in Block Copolymers-I*, Applied Science Publishers, London **1982**.
- [40] D.A. Hajduk, P.E. Harper, S.M. Gruner, C.C. Honeker, G. Kim, E.L. Thomas, L.J. Fetters, *Macromolecules* **1994**, *27*, 4063–4075.
- [41] S. Koizumij, H. Hasegawa, T. Hashimoto, *Macromolecular Symposia* **1994**, *27*, 4371–4381.
- [42] P.-T. Wu, G. Ren, C. Li, R. Mezzenga, S. a. Jenekhe, *Macromolecules* **2009**, *42*, 2317–2320.
- [43] S. Barth, H. B  ssler, *Physical Review Letters* **1997**, *79*, 4445–4448.

- [44] T.-Q. Nguyen, I.B. Martini, J. Liu, B.J. Schwartz, *The Journal of Physical Chemistry B* **2000**, *104*, 237–255.
- [45] U. Stalmach, B. De Boer, C. Videlot, P.F. Van Hutten, G. Hadziioannou, *Journal of American Chemical Society* **2000**, *122*, 5464–5472.
- [46] Y. Lim, K.-S. Moon, M. Lee, *Journal of Materials Chemistry* **2008**, *18*, 2909.
- [47] L. Yu, Z. Bao, *Advanced Functional Materials* **1994**, *6*, 1994.
- [48] J.T. Chen, E.L. Thomas, C.K. Ober, G. p Mao, *Science* **1996**, *273*, 343–6.
- [49] M.W. Matsen, C. Barrett, *The Journal of Chemical Physics* **1998**, *109*, 4108.
- [50] M. Lee, B.-K. Cho, Y.-S. Kang, W.-C. Zin, *Macromolecules* **1999**, *32*, 7688–7691.
- [51] B. Olsen, R. Segalman, *Materials Science and Engineering: R: Reports* **2008**, *62*, 37–66.
- [52] M. Reenders, G. ten Brinke, *Macromolecules* **2002**, *35*, 3266–3280.
- [53] R.A. Godfrey, G.W. Miller, *Journal of Polymer Science Part A: Polymer Chemistry* **1969**, *7*, 2387–2404.
- [54] A. Semenov, S. Vasilenko, *Sov. Phys. JETP* **1986**, *AV63*.
- [55] A. Semenov, A. Subbotin, *Sov Phys JETP* **1992**, *AV74*, 690.
- [56] A. Halperni, *Europhysics Letters (EPL)* **1989**, *10*, 549–553.
- [57] D.R.M. Williams, G.H. Fredrickson, *Macromolecules* **1992**, *25*, 3561–3568.
- [58] M. Shah, V. Ganesan, *Macromolecules* **2010**, *43*, 543–552.
- [59] U. Scherf, A. Gutacker, N. Koenen, *Accounts of Chemical Research* **2008**, *41*, 1086–97.
- [60] C. Singh, M. Goulian, A.J. Liu, G.H. Fredrickson, P. Behavior, *Macromolecules* **1994**, *277*, 2974–2986.
- [61] M.W. Matsen, *Journal of Chemical Physics* **1996**, *104*, 7758–77644.
- [62] B.D. Olsen, R.A. Segalman, *Macromolecules* **2005**, *38*, 10127–10137.
- [63] B.D. Olsen, R.A. Segalman, *Macromolecules* **2007**, 6922–6929.
- [64] J. Liu, E. Sheina, T. Kowalewski, R.D. Mccullough, *Angewandte Chemie (International Ed.)* **2002**, *41*, 329–332.
- [65] C.-A. Dai, W.-C. Yen, Y.-H. Lee, C.-C. Ho, W.-F. Su, *Journal of the American Chemical Society* **2007**, *129*, 11036–8.
- [66] J.T. Chen, E.L. Thomas, C.K. Ober, S.S. Hwang, *Macromolecules* **1995**, *28*, 1688–1697.

- [67] L.H. Radzilowski, S.I. Stupp, *Macromolecules* **1994**, *27*, 7747–7753.
- [68] L.H. Radzilowski, B.O. Carragher, S.I. Stupp, *Macromolecules* **1997**, *30*, 2110–2119.
- [69] R.L. Ph. Leclere; E.Hennebicq; A.Calderone, P.Brocovens, A.C. Grimsdale, K.Mullen; J.L; Bredas, *Progress in Polymer Science* **2003**, *28*, 55–81.
- [70] P. Leclère, M. Surin, P. Jonkheijm, O. Henze, a. P.H.J. Schenning, F. Biscarini, a. C. Grimsdale, W.J. Feast, E.W. Meijer, K. Müllen, J.L. Brédas, R. Lazzaroni, *European Polymer Journal* **2004**, *40*, 885–892.
- [71] B.P.A. Van Hal, M.M. Wienk, J.M. Kroon, W.J.H. Van Gennip, P. Jonkheijm, R.A.J. Janssen, *Advanced Materials* **2003**, *5*, 118–121.
- [72] T. Kietzke, H. Ho, D. Neher, *Chemistry of Materials* **2005**, 6532–6537.
- [73] N. Sary, C. Brochon, G. Hadziioannou, R. Mezzenga, *The European Physical Journal. E, Soft Matter* **2007**, *24*, 379–84.
- [74] N. Sary, L. Rubatat, C. Brochon, G. Hadziioannou, J. Ruokolainen, R. Mezzenga, *Macromolecules* **2007**, *40*, 6990–6997.
- [75] W. Li, H. Wang, L. Yu, T.L. Morkved, H.M. Jaeger, *Macromolecules* **1999**, *32*, 3034–3044.
- [76] H. Wang, H.H. Wang, V.S. Urban, K.C. Littrell, P. Thiyagarajan, *Journal of American Chemical Society* **2000**, *122*, 6861.
- [77] H. Wang, W. You, P. Jiang, L. Yu, H.H. Wang, *Chemistry (Weinheim an Der Bergstrasse, Germany)* **2004**, *10*, 986–93.
- [78] B.D. Olsen, R.A. Segalman, *Macromolecules* **2006**, *39*, 7078–7083.
- [79] B.D. Olsen, X. Li, J. Wang, R.A. Segalman, *Macromolecules* **2007**, *40*, 3287–3295.
- [80] J. Liu, T. Tanaka, K. Sivula, A.P. Alivisatos, J.M.J. Fréchet, *Journal of the American Chemical Society* **2004**, *126*, 6550–1.
- [81] G. Li, V. Shrotriya, J. Haung, Y. Yao, T. Moriarty, K. Emery, Y. Yang, *Nature Materials* **2005**, 868, 2005.
- [82] H. Sirringhaus, *Advanced Materials* **2005**, *17*, 2411–2425.
- [83] Y.-H. Lee, W.-C. Yen, W.-F. Su, C.-A. Dai, *Soft Matter* **2011**, *7*, 10429.
- [84] M. Dante, C. Yang, B. Walker, F. Wudl, T.-Q. Nguyen, *Advanced Materials* **2010**, *22*, 1835–9.
- [85] S.Y. Choi, J.U. Lee, J.W. Lee, S. Lee, Y.J. Song, W.H. Jo, S.H. Kim, *Macromolecules* **2011**, *44*, 1771–1774.
- [86] I. Botiz, S.B. Darling, *Macromolecules* **2009**, *42*, 8211–8217.

- [87] R. Holyst, M. Schick, *The Journal of Chemical Physics* **1992**, 96, 730.
- [88] M. Muller, M. Schick, *Macromolecules* **1996**, 29, 8900–8903.
- [89] V. Pryamitsyn, V. Ganesan, *The Journal of Chemical Physics* **2004**, 120, 5824–38.
- [90] Y. Zhang, K. Tajima, K. Hirota, K. Hashimoto, *Journal of the American Chemical Society* **2008**, 130, 7812–3.
- [91] K. Ohshimizu, M. Ueda, *Macromolecules* **2008**, 41, 5289–5294.
- [92] H. Wang, M.-K. Ng, L. Wang, L. Yu, B. Lin, M. Meron, Y. Xiao, *Chemistry (Weinheim an Der Bergstrasse, Germany)* **2002**, 8, 3246–53.
- [93] H. Plank, R. Güntner, U. Scherf, E.J.W. List, *Advanced Functional Materials* **2007**, 17, 1093–1105.
- [94] D.M. Siringhaus, H.; Brown, P. J.; Friend, R. H.; Nielsen, M. M.; Bechgaard, K.; Langeveld-Voss, B. M. W.; Spiering, A. J. H.; Janssen, R. A. J.; Meijer, E. W.; Herwig, P. & de Leeuw, *Nature* **1999**, 401, 685–688.
- [95] N. Stutzmann, R.H. Friend, H. Siringhaus, *Science* **2003**, 299, 1881–1884.
- [96] H. Yang, T.J. Shin, L. Yang, K. Cho, C.Y. Ryu, Z. Bao, *Advanced Functional Materials* **2005**, 15, 671–676.
- [97] G. Ren, P.-T. Wu, S. a. Jenekhe, *Chemistry of Materials* **2010**, 22, 2020–2026.
- [98] U. Scherf, S. Adamczyk, A. Gutacker, N. Koenen, *Macromolecular Rapid Communications* **2009**, 30, 1059–65.
- [99] M. He, W. Han, J. Ge, Y. Yang, F. Qiu, Z. Lin, *Energy & Environmental Science* **2011**, 4, 2894–2902.
- [100] J. Ge, M. He, F. Qiu, Y. Yang, *Macromolecules* **2010**, 43, 6422–6428.
- [101] M. He, L. Zhao, J. Wang, W. Han, Y. Yang, F. Qiu, Z. Lin, *ACS Nano* **2010**, 4, 3241–3247.
- [102] G.H. Lu, L.G. Li, X.N. Yang, *Advanced Materials* **2007**, 19, 3594–3598.
- [103] M. He, W. Han, J. Ge, W. Yu, Y. Yang, F. Qiu, Z. Lin, *Nanoscale* **2011**, 3, 3159–3163.
- [104] A. Salleo, R.J. Kline, D.M. DeLongchamp, M.L. Chabinyc, *Advanced Materials* **2010**, 22, 3812–38.
- [105] P.-T. Wu, G. Ren, C. Li, R. Mezzenga, S. a. Jenekhe, *Macromolecules* **2009**, 42, 2317–2320.
- [106] H. Xin, G. Ren, F.S. Kim, S. a. Jenekhe, *Chemistry of Materials* **2008**, 20, 6199–6207.
- [107] S. Samitsu, T. Shimomura, S. Heike, T. Hashizume, *Macromolecules* **2008**, 41, 8000–8010.
- [108] M.C. Iovu, E.E. Sheina, R.R. Gil, R.D. McCullough, *Macromolecules* **2005**, 38, 8649–8656.
- [109] Q. Zhang, A. Cirpan, T.P. Russell, T. Emrick, *Macromolecules* **2009**, 42, 1079–1082.

- [110] M. Sommer, A.S. Lang, M. Thelakkat, *Angewandte Chemie (International Ed. in English)* **2008**, *47*, 7901–4.
- [111] N.S. Gunes, S.; Neugebauer, H.; and Sariciftci, *Chemical Reviews* **2007**, *107*, 1324–1338.
- [112] B.G. Dennler, M.C. Scharber, C.J. Brabec, *Advanced Materials* **2009**, *21*, 1323–1338.
- [113] H. Chen, J. Hou, S. Zhang, Y. Liang, G. Yang, Y. Yang, *Nature Photonics* **2009**, *3*, 649–653.
- [114] Z. He, C. Zhong, X. Huang, W.-Y. Wong, H. Wu, L. Chen, S. Su, Y. Cao, *Advanced Materials* **2011**, *23*, 4636–43.
- [115] C.E. Small, S. Chen, J. Subbiah, C.M. Amb, S. Tsang, T. Lai, J.R. Reynolds, F. So, *Nature Photonics* **2012**, *6*, 115–120.
- [116] H. Zhou, L. Yang, A.C. Stuart, S.C. Price, S. Liu, W. You, *Angewandte Chemie (International Ed.)* **2011**, *50*, 2995–8.
- [117] H. Hoppe, N.S. Sariciftci, *Journal of Materials Chemistry* **2006**, *16*, 45.
- [118] M. Campoy-Quiles, T. Ferenczi, T. Agostinelli, P.G. Etchegoin, Y. Kim, T.D. Anthopoulos, P.N. Stavrinou, D.D.C. Bradley, J. Nelson, *Nature Materials* **2008**, *7*, 158–64.
- [119] A.R. Campbell, J.M. Hodgkiss, S. Westenhoff, I. a Howard, R. a Marsh, C.R. McNeill, R.H. Friend, N.C. Greenham, *Nano Letters* **2008**, *8*, 3942–7.
- [120] C. Müller, S. Goffri, D.W. Breiby, J.W. Andreasen, H.D. Chanzy, R.A.J. Janssen, M.M. Nielsen, C.P. Radano, H. Sirringhaus, P. Smith, N. Stingelin-Stutzmann, *Advanced Functional Materials* **2007**, *17*, 2674–2679.
- [121] G. Cho, M. Jung, H. Yang, J.H. Song, M.M. Sung, *Langmuir* **2006**, *22*, 4896–8.
- [122] Y.-H. Lee, C.-J. Chang, C.-J. Kao, C.-A. Dai, *Langmuir* **2010**, *26*, 4196–206.
- [123] B.W. Boudouris, C.D. Frisbie, M.A. Hillmyer, *Macromolecules* **2008**, *41*, 67–75.
- [124] J.J. Segalman, R. A.; McCulloch, B.; Kirmayer, S.; and Urban, *Macromolecules* **2009**, *42*, 9205–9216.
- [125] E.L. Muthukumar, M.; Ober, C. K.; Thomas, *Science* **1997**, *277*, 1225–1232.
- [126] R. Leclere, Ph.; Parente, V.; Bredas, J. L.; Francois, B.; and Lazzaroni, *Chemistry of Materials* **1998**, *10*, 4010–4014.
- [127] S.A. Jenekhe, L.X. Chen, *Science* **1999**, *283*, 372–375.
- [128] P. Dong-won, R. Roe, *Macromolecules* **1991**, *24*, 5324–5329.
- [129] S. Lyu, T.D. Jones, F.S. Bates, C.W. Macosko, *Macromolecules* **2002**, *35*, 7845–7855.

- [130] W.J. Liu, H.L. Yang, Z. Wang, L.S. Dong, J.J. Liu, *Journal of Applied Polymer Science* **2002**, *86*, 2145–2152.
- [131] H. Kallmann, M. Pope, *The Journal of Chemical Physics* **1959**, *30*, 585.
- [132] C.W. Tang, *Applied Physics Letters* **1986**, *48*, 183.
- [133] N.S. Sariciftci, D. Braun, C. Zhang, V.I. Srdanov, a. J. Heeger, G. Stucky, F. Wudl, *Applied Physics Letters* **1993**, *62*, 585.
- [134] A.J. Yu, G.; Gao, J.; Hummelen, J. C.; Wudl, F.; Heeger, *Science* **1995**, *270*, 1789–1791.
- [135] G. Yua, A.J. Heeger, *Journal of Applied Physics* **1995**, *78*, 1–6.
- [136] S.C.M.& A.B.H. J. J. M. Halls, C. A. Walsh, N. C. Greenham, E. A. Marseglia, R. H. Friend, *Nature* **1995**, *376*, 498–500.
- [137] A. Yassar, L. Miozzo, R. Girona, G. Horowitz, *Progress in Polymer Science* **2012**.
- [138] R.H.F.& R.W.G. P. L. Burn, A. B. Holmes, A. Kraft, D. D. C. Bradley, A. R. Brown, *Nature* **1992**, *356*, 47.
- [139] A.R.B. and R.H.F. Paul L. Burn , Andrew B. Holmes , Arno Kraft , Donal D. C. Bradley, *Journal of Chem. Soc., Chem. Commun.*, **1992**, 32–34.
- [140] F. Meyers, A.J. Heeger, J.L. Brédas, *The Journal of Chemical Physics* **1992**, *97*, 2750.
- [141] S. Barrau, T. Heiser, F. Richard, C. Brochon, C. Ngov, K. Van De Wetering, D. V Anokhin, D.A. Ivanov, *Macromolecules* **2008**, *41*, 2701–2710.
- [142] X. Chen, B. Gholamkhash, X. Han, G. Vamvounis, S. Holdcroft, *Macromolecular Rapid Communications* **2007**, *28*, 1792–1797.
- [143] S. Sun, *Solar Energy Materials and Solar Cells* **2003**, *79*, 257–264.
- [144] F. Richard, C. Brochon, N. Leclerc, D. Eckhardt, T. Heiser, G. Hadziioannou, *Macromolecular Rapid Communications* **2008**, *29*, 885–891.
- [145] Z. Hu, J. Zou, C. Deibel, A.J. Gesquiere, L. Zhai, *Macromolecular Chemistry and Physics* **2010**, *211*, 2416–2424.
- [146] M. Heuken, H. Komber, T. Erdmann, V. Senkvisky, A. Kiriy, B. Voit, *Macromolecules* **2012**, *45*, 4101–4114.
- [147] R.C. Hiorns, P. Iratcabal, D. Bégué, A. Khoukh, R. de Bettignies, J. Leroy, M. Firon, C. Sentein, H. Martinez, H. Preud'homme, C. Dagron-lartigau, *Journal of Polymer Science Part A: Polymer Chemistry* **2009**, *47*, 2304–2317.
- [148] M. Sommer, S. Hüttner, S. Wunder, M. Thelakkat, *Advanced Materials* **2008**, *20*, 2523–2527.
- [149] J. Nakamura, C. Yokoe, K. Murata, K. Takahashi, *Journal of Applied Physics* **2004**, *96*, 6878.

- [150] R. de Bettignies, Y. Nicolas, P. Blanchard, E. Levillain, J.-M. Nunzi, J. Roncali, *Advanced Materials* **2003**, *15*, 1939–1943.
- [151] A.J. Breeze, A. Salomon, D.S. Ginley, B.A. Gregg, H. Tillmann, H.-H. Hörhold, *Applied Physics Letters* **2002**, *81*, 3085.
- [152] M. Sommer, A.S. Lang, M. Thelakkat, *Angewandte Chemie (International Ed. in English)* **2008**, *47*, 7901–4.
- [153] M. Sommer, S. Hüttner, U. Steiner, M. Thelakkat, *Applied Physics Letters* **2009**, *95*, 183308.
- [154] Y. Tao, B. McCulloch, S. Kim, R. a. Segalman, *Soft Matter* **2009**, *5*, 4219.
- [155] A. Laiho, R.H.A. Ras, S. Valkama, J. Ruokolainen, *Macromolecules* **2006**, *39*, 7648–7653.
- [156] S. Li, G. Lu, H. Li, Y. Qu, L. Li, J. Loos, X. Yang, *Macromolecular Rapid Communications* **2012**, *33*, 1882–1887.
- [157] L.M. Kozycz, D. Gao, J. Hollinger, D.S. Seferos, *Macromolecules* **2012**, *45*, 5823–5832.
- [158] C. Suspène, L. Miozzo, J. Choi, R. Gironda, B. Geffroy, D. Tondelier, Y. Bonnassieux, G. Horowitz, a. Yassar, *Journal of Materials Chemistry* **2012**, *22*, 4511.
- [159] K.E. and Y.Y. Gang Li, Vishal Shrotriya, Jinsong Huang, Yan Yao, Tom Moriarty, *Nature Materials* **2005**, *4*, 864–868.
- [160] Y. Zhao, Z. Xie, Y. Qu, Y. Geng, L. Wang, *Applied Physics Letters* **2007**, *90*, 043504.
- [161] Y. Zhao, X. Guo, Z. Xie, Y. Qu, Y. Geng, L. Wang, *Journal of Applied Polymer Science* **2009**, *111*, 1799–1804.
- [162] G. Li, Y. Yao, H. Yang, V. Shrotriya, G. Yang, Y. Yang, *Advanced Functional Materials* **2007**, *17*, 1636–1644.
- [163] C.-J. Ko, Y.-K. Lin, F.-C. Chen, *Advanced Materials* **2007**, *19*, 3520–3523.
- [164] H. Flügge, H. Schmidt, T. Riedl, S. Schmale, T. Rabe, J. Fahlbusch, M. Danilov, H. Spieker, J. Schöbel, W. Kowalsky, *Applied Physics Letters* **2010**, *97*, 123306.
- [165] X. Yang, J. Loos, S.C. Veenstra, W.J.H. Verhees, M.M. Wienk, J.M. Kroon, M.A.J. Michels, R.A.J. Janssen, *Nano Letters* **2005**, *5*, 579–83.
- [166] T. Erb, U. Zhokhavets, G. Gobsch, S. Raleva, B. Stühn, P. Schilinsky, C. Waldauf, C.J. Brabec, *Advanced Functional Materials* **2005**, *15*, 1193–1196.
- [167] M. Shin, H. Kim, J. Park, S. Nam, K. Heo, M. Ree, C.-S. Ha, Y. Kim, *Advanced Functional Materials* **2010**, *20*, 748–754.
- [168] U. Zhokhavets, T. Erb, H. Hoppe, G. Gobsch, N. Sariciftci, *Thin Solid Films* **2006**, *496*, 679–682.

- [169] Y. Kim, S.A. Choulis, J. Nelson, D.D.C. Bradley, S. Cook, J.R. Durrant, *Applied Physics Letters* **2005**, *86*, 063502.
- [170] V.D. Mihailetschi, H.X. Xie, B. de Boer, L.J.A. Koster, P.W.M. Blom, *Advanced Functional Materials* **2006**, *16*, 699–708.
- [171] C.J. Brabec, M. Heeney, I. McCulloch, J. Nelson, *Chemical Society Reviews* **2011**, *40*, 1185–99.
- [172] S. Berson, R. De Bettignies, S. Bailly, S. Guillerez, *Advanced Functional Materials* **2007**, *17*, 1377–1384.
- [173] Y. Chang, L. Wang, *J. Phys. Chem. C* **2008**, *112*, 17716–17720.
- [174] K. Kim, D.L. Carroll, *Applied Physics Letters* **2005**, *87*, 203113.
- [175] Y. Yao, J. Hou, Z. Xu, G. Li, Y. Yang, *Advanced Functional Materials* **2008**, *18*, 1783–1789.
- [176] S.K. Jang, S.C. Gong, H.J. Chang, *Synthetic Metals* **2012**, *162*, 426–430.
- [177] J.K. Park, C. Kim, B. Walker, T.-Q. Nguyen, J.H. Seo, *RSC Advances* **2012**, *2*, 2232.
- [178] J.T. Rogers, K. Schmidt, M.F. Toney, G.C. Bazan, E.J. Kramer, *Journal of American Chemical Society* **2012**, *134*, 2884–2887.
- [179] H. Chen, H. Yang, G. Yang, S. Sista, R. Zadoyan, G. Li, Y. Yang, *J. Phys. Chem. C* **2009**, *113*, 7946–7953.
- [180] J. Liu, S. Shao, H. Wang, K. Zhao, L. Xue, X. Gao, Z. Xie, Y. Han, *Organic Electronics* **2010**, *11*, 775–783.
- [181] H. Fan, H. Shang, Y. Li, X. Zhan, *Applied Physics Letters* **2010**, *97*, 133302.
- [182] D.M. Lyons, R.J. Ono, C.W. Bielawski, J.L. Sessler, *Journal of Materials Chemistry* **2012**, *22*, 18956.
- [183] J. Liu, Y. Han, *Polymer Bulletin* **2012**, *68*, 2145–2174.
- [184] B. Lim, J. Jo, S.-I. Na, J. Kim, S.-S. Kim, D.-Y. Kim, *Journal of Materials Chemistry* **2010**, *20*, 10919.
- [185] J.B. Kim, K. Allen, S.J. Oh, S. Lee, M.F. Toney, Y.S. Kim, C.R. Kagan, C. Nuckolls, Y.-L. Loo, *Chemistry of Materials* **2010**, *22*, 5762–5773.
- [186] S.D.D. V Rouhooputh, S. Hotta, A.J. Heeger, F. Wudl, *Journal of Polymer Science Part B: Polymer Physics* **1987**, *25*, 1071–1078.
- [187] A. Zen, M. Saphiannikova, I.D. Neher, S. Grigorian, U. Pietsch, U. Asawapirom, S. Janietz, U. Scherf, I. Lieberwirth, G. Wegner, *Macromolecules* **2006**, *39*, 2162–2171.
- [188] K. Sivula, Z.T. Ball, N. Watanabe, J.M.J. Fréchet, *Advanced Materials* **2006**, *18*, 206–210.
- [189] C. Yang, J.K. Lee, A.J. Heeger, F. Wudl, *Journal of Materials Chemistry* **2009**, *19*, 5416.

- [190] J.U. Lee, J.W. Jung, T. Emrick, T.P. Russell, W.H. Jo, *Journal of Materials Chemistry* **2010**, *20*, 3287–3294.
- [191] J.U. Lee, J.W. Jung, T. Emrick, T.P. Russell, W.H. Jo, *Nanotechnology* **2010**, *21*, 105201.
- [192] J. Chen, X. Yu, K. Hong, J.M. Messman, D.L. Pickel, K. Xiao, M.D. Dadmun, J.W. Mays, A.J. Rondinone, B.G. Sumpter, S.M.K. II, *Journal of Materials Chemistry* **2012**, *22*, 13013–13022.
- [193] T.H. and G.H. V. Gernigon, P. Lévêque, C. Brochon, J.-N. Audinot, N. Leclerc, R. Bechara, F. Richard, *Eur. Phys. J. Appl. Phys.* **2011**, *56*, 34107.
- [194] Z. Sun, K. Xiao, J.K. Keum, X. Yu, K. Hong, J. Browning, I.N. Ivanov, J. Chen, J. Alonzo, D. Li, B.G. Sumpter, E.A. Payzant, C.M. Rouleau, D.B. Geohegan, *Advanced Materials* **2011**, *23*, 5529–5535.
- [195] X. Yu, K. Xiao, J. Chen, N. V Lavrik, K. Hong, B.G. Sumpter, D.B. Geohegan, *ACS Nano* **2011**, *5*, 3559–3567.
- [196] S. Rajaram, P.B. Armstrong, B.J. Kim, J.M.J. Frechet, *Chemistry of Materials* **2009**, *21*, 1775–1777.
- [197] R. Bechara, N. Leclerc, P. Lèveque, F. Richard, T. Heiser, G. Hadziioannou, *Applied Physics Letters* **2008**, *93*, 013306.

Chapter - III

***Microstructure and Photovoltaic Performance
Optimizations in P3HT:PCBM Blends***

3.1. Introduction

Many of the organic based devices (mainly for PV applications) are blends of functional polymeric materials. In order to perform its function effectively, some structural organization is usually required within those polymeric blends. The organization may vary from a simple dispersion with a corresponding correlation length to some periodic mesostructures with domain sizes ranging from nano-crystallites to micro-scale aggregates. As it has been presented in the previous section, the mesostructure of those blends is strongly correlated to the processing parameters during the device fabrication. For the optimization of the mesostructure as regards to the photovoltaic properties, different techniques have been applied. For instance, annealing the films at an appropriate temperature is known to increase P3HT's crystallinity as well as promote the formation of PCBM aggregates in P3HT:PCBM blends. The highly improved P3HT crystallinity leads to higher photon absorption and an increase in charge transport as the result higher output currents. Thus, an understanding of how to manipulate the (macro-) molecular arrangement of the materials is critical for the design of more efficient solar cell devices. Therefore, this chapter deals with the optimization of P3HT:PCBM BHJ solar cells and the fundamental understanding of the different factors affecting the PV characteristics. First, the effect of thermal annealing at different temperature and annealing time on specific molecular weight (M_n) of P3HT and specific composition with PCBM is presented. Following, the effect of the M_n of P3HT on the morphology and performance of P3HT:PCBM blends will be discussed. At the same time, the effect of the blend composition of P3HT and PCBM components as a function of temperature (its phase diagram) is developed and thoroughly discussed. Finally, the effect of different interfaces (PEDOT:PSS and TiO_x) on the vertical stratification of P3HT:PCBM blends is thoroughly investigated. The film and device fabrication and the different characterization techniques employed in this investigation are presented on Chapter 7.

3.2. Effect of Thermal Annealing on Morphology and Performance for P3HT:PCBM blends

The phase separation of polymeric blends starts during film formation from a solution and results in a final structure containing phases with a distribution of sizes due to coarsening and nucleation effects.^[1] Thermal annealing is usually applied to these blends, particularly in organic photovoltaic blends in order to reorganize the components into an optimum mesostructure convenient for efficient photovoltaic processes. It is therefore necessary to find out the right annealing conditions that allow optimal micro- and nano-scale phase separations for efficient photovoltaic performance. The following experimental work and discussions gives a clue on annealing conditions by taking P3HT:PCBM BHJ PV blends as an example.

Macromolecular and thermal properties of P3HT	Values
Molecular weight, M_n , (Kg/mol)	104.5
Dispersity, D , (M_w/M_n)	1.84
Regioregularity (%)	99
Glass transition, T_g , (°C)	25.5
Melting temperature, T_m , (°C)	251.3
Crystallization temperature, T_c , (°C)	193.5

Table 3.1: Macromolecular and Thermal properties of P3HT under investigation.

A commercial P3HT from Plextronics and PCBM from Solaris were first used to determine the best annealing condition for this particular system. The P3HT macromolecular characteristic and its thermal properties are given in Table 3.1. Thin films (devices) were fabricated following the procedures described in Chapter 7. The blend composition for P3HT and PCBM was set at 1:1 (w/w). First, the annealing temperature was varied from RT to 200°C for fixed annealing time and then another set of films were prepared and annealed at fixed temperature for different annealing time. The annealing

time used for the first study was set at 20 min. This particular annealing time was selected according to a literature review survey and was chosen as a starting point for our study.

Transmission Optical Microscopy images of P3HT:PCBM blend films annealed at different temperatures are shown in Figure 3.1. Thermal Annealing results in the formation of PCBM clusters, which are clearly visible on the micrograph images. The number and size of these clusters gradually increase as the function of annealing temperature. The shape of the aggregates also varies: from needle-like to rice-shaped to star-shaped aggregates for the films annealed at 140, 180 and 200°C, respectively. This reflects the different reorganization of the P3HT and PCBM domains in the active layer at microscopic scale upon thermal annealing.

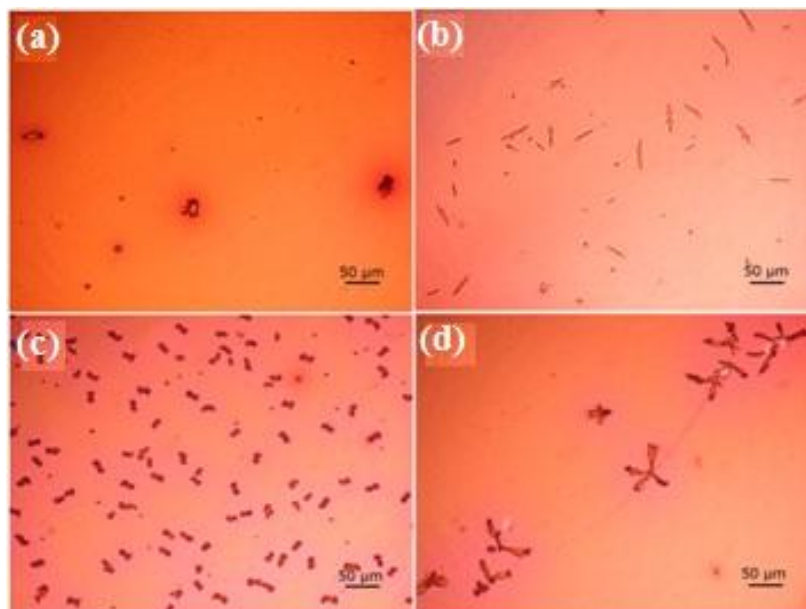


Figure 3.1 : Transmission Optical Microscopy images ($\times 40$) of P3HT:PCBM (1:1, w/w) films. (a) Without thermal annealing, (b) annealed at 140°C, (c) annealed at 180°C and (d) annealed at 200°C. All films were annealed at their respective temperatures for 20 min.

The morphological properties were also investigated using Scanning Force Microscopy (SFM) and phase images are shown in Figure 3.2. Formation of nano-sized domains is observed upon annealing the films. In these annealed films (Figure 3.2 (b-d)), the P3HT and PCBM components are uniformly dispersed throughout the film surface, with slight exception for high temperature thermal

annealed samples where domain coarsening is observed. While in the as-cast film (Figure 3.2 (a)), SFM characterization shows a strong contrast that can be associated to aggregates of the constituents. This indicates the presence of an uneven distribution between P3HT and PCBM domains in the pristine film (*i.e.* without annealing). The uneven distribution arises due to the difficulties in mixing between high M_n P3HT and PCBM; as the former has a tendency to form aggregates in solution as well as during film formation. Consequently thermal annealing is needed in order to homogenize the distribution among the components.

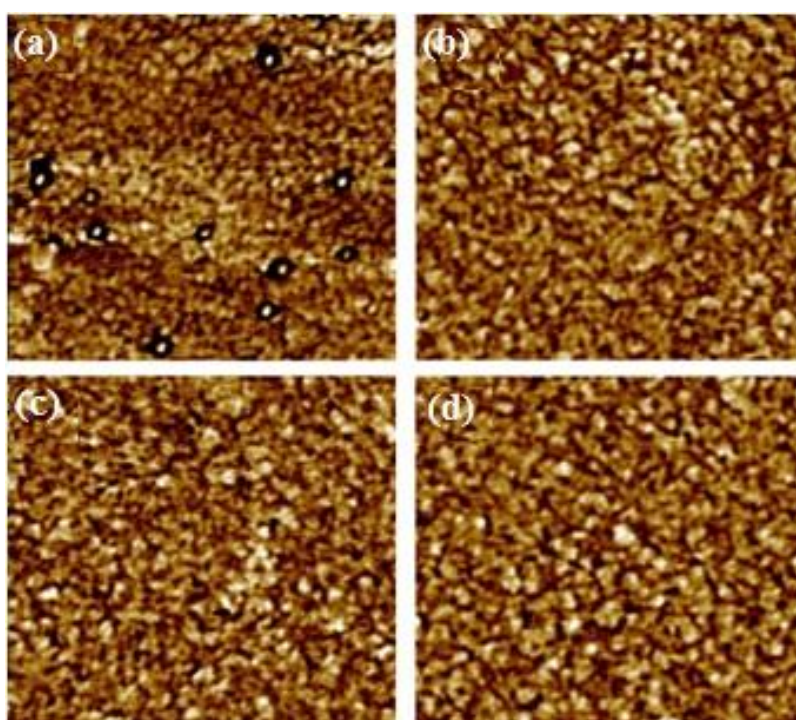


Figure 3.2: AFM phase images in tapping mode (scan size, $2 \mu\text{m} \times 2 \mu\text{m}$) of P3HT:PCBM (1:1, w/w) films. (a) Without annealing, (b) annealed at 140°C , (c) annealed at 180°C , and (d) annealed at 200°C . All films were annealed at the respective temperatures for 20 min.

The photovoltaic studies as a function of the annealing temperature have also been carried out following the morphological studies. The conventional device configuration was employed: ITO/PEDOT:PSS/P3HT:PCBM(1:1 w/w)/Al. All photovoltaic parameters show an increase up to 180°C with PCE as high as $2.9 \pm 0.3\%$ at 180°C (Figure 3.3). The Fill factor (FF) and Short-circuit Current Density (J_{sc}) at 180°C were 0.55 ± 0.01 and $9.8 \pm 0.40 \text{ mA/cm}^2$, respectively. The Open-circuit Voltage

(V_{OC}) has increased as a function of the annealing temperature until saturation ($0.56 \pm 0.02V$) for higher annealing temperatures. However, a sharp decrease for the other PV parameters was observed when the devices were annealed at 200 °C and beyond.

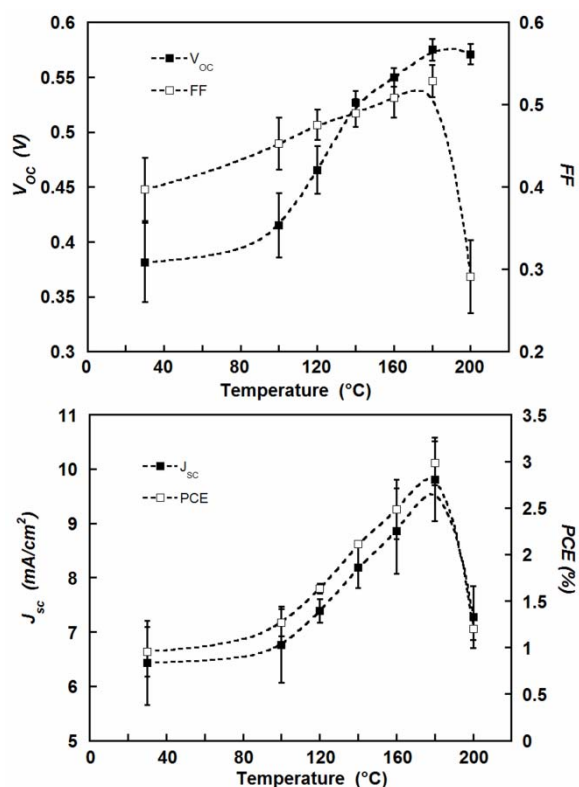


Figure 3.3: The PV characteristics of P3HT:PCBM (1:1 w/w) photoactive blends as a function of annealing temperatures. The standard deviation was calculated on 16 different devices.

The obtained PV characteristics values have to be related with the observed morphology. Annealing P3HT:PCBM blends at an appropriate temperature and time has shown to improve the crystallinity of P3HT^{[2][3][4][5][6]} and promote phase separation between P3HT and PCBM at either nano-scale (as shown in the SFM image)^{[2][7][8]} or microscopic scale (as shown in optical microscopy image).^[9] The nano-scale phase separation is initiated by the favorable π - π interactions in P3HT domains. However, the crystallization of P3HT promoted by the favorable π - π interactions leads to microscale phase segregation between P3HT and PCBM domains.^{[10][11][12][13]} The crystallization of P3HT leads to the diffusion of PCBM towards the amorphous part of P3HT.^{[9][10][14][15]} Thus, PCBM moieties will accumulate in the amorphous domains of P3HT. The miscibility of PCBM in the amorphous part of

P3HT is very advantageous as it gives sufficient interfaces for exciton dissociation while the P3HT crystallinity and the optimal sized PCBM aggregates are important for charge transport. This is the reason why the annealed devices gave higher PV performance than the as-cast devices. However, as the annealing temperature increases high enough, the diffusion of the PCBM moieties is favored and thus the PCBM domains significantly grow (in a similar way of Ostwald ripening mechanism) into different forms; mostly in needle-like or star-like microscale aggregates as shown in Figure 3.1.^{[11][16][17][18][19][20][21]} This phenomenon has a detrimental effect; a large part of the created excitons will not reach interfaces (exciton recombination will be high) and that will have a negative consequence on the performance of the devices. This has clearly been observed for devices annealed at 200°C in which the performance has significantly decreased. The degradation of the PEDOT:PSS layer with the increasing temperature may also have its own effect for the decrease in performance for devices annealed at 200°C and beyond.^{[22][23][24]} However, if the system is annealed at an appropriate temperature and annealing time (for this particular system, the optimum annealing temperature is 180°C), the trend towards the formation of large sized PCBM aggregates will be limited. This optimal mixing (formation of small sized PCBM aggregates) observed among P3HT and PCBM (Figure 3.1c) components at 180°C will allow a suitable environment for exciton creation, exciton dissociation and charge transport in the PV device and hence an improved device efficiency.

Interestingly we observed a large increase of V_{OC} as function of the temperature as shown on Figure 3.3. The open circuit voltage is hypothetically related to the energy gap between the highest occupied molecular orbital (HOMO) of the electron donor material and the lowest unoccupied molecular orbital (LUMO) of the electron acceptor material (*i.e.* which is equivalent to ionization potential and electron affinity of respective materials).^{[25][26]} But, this gap is highly sensitive to the charge density involved in the photovoltaic process.^{[27][28]} Generally, a photovoltage gain is linked with the splitting of the high quasi-Fermi energy electrons caused by the increased charge density (as the result of low recombination) and/or low leakage currents involved in the photovoltaic process.^[27] For example, the use of additional thin cathode interlayer (LiF, polyelectrolyte, etc) in conventional PV

devices has shown to increase the V_{OC} due to the improved electron extraction (by decreasing the work function of the cathode or by forming a dipole at the interface that will serve to pull electrons out of the organic film) and then decrease leakage currents (low recombination).^{[29][30]} This implies that the change of interfacial properties have a massive impact on charge extraction characteristics. Since all the other parameters in this investigation are the same (except the change in annealing temperature), the increase in V_{OC} obtained in our investigation could be related to the interfacial changes at active layer/Al interfaces due to annealing of the active layer with Al atop. For example, the active layer/Al interfacial effect of pristine and annealed devices could be explained by comparing the PV characteristics of pre- and post-annealed devices. Here, we assumed that the nature of the interfacial contact of the pristine (not annealed) and the pre-annealed samples (*i.e.* prior to Al deposition) are considered to be the same or their difference is negligible. The PV characteristics on devices which were annealed prior to the cathode deposition (pre-annealing) are presented in Figure 3.4. As opposed to the results shown on Figure 3.3, the V_{OC} remains the same regardless of the annealing temperature, while the other parameters (J_{SC} and FF) show a strong increase similar to the post-annealing condition (see Figure 3.4(a) and (b)). The pre-annealed devices have also shown lower V_{OC} as compared to the post-annealed device. Our result clearly indicates that the increase in V_{OC} for post-annealed devices is related to the interfacial changes, probably due to better contact that is taking place at the active layer/Al interfaces during the post-annealing treatments, thus lowering leakage currents. The relationship between low leakage-currents and the increase in V_{OC} will be seen in subsequent sub-chapters.

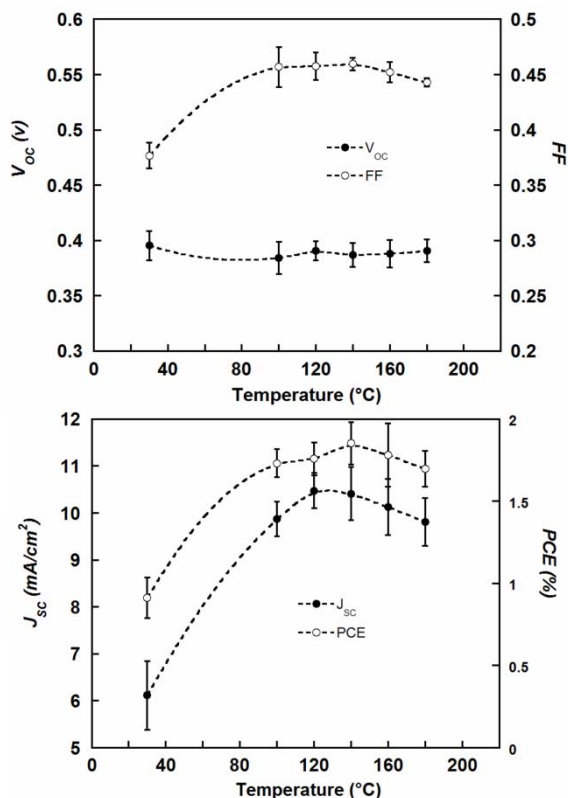


Figure 3.4: PV characteristics of P3HT:PCBM (1:1, w/w) devices. Thermal annealing is carried out prior to cathode deposition (Aluminum, Al). The standard deviation is calculated over 16 different devices.

Next, we studied the effect of annealing time on devices made of similar materials at a fixed annealing temperature (in this case 180°C was chosen as it has already given the maximum PCE). We varied the annealing time from 0 to 60 min. The photovoltaic parameters increase up to 20 min and then decreased slightly with longer annealing time. This implies that 20 min is the optimal annealing time to reorganize the components into an optimum mesostructure convenient for efficient photovoltaic processes (absorption, dissociation and charge transport) in this particular investigation.

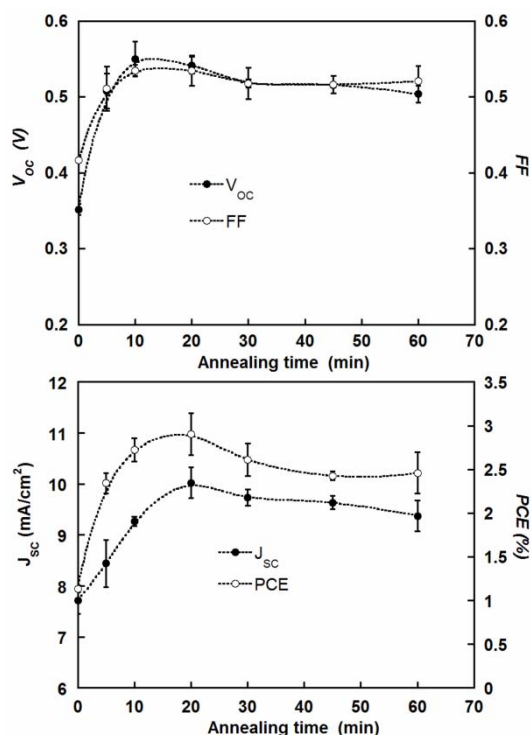


Figure 3.5: The PV characteristics of P3HT:PCBM (1:1, w/w) photoactive devices as a function of annealing time. The devices were annealed at 180°C. The standard deviation is calculated on 16 different devices.

To summarize, devices annealed at 180°C for 20 min gave the best performance for this particular P3HT. Moreover, we noticed that the changes in thin film morphology as well as the interfaces play a crucial role on the PV characteristics.

3.3. Influence of the P3HT Molecular Weight on the Thin Film Morphology and PV Characteristics

Now, five P3HTs with different molecular weights were synthesized via the Grignard metathesis route in our laboratory. The macromolecular characteristics of the different P3HT samples are listed in Table 3.2.

Table 3.2: Macromolecular characteristics of the studied P3HTs.

P3HT	P3HT-5.8k	P3HT-9.6k	P3HT-25k	P3HT-40k	P3HT-60k
M_n^a (kg/mol)	5.8	9.6	25	40	60
Dispersity ^a	1.6	1.3	1.1	1.4	1.4
Regioregularity (%) ^b	89	92	96	98	99

^a M_n determined by SEC with polystyrene standards in THF at 40°C; ^bdetermined by ¹H-NMR using CDCl₃ as solvent

The main thermal characteristics of the different P3HTs were determined by Differential Scanning Calorimetry (DSC) and are reported in Table 3.3. The degree of crystallinity is defined as the ratio between the measured enthalpy of melting and the enthalpy of melting of a perfect polymer (ΔH_u^0). For P3HT, ΔH_u^0 has been calculated by Malik *et al.* from the melting point depression in the polymer – diluents system and was determined as $\Delta H_u^0 = 99$ J/g.^[31] P3HT-5.8k presents the lowest degree of crystallinity due to its poorest regioregularity (89%, Table 3.2). Indeed, high regioregularity implies a better packing of the P3HT chains^[32] and thus an improved degree of crystallinity. For the other P3HTs, the regioregularity is comparable and it is noteworthy that the higher the molecular weight of P3HT, the lower its crystallinity and the higher its melting point.

P3HT	P3HT-5.8k	P3HT-9.6k	P3HT-25k	P3HT-40k	P3HT-60k
Melting temperature (°C)	204	217	233	234	234
Crystallization temperature (°C)	178	190	206	202	199
Degree of crystallinity (%) ^a	7.2	18.0	14.7	12.2	10.9

^adefined as the ratio between the measured enthalpy of melting and the enthalpy of melting of a perfect polymer.

Table 3.3: Melting and crystallization temperatures, degree of crystallinity for the different P3HTs.

3.3.1. Effect of the P3HT Molecular weight on the Thin Film Morphology

The annealing temperature and time for this particular set of experiments were fixed at 180 °C and 20 min, respectively (as these annealing parameters gave the best photovoltaic performance). Optical microscopy images (both in bright-field (BF) and dark-field (DF)) of films of P3HT-9.6k, P3HT-25k, and P3HT-60k blended with PCBM (1:1) are presented in Figures 3.6. A significant difference on the nature of PCBM agglomeration was noticed in the optical microscopy images: huge number of microscopic PCBM agglomerates were visualized for low M_n P3HT (P3HT-9.6k) films, while for higher M_n P3HT films (P3HT-25k and P3HT-60k) fewer but larger PCBM agglomerates were observed. These needle-like aggregates shown in the BF transmission optical microscopy images were assigned to PCBM crystals as confirmed by the DF images.^[33]

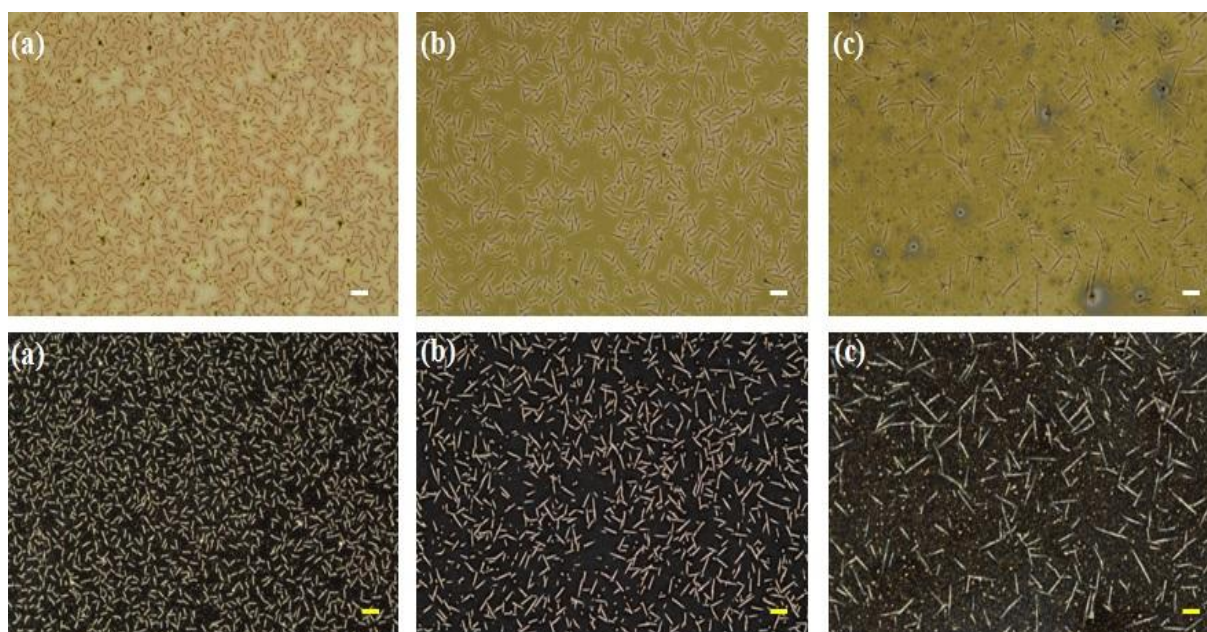


Figure 3.6: BF transmission (top) and corresponding DF (bottom) Optical Microscopy images ($\times 50$) of P3HT:PCBM (1:1 w/w) thin films prepared from different molecular weight P3HTs after annealing at 180°C for 20 min: (a) 9.6 Kg/mol, (b) 25 Kg/mol, and (c) 60 Kg/mol. The scale bar is 100 μm .

At the macroscopic scale, the appearance of numerous PCBM agglomerates for low M_n P3HT-9.6k (Figure 3.6a) upon annealing is due to the fact that PCBM diffuses faster over a short distance.^[9]

As P3HT crystallization is enhanced upon thermal annealing, PCBM is ejected from the P3HT crystallites and diffuses into the amorphous part of P3HT (it is a region where P3HT and PCBM are compatible) to form aggregates.^[15] Besides, for higher molecular weight P3HTs, the longer chains slow down the diffusion of PCBM because of the higher ratio of entanglements of the chains^[34] and thus fewer but larger PCBM microscopic agglomerates are observed after annealing (Figure 3.6b and 3.6c).

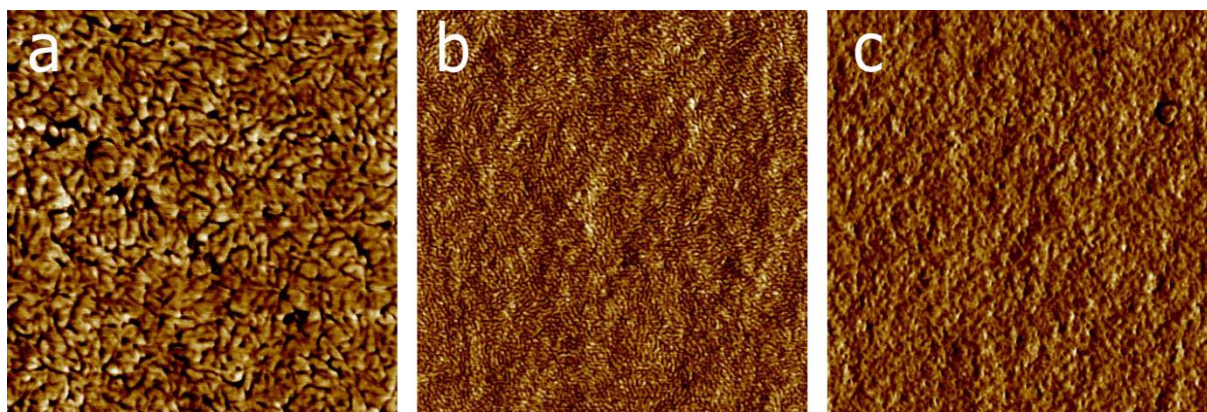


Figure 3.7: SFM phase images ($2 \times 2 \mu\text{m}^2$) of P3HT:PCBM (1:1 w/w) thin films for different molecular weight P3HTs: (a) 9.6 kg/mol, (b) 25 kg/mol, and (c) 60 kg/mol.

The influence of the different P3HT molecular weights on the nanoscale organization of P3HT:PCBM blends has also been investigated using SFM and Transmission Electron Microscopy (TEM) techniques. For the mixtures of low M_n P3HT-9.6k and PCBM, large grains composed of P3HT crystallites and PCBM agglomerates (bright areas) surrounded by soft regions (amorphous P3HT, dark areas) were observed (Figure 3.7a). By contrast, Figure 3.7b (P3HT-25k:PCBM) presents well-defined fibrillar P3HT domains. Those fibrils are P3HT crystallites.^[35] Figure 3.7c shows the SFM image of P3HT-60k:PCBM, which exhibits a much more homogeneous structure relative to Figure 3.7a, suggesting an intimate intermixing between P3HT and PCBM. The formation of this homogeneous or fine morphology as a function of molecular weight was also observed in the TEM images (Figure 3.8). Since P3HT and PCBM has a slight difference in electron density, the “gray” parts in the TEM images are supposed to be P3HT-rich fibers and the “dark” regions corresponds to PCBM-rich domains.^[36] The TEM image of P3HT-9.6k:PCBM (Figure 3.8a) shows coarse and isolated P3HT crystalline domains

without interconnection to each other, whereas Figure 3.8c shows fine and intricate pattern inherent to the intimate mixing between the P3HT-60k and PCBM domains. The observed homogeneity in the repartition of P3HT and PCBM is required in BHJ PV devices as it will lead to better exciton dissociation, higher J_{SC} and FF.

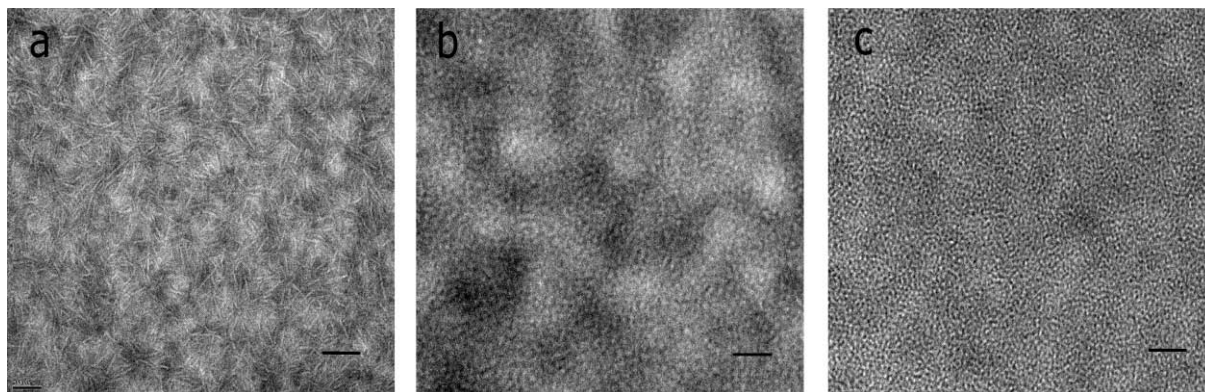


Figure 3.8: TEM images of P3HT:PCBM (1:1, w/w) thin films for different molecular weight P3HTs: (a) 9.6 kg/mol, (b) 25 kg/mol, and (c) 60 kg/mol. The scale bar represents 200 nm.

3.3.2. Effect of the P3HT Molecular weight on Device Performance

For all the P3HTs (from P3HT-5.8k to P3HT-104.9k), the photovoltaic characteristics for a 1:1 P3HT:PCBM (w/w) blend annealed at 180°C for 20 min were measured. The averaged PV parameters of 16 solar diodes and representative J-V curves are presented in Figure 3.9. J_{SC} , FF, and PCE increase with the molecular weight up to 60 kg/mol and then reach a plateau for higher molecular weights. PCE as high as $2.9 \pm 0.1\%$ was obtained for 60 and 104.9 kg/mol P3HTs. The only parameter which does not strictly follow the trend is the V_{OC} . It increases only up to $M_n = 25$ kg/mol and then decreases afterwards (but, still at higher M_n the values stay level).

J_{SC} is connected to the lifetime and mobility of the charge carriers and, thus, is strongly linked to the morphology of the active layer. The FF results from the competition between charge transport and charge recombination.^{[37][38]} In order to increase the FF, the morphology of the active layer has to be suitable for charge transport, *i.e.*, a nanostructured bicontinuous phase is compulsory. Nanosized

bicontinuous structure between a donor and an acceptor is the most appropriate candidate for exciton dissociation and transport of charges.^{[2][39][40]} With this in mind, the increase J_{SC} and FF is in agreement with the observed morphology as a function of molecular weight. For the P3HT-60k and P3HT-104.9k, all the photovoltaic parameters seem to reach a plateau. This implies that, the morphology resulting from the phase separation is relatively stable for the higher molecular weight P3HT blends. This was clearly observed in both SFM and TEM images, where a fine and homogenous morphology was obtained for P3HT-60k:PCBM blends. This provides large and well-defined interfaces convenient for efficient photovoltaic processes.

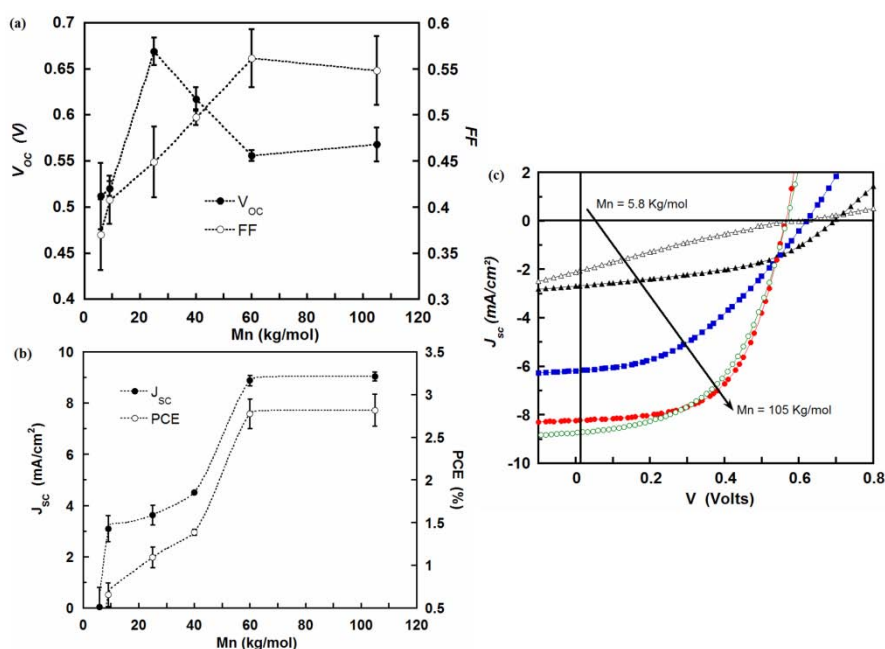


Figure 3.9: Photovoltaic characteristics of P3HT:PCBM (1:1, w/w) devices as a function of the P3HT molecular weight after post-annealed at 180°C for 20 min. The error bars represent the standard deviation measured on 16 different photovoltaic cells.

Another explanation for the increase in J_{SC} and FF is related to the regioregularity (degree of head-to-tail configuration) of the P3HT which increases with M_n , leading to a better packing of the chains through the formation of extended lamellae structure with improved π -stacking.^[41] However, this argument is still under debate since other works suggest that an optimum in regioregularity (about 95%) is needed as it gives a good mix of crystallinity and amorphous part for better exciton

dissociation and charge transport.^{[32][42]} Secondly, even though low M_n P3HTs (apart from P3HT-5.8k) have a tendency to form very crystalline domains as shown in Figure 3.7a and 3.8a, the nano-rod crystallites of P3HT domains are poorly interconnected. As a consequence, charge transport mainly hole transport in P3HT is ineffective (hindered) which results in the observed poor performance. In another case, higher M_n P3HTs exhibit a higher content of amorphous P3HT (Table 3.3) enabling the connection between the different crystalline parts leading to an interpenetrating co-continuous morphology and allowing an efficient charge transport through the volume of the film (as shown schematically Figure 3.10).^{[43][44][45][46]}

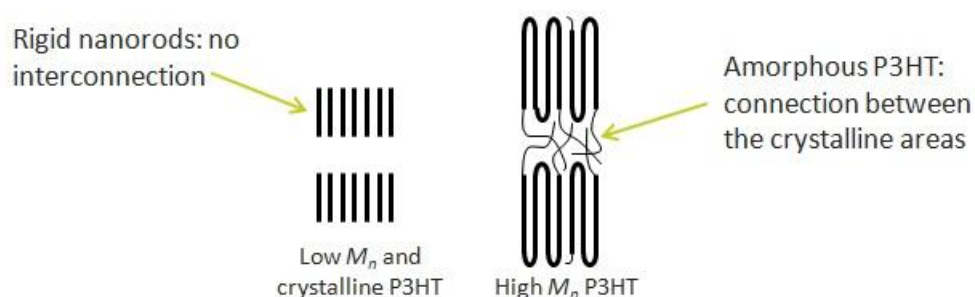


Figure 3.10: Schematic representation of low and high M_n crystalline P3HT domains.

The V_{OC} evolution over the range of molecular weight can be attributed to two distinct phenomena. One is related to the conjugation along the polymer as function to the molecular weight and the other is related to the interfacial properties at donor/acceptor and/or at the active layer/electrodes interfaces. It has been observed that the HOMO energy level of P3HT increases with the molecular weight *i.e.* the higher the M_n , the shallower is the HOMO (*i.e.* higher HOMO) with respect to the vacuum level.^{[47][48]} The relatively constant level observed for high M_n P3HTs (*i.e.* apart from P3HT-25k) is therefore due to the higher HOMO levels in high M_n P3HTs. However, the P3HT-25K:PCBM device shows higher V_{OC} than low M_n containing devices; such as P3HT-9.6k. This behavior could be associated to the active layer/electrodes interface properties.^{[49][38][50][51][52][53]} Depending on the dipole nature developed at the active layer/electrodes interface (due to vertical segregations upon annealing, etc...) it may increase or decrease the dark saturation current (the leakage current) of the

devices, J_0 , which has a significant impact on V_{OC} (Equation 3.1).^{[51][52][54]} For example, the decrease in J_0 has previously been related to the presence of additional interfacial layer that acts as carrier-injection barrier at reverse bias in the dark measurement.^{[55][56]} According to the relation stated in equation 3.1, lower J_0 implies higher V_{OC} .

$$V_{oc} \approx \frac{k_B T}{q} \ln \left(\frac{J_{sc}}{J_0} + 1 \right); \quad (3.1)$$

where k_B is the Boltzmann constant, T is the absolute room temperature and q is the elementary electron charge.

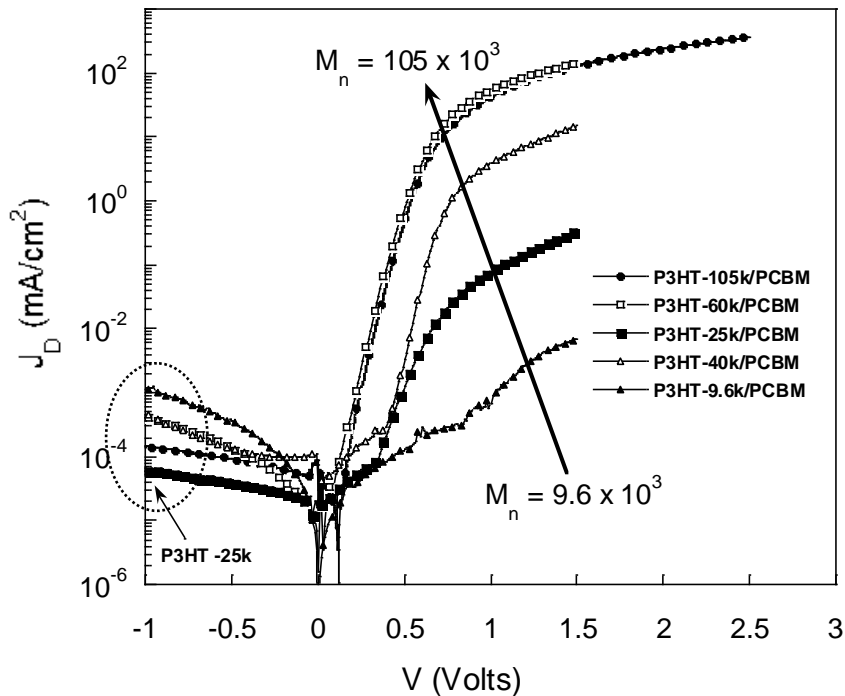


Figure 3.11: Dark current (J_D) as a function of the voltage (v) of P3HT:PCBM blend films for different P3HT molecular weights.

Figure 3.11 shows the dark J - V characteristics of P3HT:PCBM devices containing the different molecular weights of P3HT; measured from the current-voltage characteristics of the photovoltaic cells. The saturation dark currents for higher M_n P3HTs devices are found to be in the same range. However, the reverse saturation dark current for P3HT-25k based devices is strongly reduced as compared to the other devices. The reason for the low reverse saturation dark current for P3HT-25k is probably related to the observed P3HT-rich layer that has been detected at the aluminium side of the device. X-ray

Photoelectron Spectroscopy (XPS) data reveals roughly the same elemental composition for both pristine P3HT-25k thin film and P3HT-25k:PCBM blend film (Table 3.4). We ascribe such preferential segregation to the low dispersity of P3HT-25k (see Table 3.2). Indeed an enhanced miscibility of two components in the blend is expected with increased dispersity.^{[57][58][59]} The smallest chains of a polydisperse polymer are able to migrate more easily to the interface between the two constituents and thus decrease the interfacial tension enhancing the miscibility between P3HT and PCBM. However, with a monodisperse polymer such as P3HT-25k, there will be a larger tendency to phase segregate mostly to the top interface in the P3HT-25k:PCBM blends.^[58] This observed P3HT-rich layer probably acts as a carrier-injection barrier, which reduces J_0 , and thus increases the V_{OC} .

Film	C (%)	O (%)	S (%)
Pristine P3HT-25k	87.6	3.3	9.1
P3HT-25k:PCBM	87	6	7

Table 3.4: Surface (areal) composition of pristine P3HT-25k and P3HT-25k:PCBM (1:1) films as determined from X-ray photoelectron spectroscopy experiments. The oxygen in pristine P3HT and blend film is due to air contamination during the measurements.

However, since P3HT in general has a tendency to phase segregate towards film/air interface,^[60] the vertical phase segregation concept to explain why V_{OC} has increased for this particular P3HT may not be satisfactory. Further investigation at the organic/metal interface using ultraviolet photoemission spectroscopy (UPS) or other advanced techniques such as kelvin probe force microscopy (KPFM) will be needed in order to determine the exact justification.

To summarize this section, most of the PV parameters show an increase with the P3HT molecular weight. At a composition of P3HT:PCBM (1:1, w/w), SFM and TEM images confirm that P3HT-60k presents an optimum morphology which is favorable for exciton dissociation and charge transport than lower M_n P3HTs.

So far, we have investigated the influence of annealing temperature and molecular weights of P3HT on morphology and PV characteristics of P3HT:PCBM BHJ blends at a composition of 1:1 (w/w). From the results, the degree of phase separation of the blend (i.e. the nano- and microstructure) has a critical impact on the PV performance. In most reported works, the annealing temperature and composition of donor:acceptor blend are chosen as regards to the maximum PV performance. However, this method is empirical as well as time-consuming. Since the nano- and microstructure of BHJ OPVs is highly dependent on the composition and processing parameters, the selection of the optimal composition of the donor and acceptor components cannot generally be known at the starting point of an investigation. This implies that systematic investigation containing composition and temperature at the same time is needed to address the aforementioned challenges.

3.4. Study of the Phase Diagram of PHT:PCBM blends as regards to the Temperature and Composition

The phase behaviors of P3HT-9.6k, P3HT-25k and P3HT-60k blended with PCBM were investigated as a function of the composition of the blends over a large range of temperatures. The phase diagrams (temperature/composition) for all P3HT:PCBM binary blends were obtained using DSC as shown in Figure 3.12. A eutectic system was observed for all systems between 50 and 65 wt% of P3HT depending on the P3HT molecular weight as shown in Figure 3.13. The P3HT eutectic composition, C_e , was defined as the composition which exhibits the lowest melting point for the homogenous mixture of the two components. The concept of eutectic system allows to obtain finely intermixed (co-continuous) solid structures from the homogenous melt of P3HT and PCBM by rapid cooling from a temperature above the eutectic temperature T_e of blends formulated at the eutectic composition C_e . For hypo- or hyper-eutectic compositions, (hypo- $C < C_e$ and hyper-eutectic $C > C_e$ as regard to P3HT composition), when the mixture is heated at a temperature above the liquidus line and cooled down, primary crystals of the majority component are firstly formed, and then the two components solidify simultaneously at a temperature below T_e resulting in a structure with the majority

crystalline component surrounded by a matrix of both components.^[61] The eutectic point for the different molecular weight as regards to the P3HT composition is located between 60 and 65 wt%, 55 and 60 wt% and 50 and 55 wt% for P3HT-9.6k, P3HT-25k and P3HT-60k respectively. We observe that the eutectic composition is molecular weight dependant. The lower the molecular weight, the higher is the eutectic composition of P3HT.

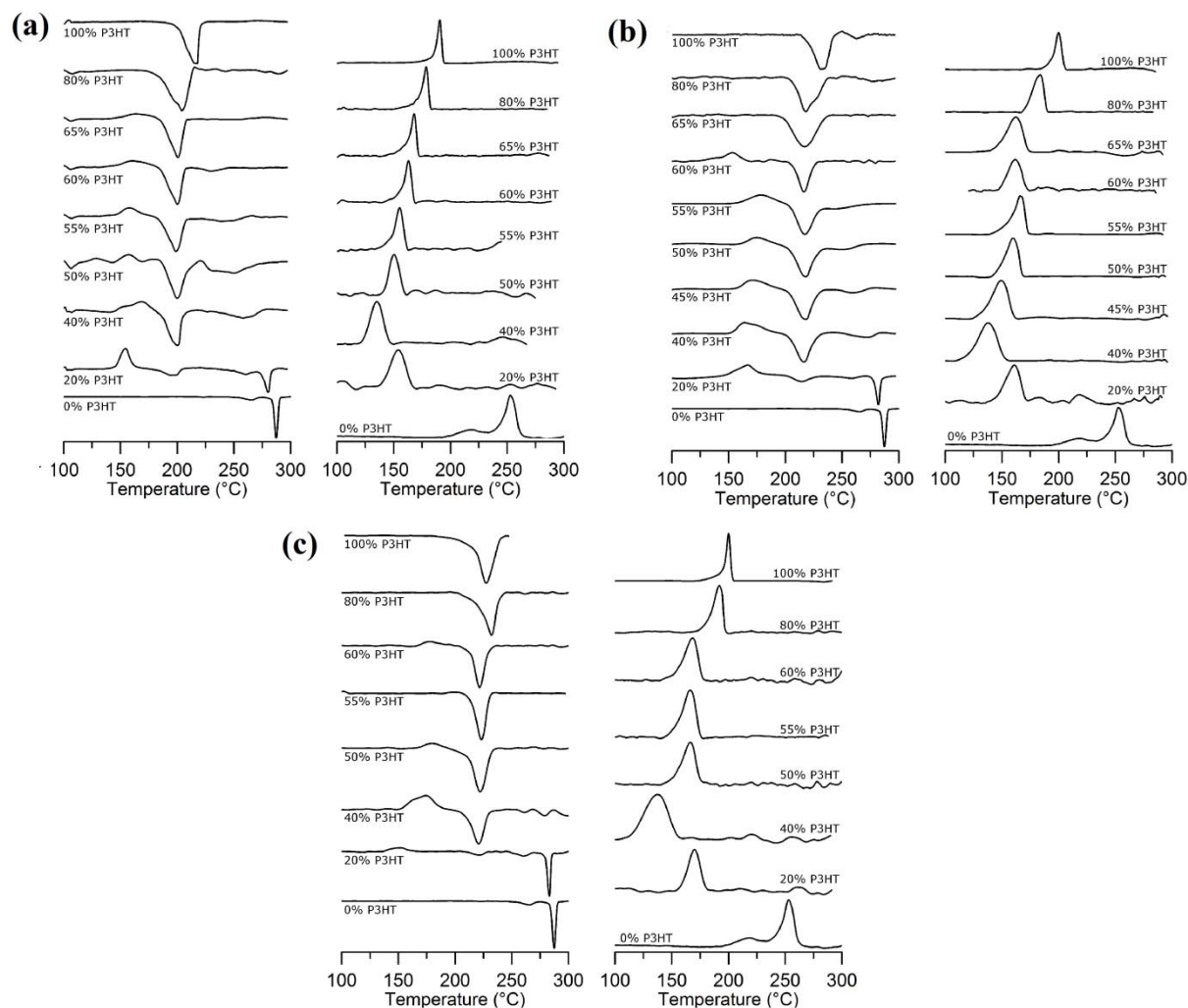


Figure 3.12: DSC thermograms of P3HT:PCBM blend films for different compositions of P3HT and different P3HT molecular weights: (a) 9.6 kg/mol, (b) 25 kg/mol, and (c) 60 kg/mol. On the left, the melting part from 100 to 300 °C; on the right, the crystallization part from 300 to 100°C.

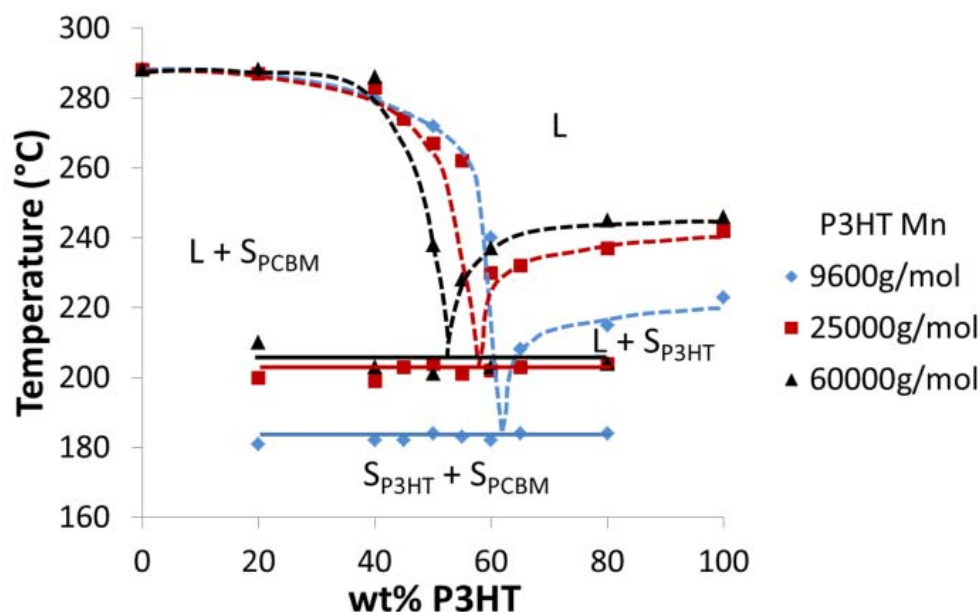


Figure 3.13: Phase diagrams of blends of different molecular weight P3HTs and PCBM obtained on the basis of the DSC thermograms (Figure 3.12). Solid lines: solidus lines; dash lines: liquidus lines. Solidus lines correspond to the appearance of the first drop of liquid (i.e., the temperature at the beginning of the first peak in the melting part). Liquidus lines correspond to the temperature at the end of the majority component peak in the melting part. L: liquid part; S_{PCBM} : solid solution of PCBM; S_{P3HT} : solid solution of P3HT.

Thin films with different compositions of P3HT:PCBM were also studied *in situ* by optical microscopy during heating as shown in Figure 3.14. For a hypo-eutectic composition, microscopic PCBM agglomerates appear at 180°C and then melt at temperatures around 240 - 280°C. These PCBM agglomerates (crystallites) only appear when there is at least 20 wt% of P3HT in the film, which supports the idea that the crystallization of the P3HT induces the agglomeration of the PCBM. The formation of PCBM agglomeration (crystallization) is also confirmed by the presence of exothermic peaks apparent on DSC thermograms upon heating around 180°C for hypo-eutectic composition. The appearance and disappearance of the PCBM agglomerates correspond to the solidus lines and the liquidus lines, have also indicated in the phase diagram (Figure 3.13). In another case, the introduction of more and more PCBM into P3HT leads to a reduction in the crystallization temperature for the

binary system since the inclusion of PCBM reduces the size of the P3HT crystallites and thus the P3HT melting point.^[62] For example, the crystallization peak of P3HT-60k was decreased from $\sim 198^\circ\text{C}$ to $\sim 160^\circ\text{C}$ for P3HT-60k:PCBM at a composition of 1:1 (w/w). It is noteworthy that the optimal (from a photovoltaic point of view) annealing temperature (180°C) which was experimentally determined previously for the high M_n binary system 50/50 (wt%) is located between the crystallization and the melting temperatures (Figure 3.12). This implies that annealing could be done at any temperature between the crystallization and the eutectic temperature for eutectic or close to eutectic compositions. These particular annealing temperature and composition induce an optimum P3HT crystallinity and PCBM aggregation without an extended phase separation among P3HT and PCBM domains or without the disruption of P3HT crystals.

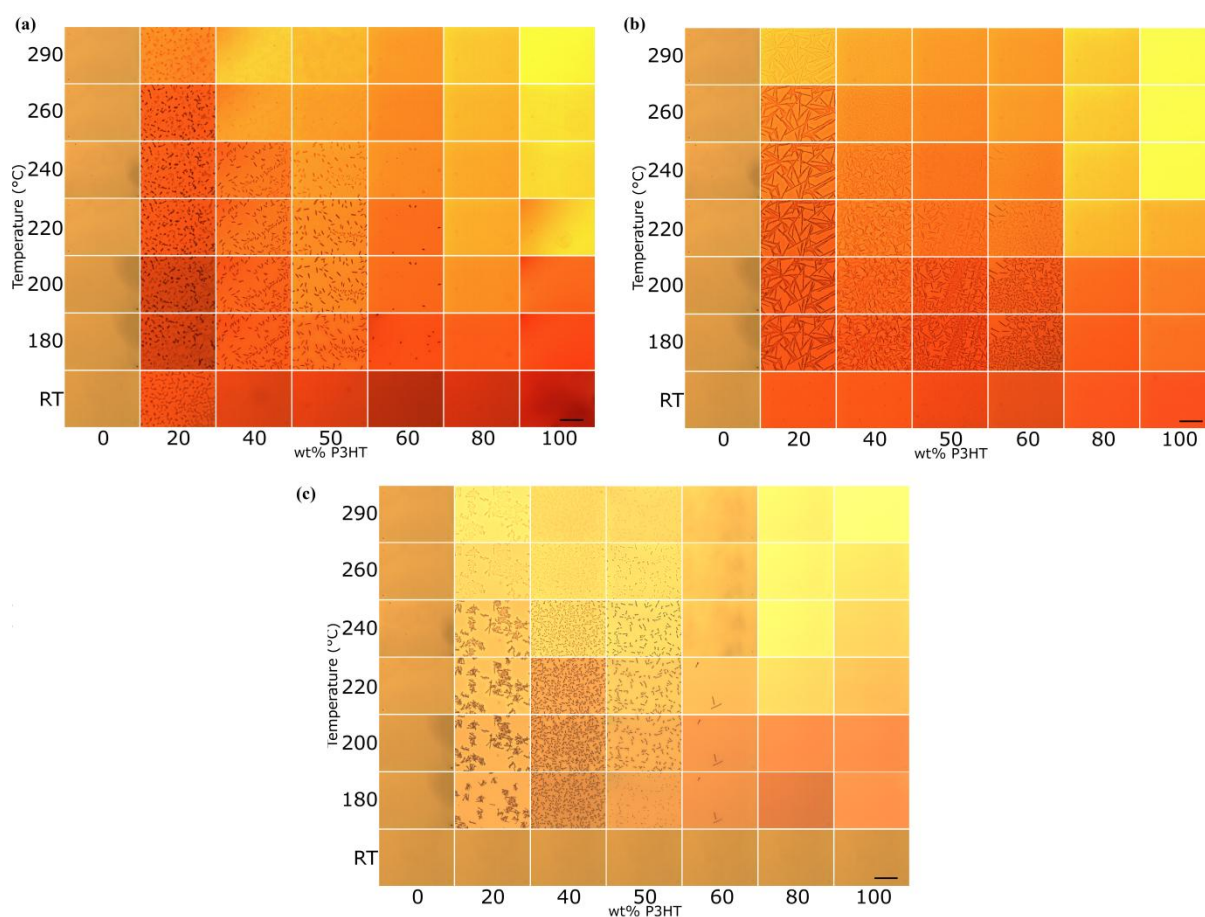


Figure 3.14: Optical microscopy images (X 40) of P3HT:PCBM thin films while heating with different amounts of P3HT and different P3HT molecular weights: (a) 9.6 kg/mol, (b) 25 kg/mol, and (c) 60 kg/mol. The scale bar represents 50 μm .

The shift in eutectic composition as a function of M_n was also confirmed by comparing the photovoltaic performance of the different P3HTs as shown in Figure 3.15. Maximum photovoltaic performance was obtained in the region of the eutectic composition for each P3HT. The crystallization behavior of the P3HT as regards to the molecular weight explains these observed shifts in composition (Table 3.3). Indeed, low molecular weight P3HTs show high crystallinity and form rigid nano-rods crystallites dispersed in a PCBM matrix which are poorly interconnected to each other. Thus, compared to higher M_n P3HT, a larger amount of low molecular weight P3HT is required to achieve the eutectic system or a bicontinuous solid structure that favors efficient exciton dissociation and charge transport.

Comparing the photovoltaic performance before and after annealing (Figure 3.15), J_{SC} is shifted towards lower P3HT content for low molecular weights. Notably, for P3HT-9.6k the maximum J_{SC} is around 80 wt% of P3HT before annealing whereas after annealing, it is around 65 wt% P3HT. Indeed the annealing process allows the system to achieve an optimum composition (close to the eutectic) convenient for PV operations. However, this shift in composition after annealing is not observed for the high molecular weight P3HT-60k. This is probably due to the higher number of entanglements in high molecular weight P3HT thus limiting the PCBM diffusion upon annealing and the formation of less phase separated domains. Consequently, for high molecular weight P3HTs, the composition for the best photovoltaic performance is largely independent of the thermal annealing.

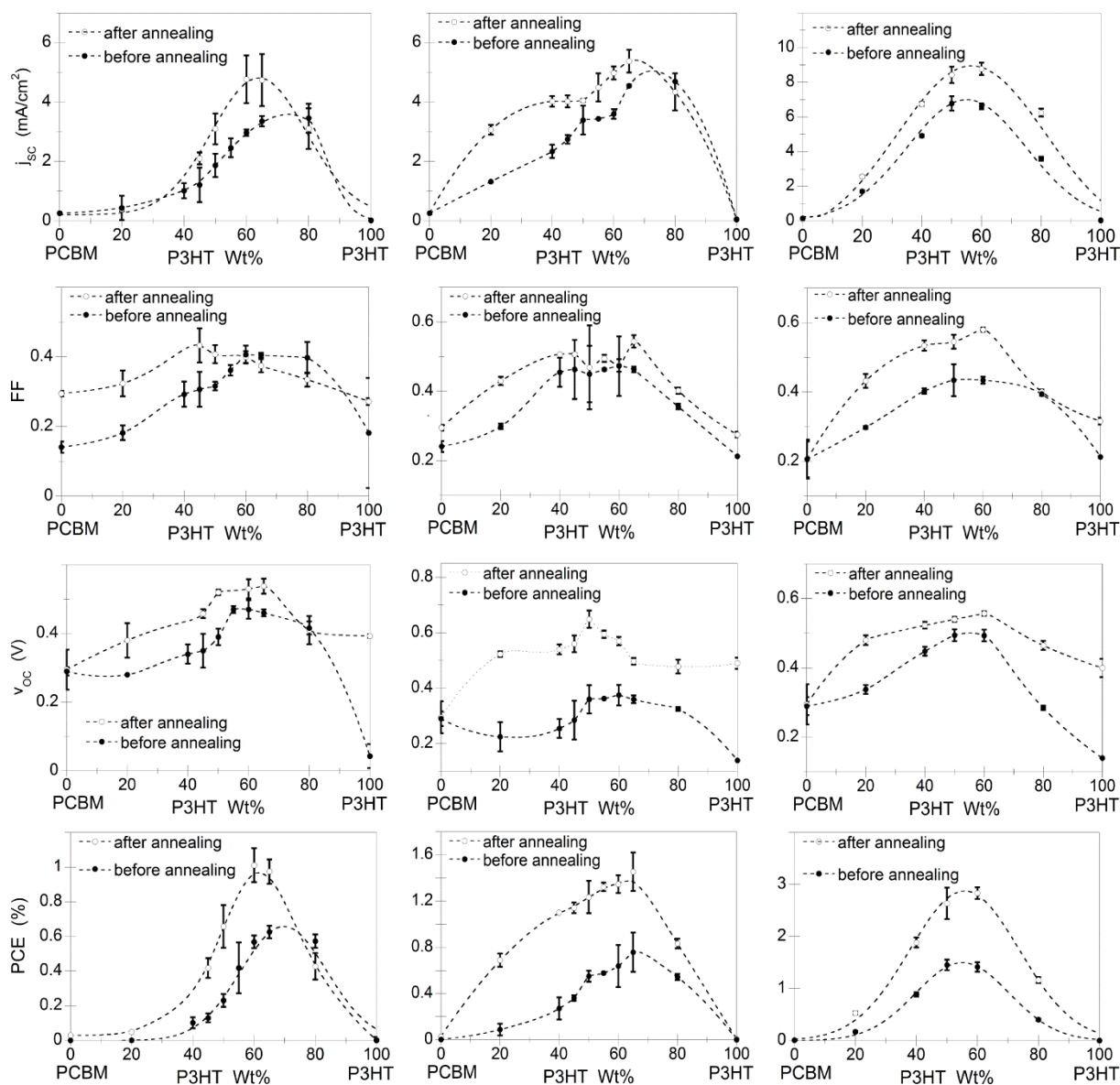


Figure 3.15: Photovoltaic performance of P3HT:PCBM devices at different composition of P3HT and PCBM for different molecular weights of P3HT before and after annealing. From left to right, 9.6 kg/mol, 25 kg/mol, and 60 kg/mol. The vertical bar on each point is the standard deviation measured on 16 different solar diodes.

To sum up, for a P3HT:PCBM (1:1, w/w) system the photovoltaic performance increases with the P3HT molecular weight. The poor performance observed for low molecular weight P3HTs is mainly due to their crystallization behavior. Low M_n P3HT form isolated crystalline nano-rods. Therefore, higher amount of P3HT compared to PCBM is needed to create connections between the different

P3HT domains. The establishment of the phase diagrams between P3HT and PCBM is necessary to determine the optimum ratio of the two compounds depending on the P3HT molecular weight.

So far, we have studied mainly the in-plane active layer's morphology (extent of phase separation in the in-plane direction) of P3HT:PCBM composite thin films using Optical, TEM and SFM characterization techniques. These analytical tools, however, provide only an in-plane view of the morphology; they cannot represent the entire morphology of the active layer in the devices. Specially, they cannot be used to investigate the vertical distribution of the components in the active layer. Even though we were able to detect the possible existence of concentration gradients perpendicular to the film plane in P3HT-25k:PCBM blends using XPS, some other powerful technique (such as, Neutron Reflectivity) are needed to accurately map out the concentration profiles of P3HT and PCBM species as a function of processing conditions (such as, annealing condition, type of transporting layers, ...). Utilizing this approach will lead to the establishment of the relationship between the relative vertical distributions of P3HT and PCBM in thin film configuration to the device performances.

3.5. Vertical Stratification Studies of P3HT:PCBM blends by Neutron Reflectometry

In photovoltaic cells, photo-generated charges are travelling along the vertical direction to reach the electrodes. Studying the concentration gradients and heterogeneities perpendicular to the film plane is thus very important in organic BHJ devices. Depending on the concentration heterogeneities next to the electrodes, charge harvesting may be either inhibited or facilitated. Indeed, in the case of polymeric blend films like those under study, it is well known that phase separation is affected by the air/polymer(s) and polymer(s)/substrate interfacial interactions,^{[1][63][64]} as well as by the dynamics during the spin-coating process,^[65] which can result in a stratification of the components along the normal to the substrate.

The concentration profile of P3HT:PCBM films (interfacial composition of the films) as a function of depth has been studied before by number of techniques: spectroscopic ellipsometry,^{[60][66]} neutron or X-ray reflectometry (NR, XRR),^{[67][68][69][70]} X-ray photoelectron spectroscopy (XPS),^[71] near-edge X-ray absorption fine structure spectroscopy (NEXAFS),^{[72][73]} and electron tomography.^[74] Most of the results obtained so far support the presence of a P3HT-rich layer at the air/film interface,^{[60][75]} consistent with the lower surface energy, γ , of P3HT ($\gamma_{\text{P3HT}} = 26.9 \text{ mN/m}^2$ as opposed to that of PCBM, where $\gamma_{\text{PCBM}} = 37.8 \text{ mN/m}^2$),^[72] although PCBM segregation on the top layer has been also reported.^{[68][69]} Concerning the film/substrate interface, a comparative study of the literature suggests that the preferential segregation of P3HT or PCBM close to that interface depends on the surface energy of the material upon which the active layer is cast. When silicon^{[68][69][75]} or quartz^{[60][66]} is used, the formation of a PCBM-rich layer close to the substrate has been revealed. The agglomeration of PCBM next to the substrate was found to be promoted when cesium carbonate (Cs_2CO_3) was used as the substrate layer.^[71] A few other exotic substrates^{[71][72][66]} have also been used. However, the concentration profile of the active layers investigated in all these works were done without taking into consideration the most commonly used hole and electron transport layers.

Herein, we use neutron reflectometry to study quantitatively the concentration-depth profile of P3HT (60 kg/mol):PCBM (1:1 w/w) active layers spun casted on top of a layer of titanium oxide (TiOx) or a film of a complex of one part poly(3,4-ethylenedioxythiophene) to six parts poly(styrene-4-sulfonate) (PEDOT:PSS). PEDOT:PSS is a common hole transport layer for conventional solar cells, while TiOx is widely used as an electron transport layer, suitable for inverted solar cells. The films under investigation were fabricated using a procedure that mimics the fabrication of the corresponding devices. In all cases silicon wafers were used as supporting substrates. The films were thermally annealed at 165°C for 20min. The detailed fabrication procedures are presented on chapter 7.

Neutrons are a unique tool for studying the P3HT:PCBM blend, due to the significant contrast between the two materials; P3HT has a scattering length density, ρ_{P3HT} , of $0.67 \times 10^{-6} \text{ \AA}^{-2}$, while for

PCBM, $\rho_{\text{PCBM}} = 4.34 \times 10^{-6} \text{ \AA}^{-2}$ (calculated using a mass density of 1.5 g/cm^3). This enables a determination of the distribution of the two components along the normal to the film plane, without need of deuteration of one of the blend components. The MOTOFIT^[76] package has been employed for fitting the reflectivity curves and a multilayer structure has been considered for modeling the films, the unknown parameters being the thickness, L , scattering length density, ρ , and roughness of each sub-layer. Thus the scattering length density profile, $\rho(z)$, z being the depth, of the film under study with respect to film thickness is evaluated. The SLDs of the two transport layers were derived experimentally by fitting the reflectivity curves obtained for a single PEDOT:PSS layer and a single TiO_x layer spun cast on Si; PEDOT:PSS is found to form a homogeneous layer with a scattering length density of $1.68 \times 10^{-6} \text{ \AA}^{-2}$, while that of TiO_x is almost $1 \times 10^{-6} \text{ \AA}^{-2}$. Neutron reflectometry data are generally not unique due to the loss of phase information in data acquisition, and require prior information to claim unambiguous scattering length density profiles. In our case, the known total scattering density of the different layers, and the asymmetry of the system give us confidence that the volume fraction profiles obtained during the fitting are unique. Certainly, we were unable to direct the fitting to produce profiles significantly different from those which we present here.

The reflectivity curves collected for the as-cast and annealed films formed on the PEDOT:PSS and TiO_x layers are shown in Figures 3.16(a) and 3.16(b), respectively. We chose to plot the product RQ_z^4 , R being the absolute reflectivity and Q_z the out-of-plane scattering vector, which allows for better visualization of the features of the reflectivity data. The introduction of the transport layer below the active blend increases the complexity of the reflectivity curve due to the addition of an extra layer. Therefore, the curves shown in Figure 3.16 contain oscillations for Q_z up to 0.06 \AA^{-1} for PEDOT:PSS and up to 0.1 \AA^{-1} for TiO_x . We note that these reflectometry data are appropriate for real devices (*i.e.* active layer cast on top of the transport layer). Depending on the sample, a 3- or 4-layer model – including the transport layer – was used for fitting the reflectivity curves; the fewest layers required to convincingly simulate our films. The best-fit curves are included in Figures 3.16(a) and 3.16(b) and are denoted by solid lines. The corresponding scattering length density profiles derived from fitting are

presented in Figures 3.17(a) and Figure 3.17(b). The zero value of the thickness axis is set at the PEDOT:PSS/active layer or TiOx/active layer interface.

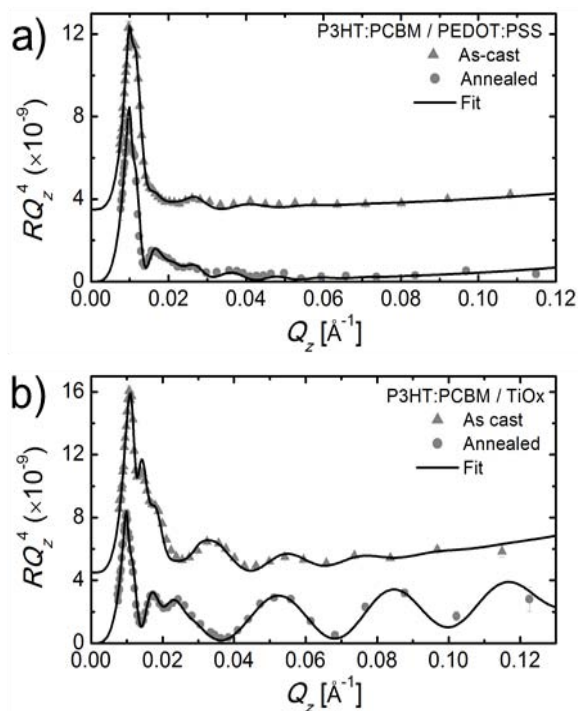


Figure 3.16: The reflectivity curves collected for the as cast and annealed P3HT:PCBM blends spun on (a) PEDOT:PSS and (b) TiOx layers, to mimic the films incorporated in conventional and inverted solar cells respectively. The corresponding best-fitting curves are included as well and they are denoted by solid lines. The curves that correspond to the not-annealed films were shifted along the y-axis for clarity.

In a conventional solar cell architecture with PEDOT:PSS being the hole transport layer, the $\rho(z)$ profile of the as-cast active layer suggests that the film is not homogeneous along the vertical direction. In fact, three sub-layers are necessary in order to describe the active layer; a relatively large SLD layer ($\rho = 3.2 \times 10^{-6} \text{ \AA}^{-2}$) next to the interface with PEDOT:PSS, followed by a layer with $\rho = 2.4 \times 10^{-6} \text{ \AA}^{-2}$ and a low-SLD layer ($\rho = 1 \times 10^{-6} \text{ \AA}^{-2}$) at the interface with air. Given the high SLD of PCBM with respect to P3HT ($4.34 \times 10^{-6} \text{ \AA}^{-2}$ as opposed to $0.67 \times 10^{-6} \text{ \AA}^{-2}$), our finding suggest that the first sub-layer is rich in PCBM, while the upper part of the film is rich in P3HT. All three layers exhibit large roughness, and therefore gradual transitions between them are apparent in the $\rho(z)$ profile. After annealing we observe a decrease in the thickness of the active layer by almost 70 Å, which suggests the evaporation of solvent trapped in the film. More importantly, our data show that upon annealing,

PCBM diffuses to the bottom of the active layer, towards the interface with PEDOT:PSS. Only two sub-layers are required to fit the reflectivity curve, a 120 Å thick with a ρ of $3.5 \times 10^{-6} \text{ \AA}^{-2}$ and a much thicker one (525 Å) with a ρ of almost $2 \times 10^{-6} \text{ \AA}^{-2}$ which are clearly distinguished in Figure 3.17(a) due to their sharp interface. The thick top layer is homogenous along the vertical direction and a surface roughness of 70 Å has been derived by fitting, which is a normal value for the P3HT:PCBM blend.

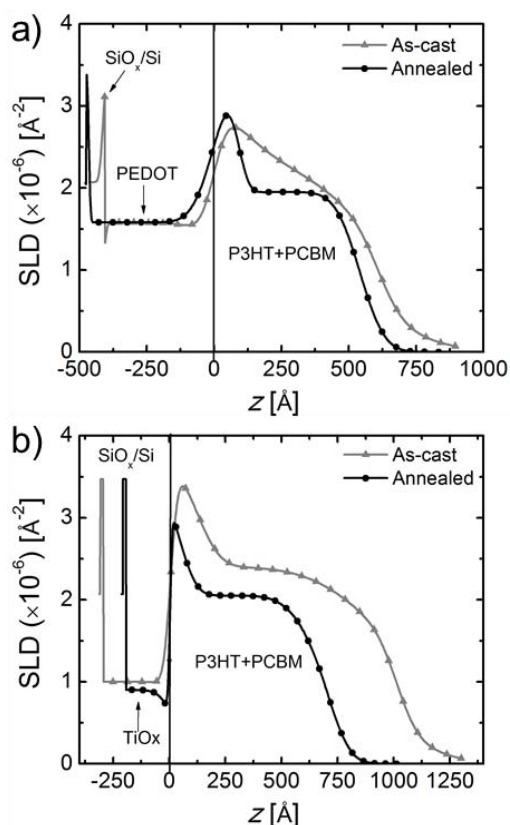


Figure 3.17: The scattering length density profiles derived by fitting the reflectivity curves of the as cast and annealed P3HT:PCBM blends spun on (a) PEDOT:PSS and (b) TiOx layers. The zero thickness value is set at the transport/active layer interface.

One could argue that the stratification within the P3HT:PCBM blend revealed in the conventional solar cell configuration is not the one promoting charge harvesting by the electrodes. The accumulation of the electron-acceptor material, *i.e.* PCBM, next to the hole-transport layer, *i.e.* PEDOT:PSS, could result in increased electron-hole recombination at the PCBM-rich sub-layer, which therefore acts as a hole-blocking layer increasing series resistance, as stated by Xu *et al.*^[71] On the other hand, the experimental findings of Germack *et al.*^[66] and Wang *et al.*^[73] suggest that device

performance is insensitive to surface-directed phase separation in the P3HT:PCBM bulk heterojunction, with Wang *et al.* stressing that a continuous P3HT layer next to the cathode is less effective at blocking electrons than a hole-blocking PCBM layer next to the anode.^[73] It is therefore important to estimate the PCBM volume fraction, ϕ_{PCBM} , profile along the active layer in order to quantify the enrichment of the active layer/PEDOT:PSS interface with PCBM.

To calculate ϕ_{PCBM} we employ the mass conservation equation $\rho(z) = \phi_{\text{PCBM}}(z) \rho_{\text{PCBM}} + \phi_{\text{P3HT}}(z) \rho_{\text{P3HT}}$, where $\phi_{\text{P3HT}} = 1 - \phi_{\text{PCBM}}$ is the P3HT volume fraction. The scattering length density of P3HT was fixed at $0.67 \times 10^{-6} \text{ \AA}^{-2}$, which corresponds to a P3HT mass density of 1.1 g/cm^3 , in accordance with other reports.^{[68][75][77]} Concerning PCBM, its mass density is reported^[68] to vary within the range $1.25 - 1.5 \text{ g/cm}^3$, that corresponds to a scattering length density variation between $3.6 \times 10^{-6} \text{ \AA}^{-2}$ and $4.34 \times 10^{-6} \text{ \AA}^{-2}$. Therefore, we opt to calculate experimentally ρ_{PCBM} rather than use a fixed value. To do so we use our prior knowledge of the total volume fraction of P3HT and PCBM to apply mass conservation equation to the neutron scattering length density, *i.e.* the integral $\int \rho(z) dz$. Thus, for the annealed active layer we calculate $\rho_{\text{PCBM}} = 4.2 \times 10^{-6} \text{ \AA}^{-2}$, corresponding to a density of 1.45 g/cm^3 , which is consistent with values reported earlier. The $\phi_{\text{PCBM}}(z)$ profile of the annealed sample is presented in Figure 3.18. Our results show that the PCBM-rich layer next to the PEDOT:PSS interface consists of 60% PCBM, as opposed to 43% in the homogeneously mixed P3HT:PCBM blend. We suggest that this PCBM volume fraction is not high enough to efficiently block holes from being harvested at the PEDOT:PSS layer. Therefore we should not expect an effect on device performance, as concluded previously.^{[73][66]} At the intermediate part of the film ϕ_{PCBM} has a constant value 36%, 7% less than the amount of PCBM in the homogeneous blend. Looking at the upper part of the active layer that will adjoin the cathode, ϕ_{PCBM} values imply that PCBM is depleted at the upper 70 Å of the film that agrees well with the surface roughness of this film. Below this sub-layer there is another layer of 70 Å that contains less than 20% of PCBM. Based on the observation of Wang *et al.*^[73] electrons are not blocked by a continuous thin layer of P3HT we conclude that the presence of this P3HT-rich layer next to the cathode cannot significantly deteriorate device performance.

It was not possible to apply a similar calculation for the as-cast active layer due to the solvent trapped inside. Given that this is a ternary system, the calculation of $\phi_{\text{PCBM}}(z)$ would require the knowledge of the trapped solvent profile within the blend, which is lacking.

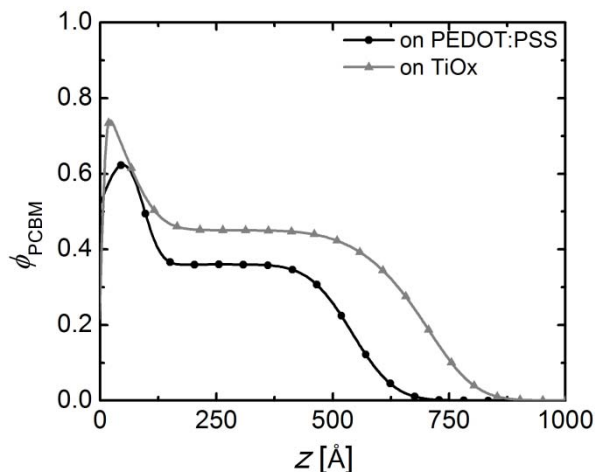


Figure 3.18: The PCBM volume fraction distribution within the annealed P3HT:PCBM blends cast on PEDOT:PSS and TiOx transport layers.

In the case of films that mimic the inverted solar cells architecture, the curves presented in Figure 3.17(b) show that the active layers cast on TiOx exhibit similar stratification as those cast on PEDOT:PSS. Three sub-layers are required to accurately fit the reflectivity data for both the as-cast and annealed film; a PCBM-rich sub-layer next to the TiOx transport layer ($\rho = 3.5 \times 10^{-6} \text{ \AA}^{-2}$ for the annealed film), a homogeneously mixed P3HT:PCBM sub-layer at the bulk of the film ($\rho = 2.15 \times 10^{-6} \text{ \AA}^{-2}$ for the annealed film) and a P3HT-rich sub-layer at the film surface. The interfaces between the sub-layers are less rough than in case of PEDOT:PSS, suggesting a larger interfacial tension, particularly at the active layer/TiOx interface. The characteristics of the upper layer are similar in all three samples that required the consideration of three sub-layers, i.e. $\rho \approx 1 \times 10^{-6} \text{ \AA}^{-2}$, a thickness of $\sim 100 \text{ \AA}$ and a roughness of $\sim 70 \text{ \AA}$. This points to a common origin of this structuration, that is the preferential segregation of P3HT to the free surface due to its lower surface energy.^[72] Once more, the as-cast film is thicker than the annealed. Our calculations showed that this thickness variation is only partially due to solvent trapped in the film, nonetheless we cannot speculate on the additional factors that resulted in the increased thickness.

Figure 3.18 includes the PCBM volume fraction profile derived for the annealed P3HT:PCBM blend cast on TiOx. ρ_{PCBM} was derived experimentally following the methodology described earlier. The PCBM-rich sub-layer consists of 75% PCBM, 15% more with respect to the film cast on PEDOT:PSS. The plateau ϕ_{PCBM} value at the bulk of the film is 45%, almost equal to the 46% PCBM volume fraction in the homogeneously mixed P3HT:PCBM blend that we obtained for this specific sample based on its total scattering power, i.e. the integral of the scattering length density over the depth of the film.

In principle, the stratification observed in the annealed P3HT:PCBM blend could be considered to be optimal for an efficient charge transport and collection at both electrodes of an inverted solar cell; a significant PCBM enrichment of the active layer close to the electron-transport layer should favor electron harvesting, as well as a P3HT enrichment at the side of the anode which favors holes collection. Xu *et al.*^[71] compared the device performance of conventional and inverted devices that incorporate PEDOT:PSS and Cs₂CO₃ as the hole-transport and electron-transport layers respectively, and claimed that the increased current collected in case of Cs₂CO₃ is a result of the favorable structure parallel to the plane of the film that reduces charge carrier recombination in the inverted architecture. However a discussion on the influence of the different top electrodes they used – Al or Ca/Al for the conventional solar cells and V₂O₅/Al or MoO₃/Ag for the inverted ones – is lacking. On the other hand, the outcomes of Germack *et al.*^[66] and Wang *et al.*^[73] concerning the insensitivity of device performance on the morphology as a function of depth have been derived for the case of an active layer cast on top of a hole transport layer. To draw a definitive conclusion further investigation of the influence of surface segregation and surface-directed spinodal decomposition on device performance is required.

3.6. Conclusion

To summarize, we showed that the P3HT macromolecular characteristics are determining factors for the morphology and the photovoltaic performance and that the optimal ratios of P3HT and PCBM in the active layer are inherent to the P3HT molecular weight. A systematic approach has been employed in order to map-out the phase diagram of P3HT:PCBM binary blend systems. The establishment of the P3HT:PCBM phase diagrams provides a better understanding of the interdependences between P3HT crystallization, the diffusion of PCBM to form microscale agglomerates, and more generally, the phase separation mechanisms occurring during the annealing process. Moreover, we have demonstrated that the maximum photovoltaic characteristics are obtained at eutectic or close to eutectic composition of the active layer. In addition, we showed that the P3HT:PCBM bulk heterojunction concentration profile within a real solar cell configuration is not homogeneous along the normal to the substrate. A 60% and 75% PCBM enrichment of the active layer at the interface with PEDOT:PSS and TiO_x respectively has been revealed, as well as a PCBM depletion at the free surface of the film which is driven by the lower surface energy of P3HT. PCBM segregation close to the substrate is further enhanced by annealing. In case of the films cast on PEDOT:PSS, this stratification could be detrimental for conventional solar cell performance, since the electron-acceptor material enriches the interface with the hole-collecting electrode. The agglomeration of PCBM at the TiO_x interface could, however, be favorable for an enhanced charge collection, thus improving device performance.

References

- [1] M. Geoghegan, G. Krausch, *Progress in Polymer Science* **2003**, *28*, 261–302.
- [2] X. Yang, J. Loos, S.C. Veenstra, W.J.H. Verhees, M.M. Wienk, J.M. Kroon, M.A.J. Michels, R.A.J. Janssen, *Nano Letters* **2005**, *5*, 579–83.
- [3] M. Shin, H. Kim, J. Park, S. Nam, K. Heo, M. Ree, C.-S. Ha, Y. Kim, *Advanced Functional Materials* **2010**, *20*, 748–754.
- [4] T. Erb, U. Zhokhavets, G. Gobsch, S. Raleva, B. Stühn, P. Schilinsky, C. Waldauf, C.J. Brabec, *Advanced Functional Materials* **2005**, *15*, 1193–1196.
- [5] M. Reyes-Reyes, K. Kim, D.L. Carroll, *Applied Physics Letters* **2005**, *87*, 083506.
- [6] U. Zhokhavets, T. Erb, H. Hoppe, G. Gobsch, N. Sariciftci, *Thin Solid Films* **2006**, *496*, 679–682.
- [7] S.S. van Bavel, M. Bärenklau, G. de With, H. Hoppe, J. Loos, *Advanced Functional Materials* **2010**, *20*, 1458–1463.
- [8] A.L. Ayzner, D.D. Wanger, C.J. Tassone, S.H. Tolbert, B.J. Schwartz, *The Journal of Physical Chemistry C* **2008**, *112*, 18711–18716.
- [9] B. Watts, W.J. Belcher, L. Thomsen, H. Ade, P.C. Dastoor, *Macromolecules* **2009**, *42*, 8392–8397.
- [10] D.R. Kozub, K. Vakhshouri, L.M. Orme, C. Wang, A. Hexemer, E.D. Gomez, *Macromolecules* **2011**, *44*, 5722–5726.
- [11] D. Chen, A. Nakahara, D. Wei, D. Nordlund, T.P. Russell, *Nano Letters* **2011**, *11*, 561–7.
- [12] N.D. Treat, M.A. Brady, G. Smith, M.F. Toney, E.J. Kramer, C.J. Hawker, M.L. Chabiny, *Advanced Energy Materials* **2011**, *1*, 82–89.
- [13] C. Yang, J.G. Hu, A.J. Heeger, *Journal of the American Chemical Society* **2006**, *128*, 12007–13.
- [14] D. Chen, F. Liu, C. Wang, A. Nakahara, T.P. Russell, *Nano Letters* **2011**, *11*, 2071–2078.
- [15] S. Bertho, G. Janssen, T.J. Cleij, B. Conings, W. Moons, *Solar Energy Materials & Solar Cells* **2008**, *92*, 753–760.
- [16] W. Yin, M. Dadmun, *ACS Nano* **2011**, 4756–4768.
- [17] T.J. Savenije, J.E. Kroeze, X. Yang, J. Loos, *Advanced Functional Materials* **2005**, *15*, 1260–1266.
- [18] A. Swinnen, I. Haeldermans, M. vande Ven, J. D’Haen, G. Vanhoyland, S. Aresu, M. D’Olieslaeger, J. Manca, *Advanced Functional Materials* **2006**, *16*, 760–765.
- [19] A. Swinnen, I. Haeldermans, P. Vanlaeke, J. D’Haen, J. Poortmans, M. D’Olieslaeger, J. V. Manca, *Eur. Phys. J. Appl. Phys.* **2006**, *36*, 251–256.

- [20] R.C. Nieuwendaal, C.R. Snyder, R.J. Kline, E.K. Lin, D.L. VanderHart, D.M. DeLongchamp, *Chemistry of Materials* **2010**, *22*, 2930–2936.
- [21] B.A. Collins, J.R. Tumbleston, H. Ade, *J. Phys. Chem. Lett* **2011**, *2*, 3135–3145.
- [22] B. Friedel, P.E. Keivanidis, T.J.K. Brenner, A. Abrusci, C.R. McNeill, R.H. Friend, N.C. Greenham, *Macromolecules* **2009**, *42*, 6741–6747.
- [23] E. Vitoratos, S. Sakkopoulos, E. Dalas, N. Paliatsas, D. Karageorgopoulos, F. Petraki, S. Kennou, S. Choulis, *Organic Electronics* **2009**, *10*, 61–66.
- [24] D.D.C.B. J. Huang, P.F. Miller, J.C. de Mello, A.J. de Mello, *Synthetic Metals* **2003**, *139*, 569–572.
- [25] H. Ma, H.-L. Yip, F. Huang, A.K.-Y. Jen, *Advanced Functional Materials* **2010**, *20*, 1371–1388.
- [26] A. Gadisa, M. Svensson, M.R. Andersson, O. Inganäs, *Applied Physics Letters* **2004**, *84*, 1609.
- [27] A.K. Thakur, G. Wantz, G. Garcia-Belmonte, J. Bisquert, L. Hirsch, *Solar Energy Materials and Solar Cells* **2011**, *95*, 2131–2135.
- [28] S.C. Veenstra, A. Heeres, G. Hadziioannou, G.A. Sawatzky, H.T. Jonkman, *Applied Physics A: Materials Science & Processing* **2002**, *75*, 661–666.
- [29] S.K.M. Jönsson, E. Carlegrim, F. Zhang, W.R. Salaneck, M. Fahlman, *Japanese Journal of Applied Physics* **2005**, *44*, 3695–3701.
- [30] J. Luo, H. Wu, C. He, A. Li, W. Yang, Y. Cao, *Applied Physics Letters* **2009**, *95*, 043301.
- [31] S. Malik, A.K. Nandi, *Journal of Polymer Science Part B: Polymer Physics* **2002**, *40*, 2073–2085.
- [32] Y. Kim, S. Cook, S.M. Tuladhar, S.A. Choulis, J. Nelson, J.R. Durrant, D.D.C. Bradley, M. Giles, I. McCulloch, C.-S. Ha, M. Ree, *Nature Materials* **2006**, *5*, 197–203.
- [33] P.G. Karagiannidis, S. Kassavetis, C. Pitsalidis, S. Logothetidis, *Thin Solid Films* **2011**, *519*, 4105–4109.
- [34] A.M. Ballantyne, L. Chen, J. Dane, T. Hammant, F.M. Braun, M. Heeney, W. Duffy, I. McCulloch, D.D.C. Bradley, J. Nelson, *Advanced Functional Materials* **2008**, *18*, 2373–2380.
- [35] S. Berson, R. De Bettignies, S. Bailly, S. Guillerez, *Advanced Functional Materials* **2007**, *17*, 1377–1384.
- [36] A.J. Heeger, *Chemical Society Reviews* **2010**, *39*, 2354–2371.
- [37] M.-S. Kim, B.-G. Kim, J. Kim, *ACS Applied Materials & Interfaces* **2009**, *1*, 1264–9.
- [38] D. Gupta, S. Mukhopadhyay, K. Narayan, *Solar Energy Materials and Solar Cells* **2008**, *94*, 1309–1313.
- [39] J.J.M. Halls, C.A. Walsh, N.C. Greenham, E.A. Marseglia, R.H. Friend, S.C. Moratti, A.B. Holmes, *Nature* **1995**, *376*, 498–500.

- [40] A.J. Yu, G.; Gao, J.; Hummelen, J. C.; Wudl, F.; Heeger, *Science* **1995**, *270*, 1789–1791.
- [41] P. Schilinsky, U. Asawapirom, U. Scherf, M. Biele, C.J. Brabec, *Chemistry of Materials* **2005**, *17*, 2175–2180.
- [42] X. Jiang, R. Patil, Y. Harima, J. Ohshita, A. Kunai, *The Journal of Physical Chemistry. B* **2005**, *109*, 221–9.
- [43] R.J. Kline, M.D. McGehee, E.N. Kadnikova, J. Liu, J.M.J. Fre, M.F. Toney, *Macromolecules* **2005**, *38*, 3312–3319.
- [44] W. Ma, J.Y. Kim, K. Lee, A.J. Heeger, *Macromolecular Rapid Communications* **2007**, *28*, 1776–1780.
- [45] M. Brinkmann, P. Rannou, *Advanced Functional Materials* **2007**, *17*, 101–108.
- [46] M. Brinkmann, P. Rannou, *Macromolecules* **2009**, *42*, 1125–1130.
- [47] R. Hoffmann, C. Janiak, C. Kollmar, *Macromolecules* **1991**, *24*.
- [48] D.J.D. Moet, M. Lenes, J.D. Kotlarski, S.C. Veenstra, J. Sweelssen, M.M. Koetse, B. de Boer, P.W.M. Blom, *Organic Electronics* **2009**, *10*, 1275–1281.
- [49] G. Li, Y. Yao, H. Yang, V. Shrotriya, G. Yang, Y. Yang, *Advanced Functional Materials* **2007**, *17*, 1636–1644.
- [50] W.J. Potscavage, S. Yoo, B. Kippelen, *Applied Physics Letters* **2008**, *93*, 193308.
- [51] K. Vandewal, K. Tvingstedt, A. Gadisa, O. Inganäs, J. V Manca, *Nature Materials* **2009**, *8*, 904–9.
- [52] N. Li, B.E. Lassiter, R.R. Lunt, G. Wei, S.R. Forrest, *Applied Physics Letters* **2009**, *94*, 023307.
- [53] A.K. Thakur, G. Wantz, G. Garcia-Belmonte, J. Bisquert, L. Hirsch, *Solar Energy Materials and Solar Cells* **2011**, *95*, 2131–2135.
- [54] F. Zhang, M. Ceder, O. Inganäs, *Advanced Materials* **2007**, *19*, 1835–1838.
- [55] Y. Yuan, T.J. Reece, P. Sharma, S. Poddar, S. Ducharme, A. Gruverman, Y. Yang, J. Huang, *Nature Materials* **2011**, *10*, 296–302.
- [56] B. Yang, Y. Yuan, P. Sharma, S. Poddar, R. Korlacki, S. Ducharme, A. Gruverman, R. Saraf, J. Huang, *Advanced Materials* **2012**, *24*, 1455–60.
- [57] R. Gelles, C.W. Frank, *Macromolecules* **1983**, *16*, 1448–1456.
- [58] D. Broseta, G.H. Fredrickson, E. Helfand, L. Leibler, *Macromolecules* **1990**, *23*, 132–139.
- [59] S. Enders, A. Hinrichs, R. Horst, B.A. Wolf, M. Mass, *J. Macromol. Sci. Part A: Pure Appl. Chem.* **1996**, *33*, 1097–1111.

- [60] M. Campoy-Quiles, T. Ferenczi, T. Agostinelli, P.G. Etchegoin, Y. Kim, T.D. Anthopoulos, P.N. Stavrinou, D.D.C. Bradley, J. Nelson, *Nature Materials* **2008**, 7, 158–64.
- [61] C. Müller, T.A.M. Ferenczi, M. Campoy-Quiles, J.M. Frost, D.D.C. Bradley, P. Smith, N. Stingelin-Stutzmann, J. Nelson, *Advanced Materials* **2008**, 20, 3510–3515.
- [62] E. Verploegen, R. Mondal, C.J. Bettinger, S. Sok, M.F. Toney, Z. Bao, *Advanced Functional Materials* **2010**, 20, 3519–3529.
- [63] R.A.L. Jones, L.J. Norton, E.J. Kramer, F.S. Bates, P. Wiltzius, *Phys. Rev. Lett.* **1991**, 66, 1326–1329.
- [64] M. Geoghegan, R.A.L. Jones, R.S. Payne, P. Sakellariou, A.S.J.P. Clough, *Polymer* **1994**, 35, 2019–2027.
- [65] S.Y. Heriot, R.A.L. Jones, *Nature Materials* **2005**, 4, 782–6.
- [66] D.S. Germack, C.K. Chan, R.J. Kline, D.A. Fischer, D.J. Gundlach, M.F. Toney, L.J. Richter, D.M. DeLongchamp, *Macromolecules* **2010**, 43, 3828–3836.
- [67] A.J. Parnell, A.D.F. Dunbar, A.J. Pearson, P.A. Staniec, A.J.C. Dennison, H. Hamamatsu, M.W.A. Skoda, D.G. Lidzey, R.A.L. Jones, *Advanced Materials* **2010**, 22, 2444–2447.
- [68] J.W. Kiel, B.J. Kirby, C.F. Majkrzak, B.B. Maranville, M.E. Mackay, *Soft Matter* **2010**, 6, 641–646.
- [69] Z. Sun, K. Xiao, J.K. Keum, X. Yu, K. Hong, J. Browning, I.N. Ivanov, J. Chen, J. Alonzo, D. Li, B.G. Sumpter, E.A. Payzant, C.M. Rouleau, D.B. Geohegan, *Advanced Materials* **2011**, 23, 5529–35.
- [70] M.A. Ruderer, S. Guo, R. Meier, H.-Y. Chiang, V. Körstgens, J. Wiedersich, J. Perlich, S. V. Roth, P. Müller-Buschbaum, *Advanced Functional Materials* **2011**, 21, 3382–3391.
- [71] Z. Xu, L.-M. Chen, G. Yang, C.-H. Huang, J. Hou, Y. Wu, G. Li, C.-S. Hsu, Y. Yang, *Advanced Functional Materials* **2009**, 19, 1227–1234.
- [72] D.S. Germack, C.K. Chan, B.H. Hamadani, L.J. Richter, D.A. Fischer, D.J. Gundlach, D.M. DeLongchamp, *Journal of Applied Physics* **2009**, 94, 233303.
- [73] H. Wang, E.D. Gomez, J. Kim, Z. Guan, C. Jaye, D.A. Fischer, A. Kahn, Y. Loo, *Chemistry of Materials* **2011**, 23, 2020–2023.
- [74] S.S. Van-Bavel, E. Sourty, G. de With, J. Loos, *Nano Letters* **2009**, 9, 507–13.
- [75] A.J. Parnell, A.D.F. Dunbar, A.J. Pearson, P.A. Staniec, A.J.C. Dennison, H. Hamamatsu, M.W.A. Skoda, D.G. Lidzey, R.A.L. Jones, *Advanced Materials* **2010**, 22, 2444–2447.
- [76] A. Nelson, *Journal of Applied Crystallography* **2006**, 39, 273–276.
- [77] J.W. Kiel, M.E. Mackay, B.J. Kirby, B.B. Maranville, C.F. Majkrzak, *The Journal of Chemical Physics* **2010**, 133, 074902.

Chapter – IV

***Semi-rigid Rod-coil Block Copolymers for Optimizing
Active layer Morphology and Enhancing Device
Performance in P3HT:PCBM Blends***

4.1. Introduction

We have shown the critical importance of the active layer morphology to optimize the final device performance of P3HT:PCBM blends. Among the different processing conditions affecting the morphology of P3HT:PCBM blends, thermal annealing of the P3HT:PCBM thin films was found to be one of the most decisive factor in reorganizing the P3HT and PCBM components, and thus increase the performance of P3HT:PCBM BHJ devices. However, the apparent effect of annealing in improving the device efficiency is not yet clearly identified: some relate this enhanced efficiency to the increase in P3HT's crystallinity as well as to the coarsening of the PCBM domains upon annealing^[1] leading to more efficient charge transport in the PV device. Consequently this chapter will be dedicated to the optimization of the BHJ active layer morphology for enhanced photovoltaic performance through macromolecular design instead of from external parameters. In order to achieve this goal, the classical phenomenon of microphase separation and self-assembly properties of block copolymers (usually, on a scale of exciton diffusion length) can be exploited to tailor the BHJ morphologies (*i.e.* self-structuring and phase separations) of P3HT:PCBM blends. As we have indicated in the literature review, the block copolymers are used either as self-structured active layer material (donor-*b*-acceptor copolymer or donor block copolymer blended with fullerene derivatives) or as compatibilizer/crystallization agent in BHJ systems. In this study, we used different semiflexible-flexible diblock copolymer architectures as additives to control the macro-phase segregation or to promote the crystallization of P3HT. As it has mentioned previously, the semiflexible rod-block in the rod-coil block copolymer system should have some chemical affinity with the donor part of the PV blend when used as additives. Based on this concept, we have synthesized different P3HT based block copolymers (listed in Figure 4.1), keeping in mind that each copolymer can bring a different functionality to the system mainly through the second coil block. The selection mechanism of the different coil blocks to functionalize the P3HT block and their effect on structure-performance relationship are presented in details in the subsequent sections.

Depending on the nature of the diblock copolymer additives, different types of device configurations (direct and inverted) were also employed.

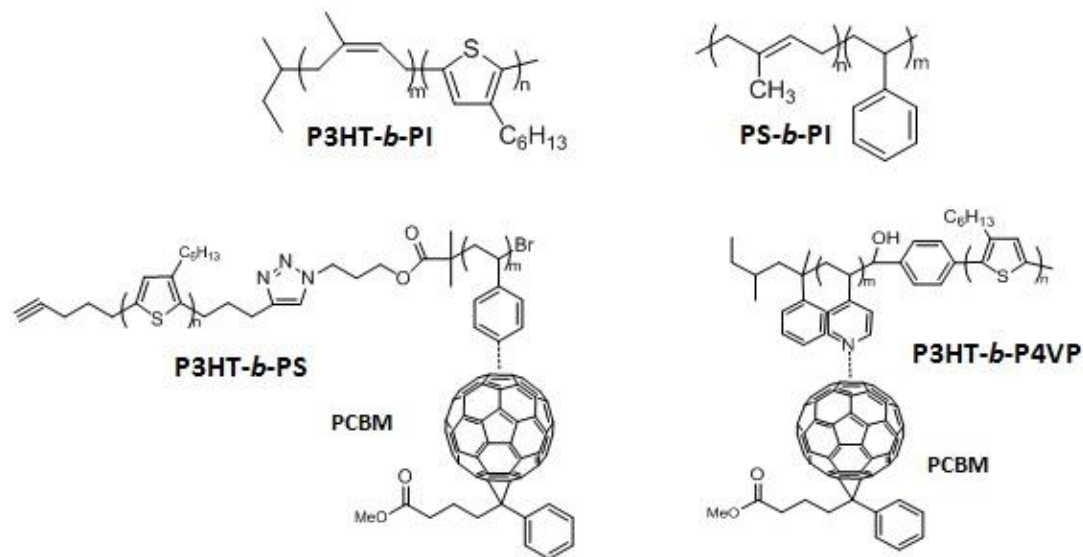


Figure 4.1: Chemical Structures of the different block copolymers employed as additives in P3HT:PCBM BHJ blends.

All these block copolymers have a chemical architecture consisting of a semi-conducting semi-flexible block (P3HT) covalently linked to an insulating coil block (PI, PS and P4VP). The question which remains through this macromolecular design is that the effect of these insulating blocks on the electronic properties. In order to investigate the effect of this insulating block, we have first incorporated an insulating coil-coil block copolymer, PS-*b*-PI, as additives into P3HT:PCBM BHJ photovoltaic devices.

4.2. Incorporation of Insulating Material into P3HT:PCBM blends and its effect on Device Performance: the case of PS-*b*-PI block copolymer

Though, the blend of insulating materials (like PS or PMMA, ...) with P3HT or the presence of a significant fraction of insulating block in P3HT (*i.e.* in the form of block copolymer) has shown little damage on the electrical conductivity of P3HT in FET device configurations,^[2-6] the addition of an insulating component into organic semiconductors is generally expected to degrade the electronic properties by reducing the electronic “contact” between molecules. The incorporation of insulating materials might have even more detrimental effect in organic BHJ photovoltaics than in FETs due to the rigorous microstructure requirements in the former case (such as; the donor and acceptor components has to mix intimately in order to retain a high interfacial area between them for an efficient exciton dissociation; each functional species should form an interpenetrating network in order to allow efficient charge transport to the relevant collection electrode).^[7]

In order to first establish whether acceptable electronic properties are possible to achieve in ternary blends of PCBM and P3HT, PV devices were prepared with active layers made from (P3HT-60 kg/mol:PCBM, 1:1 w/w): PS-*b*-PI (M_n of PS = 1.5 kg/mol and PI = 0.8 kg/mol) blend films, with the amount of PS-*b*-PI ranging from 0 to 10% as regards to P3HT:PCBM blends. Following the fabrication procedures described in chapter 7, active films of thicknesses up to ~ 100 nm were made and subsequently the devices were thermally annealed (after cathode deposition) at 165°C for 20 min. The conventional device architecture was utilized to fabricate all PV devices. The PV characteristics of such devices obtained for different weight fractions of PS-*b*-PI are presented in Figure 4.2.

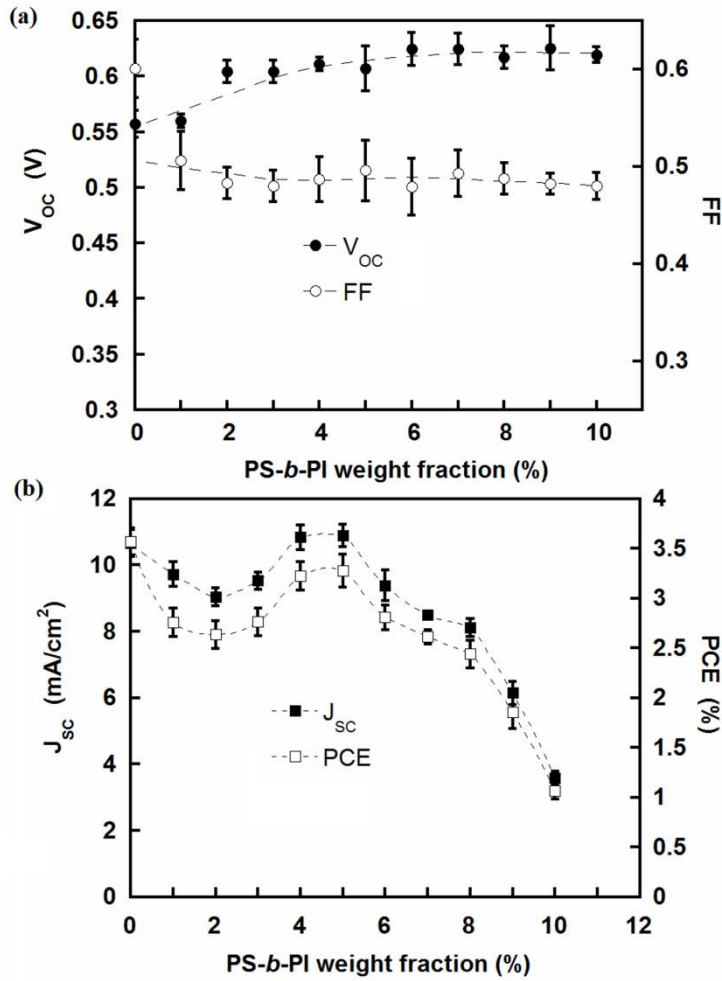


Figure 4.2: (a) V_{OC} and FF, (b) J_{SC} and PCE of P3HT:PCBM with different weight fractions of the PS-b-PI block copolymer (0 to 10% of the blend weight as a reference). The measurements have been performed after post annealing treatment at 165°C for 20 min. The error bars were calculated by averaging the results obtained over 8 devices. The broken lines are guides to the eye.

The incorporation of PS-*b*-PI leads to an increase of V_{OC} ; from 0.55 ± 0.1 V in the pristine device up to 0.63 ± 0.1 V for higher weight fractions of the PS-*b*-PI additive. A FF of 0.60 ± 0.1 is obtained for the pristine device, but considerably decreases when PS-*b*-PI is added to the system. However; the decrease in FF is not dependent on the weight fraction of PS-*b*-PI. A relatively constant value of 0.48 ± 0.1 was obtained for higher weight fractions of the block copolymer. The addition of PS-*b*-PI greatly affects the J_{SC} . A current density of 10.7 ± 0.4 mA/cm² was initially recorded for pristine devices before dropping to 9.0 ± 0.2 mA/cm² upon the addition of 2% PS-*b*-PI. For higher weight fractions, a

maximum value of $10.9 \pm 0.3 \text{ mA/cm}^2$ was obtained by adding 5% PS-*b*-PI. But further increase in copolymer weight ratio leads the J_{SC} to decrease again to reach a minimum value of 3.6 mA/cm^2 . The *PCE* follows exactly the same trend as the J_{SC} . A maximum photovoltaic efficiency of 3.3%, which is equivalent to the performance of the pristine device ($\sim 3.5\%$), was obtained for 5% PS-*b*-PI incorporation into P3HT:PCBM blends. This indeed indicates that the incorporation of a small weight fraction of block copolymer consisting of all insulating blocks into P3HT:PCBM BHJ yields to a power conversion efficiency equivalent to the pristine devices.

Morphological investigations have also been carried out using TEM to visualize the blend organization upon the addition of the PS-*b*-PI copolymer. The obtained images on the P3HT:PCBM:PS-*b*-PI ternary systems are shown in Figure 4.3. The pure blend film (Figure 4.3(a)) shows a uniform domain size distribution. More extended phase segregation upon the addition 3% PS-*b*-PI was clearly observed in Figure 4.3(b). Formation of PCBM-rich domains (dark regions) and crystalline P3HT-rich domains (light regions) distributed all over the blend were evidently identified. However, the addition of 5% PS-*b*-PI into the P3HT:PCBM leads to a relatively fine domain size distribution showing an intimate mixing between the P3HT and PCBM components and comparable with the pristine device morphology (Figure 4.3(c)). This morphology is lost when higher weight fractions of PS-*b*-PI are added to the system. Upon the incorporation of 10% PS-*b*-PI (Figure 4.3(d)), we observed a highly phase separated systems with larger sized P3HT and PCBM domains.

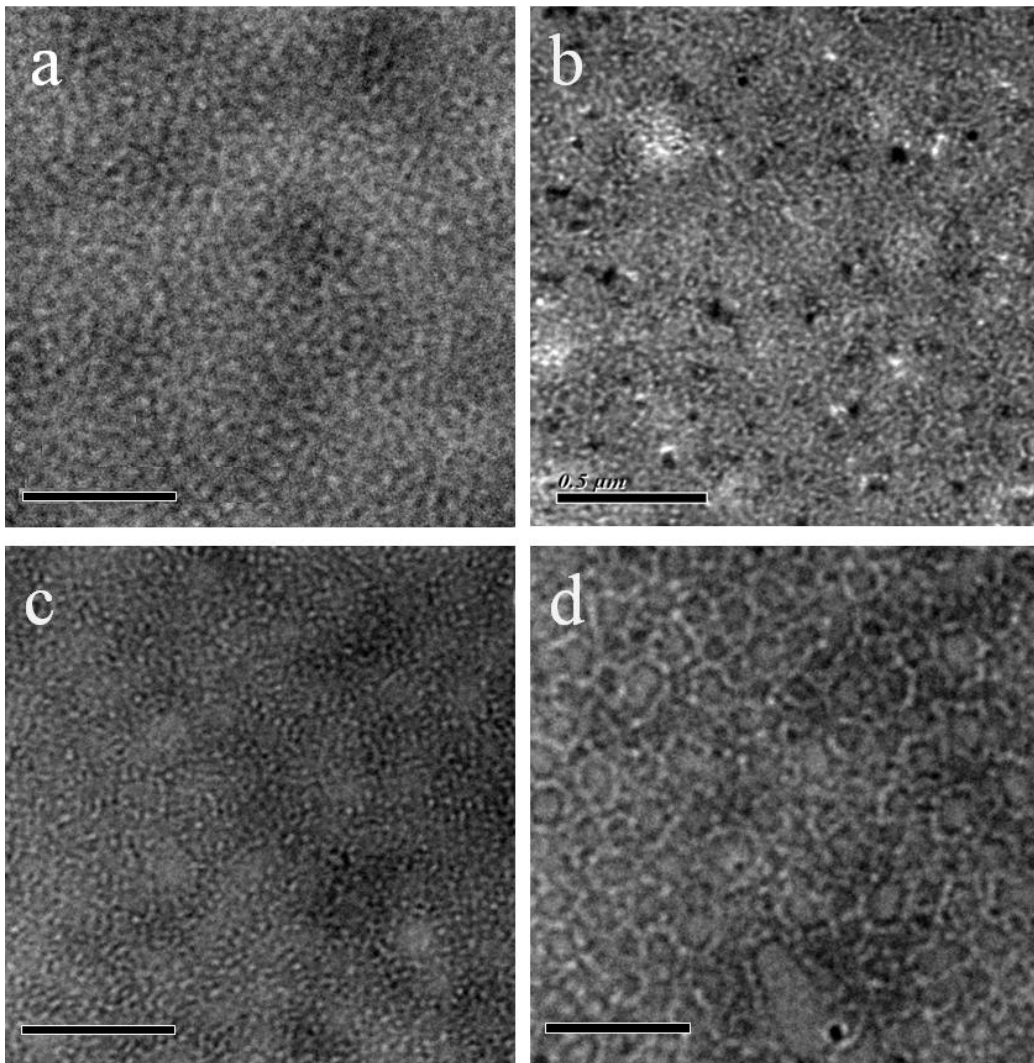


Figure 4.3: TEM images of P3HT:PCBM films with different weight fractions of PS-*b*-PI: (a) pristine (pure blend), (b) 3% (wt.) PS-*b*-PI, (c) 5% (wt.) PS-*b*-PI and (d) 10% (wt.) PS-*b*-PI. The images were taken from real PV devices.

The addition of PS-*b*-PI block copolymer into P3HT:PCBM BHJ devices has shown a large influence on PV characteristics, specifically on the values of the J_{SC} . These variations are related to the observed morphological changes resulting from the addition of different weight fractions of PS-*b*-PI into the P3HT:PCBM blend. The decrease in PCE, particularly for the case of higher weight fraction of PS-*b*-PI block copolymer, is inherent to the more extended phase separated domains which negatively affect the charge generation and transports properties the PV device. Factors other than transport,

such as the negative effect of the insulator on charge separation (acting as a trap site), might also contribute to the reduction in photocurrent generation at high insulator content.^[7]

To summarize, the incorporation of an optimum weight fraction of a low molecular weight of insulating PS-*b*-PI diblock copolymer into P3HT:PCBM system yields to a PCE equivalent to the pristine devices. The negative effect (*i.e.* on the charge dissociation and transport properties) expected from the incorporation of block copolymers containing all insulating blocks into P3HT:PCBM BHJ blends has to be compensated by favorable morphological changes in the P3HT:PCBM blends for an optimal PS-*b*-PI weight fraction as noticed on the TEM images. Thus the addition of a low weight fraction of insulating materials into P3HT:PCBM blends does not appear as a detrimental factor and could be even beneficial to the overall performance of the system if the functionality added through the coil block is well-thought. Consequently block copolymer designed with a semi-conducting block covalently linked with a "functional block" as regards to the BHJ mesostructure will be examined in the next sections.

4.3. P3HT-*b*-PI as P3HT Crystallization Agent and the Enhancement of Device Efficiency in P3HT:PCBM PV Blends

As described in the literature review (see Chapter 2), the incorporation of P3HT-based semiflexible rod-coil block copolymers into P3HT based BHJ in order to improve the stability of the thin film morphology upon thermal annealing has been reported in several studies.^[8-11] These studies show the ability of rod-coil block copolymers to modify the structure of the active layer and, thus, improve the device performance. However, the mechanism related to the structural modification brought by the coil block of P3HT-*b*-coil copolymers in OPV systems has still to be investigated. In the search of a P3HT-*b*-coil copolymer that can induce the optimum morphology in the archetypical P3HT:PCBM photoactive blend, we have explored herein the use of P3HT-*b*-polyisoprene. Polyisoprene, PI, is a low T_g polymer ($T_g = -71^\circ\text{C}$ for the PI-block studied herein) which means that at room temperature the PI chains are not frozen. Thus, we expect the PI block to increase the segmental

mobility of P3HT as well as favoring crystallization by promoting rearrangements of the P3HT chains (through π - π interactions) to their equilibrium state.^[12] In order to investigate the effect of the volume fraction of the PI block on the morphology and PV characteristics, we synthesized three P3HT-*b*-PI (using Grignard metathesis for the P3HT block coupled with living anionic polymerization for the PI block) with various PI molecular weights while keeping the P3HT molecular weight constant as shown in table 4.1.

Block copolymer	M _n P3HT (g/mol)	M _n PI (g/mol)
P3HT- <i>b</i> -PI	25 000	1900
P3HT- <i>b</i> -PI	25 000	8000
P3HT- <i>b</i> -PI	25 000	19000

Table 4.1: Macromolecular characteristics of the P3HT-*b*-PI block copolymers.

Before the block copolymer was incorporated into P3HT:PCBM blends, we have first investigated the morphological features of P3HT-*b*-PI films for the different volume fractions of the PI-block ranging from 0.08 (for PI = 1.9 kg/mol) to 0.47 (for PI = 19 kg/mol). The SFM images presented in Figure 4.4 shows dominant fibrillar nanostructures in all ranges of the volume fractions, indicating strong P3HT-P3HT interactions. However, the sizes of these P3HT fibers are modified with the volume fraction of the PI block. Smaller fibers is observed for low volume fraction of PI (Figure 4.4(a)) while at higher PI content the PI block inhibits strongly the formation of the P3HT fibrils.

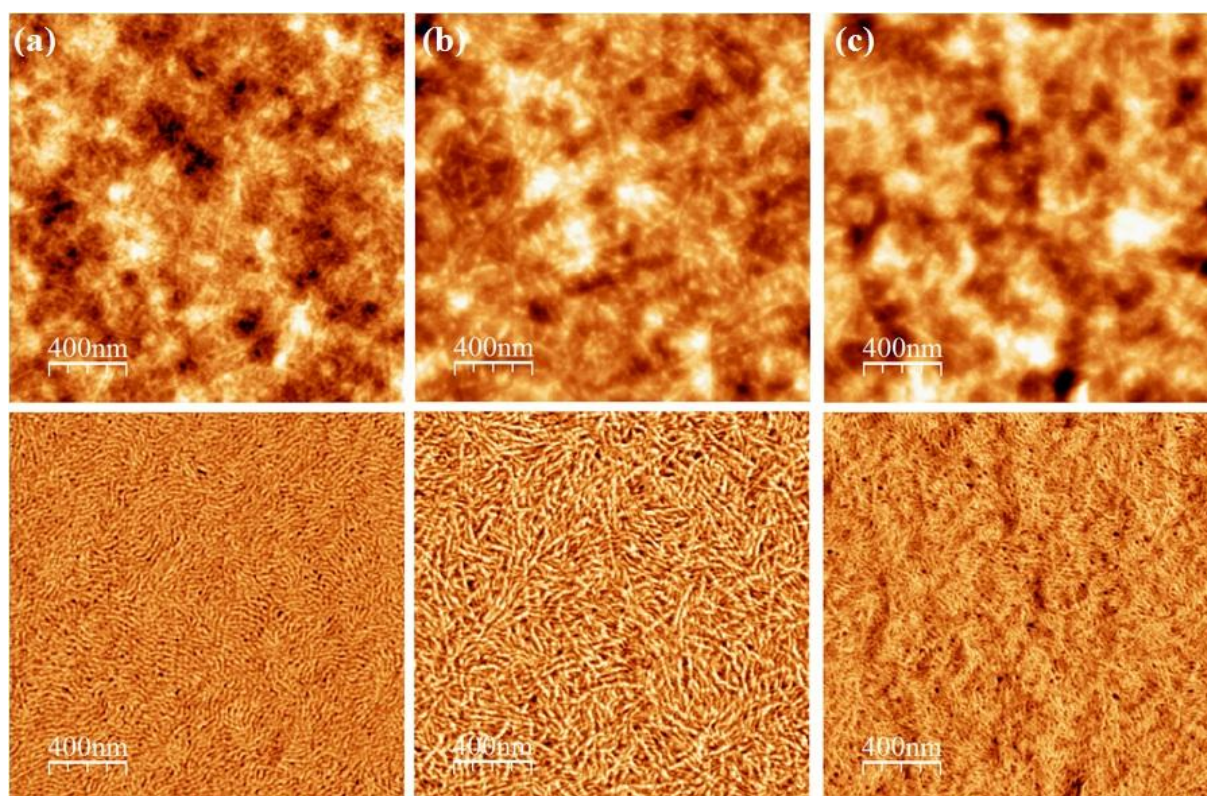


Figure 4.4: SFM topology (top) and corresponding phase (bottom) images of P3HT-*b*-PI. (a) PI = 1.9 kg/mol (b) PI = 8 kg/mol and (c) 19 kg/mol. In all cases the molecular weight of P3HT is 25 kg/mol. To keep the thickness of the film similar, the films were prepared by spin-casting from dichlorobenzene solution using similar film forming parameters. Prior to imaging, the films were first annealed at 165°C for 20 min.

4.3.1. Effect of P3HT-*b*-PI on Morphology and Structural Properties of P3HT:PCBM BHJ Photovoltaic Blends

The effect of the incorporation of P3HT-*b*-PI on the morphology of P3HT-60 kg/mol:PCBM (1:1 wt) films was studied for thermally annealed films. Optical Microscopy images of P3HT:PCBM blends with various weight fractions of the P3HT-*b*-PI copolymer (the M_n of P3HT and PI are 25 and 1.9 kg/mol, respectively) are presented in Figure 4.5. Again, needle-like structures are apparent in all images, indicating microscopic phase separations due to the crystallization process. These structures are three-dimensional PCBM aggregates formed by the diffusion of PCBM moieties upon annealing.

The diffusion process and growth mechanism of these PCBM aggregates have already been discussed in details in Chapter 3. However the number density of these PCBM needles decreases with the addition of the copolymer in the blend. Our data suggest that the presence of the copolymer in the blend inhibits the diffusion of PCBM moieties, which results in a reduced PCBM agglomeration.

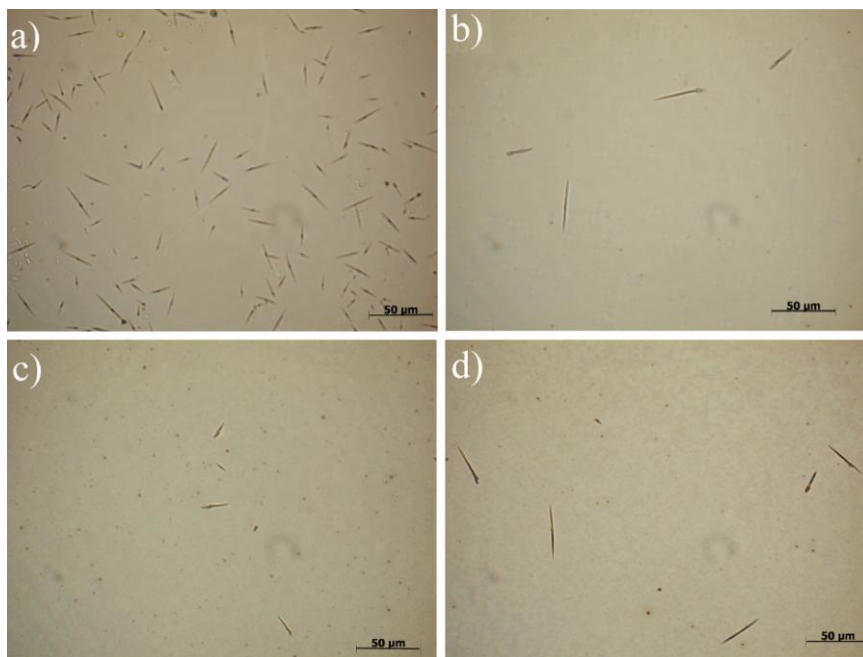


Figure 4.5: Optical microscopy images of annealed P3HT:PCBM blend films that contain (a) pristine P3HT:PCBM, (b) 3% (wt.), (c) 7% (wt.) and (d) 10% (wt.) of the P3HT-*b*-PI block copolymer. All films were annealed at 165°C for 20 min. The scale bar corresponds to 50 μm.

In order to get additional information on film organization, TEM characterization has been carried out. The TEM images of the P3HT:PCBM films that contain various weight fractions of P3HT-*b*-PI are presented in Figure 4.6. The formation of gray and darker domains is apparent in all films. In the literature it is well-stated that those “bright or gray” regions are related to P3HT crystallites.^{[13][14]} However, the size of those P3HT domains changes with the incorporation of P3HT-*b*-PI into the BHJ system. For example, upon the addition of 3% (wt.) and 7% (wt.) of P3HT-*b*-PI (Figures 4.6(b) and 3(c), respectively), very fine and uniform morphology is clearly resolved. However, these finer morphology were not kept for higher weight ratios of the copolymer. The 10% (wt.) copolymer-containing blend

exhibits higher phase contrast (formations of big aggregates) than the rest of the blends under study, suggesting a more extended phase separation. These all change in the size and uniformity of the films upon the block copolymer incorporation indicate that the crystallization characteristics of P3HT are modified.

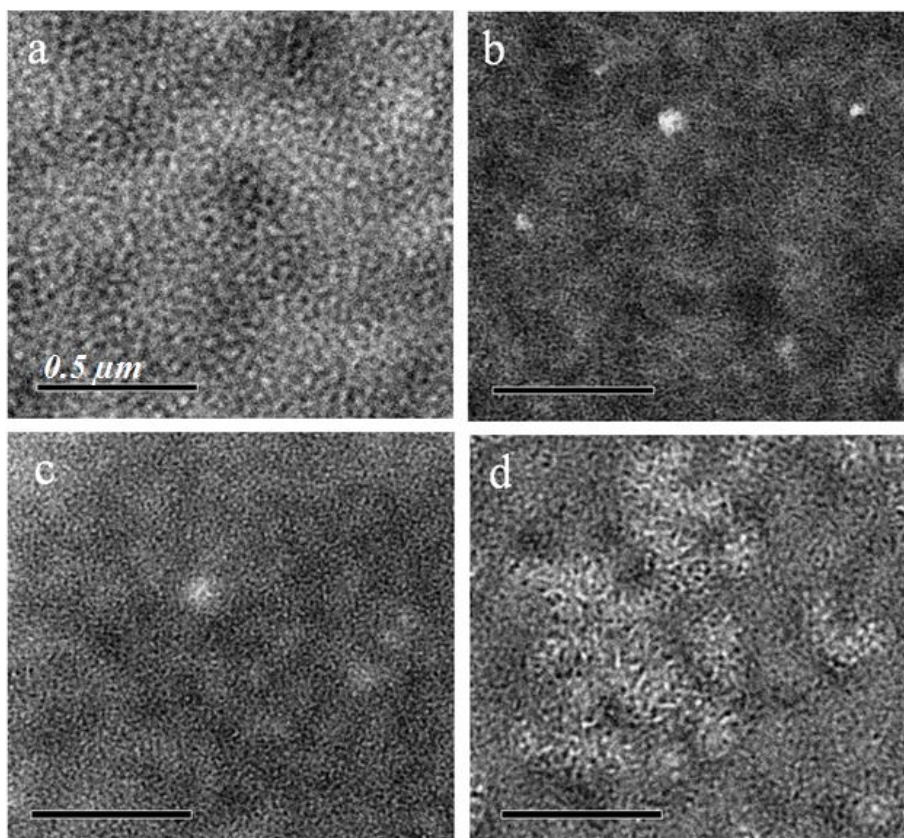


Figure 4.6: TEM images of P3HT:PCBM films containing various weight fractions of P3HT-*b*-PI block copolymer: (a) pristine P3HT:PCBM film, (b) 3% (wt.) (c) 7% (wt.) and (d) 10% (wt.) of the block copolymer. The images are taken from real PV devices.

To summarize, both imaging techniques employed herein suggest that phase separation between P3HT and PCBM is modified when an P3HT-*b*-PI copolymer is added into P3HT:PCBM blends leading to more homogeneous films – at either micro- or nanoscopic scale – are obtained.

In order to investigate the effect of the copolymer on the crystallization properties of P3HT we performed grazing incidence X-ray diffraction (GIXD) measurements. The 2-D diffraction images

recorded for the pure P3HT:PCBM and the 7% (wt.) P3HT-*b*-PI containing ternary blend films are presented in Figure 4.7(a). The reflections of P3HT are well-apparent and are mainly located along the out-of-plane axis (perpendicular to the substrate), due to the preferential orientation of the P3HT chains with edges-on. In order to compare the two samples we have plotted the radially averaged diffracted intensity with respect to the scattering vector q (Figure 4.7(b), upper panel), after subtraction of the PEDOT:PSS/ITO background scattering. The (100) reflection of P3HT, that is assigned to the repetition of the unit cell along the alkyl chain direction, is apparent at 0.38 \AA^{-1} and it is followed by two higher order reflections, namely the (200) and (300) diffraction peaks at 0.76 \AA^{-1} and 1.14 \AA^{-1} respectively. In spite of their feeble intensity and being superimposed on a broad amorphous peak, another two reflections are apparent in the radially averaged intensity plot; one at around 1.4 \AA^{-1} that corresponds to the diffraction by PCBM crystallites and one at 1.63 \AA^{-1} that corresponds to the π - π stacking of P3HT, related to the (010) P3HT reflection. We observe that the integrated intensities of the (100) P3HT reflection and the higher order reflections of the (h00) family increased upon P3HT-*b*-PI addition (Figure 4.7(b), upper layer), which is indicative of an increase in P3HT crystallinity. At the same time, the full width at half maximum of the (100) reflection is not affected, implying that the P3HT crystallite size is similar in the two cases. This suggests that the observed increase in crystallinity after the incorporation of the P3HT-*b*-PI diblock copolymer results from a number density increase of the nucleation centers within the films, rather than a thickening of the P3HT crystallites, pointing to the conclusion that the P3HT-*b*-PI chains act as nucleation agents. This observation is consistent with our initial hypothesis according to which the incorporation of a copolymer that comprises a low T_g coil-block in a low volume fraction in the copolymer, could plasticize P3HT, and thus promote its crystallization. On the other hand, the incorporation of P3HT-*b*-PI into the blend does not modify the diffraction of PCBM, suggesting that this particular copolymer does not directly interact with the PCBM moieties.

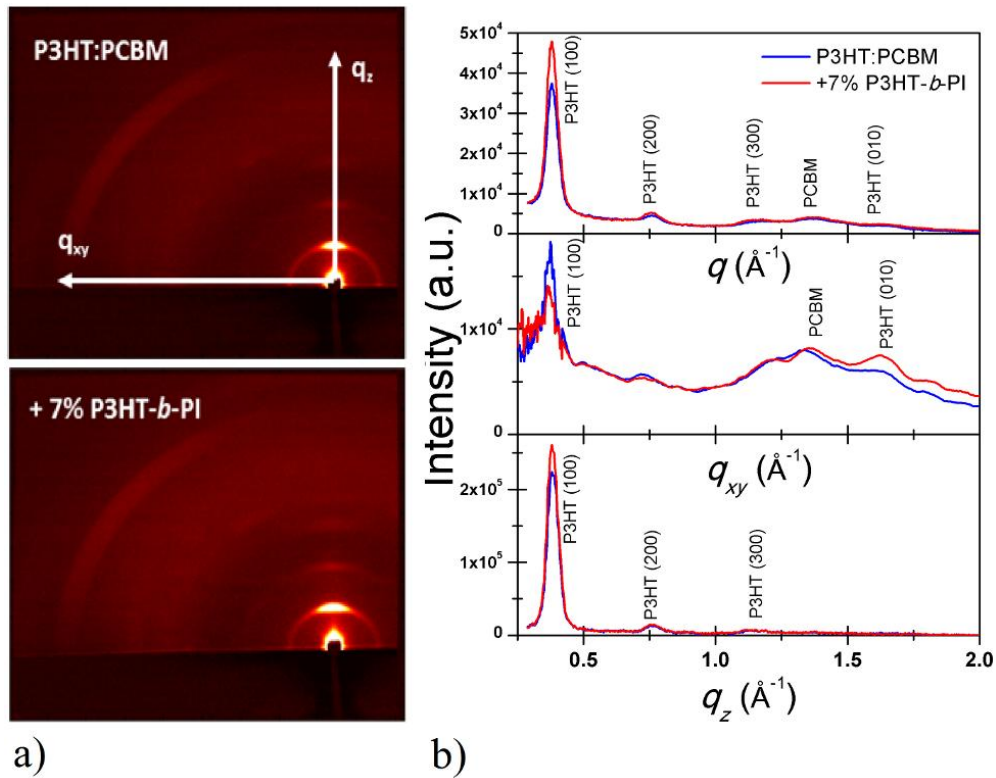


Figure 4.7: (a) 2-D GIXD images recorded for the pristine and the 7% (wt.) P3HT-b-PI containing P3HT:PCBM blend. Both correspond to annealed films, spin-coated on PEDOT:PSS/ITO substrates to mimic the device preparation conditions. (b) The corresponding 1-D radially averaged intensity plots with respect to the scattering vector q (upper part), and the two intensity line cuts, across the in-plane (q_{xy}) and out-of-plane (q_z) directions (intermediate and lower parts respectively). In all cases the contribution to scattering from the PEDOT:PSS/ITO substrate has been subtracted.

Next we have plotted the diffracted intensities parallel and normal to the plane of the film versus the in-plane, q_{xy} , and out-of-plane, q_z , components of the scattering vector (middle and lower panel in Figure 4.7(b), respectively). A decrease of the in-plane intensity of the (100) P3HT reflection is observed upon addition of the copolymer, concomitant with an increase of the out-of-plane intensity of the same peak. Additionally, the intensity of the π - π reflection of P3HT increases significantly in the in-plane diffraction pattern. All these remarks suggest that there is an increase of the population of the edge-on oriented P3HT crystallites when the copolymer is added to the blend.

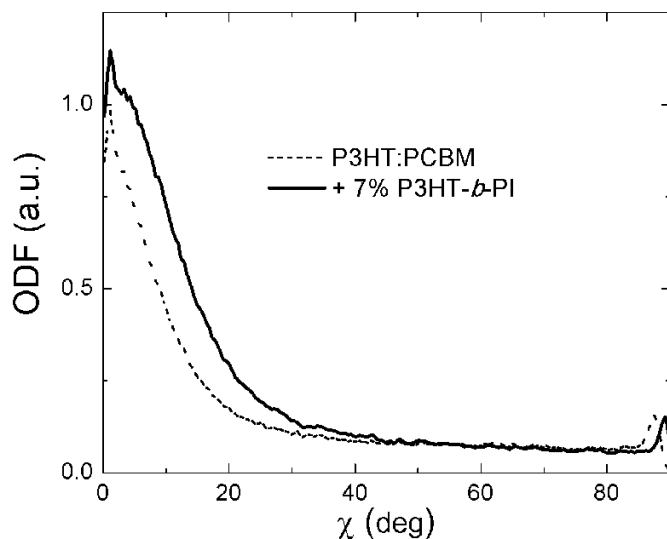


Figure 4.8: The orientation distribution function (ODF) of the (100) P3HT crystallites, derived by plotting the integrated intensity of the (100) peak as a function of the polar angle, χ . χ is defined with respect to the normal of the substrate.

Furthermore, a close look at the azimuthal width of the (100) P3HT reflection in the two GIXD images (Figure 4.7(a)) reveals a broader peak for the copolymer-containing film than the pristine P3HT:PCBM blend. This is better viewed by the orientation distribution function (ODF) derived by plotting the integrated intensity of the (100) peak as a function of the polar angle, χ , defined with respect to the normal to the substrate (Figure 4.8). Upon copolymer addition, the ODF becomes wider, which is indicative of a more pronounced misalignment of the P3HT crystallites in the copolymer containing film; the majority of the crystallites orient themselves with the alkyl chain direction forming an angle between 0° and 20° with respect to the normal to the substrate while for the pristine film the crystallites are better aligned with each other, covering a distribution range of $0^\circ - 10^\circ$. At the same time, both the integrated intensity and the intensity at the out-of-plane direction ($\chi = 0$) of the ODF increase when the copolymer is added, in agreement with the increases in crystallinity and in the number of edge-on oriented crystallites respectively. In summary the GIXD characterization revealed an increase in P3HT crystallinity upon addition of P3HT-*b*-PI due to an increase of the P3HT crystallites

population. Although the number of edge-on oriented crystallites is now increased, overall the P3HT crystallites exhibit a broader orientation distribution compared to the crystallites embedded in the pure P3HT:PCBM blend.

In order to provide solid evidence on the origin of the observed enhancement in the crystallinity of P3HT we performed DSC experiments. Figure 4.9 shows the crystallization peak of the pristine P3HT sample, the blend of P3HT with 7% (wt.) of the P3HT-*b*-PI copolymer and the pristine copolymer, as recorded upon cooling with a 5°C/min rate. As expected, the crystallization temperature of the pristine copolymer is lower than that of the homopolymer (197.1°C as opposed to 205.4°C) while the homopolymer:copolymer blend crystallizes a bit higher than the P3HT homopolymer, at 207.1°C. The shift of the crystallization peak towards higher temperatures suggests that P3HT-*b*-PI acts as an external nucleating agent, promoting, thus, the crystallization of P3HT, in accordance to our initial hypothesis and the GIXD results. However, one could advocate that the 2°C shift recorded is not significant enough. To further support our case we conducted complementary self-nucleation thermal experiments^[15-17] of P3HT, which are thoroughly described in the experimental method (see Chapter 7 of section 7.3). This methodology is based on the principle that the best nucleating agent for a polymer is the polymer it-self. Our data show that the self-nucleation of pure P3HT results in an increase of the crystallization temperature by 5.6°C, which is comparable to the increase observed upon copolymer addition. Therefore, we can safely conclude that P3HT-*b*-PI promotes P3HT crystallization through heterogeneous nucleation; as external nucleating agents are added in the blend, the number of nuclei increases resulting in the increased number density of P3HT crystallites suggested by the GIXD data. Going one step further, we calculate the nucleation efficiency of the P3HT-*b*-PI copolymer in P3HT by comparing the crystallization temperature shifts between the copolymer-induced nucleation and P3HT self-nucleation (see Chapter 7). It follows that the nucleation efficiency of P3HT-*b*-PI in P3HT is 31% when 7% (wt.) of the copolymer is added in P3HT – the

efficiency being 100% for the best nucleating agent, *i.e.* P3HT itself. This implies that despite the low amount of copolymer added, its impact in P3HT crystallization is significant.

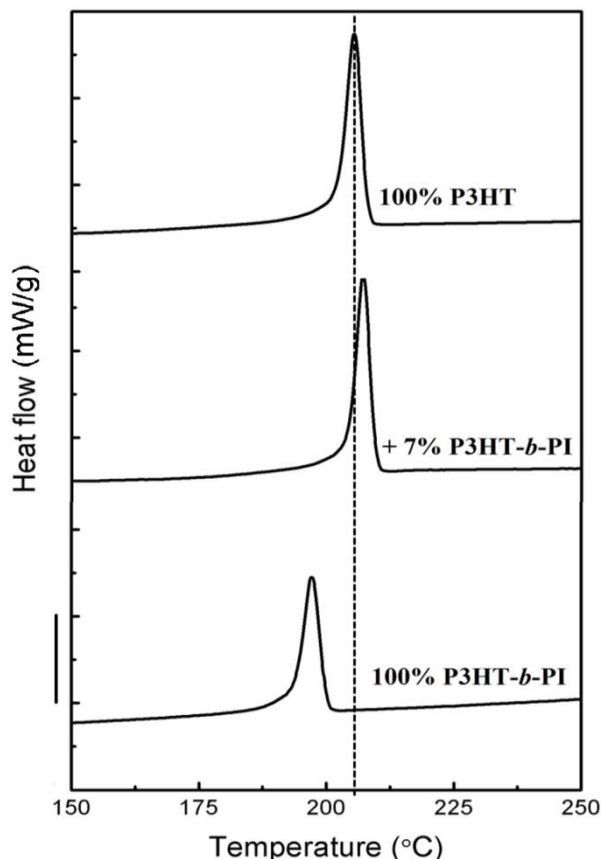


Figure 4.9: DSC cooling scans of pristine P3HT, P3HT:P3HT-*b*-PI blend and pristine P3HT-*b*-PI. The segmented vertical line indicates the deviation from the standard peak crystallization temperature of P3HT. The vertical line shown on the left side of the graph represents the scale of the exothermic enthalpy changes (it represents 1 mW/g).

It is noted that the increase in P3HT crystallinity is also evident in the UV-vis absorption spectra that were collected for the active layers that comprise various concentrations of P3HT-*b*-PI within the P3HT:PCBM matrix (Figure 4.10). The spectra presented are normalized with respect to the 0-1 vibronic peak, which is located at 550 nm, in accordance with recent reports.^{[18][19]} In all copolymer-containing films the normalized intensity of the 0-0 vibronic peak at 605 nm is higher than that of the

pristine P3HT:PCBM blend. This is indicative of an enhanced intrachain ordering and, consequently, of enhanced P3HT crystallinity when the P3HT-*b*-PI copolymer is participating in the blend.

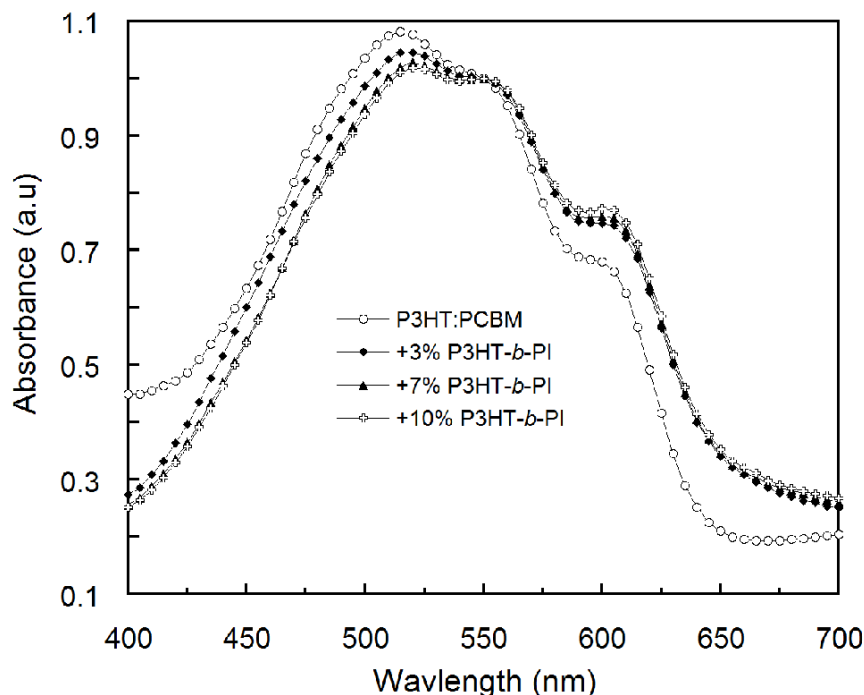


Figure 4.10: UV-vis absorption data acquired for pristine P3HT:PCBM as well as different weight fraction P3HT-*b*-PI block copolymer containing blends. The spectra are normalized with respect to the 550 nm peak. All films were annealed at 165°C for 20 min.

Both GIXD and UV-vis provide unambiguous data on the increased crystallinity of P3HT upon copolymer addition. Based on these results we can now justify the formation of smaller PCBM aggregates observed in the Optical Microscopy images. As already stated, the enhanced crystallization of P3HT results an increased demixing among film components; PCBM is depleted from the film areas that are filled by P3HT crystallites. Nonetheless, the fact that the increase of crystallinity is driven by an increase in the crystallites number density, coupled with the mass conservation of P3HT and PCBM in the films, implies that the spaces available for PCBM aggregation are of numerically more, but smaller in size. Consequently, the size of the PCBM aggregates apparent in the microscopy images decreases with increasing number of crystallites.

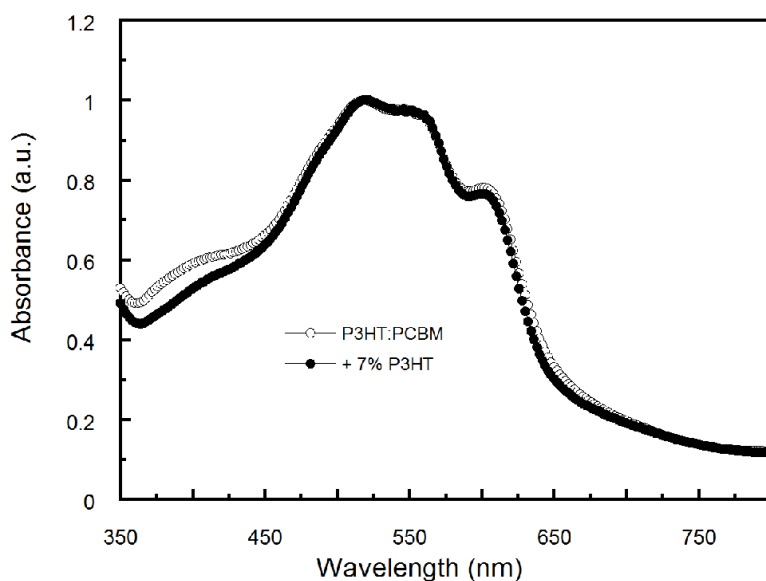


Figure 4.11: UV-Vis absorption spectra of pristine P3HT:PCBM blend and films containing 7 wt% of a P3HT homopolymer with M_n equal to that of the P3HT-block of the copolymer (25 kg.mol^{-1}). The spectra are normalized with respect to the 515 nm intensity peak.

To determine whether the morphology-driven changes in the optical properties of P3HT in the blend are related to the nanostructuring effect of the copolymer or to the addition of an extra quantity of P3HT, namely the P3HT block, we carried out UV-vis spectroscopy measurements on P3HT:PCBM films containing a short P3HT homopolymer, with M_n equal to that of the P3HT in block copolymer. The addition of an equivalent weight fraction of short homopolymer to the blend shows no change in absorption (see Figure 4.11). Thus, we conclude that it is the P3HT-*b*-PI copolymer itself that is responsible for inducing enhanced packing and crystallization of P3HT in the blend and not just the P3HT block that it contains.

To complete the structural characterization, neutron reflectometry was used to determine the composition of the blend films as a function of depth. This technique allows us to visualize the influence of the addition of block copolymer on the P3HT:PCBM composition along the normal to the substrate. The P3HT:PCBM films were casted onto PEDOT:PSS layers, to mimic the procedure followed for the fabrication of conventional organic photovoltaics. Figure 4.12(a) shows the reflectivity curves

recorded from these measurements, ($Rq_z^4 = f(q_z)$, where q_z is the scattering vector along the normal to the film) for two films, the pristine P3HT:PCBM blend and the blend that contains 7% (wt.) of P3HT-*b*-PI. In order to estimate the scattering length density (SLD) profile as a function of the sample thickness, we used similar techniques and procedures to that of the previous work shown in Chapter 3 of section 3.5. We first modeled the samples with a series of layers with interfacial layer roughness, and employed the MOTOFIT package^[20], to calculate the corresponding reflectivity curves and fit the experimental data. The best fits of the two blend films were obtained by using a four-layer model that consists of a native SiO₂ layer (thickness ~0.8 nm), a PEDOT:PSS layer (thickness ~47 nm) and two layers that describe the polymeric blend. Figure 4.12(b) shows the SLD profiles derived for the two films. We see that in both samples the active layer is composed of two stacks: a 7-8 nm thick layer with a high SLD value (around $2.7 \times 10^{-6} \text{ \AA}^{-2}$) next to the film/PEDOT:PSS interface followed by a thicker one (~50 nm) with a SLD value close to $2 \times 10^{-6} \text{ \AA}^{-2}$. Given that P3HT and PCBM have SLDs of $0.67 \times 10^{-6} \text{ \AA}^{-2}$ and $4.34 \times 10^{-6} \text{ \AA}^{-2}$ respectively (calculated using the NIST database^[21] and respective mass densities of 1.1 and 1.5 g/cm³),^{[22][23]} we conclude that these two layers correspond to a PCBM-rich layer next to the PEDOT:PSS film and a homogeneously mixed P3HT:PCBM:P3HT-*b*-PI layer at the intermediate and top (surface) regions of the polymeric blends. Thus, the NR results show significant stratification along the P3HT:PCBM blends. The origin of this stratification and its implications in device performance has been presented in Chapter 3 (see section 3.5). More importantly, the reflectivity results suggest that both films exhibit similar depth profiles. Consequently the copolymer addition does not affect the vertical stratification within the P3HT:PCBM:P3HT-*b*-PI heterojunctions.

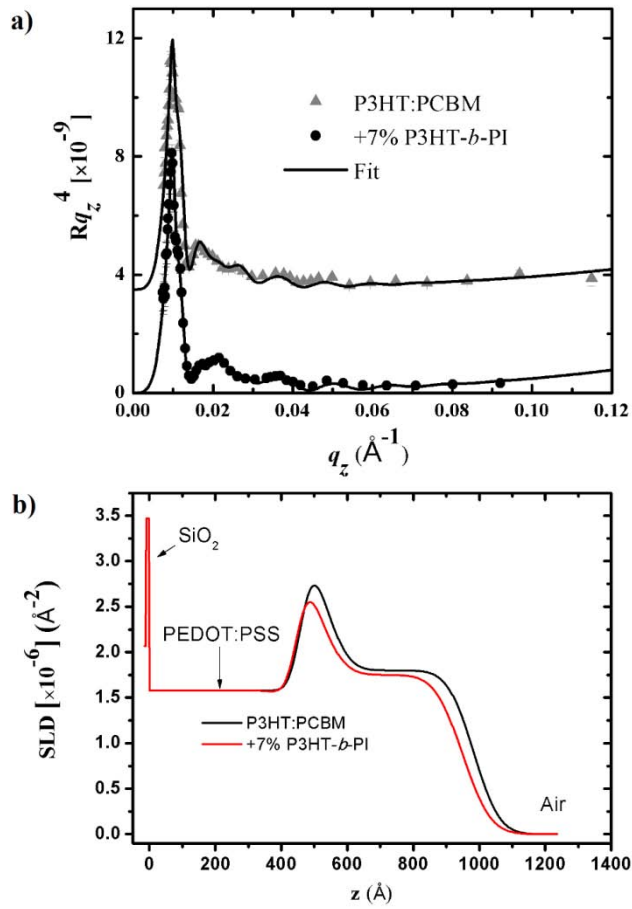


Figure 4.12: (a) The absolute neutron reflectivity curves of the pristine P3HT:PCBM and the 7% (wt.) P3HT-*b*-PI containing films. The P3HT:PCBM curve has been vertically shifted for clarity. The films were casted on PEDOT:PSS coated silicon wafers and subsequently annealed at 165°C for 20 min. The best fits are presented as well (solid lines). (b) The corresponding SLD profiles determined from the fitted reflectivity curves.

4.3.2. Effect of P3HT-*b*-PI on the Performance of P3HT:PCBM BHJ Photovoltaic cells

Finally, the well-characterized P3HT:PCBM:P3HT-*b*-PI films were incorporated in photovoltaic devices (*i.e.* conventional device architecture) and the influence of the copolymer addition on device performance has been investigated. Eight devices have been studied for each case, fabricated and characterized following the protocols described on Chapter 7. As shown in Figure 4.13 (a) the incorporation of the block copolymer significantly affects J_{SC} . Upon copolymer addition, J_{SC} increases from 10.6 ± 0.2 mA/cm² for the pristine device to a maximum value of 13.0 ± 0.5 mA/cm² when 7% (wt.) of the copolymer is added and then decreases, reaching 10.1 ± 1.0 mA/cm² for the 10% (wt.) copolymer-containing blend. The V_{oc} and the FF are 0.56 ± 0.01 V and 0.58 ± 0.03 respectively, and are independent of the copolymer concentration in the active layers (Figure 4.13(b)). Therefore, the power conversion efficiency follows the trend of J_{SC} . The pristine P3HT:PCBM device has a PCE of $3.5 \pm 0.2\%$ that increases to $4.5 \pm 0.1\%$ for the 7% (wt.) blend and then decreases to $3.0 \pm 0.3\%$ when 10% (wt.) of the copolymer is added. The current density – voltage curves obtained for the pristine and the 7% (wt.) copolymer-containing devices are shown in Figure 4.13(c). $IPCE$ measurements were carried out in order to complement the device characterization. As shown in Figure 4.14, when 7% (wt.) of the copolymer is added in the BHJ, the $IPCE$ increases which indicates that more charges are generated, in agreement with the observed increase in J_{SC} .

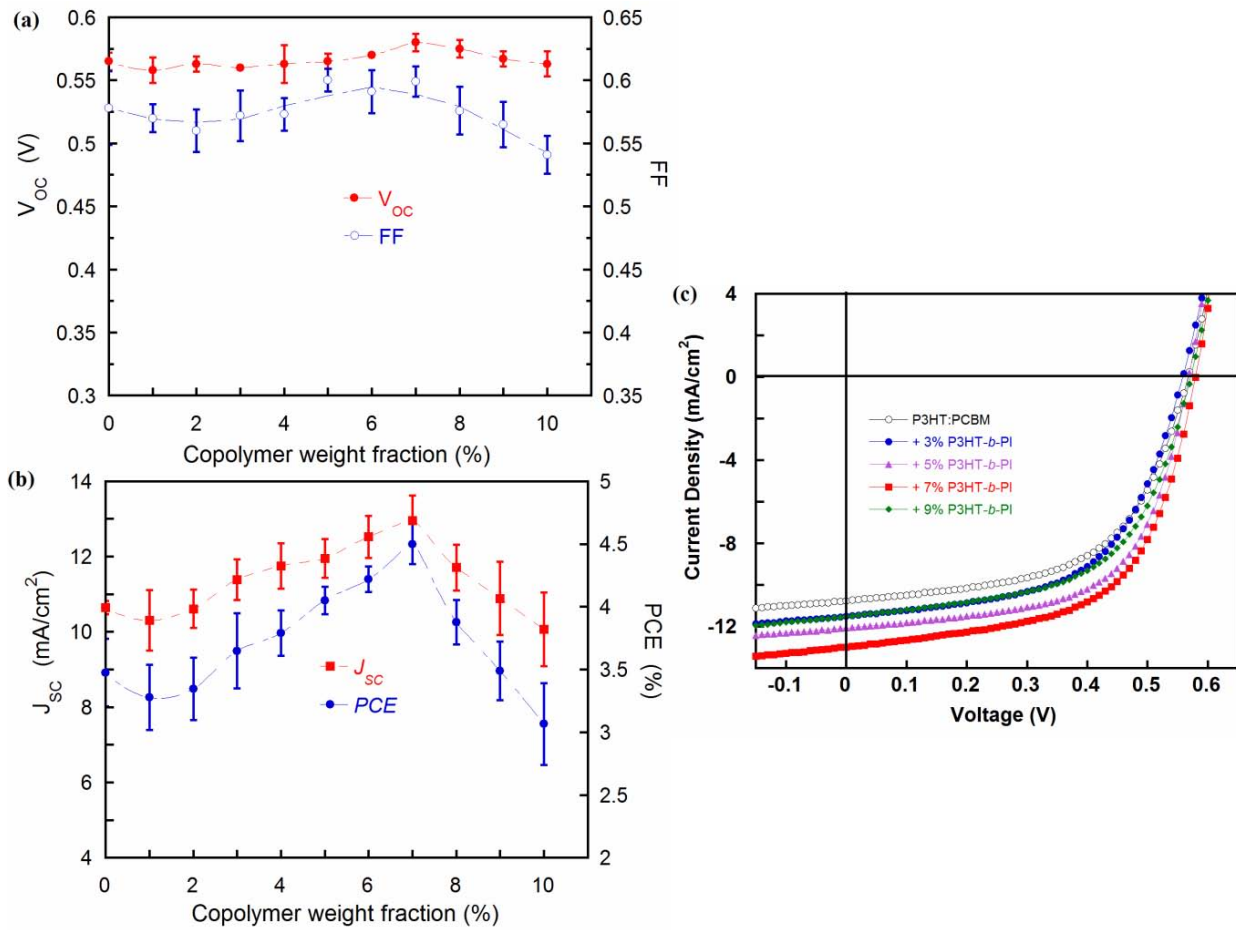


Figure 4.13: Device characteristics of the P3HT:PCBM:P3HT-b-PI BHJ organic solar cells with respect the added copolymer concentration: (a) J_{SC} and PCE and (b) V_{OC} and FF (c) Current density - voltage curves shown for some of the best devices as a function of P3HT-b-PI weight ratios. The measurements have been performed after post annealing treatment at 165°C for 20 min. The error bars were calculated by averaging the results obtained over 8 devices. The broken lines are guides to the eye.

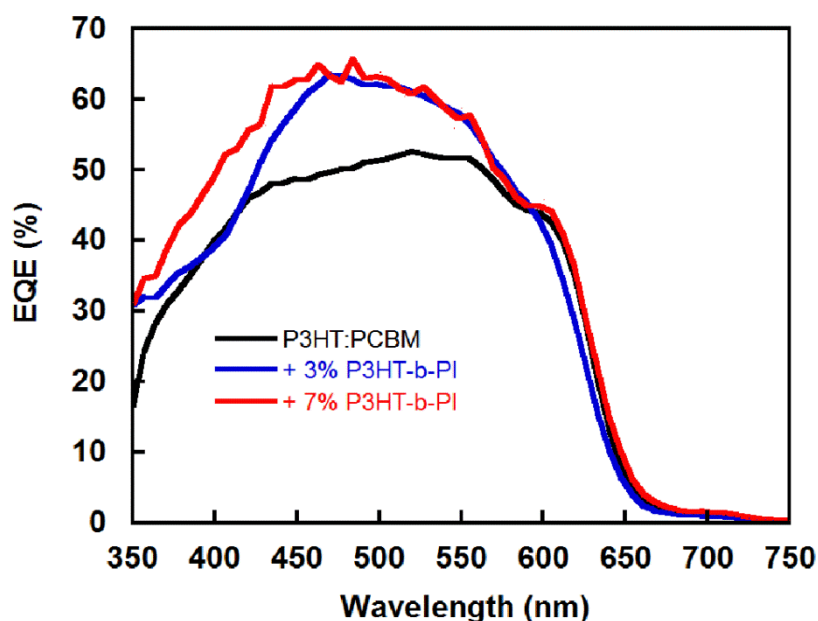


Figure 4.14: IPCE spectra of the pristine P3HT:PCBM and P3HT-b-PI containing blends.

Control experiments have been performed to test the role of the semiflexible rod-coil copolymer in device performance. Similarly as in UV-vis experiments, the block copolymer was substituted in the blend by a short P3HT homopolymer (with M_n equal to that of the P3HT-block in the copolymer) and the results showed that the devices that comprise 7% (wt.) of the P3HT homopolymer have similar $J-V$ curves to those obtained for the pristine devices (Figure 4.15). The small deviations in the J_{SC} and PCE values obtained for the two sets of samples are within the experimental error bars. These results confirm the crucial role played by the semiflexible-coil block copolymer in the enhanced performance of the copolymer-containing BHJs.

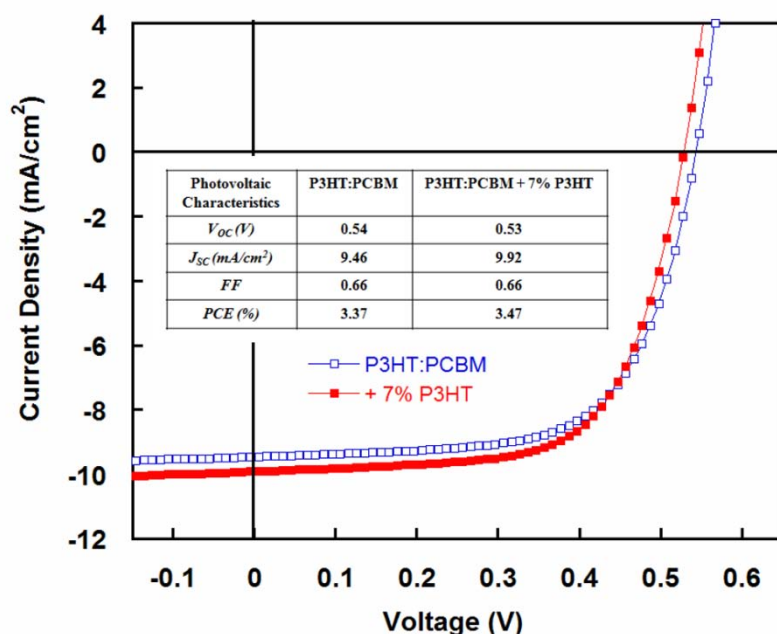


Figure 4.15: Current density - voltage curves and the resulting device performance characteristics obtained for the P3HT:PCBM BHJ and the one containing 7 wt% of a P3HT homopolymer, with M_n equal to that of the P3HT-block of the copolymer ($25 \text{ kg}\cdot\text{mol}^{-1}$). The devices were post-annealed at 165°C for 20 min.

We have also investigated the effect of the PI block molecular weight within the P3HT-*b*-PI in the P3HT:PCBM BHJ photovoltaic blends. We increased the PI molecular weight by a factor of 10 and kept the size of the P3HT block constant in the block copolymer. As it is indicated in Figure 4.16(a), the PCE is highly affected by the PI length. Lower PV performance was achieved for higher PI molecular weight (19 kg/mol) as compared to the pristine device. The reason for the observed difference in PV characteristics could be related either to the morphology or to the highest weight fraction of insulating material incorporated in the PV blend. Further addition of the P3HT-*b*-PI copolymer likely introduces too much insulating PI component in the P3HT:PCBM blend, thereby degrading the device performance.

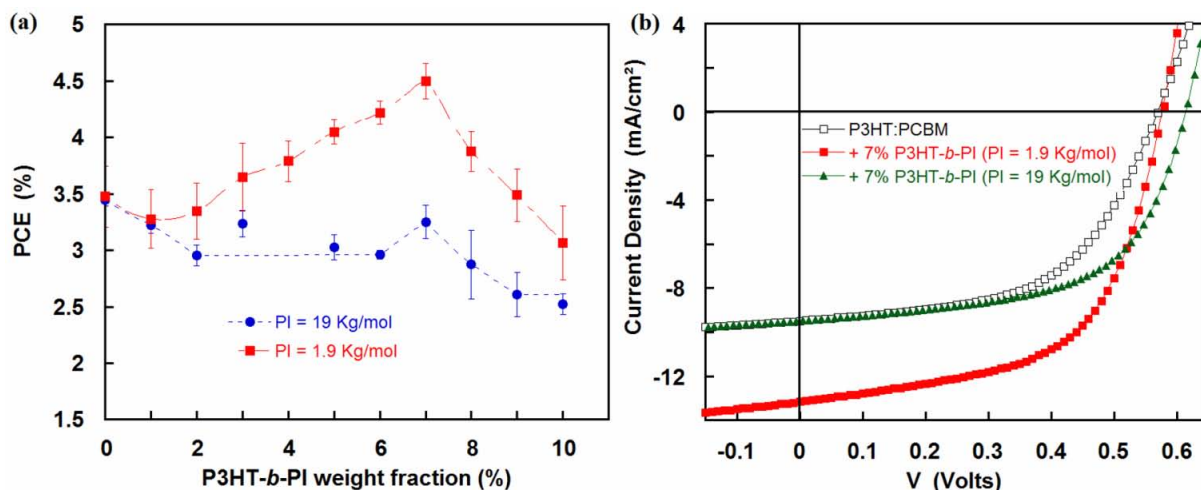


Figure 4.16: Device characteristics of the P3HT:PCBM:P3HT-*b*-PI BHJ organic solar cells with respect to the copolymer concentration and PI length. (a) Average PCE (%) and (b) The Current density - voltage curves of representing the best devices. The error bars were calculated by averaging the results obtained over 8 devices. The broken lines are guides to the eye.

To summarize, the evolution of the photovoltaic characteristics is inherent to the morphology of the P3HT:PCBM BHJ upon the P3HT-*b*-PI addition. As highlighted before, GIXD measurements showed that the crystallinity of P3HT is enhanced upon copolymer addition, due to the nucleation effect of the P3HT-*b*-PI chains in the blend. An increase in P3HT crystallinity is highly desirable since it is generally accepted to improve device performance. When crystallinity is enhanced, light absorption increases and consequently more excitons are formed. On top of that, it has been recently reported that charge-carrier mobility increases when crystallinity is increased^[24] which is also favorable for device performance. Concomitantly, the formation of more P3HT crystallites when P3HT-*b*-PI is added offers more P3HT/PCBM interfaces, which results in more efficient exciton dissociation at the domain interfaces in the copolymer-containing BHJs and, consequently, an increased charge generation, in consistency with the *IPCE* measurements. Additionally, we consider that charge transport is promoted in the copolymer-containing blends. Indeed the high M_n of the P3HT homopolymer that allows the participation of one chain in multiple crystallites, coupled with the increased number of P3HT

crystallites in these blends, can improve charge transport to the electrodes through the increase of connectivity between the crystallites.^[25] Moreover, the improved intrachain ordering of the P3HT chains as determined from the UV-vis data signifies that fewer defects exist in the P3HT crystallites and that the planarity of the polymer chains is improved, which also favors efficient charge transport. Given that holes mobility in P3HT is enhanced along the π - π direction,^[26] the orientation of the P3HT crystallites with respect to the substrate can also affect charge carrier transport with the face-on orientation being optimal for photovoltaic applications. Our results point to an increase in the number of edge-on oriented crystallites which is therefore, not desirable. However, the overall increase of the orientational distribution of the crystallites that is observed could compensate for the increase in edge-on oriented crystallites. This broader orientational distribution could also contribute to the improved charge transport in the device. Finally, the optimized phase separation that occurs when small quantities of P3HT-*b*-PI are added in the P3HT:PCBM blend – as apparent in the optical microscopy and SFM images – is indicative of a less extended domain coarsening and is reported to be favorable for improved device performance.^{[27][28]} In accordance with these observations, the incorporation of P3HT-*b*-PI semiflexible-coil block copolymer in the active layer results in improved J_{sc} and enhanced device efficiency leading to a maximum *PCE* of $4.5 \pm 0.1\%$ for the 7% (wt.) P3HT-*b*-PI containing blend. We speculate that the decrease in efficiency observed for copolymer concentrations higher than 7% (wt.) is due to the increased phase separation shown in the TEM phase images of the 10% (wt.) film.

4.4. Diblock Copolymers as Interfacial compatibilizers and Nanostructuring agents - A Trend towards Fabricating Annealing-free Photovoltaic Devices

In this study, we utilize two diblock copolymer systems, as interfacial compatibilizers to control the morphology of P3HT:PCBM blend, thereby aiming at the improvement of the power-conversion efficiency. As it has been indicated in the literature review, this methodology is inspired by the improved compatibility obtained in common A:B polymer blends when an A-B block copolymer is

added to the system.^[29] Consequently, we synthesized P3HT-*b*-PS and P3HT-*b*-P4VP diblock copolymers and exploited them as additives in P3HT:PCBM blends. Because of the similarities in the chemical structure of P3HT-*b*-PS diblock copolymer to the P3HT:PCBM blend (*i.e.* P3HT of the block copolymer with the homopolymer of P3HT and the PS block with PCBM), significant interactions between the diblock copolymer and the P3HT:PCBM blend are expected. The same is true for the P3HT:PCBM:P3HT-*b*-P4VP ternary blends. Due to the chemical affinity between the P4VP block and PCBM moieties, the P4VP coil block acts as a molecular dispersant of PCBM through the non-covalent interactions.^{[30][31]} Therefore, it is anticipated that P3HT-*b*-PS and P3HT-*b*-P4VP can act as interfacial compatibilizers between the P3HT and PCBM phases through their localization at the P3HT-PCBM interface. These favorable interactions could thus facilitate a morphological optimization of the P3HT:PCBM blend as well as stabilize the system against the “destructive” thermal phase segregation.^[32] The efficient charge transport that is also observed in P3HT-*b*-PS diblock copolymer in FET configurations^{[33][34]} is also another source of inspiration^[34] to incorporate P3HT-*b*-PS block copolymer as additives in a P3HT:PCBM blends. In this work the effects of different amounts of P3HT-*b*-PS and P3HT-*b*-P4VP block copolymers were studied and correlated to solar cell performance.

4.4.1. P3HT-*b*-PS as Interfacial Compatibilizer in P3HT:PCBM blends

The PV devices were prepared following procedures indicated in Chapter 7. The size of the P3HT and PS block used in this study is 37 kg/mol and 1.9 kg/mol. The SFM images (both topography and phase) depicted in Figure 4.17 show the different morphological features of P3HT (60kg/mol):PCBM films as regard to the incorporated weight fraction of block copolymer. As we can see from the phase images, P3HT fibers are observed in the pristine device (Figure 4.17(a)) due to the P3HT crystallization. However, the length of these P3HT fibrils is increased with the incorporation of P3HT-*b*-PS (Figure 4.17(b) and (c)). Upon the addition of 4% P3HT-*b*-PS (Figure 4.17 (b)), a fibrillar network with length scale up to ~500 nm and an interfacial width (spatial length) of about ~20 nm were observed. However, further increasing in the weight fractions of the block copolymer into

P3HT:PCBM (Figure 4.17(d)) leads to the disruption of the fibrillar morphology (*i.e.* the P3HT fibrils are lost). The addition of higher weight fractions of P3HT-*b*-PS may favor the strong interactions between PCBM and the PS segment and thus the block copolymer may lead to the formation of large segregated PCBM clusters.^[32] However, this is a plain explanation and further investigation is needed to understand the formation of the different morphological characteristics.

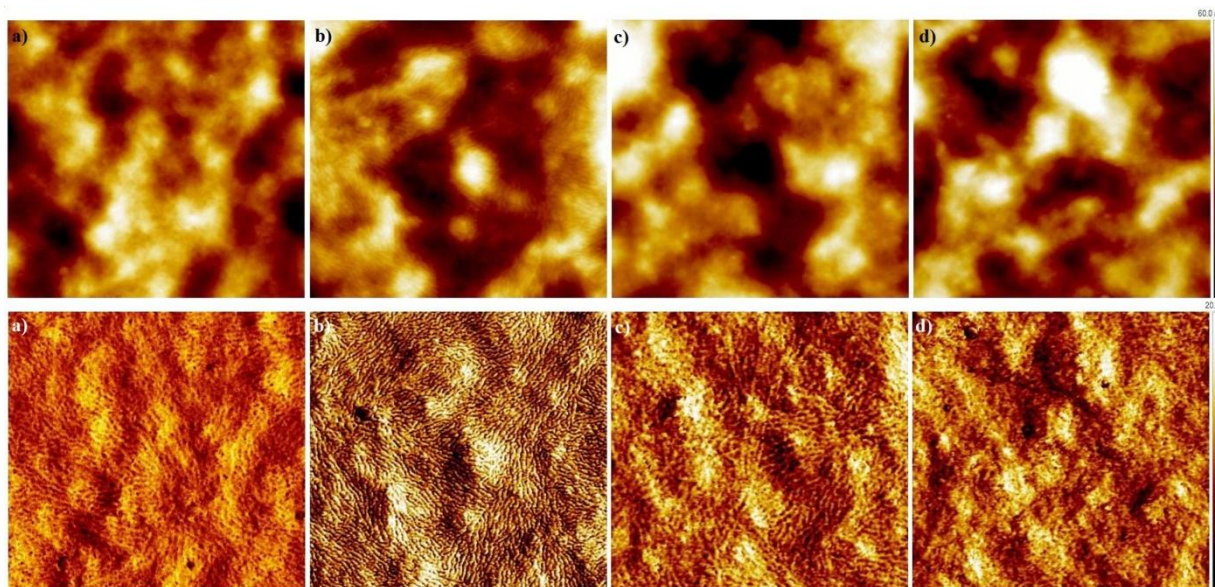


Figure 4.17: $2 \times 2 \mu\text{m}^2$ SFM topography (top) and corresponding phase (bottom) images of P3HT:PCBM:PS-*b*-PI films: (a) Pristine blend (without copolymer), (b) 2% (wt.) P3HT-*b*-PS, (c) 4% (wt.) P3HT-*b*-PS and (d) 8% (wt.) P3HT-*b*-PS. The images are taken from real PV devices.

Morphological characterizations have also been performed through TEM. The morphological characteristics deduced from TEM are presented in Figure 4.18. For the pure blend, both fibrillar P3HT (which are relatively bright) and aggregates of PCBM-rich domains (dark regions) are observed. As P3HT-*b*-PS is added to the system; quite homogeneously distributed P3HT and PCBM domains are observed at all weight fraction of the block copolymer, contrary to the SFM images indicated above where high phase contrast was observed in most block copolymer containing blends.

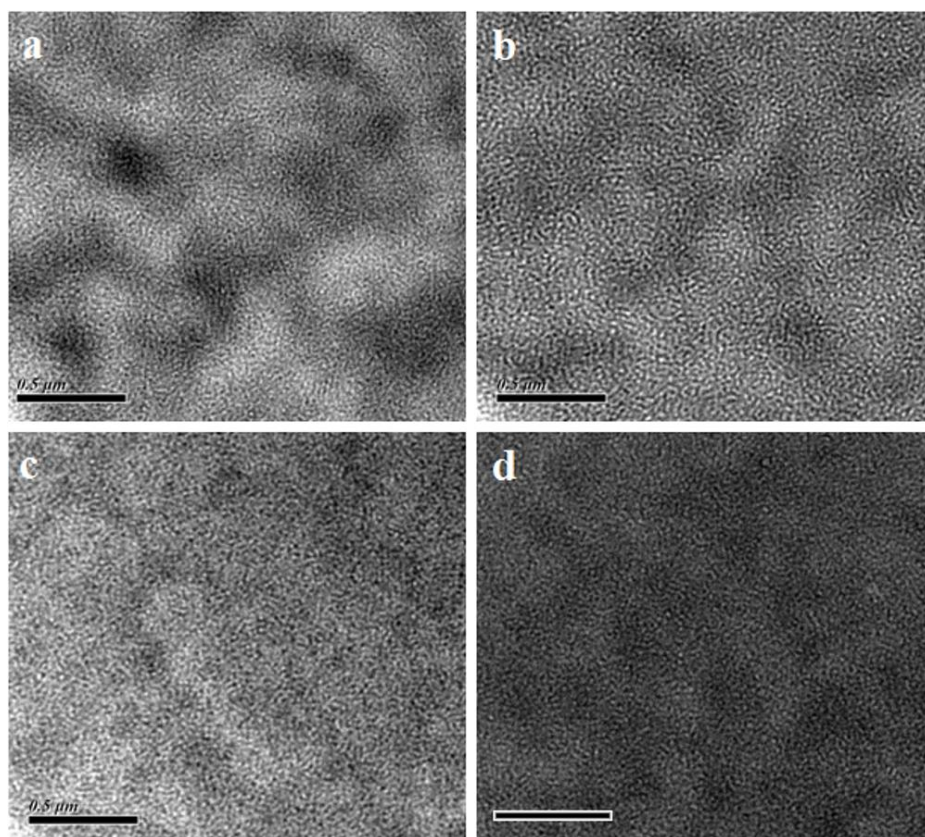


Figure 4.18: TEM images of P3HT:PCBM films containing various weight fractions of P3HT-*b*-PS block copolymer: (a) Pristine blend (without copolymer), (b) 2% (wt.) P3HT-*b*-PS, (c) 4% (wt.) P3HT-*b*-PS, and (d) 8% (wt.) P3HT-*b*-PS. The images are taken from real PV devices.

By keeping similar processing parameters, a similar investigation has been carried out on the effect of P3HT-*b*-PS semiflexible rod-coil on the photovoltaic properties P3HT:PCBM BHJ devices. Figure 4.19 shows the photovoltaic performance of BHJ devices obtained with the addition of different weight fractions of P3HT-*b*-PS into the P3HT:PCBM blend. The addition of P3HT-*b*-PS has no pronounced effect on V_{OC} which appears to be more or less constant ($V_{OC} \sim 0.55 \pm 0.1V$). J_{SC} varies slightly as a function of copolymer weight fraction and achieves a maximum, $J_{SC} \sim 12.4 \pm 0.5 \text{ mA/cm}^2$ at 4% of P3HT-*b*-PS. FF drops drastically when small P3HT-*b*-PS weight fraction is added into P3HT:PCBM blend before increasing to a maximum value of 0.61 ± 0.1 for 4% P3HT-*b*-PS. For higher copolymer ratios, FF declines again to a minimum value of 0.44 at 9% P3HT-*b*-PS. The observed trend in the value of the FF has a significant influence on the value of the $PCEs$. For a 4% P3HT-*b*-PS-based

device $V_{OC} = 0.55 \pm 0.1V$, $J_{SC} = 12.4 \pm 0.5 \text{ mA/cm}^2$ and $FF = 0.61 \pm 0.1$, lead to a maximum PCE of $\sim 4.2\%$.

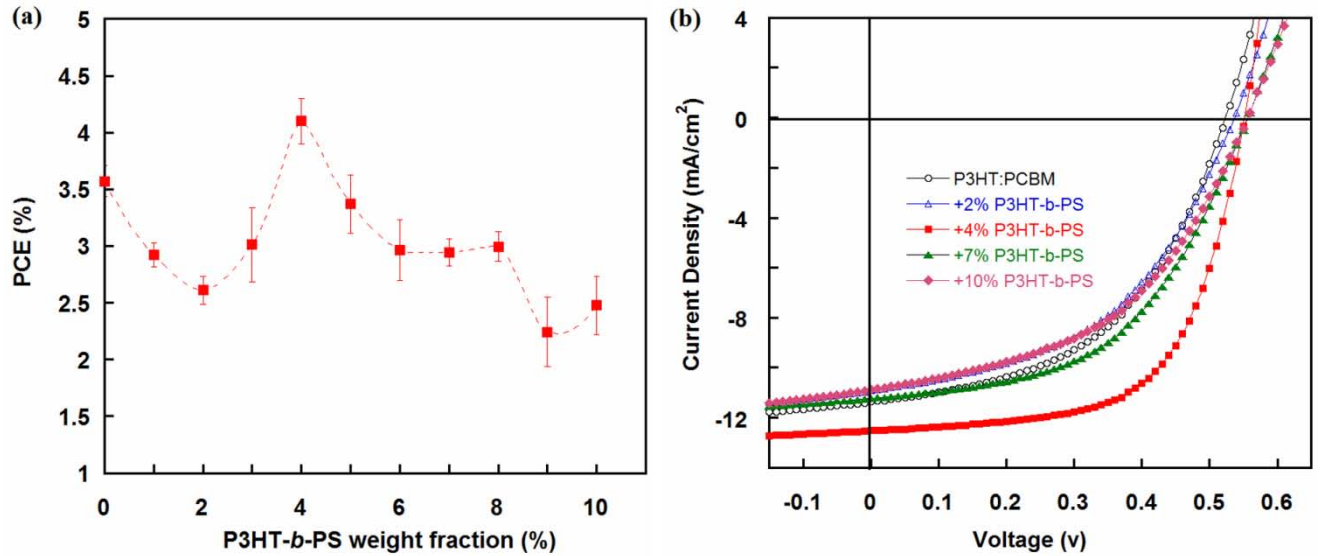


Figure 4.19: (a) Power-conversion efficiency, (b) J - V characteristics of P3HT:PCBM:P3HT-b-PS BHJ polymer solar cells. The devices were post-annealed at 165°C for 20 min. The error bars were calculated by averaging the results obtained over 8 devices. The broken lines are guides to the eye.

In order to complete the study of the J - V curves and deeper resolve the mechanisms involved in this increase of efficiency, the evolution of the series (R_s) and shunt resistances (R_{sh}) was investigated as a function of the P3HT- b -PS content. For high performance photovoltaic cells, a low R_s and a high R_{sh} values are required. A high value of R_{sh} is related to the minimization of leakage currents and to a low charge carrier recombination yield, while a low value of R_s is associated to the decrease of the intrinsic resistances, including the resistances at the contacts. The evolution of R_s and R_{sh} as function of the semiflexible rod-coil block copolymer weight fraction is shown in Figure 4.20. An increase in R_s from 14Ω to 24Ω and a sharp decrease of the fill factor from 0.6 to 0.47 were obtained upon the addition of 2% P3HT- b -PS. The increase in R_s can be due to the poor interfaces developed between the active layer and the aluminum electrode caused by the preferential segregation of the film components.^[35] In a recent report, a pronounced vertical phase segregation has been attested in the

P3HT:PCBM blends containing P3HT-*b*-PS block copolymer.^[32] The presence of this interface irregularity affects the PV characteristics significantly by either blocking the charge transport or by increasing the serial (bulk) resistance of the device as shown in Figure 4.20. On the contrary, the longer sized P3HT fibers observed upon the addition of 4% P3HT-*b*-PS have a great advantage for increasing the overall (effective) charge transport (hole) by lowering the R_s and increasing the R_{sh} . These properties have contributed for highly improved FF and J_{SC} and thus enhance the overall device efficiency. An improved device performance has also been achieved in the work of Sun *et al.* attributed to the improved morphological properties when an equivalent weight fraction (~ 5% wt.) of P3HT-*b*-PS block copolymer was incorporated into P3HT:PCBM PV blends.^[32]

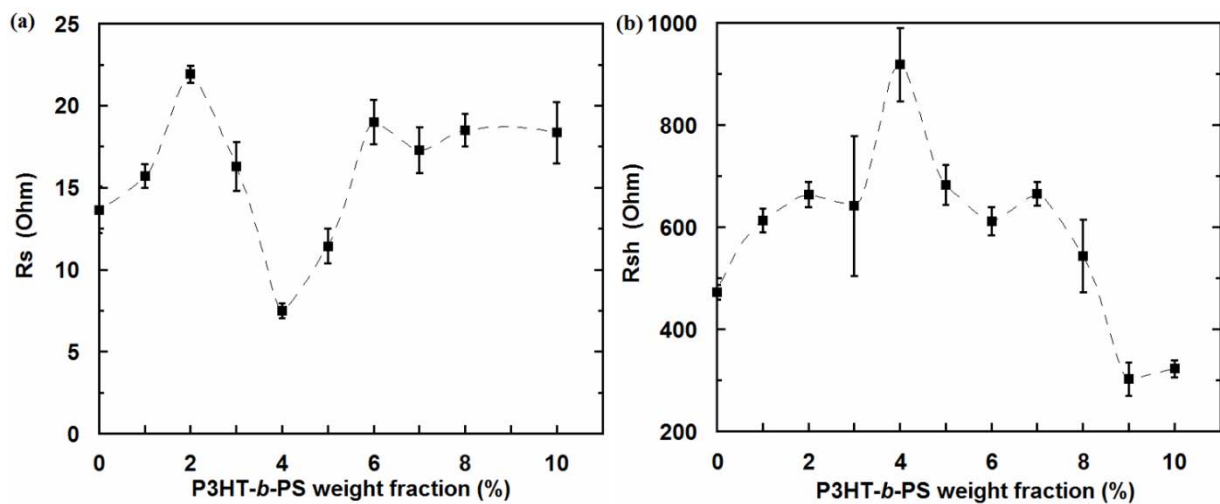


Figure 4.20: (a) R_s and (b) R_{sh} respectively the series and shunt resistances at different P3HT-*b*-PS weight fractions incorporated into P3HT:PCBM PV blends. The error bars were calculated by averaging the results obtained over 8 devices. The broken lines are guides to the eye.

In summary, we demonstrated that the addition of a small weight fraction of P3HT-*b*-PS into the blend of P3HT:PCBM favors for the appearance of more P3HT fibers at the surface of the BHJ film while the disruption of the mesostructures were attested for the higher weight fractions. This will have an effect in reducing the FF of the devices. However; at 4% P3HT-*b*-PS, the film morphology is only modified; longer P3HT fibrillar domains were obtained. These domains offer continuous pathway for

efficient charge transport (electrons and holes) and thus an improve device performance in P3HT:PCBM PV blends.

4.4.2. P3HT-*b*-P4VP: A novel Nanostructuring Agent in Controlling the Macrophase Separation of P3HT:PCBM blends

So far we have shown that a combination of annealing and the use of specific types of block copolymers as additive can enhance the performance of P3HT:PCBM solar cell devices through developing an optimum mesostructures and/or through improving the crystallinity of P3HT in the active layer. However, the implementation of common printing technologies for the fabrication of polymer solar cells on a mechanically flexible polymer substrate is impeded by the use of high temperature annealing steps. Moreover, high temperature annealing can also damage other parts of the devices such as the electrodes via oxidative mechanisms or thermal decomposition.^[36] In order to overcome the limitations inherent to the conventional thermal and solvent annealing, chemical processing solvents as additives have been used.^{[37][38][39]} However, some low volatile additives which still remain in the film after the film-forming process can also disrupt the stability of the morphology over time and influence the device performance as a result.^[40]

In this part of our investigation, we explored a novel approach to use P3HT-*b*-P4VP as a nanostructuring agent for the P3HT:PCBM BHJ PV blend for the fabrication of annealing-free polymer solar cells. The use of P3HT-*b*-P4VP in photovoltaics is not new. Previously, Sary *et al.* blended P3HT-*b*-P4VP semiflexible rod-coil block copolymer with PCBM to form the active layer of polymer solar cell devices. In their study, the P3HT rod block have been used as the electron donor material, while the P4VP coil block acts as a molecular dispersant of PCBM through non-covalent interactions.^{[30][31]} By this approach, only moderate *PCE* were obtained (around 1.5%; yet a record for a binary blend system comprising a semiconducting block copolymer as the donor and PCBM as the acceptor). This was attributed to a poorly developed co-continuous network structure and to the presence of an important

volume fraction of non-conducting material introduced in the blend. Thus, instead of using P3HT-*b*-P4VP solely as donor material, we utilized the block copolymer as nano-structuring agents in P3HT:PCBM BHJs in order to promote the structural organization of the active layer at room temperature, while impeding in the same time the macro-phase separation and agglomeration of PCBM by taking advantage of the non-covalent supramolecular interactions between the P4VP block and the PCBM moieties. Moreover, the use of the P3HT-*b*-P4VP block copolymer as a surfactant allows us to decrease the fraction of the non-conducting material introduced into the blend. Most importantly, we demonstrate in this work that the addition of a low weight fraction of a well-designed P3HT-*b*-P4VP semi-conducting diblock copolymer results in high efficient solar cells without necessitating any additional thermal or solvent annealing of the active layer. The *PCE* obtained are far beyond the state-of-the-art performance of non-annealed devices and, in fact, they are comparable to those achieved for the thermal annealed pristine P3HT:PCBM bulk heterojunctions.

The semiflexible rod-coil P3HT-*b*-P4VP copolymer utilized herein was synthesized according to a previously described strategy by Mougner *et al*, using a synthetic route designed for organic electronic requirements.^[41] The size of P3HT and P4VP in the block copolymer is 2.5 and 5.0 kg/mol, respectively. Since the work of Sary *et al*. had shown that the poor performance of conventional ITO/PEDOT:PSS/P3HT-*b*-P4VP:PCBM/Al solar cells was attributed to the presence of a P4VP-rich layer on top of the PEDOT:PSS film (can block hole transport and/or interfacial dipoles),^[30] inverted device architecture was adopted here. For the inverted solar cells prepared herein titanium oxide (TiO_x) was used as the electron selective layer and molybdenum oxide (MoO₃) as the hole selective layer. The conversion procedure from the titanium precursor to TiO_x as well as the MoO₃ thickness were optimised on inverted P3HT:PCBM cells so as to obtain photovoltaic performance comparable to those of conventional solar cells.^{[42][43]} The detailed device fabrication techniques are presented on Chapter 7.

The effect of the incorporation of P3HT-*b*-P4VP as an additive in 1:1 w/w P3HT:PCBM blends on the performance of the resulting solar cells was studied for both as cast and thermal annealed

devices. The photovoltaic characteristics obtained are reported in Figure 4.21, where (a), (b), (c) and (d) show the variations in open circuit voltage (V_{oc}), short circuit current density (J_{sc}), fill factor (FF) and PCE , respectively, when the composition in P3HT-*b*-P4VP is increased. Representative current density (J) – voltage (V) curves are presented in Figure 4.22, and they correspond to the data acquired for the reference (pure P3HT:PCBM) and the 8% copolymer-containing solar cells. We chose to present the curves obtained for this weight fraction since it exhibits the best performance with and without thermal treatment.

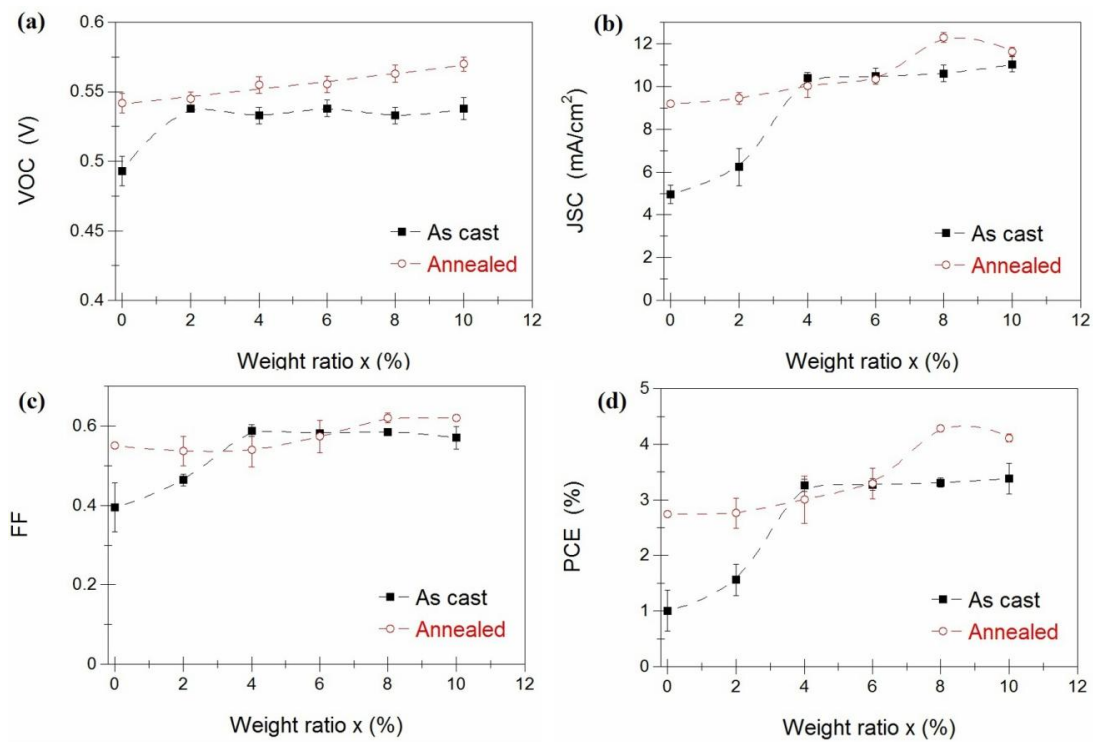


Figure 4.21: (a) V_{oc} , (b) J_{sc} , (c) FF , and (d) PCE , obtained for as cast (\square) and annealed (\bullet) solar cells at different P3HT-*b*-P4VP weight fractions. The error bars were calculated by averaging the results obtained over 16 devices. The broken lines are guides to the eye.

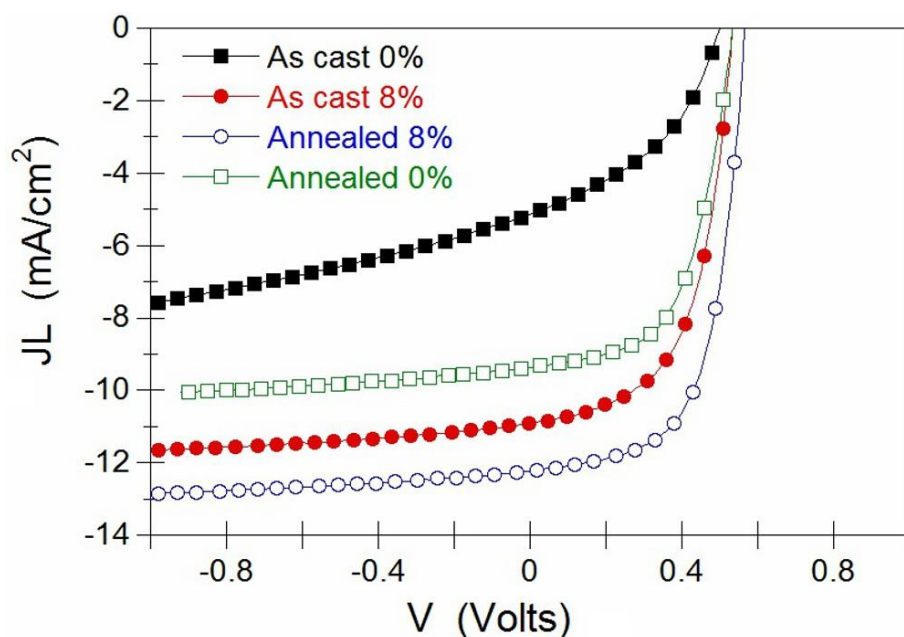


Figure 4.22: *J-V characteristics P3HT:PCBM:P3HT-*b*-P4VP (1:1:*x*) devices: with *x* = 0% and 8% (wt.). Thermal annealing was performed at 165°C for 20 min.*

Concerning the pristine P3HT:PCBM devices, the thermal annealing treatment leads to an increase in *PCE* from $1 \pm 0.1 \%$ to $2.7 \pm 0.1 \%$, as displayed in Figure 4.21d. This performance improvement is attributed to thermally induced crystallisation and nano-structuring of the blend components which results in enhanced charge generation and improved charge transport (see Chapter 3 for more explanations).

When P3HT-*b*-P4VP is added as a nano-structuring agent a considerable improvement in the overall performance is observed with respect to the pristine P3HT:PCBM device, for both the as cast and annealed cells. In the case of annealed devices, the addition of P3HT-*b*-P4VP slightly increases all photovoltaic parameters (V_{oc} , J_{sc} , *FF* and *PCE*). The highest efficiency is achieved when 8% of copolymer is added and *PCE* increases from 2.7 % to 4.3 %. However, the most astonishing effect with the addition of the copolymer is obtained for the annealing-free devices. The addition of 2% of P3HT-*b*-P4VP within the active layer leads to an increase in V_{oc} from 0.49 ± 0.02 V to 0.54 ± 0.01 V while it remains constant when the copolymer content increases further. More importantly, the incorporation

of the block copolymer strongly improves J_{sc} and FF . In fact, J_{sc} is doubled when 4% of P3HT-*b*-P4VP is added, from 5.0 ± 0.4 mA/cm² to 10.5 ± 0.3 mA/cm², while FF increases by 50%, from 0.40 ± 0.02 to 0.59 ± 0.02 . Consequently, a PCE of 3.4 ± 0.2 % is achieved for the 4% copolymer-containing devices, which suggests a three-fold enhancement of the efficiency. For copolymer concentrations higher than 4% J_{sc} , FF and PCE remain roughly constant with respect to the P3HT-*b*-P4VP weight fraction. It is worth noticing that the PCE of the as cast solar cells that contain 4% of P3HT-*b*-P4VP is even higher than the 2.7 % efficiency achieved for the pristine P3HT:PCBM bulk heterojunctions that were thermally treated at high temperature.

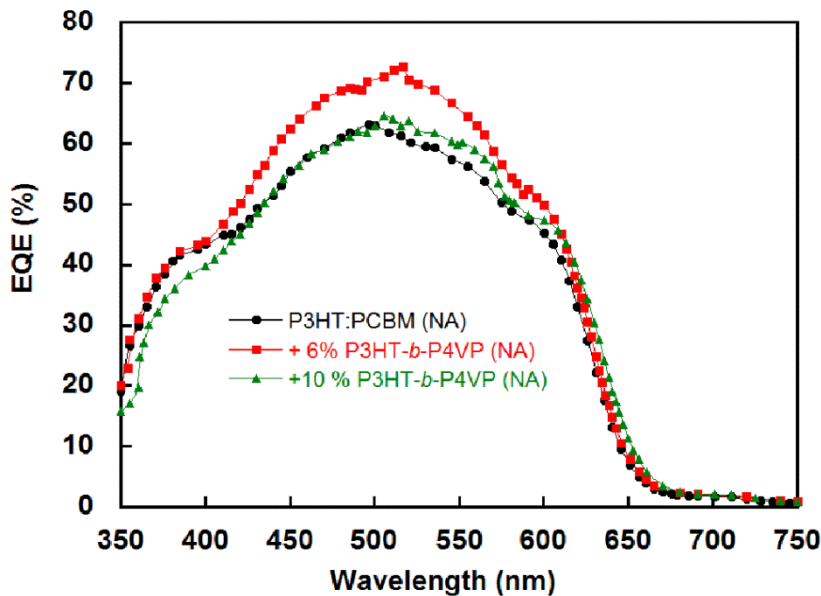


Figure 4.23: EQE spectra of the P3HT-*b*-P4VP-containing non-annealed devices.

Complementary to the J - V characterization, external quantum efficiency (EQE) measurements were conducted. The data presented in Figure 4.23 show an increase in EQE when the block copolymer is added to the blend. This result suggests an enhanced exciton dissociation yield and/or reduced charge recombination. It is noted that the increase in the integrated EQE is consistent with the increase in J_{sc} and the decrease in charge losses as discussed above.

We also checked the devices performance when a higher molecular weight P3HT-*b*-P4VP copolymer is utilized. The molecular weight of the rod block was kept constant (2.5 kg/mol) while that of the coil block varied from 5 to 28 kg/mol. The results are presented in Figure 4.24. In the investigated range of P4VP volume fractions in the copolymer, there is no significant effect on the *PCE*, neither for the as cast, nor for the annealed devices. However a new series of P3HT-*b*-P4VP copolymers is required in order to access the whole range of P4VP block volume fractions, which is lacking here.

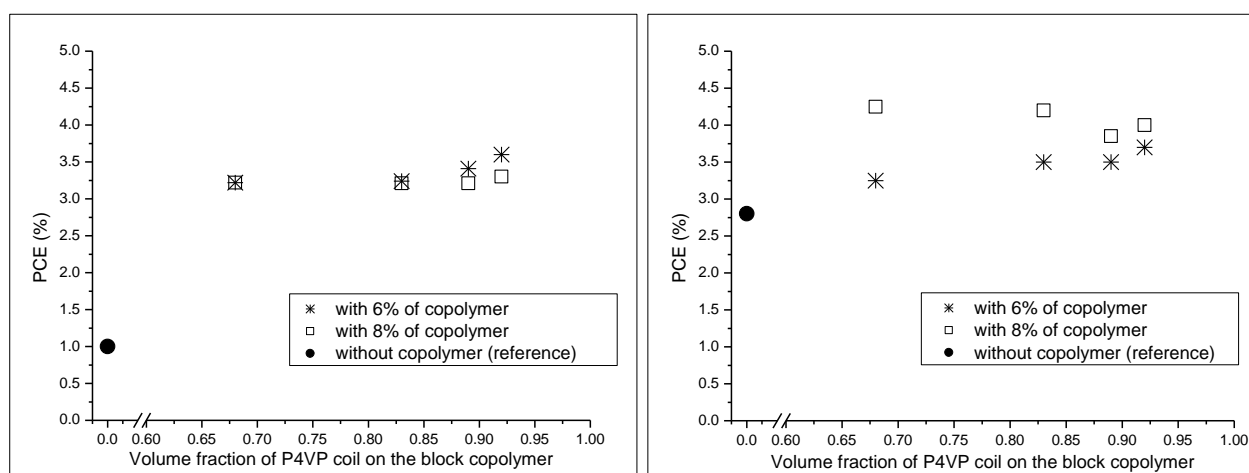


Figure 4.24: *PCE* at two different P3HT-*b*-P4VP weight fraction compositions (6% and 8%) without performing any annealing treatment (left) and after annealing treatment at 165°C for 20 min (right) versus volume fraction of P4VP coil block in block copolymer (corresponding to 5 kg/mol, 12 kg/mol, 20 kg/mol and 28 kg/mol with a rod block of 2.5 kg/mol).

The results presented so far concerning the improved device performance should originate from structural changes in the active layers that are induced by the incorporation of the block copolymer. As it was already emphasized, the P3HT-*b*-P4VP copolymer is utilized herein as a nano-structuring agent. This means that the copolymer is expected to act as a compatibilizer between the P3HT and PCBM phases, due to the chemical affinity of the two blocks with the components of the

blend. Therefore, it is expected to be localized at the P3HT-PCBM interface, thus stabilizing the structure.

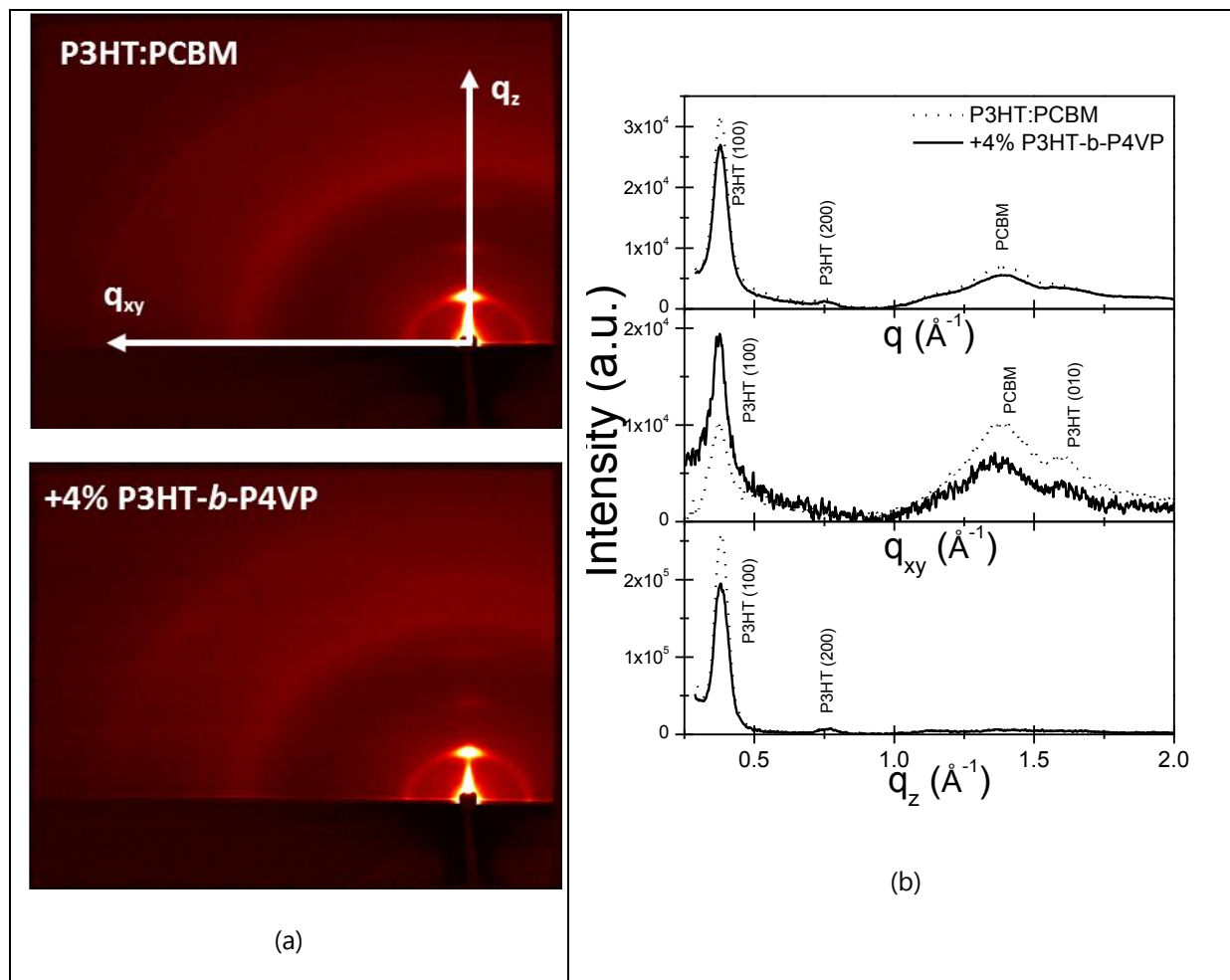


Figure 4.25: (a) 2-D GIXD images recorded for the pristine and the 4% P3HT-b-P4VP – containing P3HT:PCBM blend. Both correspond to as-cast films, spin-coated on TiO_x/ITO substrates to mimic the device preparation conditions. (b) The corresponding 1-D radially averaged intensity plot with respect to the scattering vector q , and the two intensity line cuts, across the in-plane (q_{xy}) and out-of-plane (q_z) directions. In all three cases the contribution to scattering from the TiO_x/ITO substrate has been subtracted.

In order to get more insight into the morphology of the copolymer-containing films, GIXD measurements have been performed on films coated on TiO_x/ITO substrates, prepared following the same methodology as for the active layers of the devices. The 2-D images recorded for the as cast

P3HT:PCBM blend and the non-annealed film that contains 4% of P3HT-*b*-P4VP are presented in Figure 4.25a. By radially averaging with respect to the centre of the incident beam, we obtain the corresponding 1-D intensity vs scattering vector, q , profiles, which are presented in the upper part of Figure 4.25b. The integrated intensity of the (100) reflection of P3HT, which corresponds to the alkyl chain periodicity, appears to decrease slightly after the incorporation of the copolymer in the blend, which suggests that the crystallinity of P3HT is reduced. This is also evident in the UV-vis absorption data (Figure 4.26). The intensity of the P3HT absorption band located between 450-650 nm slightly decreases with increasing the fraction of copolymer in the blend, which is indicative of a small decrease in the optical density of the film and suggests less densely-packed chains in the crystalline phase.^[44] Additionally, a close look at the (100) diffraction peak shows that the peak width is the same for the two films, indicating that the size of the P3HT domains is not affected by the presence of the copolymer. We suppose, thus, that although the crystallinity of P3HT decreases after addition of the P3HT-*b*-P4VP copolymer, this decrease is relatively small. Moreover, it is interesting to note in the same diffraction pattern that the intensity of the peak located at around 1.4 \AA^{-1} , which is assigned to PCBM, also decreases upon addition of P3HT-*b*-P4VP. This suggests that less PCBM agglomerates are embedded in the films and testifies that the P4VP blocks interact with the PCBM domains, inhibiting the formation of large PCBM domains.^[45] Finally, by comparing the in-plane and out-of-plane diffraction patterns (Figure 4.26b, I vs q_{xy} and I vs q_z respectively), we can see that the copolymer incorporation results in an increase of the (100) peak intensity in the in-plane direction and a subsequent decrease of the intensity of the same peak in the out-of-plane direction. In the same time, the intensity of the (010) reflection of P3HT, which is located at around 1.65 \AA^{-1} and is assigned to the π - π stacking periodicity, decreases in the in-plane diffraction pattern. All these strongly suggest that the population of the face-on oriented P3HT crystallites increases upon incorporation of P3HT-*b*-P4VP in the active layer.

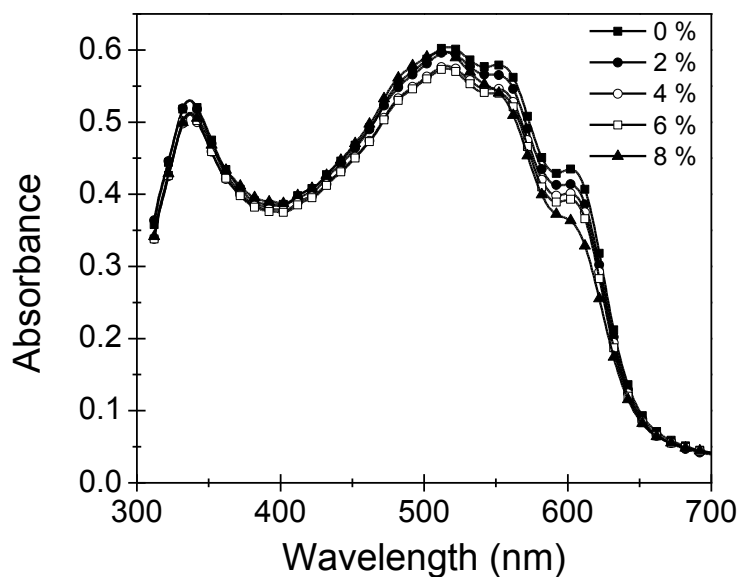


Figure 4.26: UV-Vis absorption spectra acquired for the pristine and the P3HT-*b*-P4VP – containing P3HT:PCBM blends, for various copolymer concentrations. No thermal annealing has been applied, while the polymeric blends were spin-coated on TiO_x/ITO substrates to mimic the device preparation conditions.

To sum up, the results obtained on the structural properties of the as cast films indicate that when P3HT-*b*-P4VP is added in the P3HT:PCBM blend the crystallinity of P3HT is slightly decreasing. However, the P3HT crystallites prefer to orient themselves with faces-on. This is well-desirable in photovoltaic devices, since hole extraction through the electrodes is enhanced,^[26] resulting in an improved performance of the devices. On the other hand, PCBM crystallization is inhibited by the presence of the P4VP blocks. We suppose that this also contributes to the improvement of the device performance, by decreasing the size of the PCBM domains, increasing, thus, the interfaces available for exciton dissociation. This results in increased exciton dissociation and reduced charge recombination, as confirmed by the EQE and *J-V* data. Unfortunately we cannot provide experimental proof on the PCBM domain size by applying the Scherrer's equation on our data, due to the broadness of the PCBM reflection and the overlapping with the (010) P3HT peak, that hinder the accurate estimation of the

peak full width at half maximum. Still, our results strongly suggest that the improved performance is related to the formation of a well-optimized nanoscale structure that allows better exciton dissociation and charge transport. A more elaborate structural investigation is currently performed that will allow a deeper understanding of the physical mechanisms involved in the observed enhancement of the device performance.

4.5. Conclusion

In the first part, we have presented an integrated study on the implications of the addition of a P3HT-*b*-PI semiflexible rod-coil block copolymer in active layer morphology and device performance of P3HT:PCBM:P3HT-*b*-PI bulk heterojunctions. The P3HT-*b*-PI copolymer acts as nucleation agent, promoting the crystallization of P3HT, which was the hypothesis upon which we based this work. An increase in the number density of P3HT crystallites is observed in the copolymer-containing films resulting in an overall increase of crystallinity. Concurrently, the agglomeration of PCBM is embedded and more homogeneous – at the microscopic scale – blends are obtained, pointing to a less extended phase separation between P3HT and PCBM at this level. All these synergetic effects drive the formation of an optimized bulk heterojunction network that stimulates photon absorption, efficient exciton dissociation and improved charge transport, as discussed above. Subsequently, a maximum power conversion efficiency of 4.5 ± 0.1 % was achieved for the 7% (wt.) copolymer containing blend.

In the second part, we have reported a systematic investigation on the photovoltaic performance of P3HT:PCBM-based solar cell devices in inverted device configuration when a well-designed P3HT-*b*-P4VP block copolymer is added separately as a nano-structuring agent. The results have shown that the *PCE* can reach a plateau value of 3.4 % as soon as 4% w/w of P3HT-*b*-P4VP is added without performing any (thermal and/or solvent) annealing treatment. In comparison, a *PCE* of only 2.7 % is obtained after a high temperature annealing treatment for pristine P3HT:PCBM BHJ devices under the same experimental conditions. By performing a thermal annealing treatment, the

PCE reaches 4.3 % in case of the 8% w/w P3HT-*b*-P4VP-containing cells. The analysis of the *J-V* characteristics and the initial structural characterization suggest that the increase in performance is related to the formation of a well-optimized nanoscale structure that allows for a more efficient exciton dissociation and charge transport, by lowering the charge recombination and/or trapping.

Generally, the simplicity of adding a well-designed block copolymer into the archetypical P3HT:PCBM BHJ as crystallization agent or nano-structuring agent appears to be a valuable and efficient method to optimize the active layer morphology and improve device performance in polymer photovoltaic cells while allowing at the same time the implementation of a low cost fabrication printable roll-to-roll process on flexible polymer substrates.

References

- [1] J. Kiel, A. Eberle, M. Mackay, *Physical Review Letters* **2010**, *105*, 168701.
- [2] C. Müller, S. Goffri, D.W. Breiby, J.W. Andreasen, H.D. Chanzy, R.A.J. Janssen, M.M. Nielsen, C.P. Radano, H. Sirringhaus, P. Smith, N. Stingelin-Stutzmann, *Advanced Functional Materials* **2007**, *17*, 2674–2679.
- [3] S. Goffri, C. Müller, N. Stingelin-Stutzmann, D.W. Breiby, C.P. Radano, J.W. Andreasen, R. Thompson, R.A.J. Janssen, M.M. Nielsen, P. Smith, H. Sirringhaus, *Nature Materials* **2006**, *5*, 950–6.
- [4] G. Sauvé, R.D. McCullough, *Advanced Materials* **2007**, *19*, 1822–1825.
- [5] M.-B. Madec, D. Crouch, G.R. Llorente, T.J. Whittle, M. Geoghegan, S.G. Yeates, *Journal of Materials Chemistry* **2008**, *18*, 3230.
- [6] L. Qiu, W.H. Lee, X. Wang, J.S. Kim, J.A. Lim, D. Kwak, S. Lee, K. Cho, *Advanced Materials* **2009**, *21*, 1349–1353.
- [7] T.A.M. Ferenczi, C. Müller, D.D.C. Bradley, P. Smith, J. Nelson, N. Stingelin, *Advanced Materials* **2011**, *23*, 4093–7.
- [8] K. Sivula, Z.T. Ball, N. Watanabe, J.M.J. Fréchet, *Advanced Materials* **2006**, *18*, 206–210.
- [9] C. Yang, J.K. Lee, A.J. Heeger, F. Wudl, *Journal of Materials Chemistry* **2009**, *19*, 5416–5423.
- [10] J.U. Lee, J.W. Jung, T. Emrick, T.P. Russell, W.H. Jo, *Journal of Materials Chemistry* **2010**, *20*, 3287–3294.

- [11] J. Chen, X. Yu, K. Hong, J.M. Messman, D.L. Pickel, K. Xiao, M.D. Dadmun, J.W. Mays, A.J. Rondinone, B.G. Sumpter, S.M.K. II, *Journal of Materials Chemistry* **2012**, *22*, 13013–13022.
- [12] H. Lim, K. Huang, W. Su, C. Chao, *Polymer* **2010**, *48*, 3311–3322.
- [13] X. Yang, J. Loos, S.C. Veenstra, W.J.H. Verhees, M.M. Wienk, J.M. Kroon, M.A.J. Michels, R.A.J. Janssen, *Nano Letters* **2005**, *5*, 579–83.
- [14] S. Berson, R. De Bettignies, S. Bailly, S. Guillerez, *Advanced Functional Materials* **2007**, *17*, 1377–1384.
- [15] B. Fillon, A. Thierry, B. Lotz, J.C. Wittmann, *Journal of Thermal Analysis*, **1994**, *42*, 721–731.
- [16] A.J. Müller, V. Balsamo, M.L. Arnal, T. Jakob, H. Schmalz, V. Abetz, *Macromolecules* **2002**, *35*, 3048–3058.
- [17] A.T. Lorenzo, M.L. Arnal, J.J. Sanchez, A.J. Muller, *Journal of Polymer Science Part B: Polymer Physics* **2006**, *44*, 1738–1750.
- [18] P. Brown, D. Thomas, A. Köhler, J. Wilson, J.-S. Kim, C. Ramsdale, H. Sirringhaus, R. Friend, *Physical Review B* **2003**, *67*, 1–16.
- [19] J. Clark, C. Silva, R. Friend, F. Spano, *Physical Review Letters* **2007**, *98*, 1–4.
- [20] A. Nelson, *Journal of Applied Crystallography* **2006**, *39*, 273–276.
- [21] [Http://www.ncnr.nist.gov/resources/sldcalc.html](http://www.ncnr.nist.gov/resources/sldcalc.html), Last Accessed on August **2012**.
- [22] A.J. Parnell, A.D.F. Dunbar, A.J. Pearson, P.A. Staniec, A.J.C. Dennison, H. Hamamatsu, M.W.A. Skoda, D.G. Lidzey, R.A.L. Jones, *Advanced Materials* **2010**, *22*, 2444–2447.
- [23] J.W. Kiel, B.J. Kirby, C.F. Majkrzak, B.B. Maranville, M.E. Mackay, *Soft Matter* **2010**, *6*, 641–646.
- [24] J.M.J. Woo, C. H.; Piliago, C.; Holcombe, T. W.; Toney, M. F.; and Fréchet, *Macromolecules* **2012**, *45*, 3057–3062.
- [25] R.J. Kline, M.D. McGehee, E.N. Kadnikova, J. Liu, J.M.J. Fréchet, *Advanced Materials* **2003**, *15*, 1519–1522.
- [26] D.M. Sirringhaus, H.; Brown, P. J.; Friend, R. H.; Nielsen, M. M.; Bechgaard, K.; Langeveld-Voss, B. M. W.; Spiering, A. J. H.; Janssen, R. A. J.; Meijer, E. W.; Herwig, P. & de Leeuw, *Nature* **1999**, *401*, 685–688.
- [27] J.U. Lee, J.W. Jung, T. Emrick, T.P. Russell, W.H. Jo, *Nanotechnology* **2010**, *21*, 105201.
- [28] J.B. Kim, Z.-L. Guan, S. Lee, E. Pavlopoulou, M.F. Toney, A. Kahn, Y.-L. Loo, *Organic Electronics* **2011**, *12*, 1963–1972.
- [29] P. Dong-won, R. Roe, *Macromolecules* **1991**, *24*, 5324–5329.

- [30] N. Sary, F. Richard, C. Brochon, N. Leclerc, P. L  v  que, J.-N. Audinot, S. Berson, T. Heiser, G. Hadziioannou, R. Mezzenga, *Advanced Materials* **2010**, *22*, 763–8.
- [31] N. Sary, L. Rubatat, C. Brochon, G. Hadziioannou, R. Mezzenga, *Macromolecular Symposia* **2008**, *268*, 28–32.
- [32] Z. Sun, K. Xiao, J.K. Keum, X. Yu, K. Hong, J. Browning, I.N. Ivanov, J. Chen, J. Alonzo, D. Li, B.G. Sumpter, E.A. Payzant, C.M. Rouleau, D.B. Geohegan, *Advanced Materials* **2011**, *23*, 5529–5535.
- [33] X. Yu, K. Xiao, J. Chen, N. V Lavrik, K. Hong, B.G. Sumpter, D.B. Geohegan, *ACS Nano* **2011**, *5*, 3559–3567.
- [34] M. Arif, J. Liu, L. Zhai, S.I. Khondaker, *Synthetic Metals* **2012**, *162*, 1531–1536.
- [35] B.T. De Villers, C.J. Tassone, S.H. Tolbert, B.J. Schwartz, *J. Phys. Chem. C* **2009**, *113*, 18978–18982.
- [36] W. Ma, C. Yang, X. Gong, K. Lee, A.J. Heeger, *Advanced Functional Materials* **2005**, *15*, 1617–1622.
- [37] Y. Yao, J. Hou, Z. Xu, G. Li, Y. Yang, *Advanced Functional Materials* **2008**, *18*, 1783–1789.
- [38] S.K. Jang, S.C. Gong, H.J. Chang, *Synthetic Metals* **2012**, *162*, 426–430.
- [39] J.K. Park, C. Kim, B. Walker, T.-Q. Nguyen, J.H. Seo, *RSC Advances* **2012**, *2*, 2232.
- [40] J. Liu, Y. Han, *Polymer Bulletin* **2012**, *68*, 2145–2174.
- [41] S.-J. Mognier, C. Brochon, E. Cloutet, S. Magnet, C. Navarro, G. Hadziioannou, *Journal of Polymer Science Part A: Polymer Chemistry* **2012**, *50*, 2463–2470.
- [42] C. Waldauf, M. Morana, P. Denk, P. Schilinsky, K. Coakley, S. a. Choulis, C.J. Brabec, *Applied Physics Letters* **2006**, *89*, 233517.
- [43] C. Tao, S. Ruan, X. Zhang, G. Xie, L. Shen, X. Kong, W. Dong, C. Liu, W. Chen, *Applied Physics Letters* **2008**, *93*, 193307.
- [44] W.C. Tsoi, S.J. Spencer, L. Yang, A.M. Ballantyne, P.G. Nicholson, A. Turnbull, A.G. Shard, C.E. Murphy, D.D.C. Bradley, J. Nelson, J.-S. Kim, *Macromolecules* **2011**, *44*, 2944–2952.
- [45] V. Gernigon, P. L  v  que, C. Brochon, J. Audinot, R. Bechara, F. Richard, T. Heiser, G. Hadziioannou, *Eur. Phys. J. Appl. Phys.* **2011**, *56*, 34107.

Chapter – V

***Effect of Rod-coil Block Copolymers on Device
Stability***

5.1. Introduction

Due to the advancement in synthetic methods to create novel materials and the highly improved device fabrication techniques; the performance of organic solar cells has recently surpassed the 10% mark, a milestone enabling a potential for large-scale commercialization.^[1-4] Despite this progress, several issues require attention before solar cells made of semi-conducting organic materials become fully efficient and practical devices. Generally, a balance between the design (synthesis and processing), the efficiency, and the stability of a device have to be obtained before commercialization.^[5] For example, for a given set of OPV materials, understanding and controlling the phase separation of the photo-active layer morphology to the optimum level is very much compulsory (as it affects the overall performance of devices). Furthermore, the lifetime of the devices is a key factor for the commercial development of efficient polymer solar cells.

In order to improve the lifetime of organic based devices, it is essential to understand and control the degradation processes. Indeed the optical and electrical properties of organic based devices are highly affected by degradation mechanisms which subsequently govern its lifetime. The degradation of OPVs are facilitated by different factors such as: diffusion of metallic species from the electrode into the organic layers,^[6] instability of the active layer morphology,^{[7][8]} oxidation of organic layers,^[9] cathode delamination,^[10] as well as electrochemical reactions at the electrode/active layer interfaces.^{[7][11]}

Those aforementioned effects are mostly caused by several ageing mechanisms such as temperature,^{[6][8][12][13]} and environmental contamination such as oxygen.^{[9][14][15]} The presence of oxygen in the organic layers and in the vicinity of the interfaces with the electrode leads to the formation of traps and hence influences the device performance.^{[9][16]} Moreover, the contamination of the polymer layers can occur during the synthesis and/or the device fabrication. Water is also identified as a cause of device degradation, leading to damage of the photo-active and hole extraction layers such as PEDOT:PSS in conventional OPV device architectures.^{[17][18]} Indeed, water in the

atmosphere can diffuse through the photo-active layer to the PEDOT:PSS layer, resulting in an increase in the electrical resistance at the PEDOT:PSS/photo-active layer interface. The photodegradation of organic layers or their structural modifications are also considered as a source of degradation of devices.^{[19][20][21]}

However, the stability of devices can be improved by an appropriate encapsulation method (for example, proper encapsulation excludes the role of oxygen contamination or other environmental factors), by playing on the device structures (by using inverted device configuration in OPV devices for instance),^{[22][23][24]} by depositing an ultrathin barrier layer between the active layer and the top electrode,^{[5][15]} by playing on the chemical structure of the active layer (cross-linking)^{[25][26][27]} or by adding chemical species into the active layer (stabilizers).^{[28][29]} Generally, the stability of polymers can be improved upon incorporation of inorganic dopants.^[30] In the case of organic additives, the effects on polymer stability and device lifetime have not yet clearly been established.

As we have seen in our previous investigations (see Chapter 4), the addition of block copolymers into P3HT:PCBM blends has significantly enhanced the device performance. Upon incorporation of an optimum wt% of semiflexible rod-coil block copolymers (P3HT-*b*-PI, P3HT-*b*-PS and P3HT-*b*-P4VP) into P3HT:PCBM blends, an extended macrophase separation has been significantly reduced and the crystallization properties of the polymer have been modified, resulting in an improved nanoscale morphology and thus in an enhanced device efficiency. The purpose of this work is to examine the role of the block copolymer additives in the degradation processes or the stability of the P3HT:PCBM PV devices. Consequently we examined the role of P3HT-*b*-PI, P3HT-*b*-PS and PS-*b*-PI copolymers as additives and studied their effect on device stability. The PS-*b*-PI block copolymer was used as a control compound with respect to the other two block copolymers.

Several key measurements have been carried out such as the reproducibility of fabrication process, the repeatability of performance measurements and lifetime measurements with the operation time. To predict the lifetime of polymer solar cells, accelerated lifetime (ALT) measurements

are commonly used.^{[31][32][33]} In this method, the degradation is artificially accelerated by applying an increased level of stresses such as cyclic or periodic mechanical and/or electrical stresses, exposing to elevated temperatures, concentrated light, continuous illumination, humidity (effect of oxygen and water), etc. However, most ALT measurements of device stability studies reported in the literature are based on exposing samples to AM 1.5G, 100 mW/cm² illumination at 50 or 60°C under short-circuit, open-circuit or at maximum power point while measuring PV performance at constant time (every 2 h or 10 h for instance).

In this investigation, we have employed an experimental approach based on ALT and cycling electrical measurements in order to evaluate the different degradation processes occurring during the operation time in the P3HT:PCBM:copolymer devices. For this experiment, we illuminated the devices at AM 1.5G, 100 mW/cm² and held the solar cell devices in an open-circuit condition and periodically recorded the variations in the PV characteristics. Illumination of the devices was done through the ITO/PEDOT:PSS side. The temperature of the polymeric heterojunction was held at 25°C for initial *J-V* characteristic measurements in dark while the cell temperature during the illumination reached approximately 55°C. The detailed device fabrication is presented in Chapter 7. For the analysis presented here, additional stress variables or degradation factors have been carefully prevented; *i.e.* all *J-V* measurements have been performed only under constant illumination and in an inert atmosphere (in glove-box filled with nitrogen).

The decay process from the ALT measurements, which may be chemical in nature, can have an Arrhenius-type behavior and thus can be described using the Arrhenius model where the rate of decay is determined by an exponential function.^[31] Accordingly, we have applied this common model based on a first order kinetic degradation. The resulting degradation constant (decay rate) is described as follows:

$$k_{\text{deg}} = A \exp\left(-\frac{Ea}{k_B T}\right) \quad (5.1)$$

Where Ea is the activation energy in eV, k_B the Boltzmann constant, T the temperature in Kelvin and A is a constant dependent on the degradation mechanisms and the experimental conditions. The decay parameter is related to the dominant degradation process, which can have different origins (e.g. structural, chemical, ...). If the decay follows the Equation (5.1), it is evident that the rate of decay k_{deg} is highly dependent of the temperature and thus the model allows to determine the acceleration factor for optimum temperature following Equation (5.2).

$$K = \frac{k_{\text{deg}}(T_1)}{k_{\text{deg}}(T_2)} = \exp\left(\frac{Ea}{k_B} \left(\frac{1}{T_2} - \frac{1}{T_1}\right)\right) \quad (5.2)$$

Assuming an activation energy $Ea = 350 \text{ meV}^{[32]}$, $T_1 = 298 \text{ K}$ (25°C) as a reference temperature and $T_2 = 328 \text{ K}$ (55°C) as temperature measurement, the acceleration factor was determined at $K = 3.47$. Consequently, an extrapolation can be done to predict the lifetime of the device under illumination for optimum temperatures.

Before carrying out lifetime measurements, the reproducibility (*i.e.* the capability to achieve devices which give results accurately reproduced within the same process flow) of the fabrication process and the repeatability (*i.e.* the standard deviation of the performance by repeating measurements taken on the same item and under the same conditions) of the device performance were investigated.

5.2. Reproducibility of fabrication process

Previously investigations (Chapter 4) have shown that the highest performance were obtained by adding 5% PS-*b*-PI, 7% of P3HT-*b*-PI and 4% P3HT-*b*-PS into P3HT:PCBM BHJ blends. The reproducibility experiments were performed by using similar ratio of block copolymer additives. Two series of eight diodes were prepared and tested under the conditions described in the experimental

section. Devices were made repeatedly from a second solution prepared separately from the first one by using similar fabrication conditions (such as solvent, concentration, and annealing temperature). The performance was averaged over 6 to 8 different diodes. Table 5.1 shows the performance obtained from the pure blend and the three copolymer additives (P3HT-*b*-PI, P3HT-*b*-PS, and PS-*b*-PI). The previous PV performance results stated in Chapter 4 and the reproducibility experiments of Table 5.1, show that the device fabrication process is well controlled leading to a good reproducibility of performance with a ratio of change of *PCE* found in the range of ~ 0.5%.

Device	V_{OC} (V)	J_{SC} (mA/cm ²)	<i>FF</i>	<i>PCE</i> (%)
Pristine P3HT:PCBM	0.58 ± 0.02	10.4 ± 0.3	0.58 ± 0.03	3.5 ± 0.4
+ 7% P3HT- <i>b</i> -PI	0.57 ± 0.02	13.1 ± 0.7	0.60 ± 0.01	4.5 ± 0.3
+ 4% P3HT- <i>b</i> -PS	0.55 ± 0.01	12.5 ± 0.6	0.61 ± 0.03	4.2 ± 0.3
+5% PS- <i>b</i> -PI	0.62 ± 0.02	9.7 ± 0.3	0.55 ± 0.02	3.3 ± 0.2

Table 5.1: Photovoltaic performance of P3HT:PCBM: block copolymer-based solar cells obtained from three different block copolymer additives made from different blend solutions but under similar fabrication conditions.

5.3. Repeatability of device performance

The photovoltaic performance were measured several times (number of cycles) for testing the repeatability of the measurements. *J-V* measurements were carried out between -1 V and 1.5 V under illumination. Between each measurement, the samples were stored in the dark for one hour to reach equilibrium state (i.e. relaxation of free charges). For each measurement, the sample was illuminated for 3 to 4 minutes; and we assume that the slight increase of the device temperature during the *J-V* measurements under illumination for the aforementioned period has no influence on the recovery of the solar cell efficiency.

Figure 5.1 shows the variation of PV performance versus the number of repetitive electrical measurements (cycles). The values of the photovoltaic characteristics are normalized to their maximum value (*i.e.* to their initial value), for a better comparison of their respective variation with time. By repeating *J-V* measurements, the cell characteristics - V_{OC} , J_{SC} , FF , and PCE - were gradually degraded. PV performance decreases and stabilizes after 10 repetitive *J-V* measurements leading to $\sim 18\%$ reduction in PCE for pristine devices. The device performance gets then constant for more repetitive measurements.

The decay of PV performance can be well-described by using the exponential decay fitting function. To obtain the degradation constant k_{deg} , we have adjusted (fitted) the experimental data for the PCE using a simple exponential model, as described in Equation 5.3. The decay rates, named k_{deg1} , obtained from these fits and describing the PCE decays, are reported in Table 5.2.

$$PCE(t) = PCE(t = 0) \exp(-k_{deg}t) \quad (5.3)$$

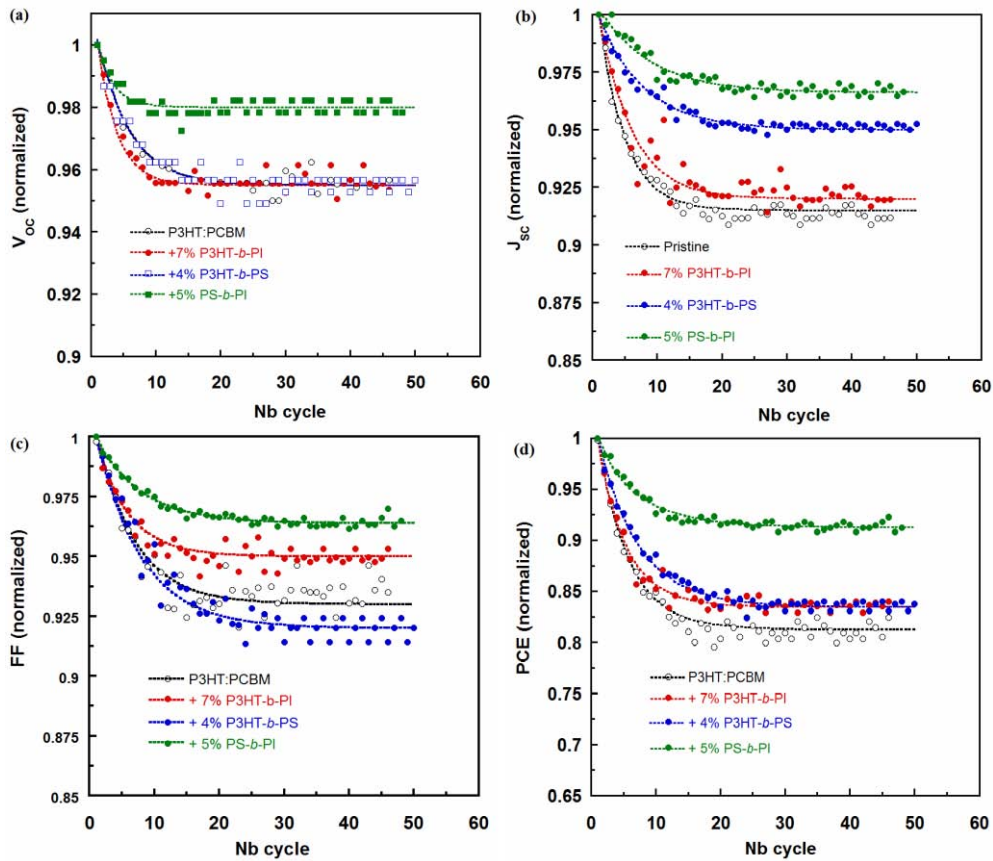


Figure 5.1: V_{OC} (a), J_{sc} (b), FF (c) and PCE (d), as a function of the number of electrical measurements for pristine and copolymer containing devices. Each value is normalized by its initial value. Each curve has been fitted by using relation 5.3.

By adding the block copolymers, the PCE decay rate is decreased suggesting that the addition of block copolymers improves the stability of devices under electrical cycling stress. As it has been indicated in Figure 5.1, PV performance is stabilized after 10 repetitive J - V measurements leading to 8%, 16% and 15% reduction in PCE for PS- b -PI, P3HT- b -PS and P3HT- b -PI based devices, respectively. It is noteworthy that the decrease in PV performance of PS- b -PI based devices is smaller than the one observed for pristine, P3HT- b -PS and P3HT- b -PI copolymer based devices. As the conditions of electrical cycling experiments are identical for all devices, PS- b -PI based devices appear to be more stable. Furthermore, the FF of P3HT- b -PI based devices is less affected by the electrical stress leading to a slight improvement of the device stability while the minor improvement in stability obtained by adding P3HT- b -PS is mainly due to the slower degradation of J_{sc} . Table 5.2 shows the results obtained

after the stabilization of the device performances (*i.e.* after 10 cycling electrical measurements). After these cycling measurements, the performance of block copolymer based devices are still higher than those of the pure blend devices. It can be concluded that the incorporation of block copolymers improves the stability of the device performance under electrical cycling measurements.

Devices	V_{OC} (V)	J_{SC} (mA/cm ²)	FF	PCE (%)	k_{deg1}
Pristine	0.55 ± 0.01	9.5 ± 0.3	0.54 ± 0.03	2.8 ± 0.4	0.23
+ 7% P3HT- <i>b</i> -PI	0.54 ± 0.01	12.1 ± 0.7	0.58 ± 0.01	3.8 ± 0.3	0.19
+ 4% P3HT- <i>b</i> -PS	0.55 ± 0.01	11.8 ± 0.6	0.54 ± 0.03	3.5 ± 0.3	0.20
+ 5% PS- <i>b</i> -PI	0.61 ± 0.01	9.4 ± 0.3	0.52 ± 0.02	3.0 ± 0.2	0.15

Table 5.2: Photovoltaic performance obtained with different copolymer additives after 10 electrical cycling measurements. Decay rate k_{deg1} , obtained for describing PCE decay by using fitting curve given by relation (5.3).

To understand the causes of the initial degradation (some call it “burn-in” period^[34]), the degraded devices (after 10 repetitive measurements) were annealed again at 165°C for 10 min. After re-annealing, the performance of the degraded devices almost returned to their initial value as shown in Figure 5.2. By repeating the electrical cycling measurement, a similar degradation of performance has been observed suggesting that the degradation process is similar to the one observed on fresh device. Similar restoration behavior was also observed with copolymer based devices. This restoration effect suggests that the cell degradation by electrical cycling is not related to some irreversible chemical damages of the organic materials or the photo-active layers. Rather, it results from an electrical deterioration such as photo-generated carrier accumulation inside the devices and/or morphological changes.

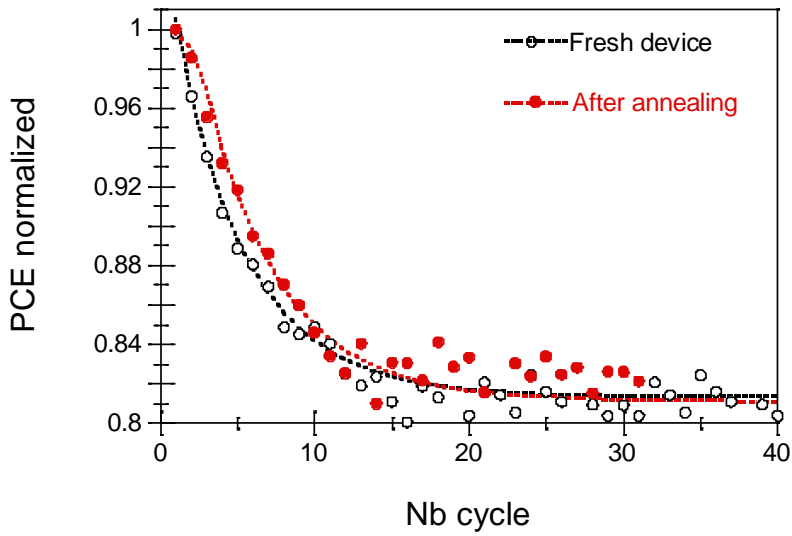


Figure 5.2: Fresh (●) and after re-annealing (○) PCE of pristine P3HT:PCBM PV device. The device was annealed at 165°C for 10 min and the PCE was measured again as a function of the number of electrical cycling measurements. Performance was normalized with respect to the initially measured value on fresh devices.

Several suggestions can be proposed to explain the degradation mechanisms in electrically stressed devices. The degradation of the organic based devices under electrical stress is closely linked to the apparition of defects in these materials.^[35] The formation of interfacial defects at the active layer/electrode interfaces generates interfacial traps. Kawano *et al.* have indentified the close relationship between device lifetime and the interfacial trap states at the active layer/electrode (active layer/PEDOT:PSS and active layer/aluminium) interfaces using thermally stimulated current techniques.^[36] They have showed that the creation of interfacial trap states in the organic solar cell leads to the initial performance degradations. The presence of defects leads to the formation of trap states at the metal/active-layer interfaces, resulting in charge accumulation.^[37] This charge accumulation at the photo active/electrode interface can cause a redistribution of electric field within the device leading to band bending (by space-charge effect) at the interfaces.^{[38][39]} This results in a voltage drop (or the reduction of V_{oc}). Furthermore, the carriers captured by the defect sites cannot participate in the transport process, and rather increase charge accumulation at the interfaces.^{[35][40]}

These accumulated charges close to the electrode lead to the creation of local electrical field opposite to the internal electrical field of the device.^[41] This field decreases the rate of charge extraction at the interface, thus reduces J_{SC} and the efficiency of devices. Therefore, it can be assumed that the degradation of performance observed on our devices under electrical cycling stress during the photodegradation study is likely related to charge accumulation at the active layer/electrode interfaces.

Furthermore, the restoration of device performance observed upon re-annealing after the repeatability measurement is another proof of the relaxation of charges from trap states located at the vicinity of interfaces. Device performance restoration phenomena have also been observed previously when degraded devices were kept in dark for some time.^{[42][43]} Katz *et al.* kept degraded devices overnight and obtained highest values of J_{SC} and V_{OC} during the first measurement of every morning compared to previous measurements. They inferred that the restoration effect is due to the disappearance of photo-induced trap sites. This effect indicates that cell degradation under electrical cycling is not due to an irreversible chemical damage in the organic materials or the photo-active layers. We can therefore attribute the initial degradation of the photovoltaic performance observed in our study to the created interfacial defects at the active layer/electrode interfaces.

5.4. Effect of the photodegradation on Device lifetime of P3HT:PCBM photovoltaic Devices – The Block Copolymer Approach

5.4.1. Fresh device performance

The operational lifetime $\tau_{1/2}$ was defined as the time for which the device efficiency reaches half of the initial value. Lifetimes are usually measured in an accelerated mode at an elevated temperature, high brightness, or both. However, accelerated cycles might introduce other aging mechanisms, making the estimation of the lifetime a complex issue. In our work, typical operating performance of devices was chosen to be driven under open-circuit conditions under illumination (100

mW/cm² with AM 1.5G filters) at an approximately constant temperature of $T = 55^{\circ}\text{C}$ until the *PCE* gets to 50% of its initial value. Lifetime experiments have been carried out on freshly prepared devices. Figure 5.3 shows the cell characteristics of the devices as a function of time under illumination by a solar simulator. Each value was normalized by its initial value. The decrease of PV performance depends on the nature of additives. The *PCE* achieves 50% of the initial value after 12 h, 18 h, 25 h and 28 h for the pristine device, 4% P3HT-*b*-PS, 5% PS-*b*-PI and 7% P3HT-*b*-PI copolymer containing blends, respectively. A loss of 4% in V_{OC} is observed for the PS-*b*-PI based devices while for the other devices a decrease of $\sim 12\%$ was recorded. Furthermore, the degradation process has a strong influence on J_{SC} and *FF*. The loss in J_{SC} leads to a decrease in *FF* resulting in a loss of device efficiency. This observation suggests that the decay of J_{SC} is a key parameter in the degradation of the device performance.

The *PCE* degradation can also be resolved by using an exponential decay function given by the relation 5.3. The degradation rate k_{deg2} obtained are reported in Table 5.3. The incorporation of copolymers as additives improve the lifetime of P3HT:PCBM photovoltaic devices. The decay rate of copolymer based devices is lower compared to the pure blend devices. Degradation rates of $3.1 \times 10^{-2} \text{ h}^{-1}$ and $2.8 \times 10^{-2} \text{ h}^{-1}$ have been obtained for P3HT-*b*-PI and PS-*b*-PI copolymer additives while $5.0 \times 10^{-2} \text{ h}^{-1}$ and $4.5 \times 10^{-2} \text{ h}^{-1}$ degradation rates were obtained for those of pristine and P3HT-*b*-PS copolymer additives, respectively, indicating that the P3HT-*b*-PI and PS-*b*-PI copolymer additives display the longer lifetime.

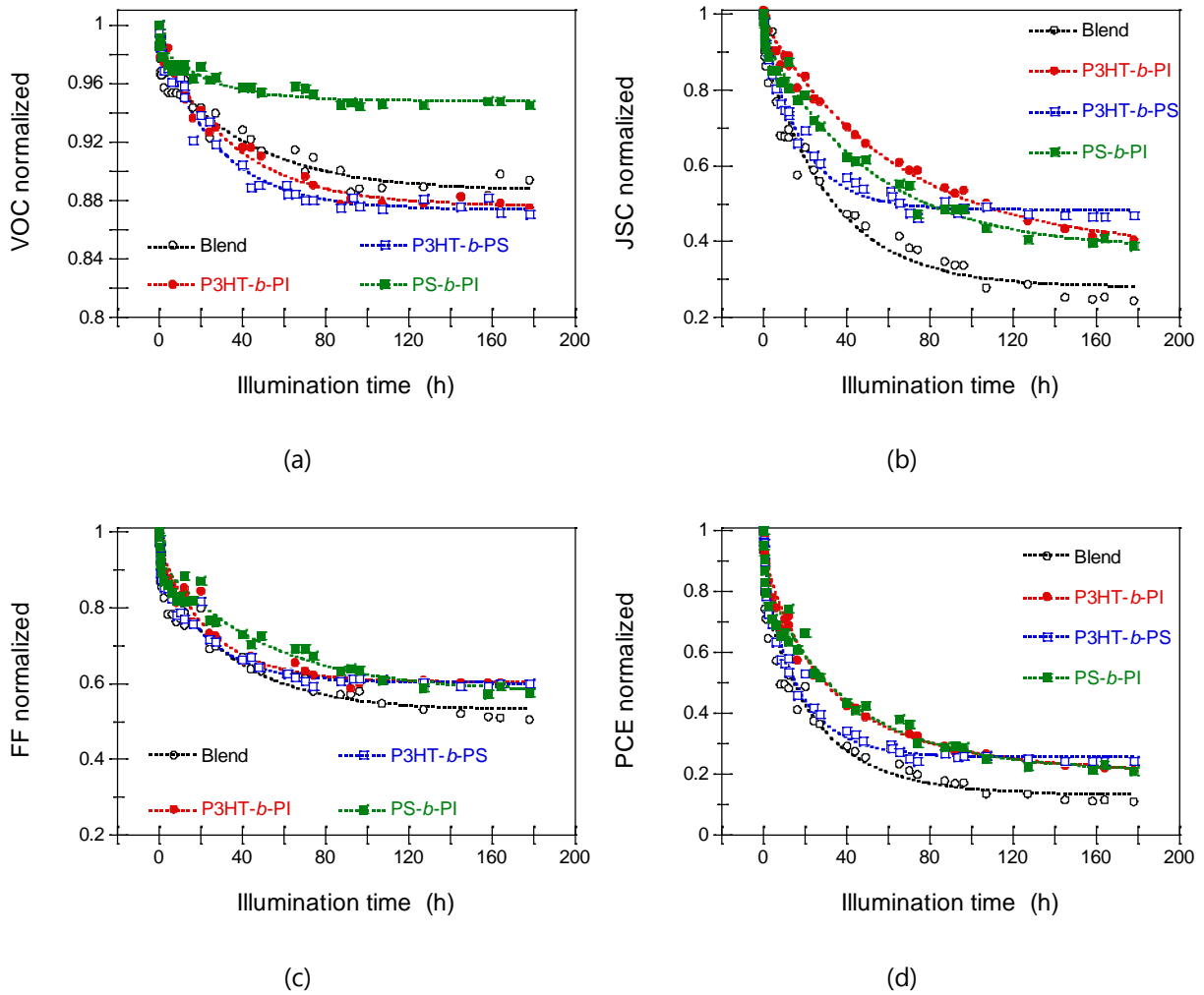


Figure 5.3: V_{OC} (a), J_{SC} (b), FF (c) and PCE (d), as a function of illumination time for pristine and copolymer containing devices. The measurements have been performed under continuous simulated AM1.5G solar irradiation of $100 \text{ mW}\cdot\text{cm}^{-2}$, on fresh devices under open-circuit conditions. Each value was normalized by its initial value. Each curve has been fitted by using relation 5.3.

Devices	k_{deg2} (h^{-1})	k_{deg3} (h^{-1})
Pristine P3HT:PCBM	5.0×10^{-2}	3.6×10^{-2}
+7% P3HT- <i>b</i> -PI	3.1×10^{-2}	1.7×10^{-2}
+4% P3HT- <i>b</i> -PS	4.5×10^{-2}	3.1×10^{-2}
+5% PS- <i>b</i> -PI	2.8×10^{-2}	2.6×10^{-2}

Table 5.3: Decay rates obtained with different additives based solar cells for describing PCE decay by using the fitting equation given by relation (5.3). k_{deg2} is PCE decay of fresh devices under illumination at 55°C. k_{deg3} is PCE decay of stabilized devices (after 10 electrical cycling measurements) under illumination at 55°C.

5.4.2. Stabilized device performance

It can be noted that during the degradation process, the initial decrease in performance likely corresponds to the degradation inherent to the repetition of the electrical measurements observed previously (Figure 5.1). Indeed, it was observed that up to 10 cycles of electrical measurements; the PV performance decreases exponentially and stabilizes afterwards. Since PV device lifetime is typically measured once “burn-in” is ended (or after the device has stabilized),^{[31][34]} we performed photo-degradation measurements (lifetime studies) on already stabilized devices (*i.e.* after 10 cycles of electrical cycling measurements). Figure 5.4 shows the variation of the photovoltaic parameters of stabilised devices versus illumination time when exposed under continuous simulated solar irradiation (100 mW/cm² illumination under AM 1.5 G and hot plate (~ 55°C)). Each value is normalized by the value measured after ten electrical cycling measurements. The lifetime of stabilized devices is greatly improved compared to the fresh devices for both pristine and copolymer incorporated devices. PCE achieves 50% of the initial value after 18 h, 28 h, 36 h and 43 h for pristine, P3HT-*b*-PS, PS-*b*-PI and P3HT-*b*-PI copolymer containing devices, respectively. P3HT-*b*-PI copolymer additive displays the longest stability. As it has been observed earlier on fresh devices (Figure 5.3), J_{sc} is again the most

affected during the degradation process leading to a decay of the PCE indicating that the photo-degradation is likely related to the active layer degradation. But, the P3HT- b -PI containing devices still shows a relatively slower J_{SC} decay than the others. Similar effect is also observed on the FF value. The FF of P3HT- b -PI copolymer additive decays relatively slower than the pristine and P3HT- b -PS copolymer containing devices and thus leads to a lower decrease of device efficiency. Generally, it implies that the active layer morphology is relatively stabilized by the P3HT- b -PI copolymer additive. The pristine and P3HT- b -PS additive displays roughly a similar decay in FF . While the effect on V_{OC} degradation for pristine as well as P3HT- b -PI and P3HT- b -PS copolymer additives is roughly similar (a loss of 8 %), the V_{OC} of PS- b -PI based devices is only decreasing by 4 % of the initial value.

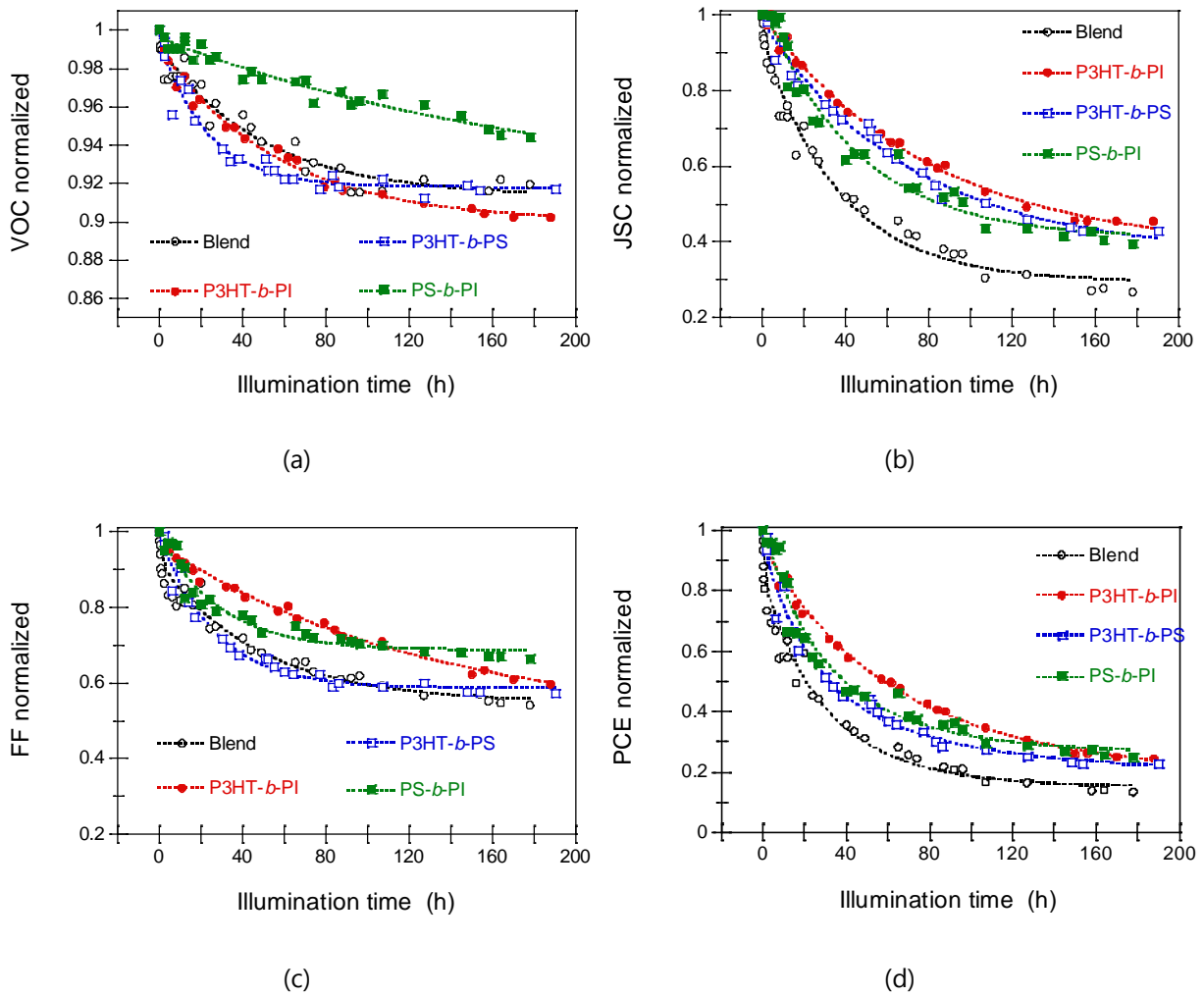


Figure 5.4: V_{OC} (a), J_{SC} (b), FF (c) and PCE (d), as a function of illumination time for pristine and

copolymer containing devices. The measurements have been performed on stabilized devices (after 10 electrical cycling measurements) under continuous simulated AM 1.5G solar irradiation of 100 mW.cm^{-2} in open-circuit condition. Each value is normalized by the value obtained after ten electrical cycling measurements. Each curve has been fitted by using relation 5.3.

The degradation process study carried out on stabilized devices has shown a lower decay of performance compared to the fresh devices. The *PCE* decrease can also be described by using an exponential decay function given by relation 5.3. The degradation rates k_{deg3} of stabilized devices are summarized in Table 5.3. The incorporation of block copolymers into P3HT:PCBM blend leads to a decrease in the decay rate (k_{deg3}) of stabilized devices. The lowest degradation rate ($k_{deg3} = 1.7 \times 10^{-2} \text{ h}^{-1}$) is obtained by adding P3HT-*b*-PI copolymer, confirming the improvement in the lifetime of stabilized devices. The decay rates of the pristine device, P3HT-*b*-PS and PS-*b*-PI additives attain $3.6 \times 10^{-2} \text{ h}^{-1}$, $3.1 \times 10^{-2} \text{ h}^{-1}$ and $2.6 \times 10^{-2} \text{ h}^{-1}$, respectively.

The lifetime measurements obtained on the fresh and stabilized devices have been performed in similar conditions. It can be noted that the decay rate k_{deg3} of stabilized devices is smaller than the one of fresh devices k_{deg2} suggesting that the degradation mechanism of fresh devices is probably more complex than the one of stabilized devices. From our understanding, the *PCE* decay obtained from the fresh devices can be related to two degradation phenomena: one of these would likely originate from the repetition of the electrical measurements while the other one would be related to the photo-degradation. In order to confirm these assumptions, a fitting curve, $PCE_{Fitting}$ given by relation (5.4), has been resolved by using two components in order to decouple each contribution.

$$PCE_{Fitting}(t) = PCE_{elec}(t) \cdot PCE_{photo}(t) \quad (5.4)$$

The first component, labelled PCE_{elec} , is related to the degradation inherent to electrical cycling measurements (obtained from the repetitive measurement indicated in Figure 5.2). The second component, labelled PCE_{photo} , corresponds to the photo-degradation at 55°C obtained from the stabilized devices (Figure 5.4). The fitting curves $PCE_{fitting}$ obtained for the pristine devices are reported

on Figure 5.5. It is noteworthy that the PCE decay of fresh pristine device (without stabilization) is well-described with fitting curve $PCE_{fitting}$. Hence, PCE_{fresh} can be resolved by using the two exponential curves, suggesting that the degradation of fresh devices can be analysed by considering two distinct degradation processes: *i*) the initial decrease can be related to the electrical cycling stress observed previously (from repeatability measurements); *ii*) the photo and temperature induced degradation. It should be noted that the decay rates; k_{deg2} and k_{deg3} , obtained from the fresh and stabilized devices of PS-*b*-PI copolymer additive are approximately similar (see Table 5.3). It suggests that devices from PS-*b*-PI copolymer additive are less sensitive to the electrical induced degradation than the other devices while the P3HT-*b*-PI additive has shown the lowest k_{deg3} suggesting that they are less affected by photo-degradation than the other devices.

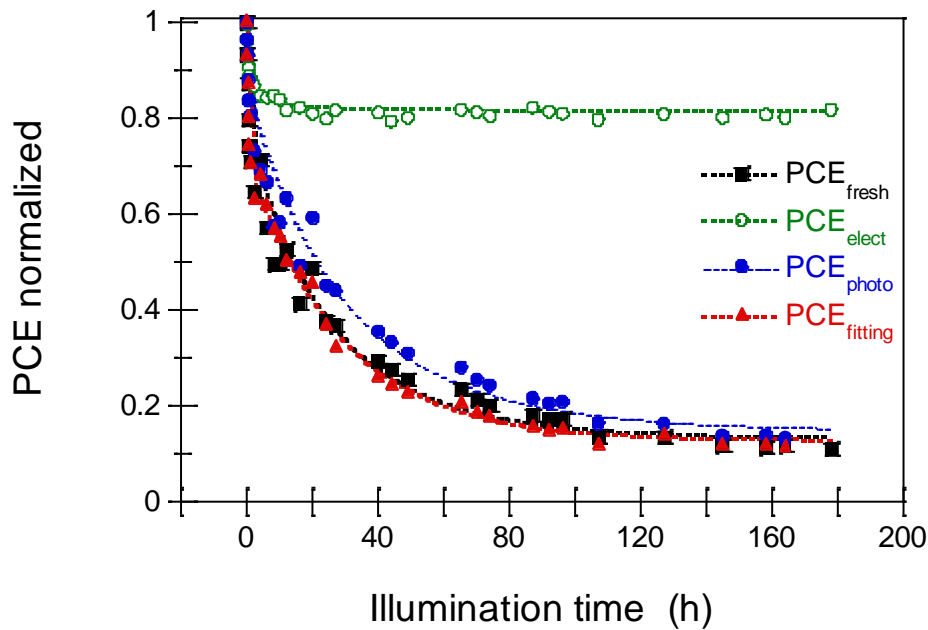


Figure 5.5: PCE decay of pure pristine devices versus the illumination time at 55°C. PCE_{fresh} (■) is the PCE decay of fresh devices under illumination. PCE_{photo} (○) is PCE decay of stabilized devices under illumination. PCE_{elec} (●) is the decay of PCE caused by repetitive electrical stress determined from repeatability measurement. $PCE_{fitting}$ (▲) is a fitting curve resolved from relation 5.4 by using two components PCE_{photo} and PCE_{elec} . Each value is normalized by their initial value.

From the results obtained, the mechanisms of degradation during the photodegradation study of the PV devices can be decoupled in two categories: i) those caused by electrical stresses (due to the cycling measurements) and ii) those resulting from illumination (photo-degradation). As the measurements were performed under inert atmosphere the degradation induced by oxygen (photo-oxidation) or other contamination has been excluded. We have already discussed in details the degradation mechanism resulting from electrical stresses during the repeatability measurements. In the next sub-chapter, we will examine some of the changes inherent to photodegradation and its influence on device performance.

5.4.3. Device Ageing Mechanisms

5.4.3.1. Photodegradation

Photo-degradation is attributed to structural modifications or/and chemical processes occurring in the active layer; *i.e.* highly phase separated microstructure evolution (morphological changes), chain-breakages, contamination or diffusion of metallic species into the active layer from the electrodes, thermal induced active layer degradation, charge accumulation at interfaces due to continuous creation of charges, etc. Herein, some of the photo induced degradation mechanisms are discussed.

i) Effect of temperature

It has been shown that the glass substrate absorbs significant UV radiation, creating a localized annealing effect due to the increase in temperature at the electrode/active layer interface.^[44] This leads to the reorganization of the mesostructures into crystalline phases that have different arrangements or conformations of the molecules or into different domain sizes due to a possible coarsening of the phase separated systems at the vicinity of the active layer/electrode interface. Thus, it can affect the lifetime and stability of devices. In addition, the global increase in temperature upon continuous

illumination is one of the accelerating factors in device ageing mechanisms. For example, in our investigation, the thermocouple of the plate where samples were analyzed was recording a temperature of $\sim 55^\circ\text{C}$ (as the result of the continuous illumination). The increase in temperature can lead to morphological instability in the active layer and degrades device performance. In order to find out about the effect of temperature, we first determined the degradation factor for the experimental data using relation 5.3 (values are shown in Table 5.3) and then we calculated the degradation factor for a given temperature $K_{deg}(T_1)$ using relation 5.2 (in this case we set T_1 to be 25°C). By using the computed degradation factor ($K_{deg}(T_1)$), we could extrapolate the variation of performance. Figure 5.6 shows the *PCE* variation of fresh (Figure 5.6a) and stabilized (Figure 5.6b) solar cells as a function of the illumination time (under AM 1.5G, 100 mW/cm^2 illumination) estimated at 25°C working conditions based on the experimental measurements at 55°C . For the fresh devices, the *PCE* achieves 50% of the initial value after 65 h, 83 h, 114 h and 125 h of illumination time for pristine, P3HT-*b*-PS, PS-*b*-PI and P3HT-*b*-PI copolymer containing devices, respectively. For the stabilized devices (corresponding to the one obtained after the electrical cycling measurements), *PCE* achieves 50% of its value after 92 h, 167 h, 190 h and 226 h of illumination for the pristine, P3HT-*b*-PS, PS-*b*-PI and P3HT-*b*-PI copolymer containing devices, respectively. As compared to the experimental results, the extrapolated results have shown a major increase in the estimated lifetime of devices at 25°C compared to 55°C .

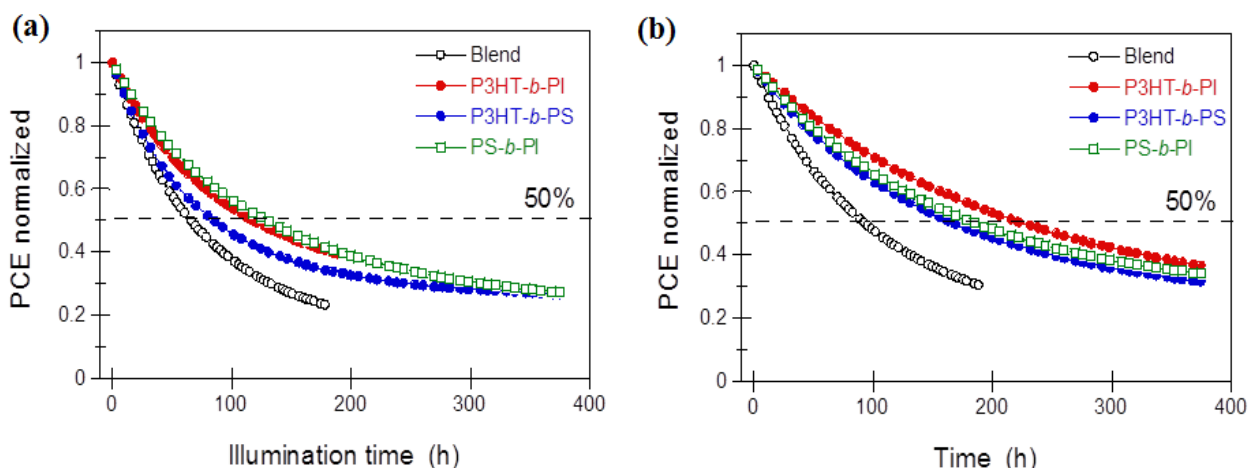
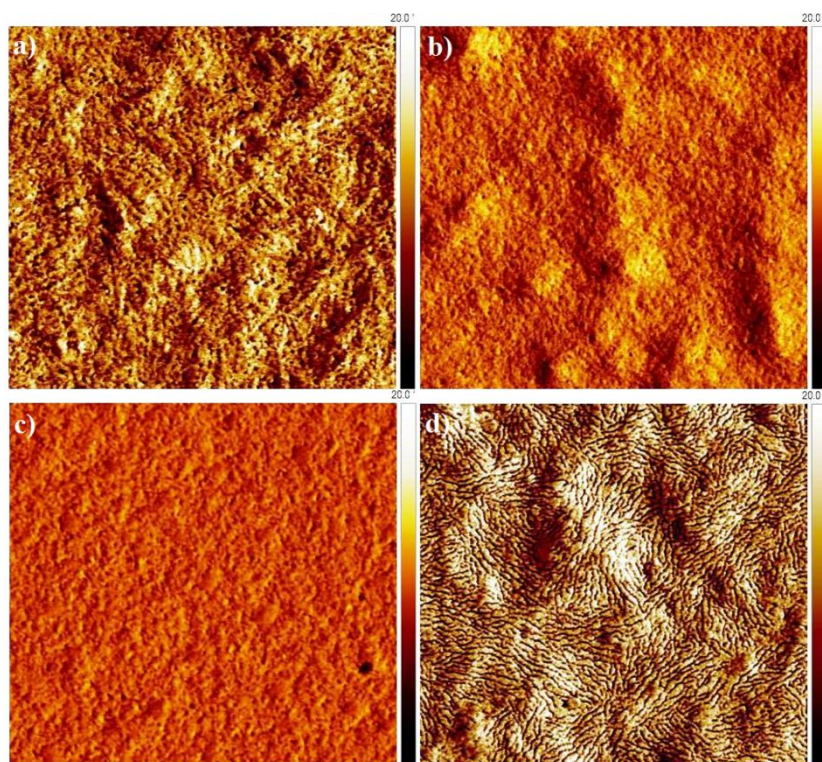


Figure 5.6: Variation of PCE for pristine and copolymer containing devices for (a) fresh and (b) stabilized solar cells as a function of illumination time under AM 1.5G, 100 mW/cm^2 illumination in open circuit condition, estimated for $25 \text{ }^\circ\text{C}$ working conditions based on measurements at $55 \text{ }^\circ\text{C}$.

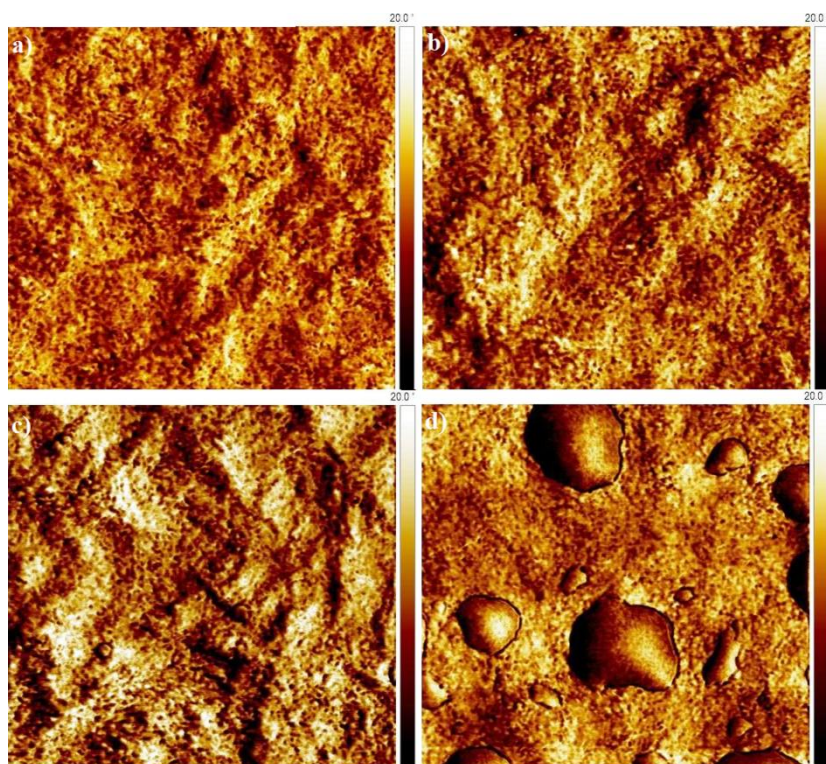
ii) Morphological changes

In another development, the continuous illumination of devices leads to a change in film morphology. Morphological instabilities at the interfaces between the organic film and the electrodes have been shown to be responsible of the reduction of device performance.^{[45][46][47]} In order to observe the morphological changes occurring through the illumination process, SFM images have been taken before and after illumination. Before illumination, similar morphological features were observed for the P3HT-*b*-PI and P3HT-*b*-PS additive films, while the pristine and the PS-*b*-PI copolymer additive exhibit fibrillar morphology, as shown in Figure 5.7 (I). However, after 200 hrs of illumination, the morphological features (like domain size and shape, and roughness) have hugely changed (see Figure 5.7 (II)). As observed in the SFM images, the prolonged solar irradiation on P3HT:PCBM films at 55°C resulted in the formation of stream like features. The biggest morphological differences was observed for PS-*b*-PI containing films; from P3HT-fibrils at the beginning of illumination to the formation of very large spherical aggregates (bubble-like) after 180 hr illuminations. The change of morphology into stream-like (hills and gorges) features or bubble-like morphologies upon illumination in the case of pristine as well as block copolymer containing films could be the responsible factor for the increase in

the degradation rate of the device performance by either increasing trap formation due to morphological defects at the donor-acceptor interface or due to the poor contact developed at the active layer/electrode interfaces. Poor contacts at the active layer/electrode interface could result in a less efficient charge collection by the electrode and hence in a decrease in FF and J_{SC} .^[48] Morphological changes of P3HT:PCBM films upon illumination have been observed by Manceau *et al.*^[49] They suggest that at 60°C with prolonged illumination time, the PCBM can diffuse into the amorphous part of the polymeric matrix, leading to the formation of large PCBM aggregates. This could result in reduction of charge generation in the active layer. Even though it was possible to observe big morphological differences in the case of PS-*b*-PI copolymer containing films, the degradation rate (k_{deg3}) was still lower than the pristine device (Table 5.3). This could be related to the resistance of UV radiation developed by polystyrene and/or polyisoprene species in PS-*b*-PI containing devices as compared to the pristine devices. Generally, the lower degradation rate that is observed upon block copolymer incorporation could be associated to the preferential interaction that exists between the block copolymers (particularly, P3HT-*b*-PI and P3HT-*b*-PS) and the components of P3HT and PCBM domains (see Chapter 4). This favourable interaction stabilizes the active layer morphology and suppresses larger phase separations among P3HT and PCBM domains during the prolonged thermal annealing at 55°C upon illumination.



(I)



(II)

Figure 5.7: $2 \times 2 \mu\text{m}^2$ Tapping mode SFM phase images showing the morphology of P3HT:PCBM devices before (I) and after (II) aging obtained for pristine device (a) 7% P3HT-*b*-PI (b), 4% P3HT-*b*-PS (c) and 5% PS-*b*-PI (d). The images are taken from the area that is found between two diodes of the real PV devices.

iii) Charge accumulation at interfaces

The results presented in the previous section concerning devices that were maintained in open-circuit conditions under illumination suggest that the photogenerated charges are accumulated inside the active layer. Hermenau *et al.* has observed that the excitons, generated through light absorption, cause the degradation of illuminated samples.^[37] They suggest that the number of extracted charge carriers is important for the state of the solar cell during ageing. Keeping this argument in mind, we have investigated the device lifetime under short-circuit conditions (at zero applied voltage) using similar experimental procedures employed in under open-circuit conditions. Figure 5.8 shows the results obtained after devices underwent photodegradation in short-circuit condition after 10 electrical cycling measurements. All the PV characteristics are less affected than under open-circuit conditions. V_{OC} is almost stable with only $\sim 3\%$ lost. The observed losses mainly occur in J_{SC} and FF . Analogously to the open-circuit condition, the decrease in PCE under short-circuit condition is also described by using an exponential decay function given by relation 5.3. The degradation rates k_{deg3} of stabilized devices under short-circuit condition are summarized in Table 5.4. In all cases, we found lowest degradation rates ($6.8 \times 10^{-3} \text{ h}^{-1}$, $4.4 \times 10^{-3} \text{ h}^{-1}$, $5.6 \times 10^{-3} \text{ h}^{-1}$ and $4.7 \times 10^{-3} \text{ h}^{-1}$ for pristine, P3HT-*b*-PI, P3HT-*b*-PS and PS-*b*-PI containing devices, respectively) confirming that charge carriers are better extracted resulting in an improvement of device lifetime under short-circuit conditions. Accordingly, the devices half-lifetime (50% of the initial value) has significantly changed from 18 hrs, 43 hrs, 28 hrs, 36 hrs when devices are left illuminated under open-circuit condition, to 170 hrs, 300 hrs, 260 hrs, 260 hrs when devices are left illuminated under short-circuit condition for pristine, 7% P3HT-*b*-PI, 4% P3HT-*b*-PS and 5% PS-*b*-PI containing blends, respectively.

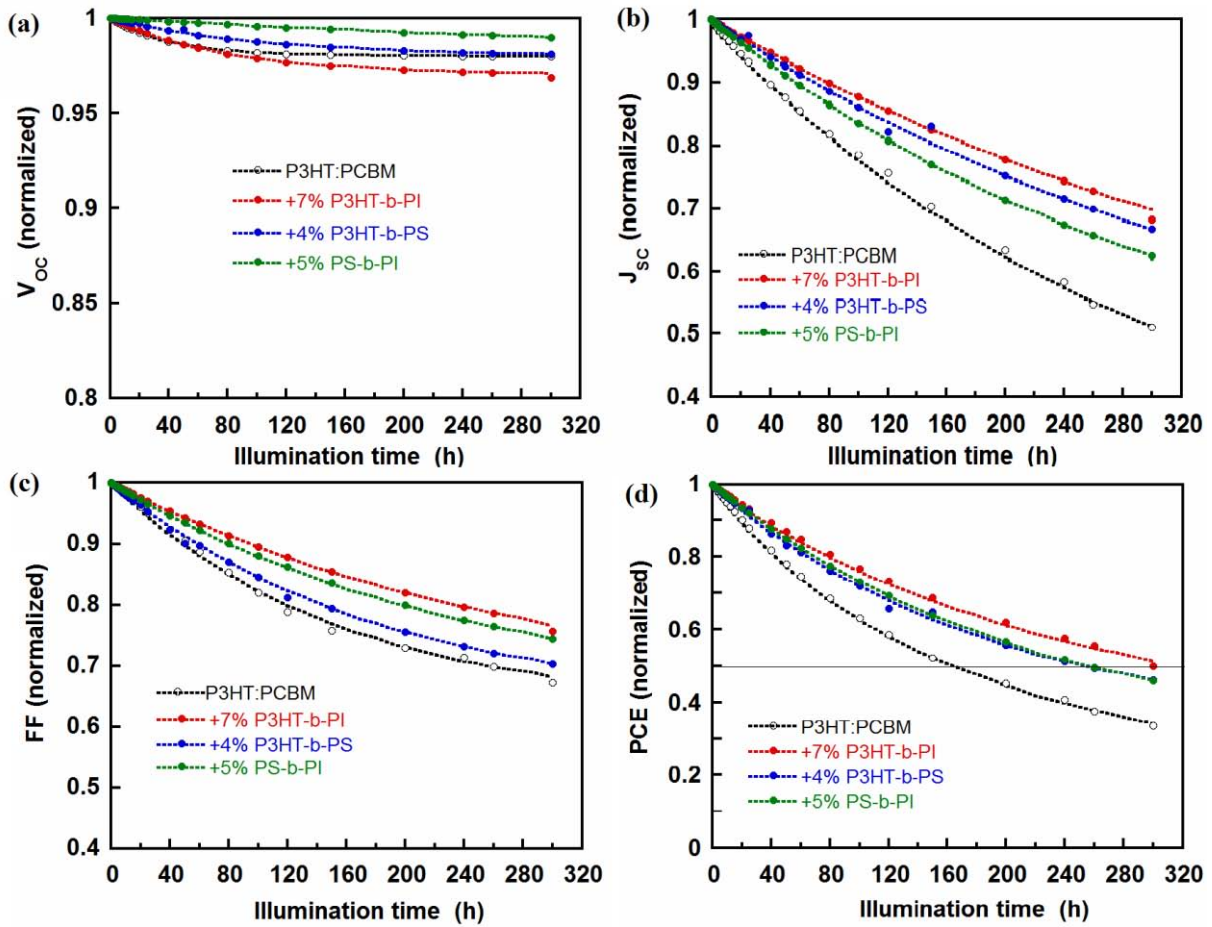


Figure 5.8: V_{OC} (a), J_{SC} (b), FF (c) and PCE (d), as a function of illumination time for pristine and copolymer containing devices. The measurements have been performed on stabilized devices (after 10 electrical cycling measurements) under continuous simulated AM 1.5G solar irradiation of 100 mW.cm^{-2} **in short-circuit condition**. Each value is normalized by the value obtained after ten electrical cycling measurements. Each curve has been fitted by using relation 5.3.

Devices	k_{deg2} (h ⁻¹)	k_{deg3} (h ⁻¹)
Blend	1.1×10^{-2}	6.8×10^{-3}
7% P3HT- <i>b</i> -PI	8.6×10^{-3}	4.4×10^{-3}
4% P3HT- <i>b</i> -PS	9.0×10^{-3}	5.6×10^{-3}
5% PS- <i>b</i> -PI	7.7×10^{-3}	4.7×10^{-3}

Table 5.4: Decay rates obtained with different additives based solar cells for describing PCE decay by using fitting curve given by relation 5.3. k_{deg2} and k_{deg3} are PCE decay rates of fresh and stabilized (after 10 electrical cycling measurements) devices measured under short-circuit condition and illuminated at 55°C.

iv) Defects or formation of traps

Several investigations have also correlated the aging of organic devices to an enhancement in defect densities.^{[50][51]} Since our devices were exposed under continuous illumination in open-circuit condition (*i.e.* excitons and charges are continuously created without collection), a model developed for OLEDs can be used to explain the degradation of organic devices. Silvestre *et al.* inferred that the transitions of higher energy such as band to band transitions may provide sufficient energy (*i.e.* energetic dissipation) to create defects and produce traps in the band gap of the polymer.^[52] This hypothesis was proposed by considering the creation of hot electrons (hot charge carriers), which would break molecular chains and produce traps.^[51] According to this analysis, the trap concentration determines the electrical aging of a device (*i.e.* the higher the trap density, the faster is the ageing in organic devices). In another case, the formation of defect states or voids upon the continuous illumination facilitates the degradation of organic devices.^[53] Though, it is possible to estimate trap densities from the trap-free region (in the *Space Charge Limited Current, SCLC*, region) of the *J-V* characteristics in the dark using Child's law,^{[54][55]} or from experimental work using impedance or thermally stimulated current spectroscopy, such studies have not been performed during this Ph.D. due to time constraints.

5.5. Conclusion

To summarize, the results of the reproducibility study reveal that the fabrication processes employed during this Ph.D. are reproducible. The electrical cycling experiments suggest that the interfacial states play a key role in the degradation processes inherent to electrical stresses. The restoration effect observed through the re-annealing treatment suggests that this degradation process is not related to irreversible chemical structure changes but to morphological changes which are reversible upon thermal annealing. Furthermore, under illumination, the degradation of performance is related to morphology and structural modification in the active layer. Besides, the charge accumulation has been seen to significantly affect the device stability. This was indirectly confirmed when devices were investigated under short-circuit condition. The analyses of the PV decays of the fresh devices show that the performance degradation under illumination is a complex mechanism which can be linked to an electrical origin such as charge flow within active layer and a photo and thermal induced active layer degradation. The influence of semiflexible rod-coil block copolymers used as additives to promote the stability of P3HT:PCBM PV devices was investigated. The stability of the P3HT:PCBM devices was improved by adding P3HT-*b*-PI, P3HT-*b*-PS and PS-*b*-PI block copolymers mostly through a morphological stabilization. The lifetime of devices is approximately doubled by adding P3HT-*b*-PI block copolymer. This implies that adding a properly selected block copolymer into polymeric PV blends is an interesting strategy for increasing device efficiency as well as for increasing device stability under solar illuminations.

References

- [1] L. Dou, J. You, J. Yang, C. Chen, Y. He, S. Murase, T. Moriarty, K. Emery, G. Li, Y. Yang, *Nature Photonics* **2012**, 6, 180–185.
- [2] Z. He, C. Zhong, S. Su, M. Xu, H. Wu, Y. Cao, *Nature Photonics* **2012**, 6, 591–595.
- [3] C.E. Small, S. Chen, J. Subbiah, C.M. Amb, S. Tsang, T. Lai, J.R. Reynolds, F. So, *Nature Photonics* **2012**, 6, 115–120.
- [4] Heliatek, [Http://www.heliatek.com/wp-content/uploads/2013/01/130116_PR_Heliatek_achieves_record_cell_efficiency_for_OPV.pdf](http://www.heliatek.com/wp-content/uploads/2013/01/130116_PR_Heliatek_achieves_record_cell_efficiency_for_OPV.pdf); Accessed on January 2013 **2013**.
- [5] M. Jørgensen, K. Norrman, F.C. Krebs, *Solar Energy Materials and Solar Cells* **2008**, 92, 686–714.
- [6] N. Grossiord, J.M. Kroon, R. Andriessen, P.W.M. Blom, *Organic Electronics* **2012**, 13, 432–456.
- [7] L.-M. Do, M. Oyamada, A. Koike, E.-M. Han, N. Yamamoto, M. Fujihira, *Thin Solid Films* **1996**, 273, 209–213.
- [8] S. Bertho, G. Janssen, T.J. Cleij, B. Conings, W. Moons, *Solar Energy Materials & Solar Cells* **2008**, 92, 753–760.
- [9] G.G. Andersson, M.P. de Jong, G.J.J. Winands, A.W.D. van der Gon, L.J. van IJzendoorn, H.H. Brongersma, M.A. de Voigt, *J. Phys. D: Solid State Phys.*, **2002**, 35, 1103–1108.
- [10] H. Aziz, Z. Popovic, C.P. Tripp, N.-X. Hu, A.-M. Hor, G. Xu, *Applied Physics Letters* **1998**, 72, 2642.
- [11] J. McElvain, H. Antoniadis, M.R. Hueschen, J.N. Miller, D.M. Roitman, J.R. Sheats, R.L. Moon, *Journal of Applied Physics* **1996**, 80, 6002.
- [12] O. Haillant, D. Dumbleton, A. Zielnik, *Solar Energy Materials and Solar Cells* **2011**, 95, 1889–1895.
- [13] W. Zhao, T. Cao, J.M. White, *Advanced Functional Materials* **2004**, 14, 783–790.
- [14] M. Hermenau, M. Riede, K. Leo, S.A. Gevorgyan, F.C. Krebs, K. Norrman, *Solar Energy Materials and Solar Cells* **2011**, 95, 1268–1277.
- [15] F.C. Krebs, K. Norrman, *Progress in Photovoltaics: Research and Applications* **2007**, 15, 697–712.
- [16] K.Z. Xing, N. Johansson, G. Beamson, D.T. Clark, J.-L. Bredas, W.R. Salaneck, *Advanced Materials* **1997**, 1027–1031.
- [17] K. Kawano, R. Pacios, D. Poplavskyy, J. Nelson, D.D.C. Bradley, J.R. Durrant, *Solar Energy Materials and Solar Cells* **2006**, 90, 3520–3530.
- [18] T. Jeranko, H. Tributsch, N. Sariciftci, J. Hummelen, *Solar Energy Materials and Solar Cells* **2004**, 83, 247–262.
- [19] A. Rivaton, S. Chambon, M. Manceau, J.-L. Gardette, N. Lemaître, S. Guillerez, *Polymer Degradation and Stability* **2010**, 95, 278–284.
- [20] B. Paci, A. Generosi, V. Rossi Albertini, P. Perfetti, R. de Bettignies, C. Sentein, *Solar Energy Materials and Solar Cells* **2008**, 92, 799–804.
- [21] M. Manceau, A. Rivaton, J.-L. Gardette, S. Guillerez, N. Lemaître, *Solar Energy Materials and Solar Cells* **2011**, 95, 1315–1325.
- [22] L.-M. Chen, Z. Hong, G. Li, Y. Yang, *Advanced Materials* **2009**, 21, 1434–1449.
- [23] J. Bandara, K. Shankar, C.A. Grimes, M. Thelakkat, *Thin Solid Films* **2011**, 520, 582–590.

- [24] J. Li, S. Kim, S. Edington, J. Nedy, S. Cho, K. Lee, A.J. Heeger, M.C. Gupta, J.T. Yates Jr, *Solar Energy Materials and Solar Cells* **2011**, *95*, 1123–1130.
- [25] H.J. Kim, A.-R. Han, C.-H. Cho, H. Kang, H.-H. Cho, M.Y. Lee, J.M.J. Fréchet, J.H. Oh, B.J. Kim, *Chemistry of Materials* **2012**, *24*, 215–221.
- [26] C.-Y. Chang, C.-E. Wu, S.-Y. Chen, C. Cui, Y.-J. Cheng, C.-S. Hsu, Y.-L. Wang, Y. Li, *Angewandte Chemie (International Ed. in English)* **2011**, *50*, 9386–9390.
- [27] J.E. Carlé, B. Andreasen, T. Tromholt, M. V. Madsen, K. Norrman, M. Jørgensen, F.C. Krebs, *Journal of Materials Chemistry* **2012**, *22*, 24417–24423.
- [28] G. Griffini, S. Turri, M. Levi, *Polymer Bulletin* **2011**, *66*, 211–222.
- [29] M. Sun Ryu, H. Jin Cha, J. Jang, *Solar Energy Materials and Solar Cells* **2010**, *94*, 152–156.
- [30] S. Xiao, M. Nguyen, X. Gong, Y. Cao, H. Wu, D. Moses, a. J. Heeger, *Advanced Functional Materials* **2003**, *13*, 25–29.
- [31] M.O. Reese, S. a. Gevorgyan, M. Jørgensen, E. Bundgaard, S.R. Kurtz, D.S. Ginley, D.C. Olson, M.T. Lloyd, P. Morvillo, E. a. Katz, A. Elschner, O. Haillant, T.R. Currier, V. Shrotriya, M. Hermenau, M. Riede, K. R. Kirov, G. Trimmel, T. Rath, O. Inganäs, F. Zhang, M. Andersson, K. Tvingstedt, M. Lira-Cantu, D. Laird, C. McGuinness, S. Gowrisanker, M. Pannone, M. Xiao, J. Hauch, R. Steim, D.M. DeLongchamp, R. Rösch, H. Hoppe, N. Espinosa, A. Urbina, G. Yaman-Uzunoglu, J.-B. Bonekamp, A.J.J.M. van Breemen, C. Girotto, E. Voroshazi, F.C. Krebs, *Solar Energy Materials and Solar Cells* **2011**, *95*, 1253–1267.
- [32] S. Schuller, P. Schilinsky, J. Hauch, C.J. Brabec, *Applied Physics A: Materials Science & Processing* **2004**, *79*, 37–40.
- [33] R. De Bettignies, J. Leroy, M. Firon, C. Sentain, *Synthetic Metals* **2006**, *156*, 510–513.
- [34] C.H. Peters, I.T. Sachs-Quintana, J.P. Kastrop, S. Beaupré, M. Leclerc, M.D. McGehee, *Advanced Energy Materials* **2011**, *1*, 491–494.
- [35] C. Renaud, T.-P. Nguyen, *Journal of Applied Physics* **2009**, *106*, 053707.
- [36] K. Kawano, C. Adachi, *Advanced Functional Materials* **2009**, *19*, 3934–3940.
- [37] M. Hermenau, S. Scholz, K. Leo, M. Riede, *Solar Energy Materials and Solar Cells* **2011**, *95*, 1278–1283.
- [38] G.G. Malliaras, J.R. Salem, P.J. Brock, J.C. Scott, *Journal of Applied Physics* **1998**, *84*, 1583.
- [39] V.D. Mihailetschi, P.W.M. Blom, J.C. Hummelen, M.T. Rispens, *Journal of Applied Physics* **2003**, *94*, 6849.
- [40] T.P. Nguyen, C. Renaud, *Proc. SPIE* **2009**, *7213*, 721314.
- [41] P.J. Brewer, P.A. Lane, J. Huang, J. Andrew, D.D.C. Bradley, *Physical Review B* **2005**, *71*, 205209.
- [42] E.A. Katz, S. Gevorgyan, M.S. Orynbayev, F.C. Krebs, *Eur. Phys. J. Appl. Phys.* **2007**, *36*, 307–311.
- [43] N. Camaioni, G. Ridolfi, G. Casalbore-miceli, G. Possamai, *Solar Energy Materials and Solar Cells* **2003**, *76*, 107–113.
- [44] P. Sullivan, T.S. Jones, *Organic Electronics* **2008**, *9*, 656–660.
- [45] M.O. Reese, A.J. Morfa, M.S. White, N. Kopidakis, S.E. Shaheen, G. Rumbles, D.S. Ginley, *Solar Energy Materials and Solar Cells* **2008**, *92*, 746–752.
- [46] B. Paci, a. Generosi, D. Bailo, V. Rossi Albertini, R. de Bettignies, *Chemical Physics Letters* **2010**, *494*, 69–74.

- [47] G.F. Malgas, C.J. Arendse, S. Mavundla, F.R. Cummings, *Journal of Materials Science* **2008**, *43*, 5599–5604.
- [48] A. Kumar, G. Li, Z. Hong, Y. Yang, *Nanotechnology* **2009**, *20*, 165202.
- [49] M. Manceau, A. Rivaton, J.-L. Gardette, S. Guillerez, N. Lemaitre, *Solar Energy Materials & Solar Cells* **2011**, *95*, 1315–1325.
- [50] P.P. Boix, J. Ajuria, I. Etxebarria, R. Pacios, G. Garcia-Belmonte, *Thin Solid Films* **2012**, *520*, 2265–2268.
- [51] K.C. Kao, *Journal of Applied Physics* **1984**, *55*, 752.
- [52] G.C.M. Silvestre, M.T. Johnson, a. Giraldo, J.M. Shannon, *Applied Physics Letters* **2001**, *78*, 1619.
- [53] D. Liufu, X.S. Wang, D.M. Tu, K.C. Kao, *Journal of Applied Physics* **1998**, *83*, 2209.
- [54] A. Carbone, C. Pennetta, L. Reggiani, *Applied Physics Letters* **2009**, *95*, 233303.
- [55] F.-C. Chiu, H.-W. Chou, J.Y. Lee, *Journal of Applied Physics* **2005**, *97*, 103503.

Chapter - VI
Conclusions and Outlook

6.1. Conclusions

One of the features that render organic photovoltaics as an attractive alternative to their inorganic counterparts is the solution processability of the organic constituents that form the active layer. Solar cells made of a photo-active conjugated polymer as the electron donor and a soluble fullerene derivative as the electron acceptor have consequently shown great potential in the field of renewable energy technologies despite of some limitations in performance. In order to enhance the performance of organic photovoltaic cells, the morphology of this phase-separated donor/acceptor blend has to be tailored; *i.e.* exciton dissociation at the interfaces should be maximized by tuning the domain size to be comparable to the excitonic diffusion length (~10 nm) and charge transport to the electrodes should be promoted through a co-continuous network that provides pathways to the corresponding electrodes. Consequently the main objective of this study was: i) to understand the phase separation (both in plane and normal to the substrate) of the archetypical P3HT:PCBM blend; ii) to tailor this phase separation by the addition of a third component able to add a desired functionality to the system.

Consequently the effect of the macromolecular characteristics of P3HT (molecular weights and dispersity) and the different processing parameters (thermal annealing and ratio of the components) on the microstructure and performance of P3HT:PCBM BHJ organic solar cells have been thoroughly investigated in this manuscript. The results have showed that the P3HT macromolecular characteristics are determining factors for the resulting morphologies of P3HT:PCBM blends. In order to optimize the PV performance, the optimal ratios between P3HT and PCBM has to be correlated with the P3HT molecular weight. Besides the establishment of the P3HT:PCBM phase diagram had consequently provided a better understanding of the interdependences between P3HT crystallization, the formation of PCBM microscale agglomerates, and more generally, the phase separation mechanisms occurring during the annealing process. We have demonstrated that the maximum photovoltaic characteristics were obtained at eutectic or close to eutectic composition for the different Mn of P3HT under study.

This study has shown the crucial importance of the determination of the phase diagram for the optimization of OPV cells, and thus, underlines the usefulness of such approach for the evaluation of new materials for OPV applications.

In addition, neutron reflectometry has provided us valuable information about the P3HT:PCBM BHJ concentration profile within a real solar cell configuration (*i.e.* the active layers are casted on PEDOT:PSS and TiO_x layers). It was shown that the concentration profile is not homogeneous along the normal to the substrate. A 60% and 75% PCBM enrichment at the interface with PEDOT:PSS and TiO_x, respectively, has been revealed as well as a PCBM depletion at the free surface of the film which is driven by the lower surface energy of P3HT. Besides the PCBM segregation close to the substrate is further enhanced by annealing. This stratification can be detrimental for conventional solar cell performance, since the electron-acceptor material enriches the interface of the hole-collecting electrode. The agglomeration of PCBM at the TiO_x interface could, however, be favorable for an enhanced charge collection, thus improving device performance.

In order to enhance the photovoltaic properties, we adopt a methodology for the optimization of the active layer mesostructure involving the use of well-defined block copolymers. Three main added functionalities were obtained through this approach: i) the compatibilization between the P3HT and the PCBM in order to limit an extended phase separation with the P3HT-*b*-PS system; ii) an improved P3HT crystallization for PV applications leading to a less extended PCBM agglomeration with the P3HT-*b*-PI system; iii) the definition of a solar cell device fabrication process not involving thermal annealing for the P3HT:PCBM blend with the P3HT-*b*-P4VP system. The results obtained in this work have indicated that the incorporation of materials with self-assembling properties into P3HT:PCBM PV blends leads to minimize the microscale phase separation among the donor:acceptor components through an improved miscibility between the donor:acceptor phases. Concurrently, more homogeneous (less PCBM agglomerates) – at the microscopic scale – blends were observed, underlining the less extended macro-scale phase separation between P3HT and PCBM. Besides it has

been shown that P3HT-*b*-PI can also interfere with the P3HT crystallization. Indeed this kind of block copolymers have shown to enhance the polymer crystallinity in P3HT:PCBM PV blends, and consequently improve the power conversion efficiency (4.5 ± 0.1 % was achieved for the 7% (wt.) P3HT-*b*-PI containing blend). A key result was also obtained through the incorporation of P3HT-*b*-P4VP block copolymer into P3HT:PCBM blends. Indeed such additive has shown the possibility to optimize the active layer morphology as regards to the PV performance without the use of thermal annealing while keeping efficiency as high as or higher than the corresponding thermal annealing device. This result paves the way for the fabrication of OPV cells through low cost roll-to-roll process on flexible polymer substrates where thermal annealing at elevated temperature is detrimental.

In addition to the increase in PV performance, the incorporation of rod-coil block copolymers into P3HT:PCBM PV blends has been shown the increase in the stability of devices under prolonged illumination. The highest lifetime under illumination (both in open-circuit and short-circuit condition) was obtained by adding P3HT-*b*-PI block copolymer. The lifetime of devices is approximately doubled. The analyses of the PV decays of the fresh devices show that the performance degradation under illumination is a complex mechanism which can be linked to an electrical origin such as charge flow within active layer and to a photo induced degradation process.

6.2. Outlook

The incorporation of block copolymers into OPV blends has shown their ability to modify the crystallization properties of the donor polymer as well as to control the micro- and nano-scale morphology of the composite PV blends. The different positive effects observed in the PV blends (mainly the morphological changes) due to the incorporation of the block copolymers are mainly associated to the nature of the coil blocks attached to the P3HT block. This implies that additional functionalities brought by coil blocks could still be explored and exploited. For example, the positive effect of *PI* and *P4VP* could be eventually coupled by synthesizing a triblock copolymer architecture, such as *PI-b-P3HT-b-P4VP* following by the investigation of the expected dual effect.

Besides, this methodology should be examined as regards to new photovoltaic materials such as low band-gap polymers by the synthesis and characterization of block copolymers with a “low band-gap” block coupled with a coil block. This route could provide an effective way to achieve highly efficient and stable organic solar cells if the methodology developed through this work is transposable to such systems.

Chapter – VII

Materials and Experimental Methods

7.1. Thin film and device fabrication techniques

i) Materials

As it has been mentioned previously, all P3HT based materials were synthesized in the laboratory. The homopolymer P3HT used in the blend with PCBM was synthesized via the Grignard metathesis route.^[1-3] Its macromolecular characteristics are; $M_n = 60$ kg/mol, dispersity $D = 1.4$, regioregularity = 99%. A P3HT-*b*-PI copolymer was synthesized using Grignard metathesis for the P3HT block coupled with living anionic polymerization for the PI block.^[4] The other two block copolymers, P3HT-*b*-PS and PS-*b*-PI, were synthesized following a similar procedure previously reported by Urien *et al.*^[5] and Fetters *et al.*^[4], respectively. The synthesis of P3HT-*b*-P4VP rod-coil block copolymer is presented in detailed in the work of Mougner *et al.*^[6] PCBM molecule and indium tin oxide (ITO) (10 Ω /sq) coated-glass substrates (15 mm \times 15 mm \times 0.7 mm) were purchased from Solaris and Kintec Company, respectively. The thickness of the ITO layer is ~ 160 nm and its transmittance at this thickness is $\sim 85\%$. PEDOT:PSS, ortho-dichlorobenzene (*o*-DCB) and Chloroform were purchased from H.C. Starck GmbH and Aldrich and used as received.

ii) Solution preparation

P3HT:PCBM 1:1 w/w solution (40 mg/mL) was prepared in ortho-dichlorobenzene (*o*-DCB). The different block copolymer additive solutions were prepared separately. P3HT-*b*-PI, P3HT-*b*-PS and PS-*b*-PI (each 7 mg/mL) were prepared in *o*-DCB and P3HT-*b*-P4VP solution (5 mg/mL) was prepared in chloroform. Each block copolymer solution was then mixed with the P3HT:PCBM solution at different block copolymer weight ratios x as regard to the total blend amount. To fabricate two set of samples (each sample contains 4 devices), we used 100 μ L P3HT:PCBM blend solutions, which corresponds to 4 mg in weight. Therefore, the percentage of the block copolymer was calculated based on this amount. In order to adjust the thickness of active layer, the concentration of the ternary blend was corrected by adding a proportional amount of solvent (see Table 7.1(a) and (b)).

(a)

x (%) [a]	P3HT:PCBM (μL) [b]	P3HT- <i>b</i> -PI (μL) [c]	ODCB (μL)
0	100	0	57.0
1	100	5.7	51.4
2	100	11.4	45.7
3	100	17.0	40.0
4	100	23.0	34.0
5	100	28.5	28.5
6	100	34.0	23.0
7	100	40.0	17.0
8	100	45.7	11.4
9	100	51.4	5.7
10	100	57.0	0

(b)

x (%) [a]	P3HT:PCBM (μL) [b]	P3HT- <i>b</i> -P4VP (μL) [c]	Chloroform (μL)
0	100	0	80
2	100	16	64
4	100	32	48
6	100	48	32
8	100	64	16
10	100	80	0

[a] Weight ratio of the copolymer with respect to the blend amount.

[b] P3HT:PCBM 1:1 solution, 40 mg.mL^{-1} in o-DCB.

[c] 7 mg.mL^{-1} of P3HT-*b*-PI and 5 mg.mL^{-1} of P3HT-*b*-P4VP solutions in o-DCB and chloroform, respectively.

Table 7.1: Compositions of the solutions of the active layer. (a) P3HT-*b*-PI and (b) P3HT-*b*-P4VP

For the case of P3HT-*b*-P4VP, since the block copolymer solution was prepared from chloroform, chloroform has to be added in the final solutions in order to have the same ratio between *o*-DCB and chloroform in all solutions. For example, the reference solution (*i.e.* the P3HT:PCBM 1:1 solution in *o*-DCB) was complemented by adding chloroform. Depending on the percentage of the additive, the quantity of the ternary blend used is presented in Table 7.1(b).

iii) Device fabrication

Substrates - glass coated ITO - (used as anode or cathode, depending on the type of device configuration) were cleaned in an ultrasonic bath of acetone, ethanol and isopropanol for 15 min. The fabrication methods of the two types of device configurations employed in this work are presented in the following sections.

a) Direct device configuration

Following its cleaning, the substrate was dried and treated in a UV-ozone oven for 15 min. A thin layer of PEDOT-PSS (Baytron P, Bayer AG/Germany) was subsequently spin-coated at 4000 rpm and dried at 110 °C in a vacuum oven for 30 min. The thickness of PEDOT:PSS layer was determined to be ~ 50 nm as measured by using an *Alpha-step IQ 500* surface Profilometer. All procedures after the PEDOT:PSS deposition were performed in a glovebox filled with nitrogen (O_2 and $H_2O < 0.1$ ppm). The photoactive layer (P3HT:PCBM 1:1 wt%) was spin-coated on the top of the PEDOT:PSS layer from *o*-dichlorobenzene (*o*-DCB) solutions at 1000 rpm for 60 sec. The thickness of the photoactive layer was typically in the range of ~ 100 nm. The aluminium cathode was thermally deposited (80 nm) through a shadow mask with a pressure below 10^{-6} mbar. The active area of the devices ranges from 8.2 to 8.6 mm². Thermal annealing treatment was performed either before the cathode deposition (pre-treatment) or after cathode deposition (post-treatment). For most of this work, thermal annealing was performed on a temperature-controlled hotplate at a temperature of 165°C. Devices were left to cool down to room temperature before the PV characterizations. Each procedure is presented in Figure 7.1.

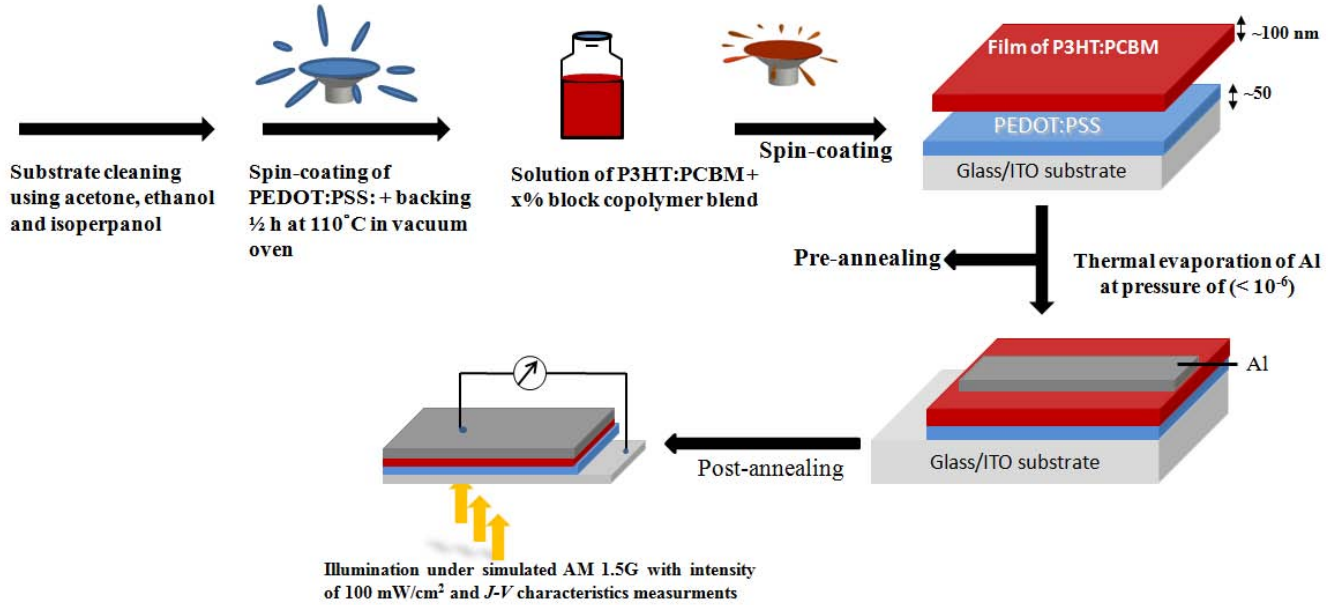


Figure 7.1: Device fabrication procedure for a conventional type architecture: Glass/ITO/PEDOT:PSS/P3HT:PCBM/Al.

b) Inverted device configuration

Inverted solar cells were fabricated using the following structure: ITO/TiO_x/active layer/MoO₃/Ag. After the Glass/ITO substrates were cleaned according to the procedure mentioned before, the substrate was spin-coated with an organic precursor of titania (Titanium (IV) isopropoxide, Aldrich, 99.999%) diluted in absolute ethanol ($C = 0.05 \text{ mol.L}^{-1}$) and stabilized with HCl (pH = 1.9). Conversion of the precursor to TiO_x via hydrolysis was achieved by storing the films for 1 h in air at room temperature. This procedure was derived from the work of Burgos *et al.*^[7] The thickness of the TiO_x layer was ~ 20 nm as measured using an *Alpha-step IQ 500* surface Profilometer. In order to decrease the activation time, the TiO_x layer was annealed prior to active layer deposition at 110 °C for 10 min. Again, all following procedures after TiO_x deposition were performed in glove box under nitrogen (O_2 and $H_2O < 0.5 \text{ ppm}$). TiO_x was used as electron transporting layer in this inverted configuration. Subsequently, the P3HT:PCBM:P3HT-*b*-P4VP solution (the solution was stirred over night at 50 °C) was spin-coated at 1000 rpm for 60 seconds on top of TiO_x layer. The thickness of the photo-active layer was typically of ~ 100 nm. Molybdenum oxide (MoO₃) and the silver electrode were

thermally evaporated (10 nm/80 nm) through a shadow mask with a pressure of $< 10^{-6}$ mbar. MoO₃ is a hole-selective (electron-blocking) layer; thus improving holes extraction and transport from the active layer to the silver electrode. The active area of the devices fabricated by this procedure ranges from 8.2 to 8.6 mm². If thermal annealing of the active layer was needed, it was performed before the MoO₃ and silver deposition on a temperature-controlled hotplate at 165°C for 20 min. Devices were left to cool down to room temperature before testing.

In all device architectures (direct or inverted), one sample contains four diodes. In order to check the repeatability of the performances for each experimental parameters (annealing temperature, time, and percentage of additives ...), the PV measurements have been performed on 8 to 16 different solar cells (e.g. four or eight solar cells were characterized from two solutions prepared separately).

7.2. Device characterizations

The performance of PV cells is commonly rated in terms of their efficiency with respect to standard operating conditions defined by temperature and spectral irradiance. The *PCE* of a PV cell is given as:

$$PCE = \frac{P_{out}}{P_{in}} * 100 \quad (7.1)$$

Where P_{in} is the measured peak power of the cell (W/m²) and P_{in} is the total incident irradiance (W/m²). For Equation 7.1 to give a unique efficiency, P_{in} must be measured with respect to a reference spectral irradiance. For illuminating the PV cells, we used the most common reference spectrum; the Air Mass 1.5 Global (AM 1.5G). It is determined according to the following: for a path length L through the atmosphere, for a solar radiation incident at an angle θ from the Zenith, the air mass coefficient is given by: $AM = L/L_0 \approx 1/\cos(\theta)$; where L_0 is the zenith path length (i.e. normal to the Earth's surface) at sea level (Figure 6.2). According to the American Society for Testing and Materials (ASTM E892-87:1992), the intensity of insolation of AM 1.5G is equivalent to the sun shining through the atmosphere to sea level, with oxygen and nitrogen absorption, at an oblique angle of 48.2° from the

zenith (Figure 7.2). The AM 1.5G solar radiation is preferred since it covers a wide range of wavelengths. In this spectrum, the maximum irradiation is set at 480 nm and 70% of the photons are located in the range of 400-920 nm. As we have mentioned in bibliographic chapter, the first prerequisite for an efficient solar cell is the capture of a large fraction of the incoming sun light by the active layer.

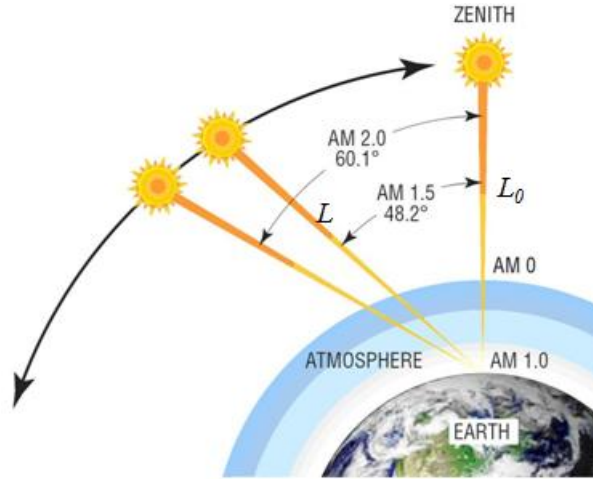


Figure 7.2: The path length in units of Air Mass as function of the zenith angle.

7.2.1. Quantum Efficiency Measurements

From the photo-physical point of view, the efficiency of a solar cell is related to the external quantum efficiency (EQE), which is defined as the conversion efficiency of the solar radiation into electrical energy. In another way, it is the ratio of the absorbed photocurrent divided by the incident photon flux as a function of the excitation wavelength, and is also called incident photon to current conversion efficiency (IPCE).

$$EQE = \frac{\text{number_of_electrons}}{\text{number_of_incident_photons}} \quad (7.2)$$

EQE is measured by recording the photocurrent response while continuously varying the wavelength of the incident light and can be used to determine the efficiency of conversion of photons to electrons. The maximum EQE is named EQE_{max} , which is a key parameter for describing the device. The higher the EQE_{max} , the more efficient the device is. The short circuit current given by the solar cell

can be estimated by performing integration over the whole wavelength range. Herein, a Triax Monochromator was utilized for the EQE measurements.

7.2.2. The Photovoltaic Parameters

The overall *PCE* is the ratio between the power generated (W/m^2) and the power of the incident light (W/m^2) given by equation (7.1). However, the *PCE* in photovoltaic cells are described by three parameters, extracted from the common *J - V* characteristic curve as shown in Figure 7.3.

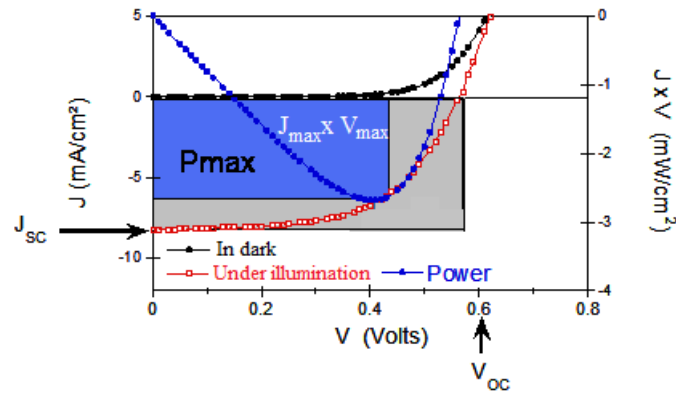


Figure 7.3: *J - V* characteristic of solar cells under illumination and in dark condition

Hence, the *PCE* is calculated according to the following equation:

$$PCE = FF \frac{J_{SC} \times V_{OC}}{P_{in}} \quad (7.3)$$

Where; J_{SC} is the short circuit current in mA/cm^2 , V_{OC} is the open circuit voltage in V, and FF the fill factor. As we have shown in previous chapters, the J_{SC} is the maximum current which flow in the device under illumination when no voltage is applied. As we have also observed, J_{SC} is highly dependent on the morphology of the device, the lifetime and mobility of the charge carriers.^[8, 9] Furthermore, it was shown that a decrease in the band gap results in a higher maximum theoretical current since more sun light, *i.e.* photons, is harvested. V_{OC} is the maximum voltage that a bulk heterojunction device can produce under open circuit. It is hypothetically associated to the difference between the HOMO of the donor (polymer) and the LUMO of the acceptor (e.g. PCBM)^[10, 11] but it also strongly depends on the

donor/acceptor and organic/electrode interfaces (presence of interfacial dipoles), illumination intensity, temperature and the type of electrodes.^[12] In addition, it has been proposed that lowering the HOMO of the polymer and increasing the LUMO of the acceptor will cause an increase in V_{OC} resulting in higher efficiency.^[10, 11]

The fill factor is the ratio between the maximum power output of the device at the maximum power point (V_{max}, J_{max}) to the maximum theoretical power output, which can be achieved if the device is an ideal diode (V_{OC}, J_{SC}) (given by equation (7.4)). An ideal device would have a rectangular shaped J - V curve and therefore a fill factor $FF = 1$. The FF provides information about the quality of charge extraction in the device, the evolution of the interfaces between the different layers of the stack, and the charge transport through each layer. In other words, FF represents the overall quality of the diode.^[13]

$$FF = \frac{J_{max} \times V_{max}}{J_{SC} \times V_{OC}} \quad (7.4)$$

In this work, the current density – voltage (J - V) characteristics of the devices were measured using a *Keithley 4200* semiconductor characterization system both in dark and light conditions at 100 mW/cm^2 illumination provided from a *K.H.S. Solar Cell Test 575* simulator equipped by a *Xenon* arc lamp with AM 1.5G filters. *Karl Suss PM5* prober was used to make contacts between the solar cell device and the *Keithley 4200 SCS*. Those characteristics allow the determination of the PCE , the V_{OC} , the J_{SC} and the FF .

7.2.3. The Real Cell Condition and the Equivalent Circuit diagram

All the above PV parameters are extracted from the solar cells considering the solar cell is working as a diode. For that, an equivalent electrical circuit diagram is modeled as shown in Figure 7.4(a). In real cells, power is dissipated through the resistance at the contacts and through interfaces in the device. These effects are electrically equivalent to two parasitic resistances, one in series (called R_s) and the other in parallel (shunt resistance, called R_{sh}) in addition to the electrical circuit of the cell as

shown in Figure 7.4(a). R_s and R_{sh} express the behavior (change) of the current-voltage curve around the open-circuit voltage and the short-circuit current, respectively, as shown in Figure 7.4(b):

$$R_s = \left(\frac{dV}{dI} \right)_{V=V_{oc}} \quad (7.5)$$

$$R_{sh} = \left(\frac{dV}{dI} \right)_{J=J_{sc}} \quad (7.6)$$

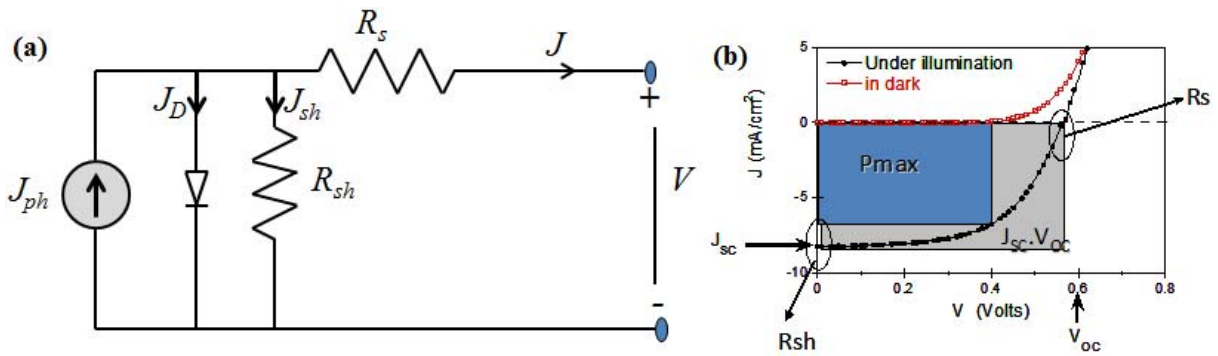


Figure 7.4: Equivalent electrical circuit of a real solar cell under illumination. The equivalent electrical circuit of a solar cell contains a current generator (generates a constant current J_{ph} under illumination), the diode current (J_D) and the power loss from the leakage current (J_{sh}) at the donor:acceptor interfaces. The series connected resistance, R_s , simulates a resistance at the electrode-active layer interface. The shunt resistance R_{sh} simulates a leakage around the polymer layer between the two electrodes.

The R_{sh} which is generally associated to the degree of leakage current^[14] through the whole device or the recombination of charge carriers near the dissociation site (e.g. donor:acceptor interface). It is often linked to imperfections during the fabrication processes leading to the loss of charge carriers through leakage paths including pinholes in the films, exciton recombination at donor/acceptor interface, trapping of the carriers, and surface defects. The R_s is attributed to the bulk conductivity of each of the functional layers (i.e. mobility of the specific charge carrier in the respective transport medium) and the contact resistance between them as well as the contact resistance developed at the active layer/electrode interfaces. The series and shunt resistances affect the PV characteristics of organic solar cell, and particularly the FF and J_{sc} . For example, large serial resistances, which can be

due to the degradation of a material or to the poor quality of the electrode/active layer interface, tend to reduce the value of the FF . This implies that the performances of solar cells should be improved by minimizing the effects of these parasitic resistances.

The current-voltage characteristics can also be monitored in dark conditions. The dark current-voltage characteristics give information exclusively about the recombination of excitons formed by injection of charges from the electrodes into active layer. From the equivalent circuit shown in Figure 7.4(a), it is evident that the total current produced by the solar cell, J , is equal to that produced by the photocurrent (J_{ph}), minus that flows through the diode (J_d), minus that flows through the shunt resistor (J_{sh}):

$$J = J_{ph} - J_d - J_{sh} \quad (7.7)$$

In an ideal diode condition, the diode current J_d follows the Shockley relation and can then be expressed by the generalized Shockley equation:^[15]

$$J_d = J_0 \left[\exp \left(\frac{q(V - JR_s)}{nk_B T} \right) - 1 \right] \quad (7.8)$$

Where J_0 is the reverse dark saturation current, n is the diode ideality factor, q is the electron charge, k_B is Boltzmann's constant, T is the absolute temperature, and V is the bias voltage (voltage across the output terminals). The current through the R_{sh} follows the Ohm's law and accordingly stated as: $J_{sh} = V/R_{sh}$. Since R_{sh} is very large for the case of best working diodes, the current through R_{sh} is considered as null. Therefore, the total current, J , will be expressed:

$$J \approx J_{ph} - J_0 \left[\exp \left(\frac{q(V - JR_s)}{nk_B T} \right) - 1 \right] \quad (7.9)$$

Under open circuit conditions; when $V = V_{OC}$ and $J = 0$, V_{OC} can be expressed as;

$$J_{ph} = J_0 \left[\exp \left(\frac{qV_{OC}}{nk_B T} \right) - 1 \right] \quad (7.10)$$

and in the ideal case, the photo-generated current J_{ph} is equal to the short circuit current J_{SC} . Thus, the relationship between the dark current and the V_{OC} is inferred by:

$$V_{OC} \approx \frac{nk_B T}{q} \ln \left[\frac{J_{SC}}{J_0} + 1 \right] \quad (7.11)$$

7.3. Differential Scanning Calorimetry (DSC)

DSC measures the temperatures and heat flows associated with transitions in materials as a function of time and temperature in a controlled atmosphere. These measurements provide quantitative information about physical and chemical changes that involve endothermic or exothermic processes as well as changes in heat capacity.^[16]

In our experiment, we used DSC to investigate the thermal properties of P3HT:PCBM blends. Through DSC, we systematically develop the phase diagram of P3HT:PCBM blends as well as their modifications upon the addition of block copolymers (mainly for the P3HT-*b*-PI system). DSC thermograms were measured using a DSC Q100 apparatus from TA instruments. Samples for the DSC analysis were prepared by drop-casting the active layer blends onto a PEDOT:PSS/glass substrate. By floating the film onto deionized water, active layer blends in the same thin film morphology as the one used for the PV devices can be recovered for further thermal analysis.

Phase diagram

The samples with different compositions used for the construction of the phase diagram were first heated from 0 to 300°C, cooled back to 0°C, and then heated again for the second time from 0 to 300°C. The cooling and heating rate was fixed at 10°C.min⁻¹. The first heating removes all the previous thermal histories of the samples. The second heating cycle was used for the construction of the phase diagram.

Self-nucleation experiment

In the chapter 4, we have observed that the incorporation 7% (wt.) P3HT-*b*-PI into P3HT leads to a shift of the crystallization temperature towards higher temperatures (by almost 2°C). To determine whether the 2 °C increase in crystallization temperature induced by the block copolymer addition was significant or not, we studied the self-nucleation of pure P3HT. This technique is based on the principle that the best nucleating agent for a polymer is the polymer itself.^[17-19] Prior to the self-nucleation experiment the sample first undergoes heating and cooling cycles to determine the crystallization and melting temperatures. It was heated from room temperature to a temperature high enough (280°C) to completely melt the polymer while erasing the thermal history of the polymer. Subsequently, the sample was cooled back at 100°C to obtain a standard state as regard to the thermal properties. The sample was then heated 280°C and cooled back to 100°C for a second run to precisely determine the melting and crystallization temperatures. The melting and crystallization temperatures were determined at 239.0°C and 205.4°C, respectively. All, the heating and cooling rate was fixed at 5°C/min.

To carry out the self-nucleation experiment, we first determine the optimum self-nucleation temperature (T_s). If the DSC heating is stopped in the melting region and cooled it back, there is a possibility for the sample to undergo different form of crystallization processes. For the pristine P3HT under study the DSC profiles obtained upon cooling and heating for several T_s are shown in Figure 7.5, according to which the domains apparent in Figure 7.6 were defined. Depending on the behavior of melting temperatures (T_m) and crystallization temperatures (T_c) recorded from the value of T_s , the temperatures in the melting region is divided into three Domains. In Domain I, T_m and T_c are both independent on T_s . In Domain II, T_c increases as T_s decreases while T_m remains constant. In Domain III, both T_m and T_c increase with decreasing T_s . These properties are clearly observed in Figure 7.5(a). If melting process stops above ~ 255 °C and cooled it back, we don't see any difference in crystallization and melting temperature to that of the completely molten system. If melting process is stopped below 245 °C and cooled it back, the sample shows an additional crystallization peak (an increase in crystallization peak as shown by the arrow) and a higher melting temperature as shown in Figure

7.5(b). The additional crystallization peak observed in those systems is an indication of the annealing of the unmelted crystals upon cooling. However, stopping the heating process at 245 °C and cooled it back has only shown an increase in the crystallization temperature while still maintain the same melting temperature to that of the completely molten system.

From this understanding, maximum self-nucleation effect is possible to be achieved if the sample is cooled from $T_s = 245$ °C. This temperature lays exactly at the edge of Domains II and III (because, cooling below this temperature has shown the evolution of additional crystallization peak, see Figure 7.5(a)). Since the sample in Domain II is not completely molten (i.e. still small crystallites exist), those unmelted crystallites will act as self-nuclei and thus increase the crystallization temperature. Therefore, 245 °C is the best self-nucleation temperature of the P3HT under study. The corresponding crystallization temperature at this optimal T_s is 211 °C, which is 5.6 °C higher than the crystallization temperature recorded upon cooling from the completely molten state (i.e Domain I) which is 205.4 °C. Keeping the 5.6 °C shift of the crystallization peak recorded for the optimum self-nucleating condition as a reference, we compare with the 2 °C shift induced by the nucleating agent under study. Since 5.6 °C is the maximum shift that can be obtained, the 2 °C shift induced by the P3HT-*b*-PI copolymer is considered to be significant.

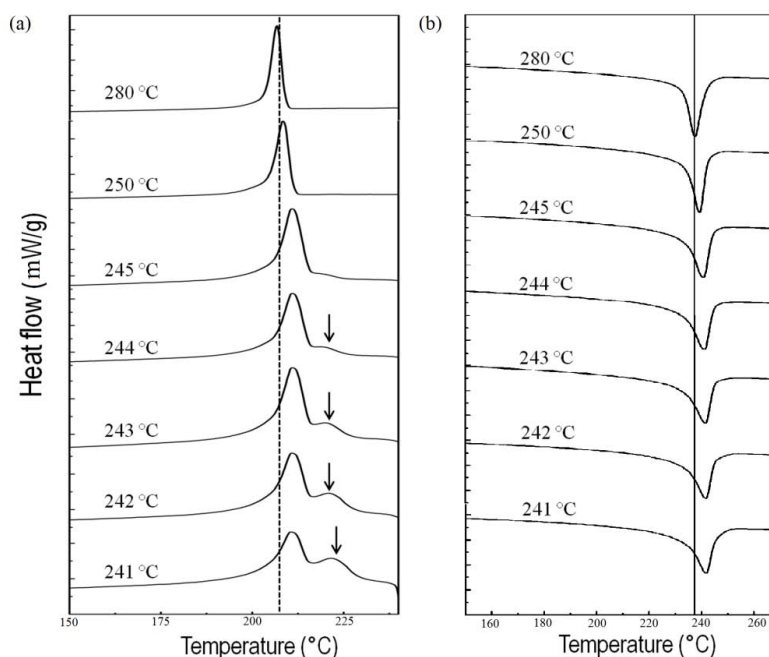


Figure 7.5: The DSC cooling scans (a) and heating scans that were subsequently recorded (b) at a rate of 5°C/min for a P3HT sample that has been previously heated at various temperatures T_s (250, 245, 244, 243, 242 and 241°C). Before each cycle the sample was completely molten (280°C) to erase thermal history. These scans allow us to determine the borders of Domains I, II and III, as discussed in the text. The segmented vertical line in figure (a) indicates the standard crystallization peak of the polymer. The additional crystallization peak shown by an arrow indicates the annealing of unmelted crystals (i.e. the sample is Domain III).

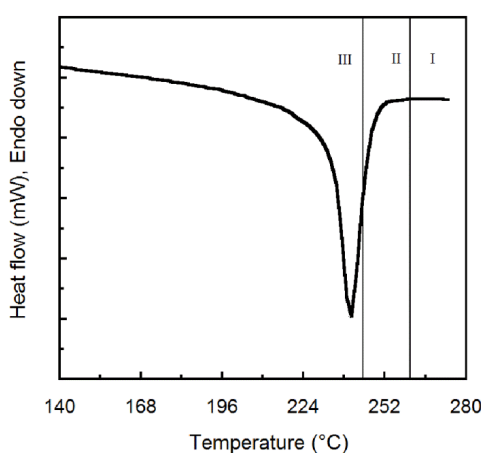


Figure 7.6: The melting peak of pure P3HT recorded upon cooling from the molten state (280°C) with a rate of 5°C/min. The vertical lines correspond to the limits between domains I, II and III and were derived after the evaluation of the DSC scans presented in Figure 7.5.

Finally, the nucleation efficiency (NE) of the agent used can be estimated from the relation given below^[17]:

$$NE = \frac{T_{c,nucleating\ agent} - T_{c,not\ self-nucleated}}{T_{c,self-nucleated} - T_{c,not\ self-nucleated}} * 100$$

The nucleating efficiency is equal to 0% when no nucleating agent is added and equals 100% for optimum self-nucleation. Thus, the 7% (wt.) P3HT-*b*-PI used herein has 31% nucleation efficiency when added in P3HT. This shows that even though the increase in crystallization temperature upon addition P3HT-*b*-PI was very small, P3HT-*b*-PI has a big impact as a nucleating agent.

7.4. Morphology and Structural Characterization Techniques

7.4.1. Optical microscopy

Bright-field transmission optical microscopy observations were carried out with a *Leitz Laborlux K* Microscope equipped with a *Moticam 2000 compact* professional camera and a *Mettler Toledo FP82HT* hot stage. For the *in situ* heating, the sample was placed in a sample holder with a closed loop heating system. Image capturing was started when the temperature of the sample holder was ramped to 160°C. The thin films used to depict the phase diagram of P3HT:PCBM blends for the different Mn of P3HT were spin-coated directly onto ITO under the same conditions as for devices. The PEDOT:PSS thin layer was not included here as it can be damaged when heated above 200°C. The other optical microscopy images stated in this thesis were acquired from the actual devices. For the case of dark-field imaging, we used *Zeiss Imager.A1* equipped with a *Nikon D90* camera and *ZEISS EC EPIPLAN* objective lens (x10). Unlike in bright field where image contrast comes from absorbance (transmittance) of light in the sample, in dark field illumination, the contrast comes from the scattered light by the sample.

7.4.2. Scanning Force Microscopy

Scanning Force Microscopy (SFM), also known as Atomic Force Microscope (AFM), is a very high-resolution type of scanning probe microscopy technique. It is one of the foremost tools for imaging, measuring and manipulating surface features at the nanoscale level. Information is gathered by “feeling” the surface with a mechanical probe. It operates by measuring the attractive or repulsive forces between a tip and the sample surface. In SFM, the tip is mounted on a reflective cantilever (the cantilever and tip together are known as the probe) made of silicon nitride, silicon oxide or pure silicon fabricated with standard techniques used in semiconductor industry. Laser is focused onto the back of the reflective cantilever (Figure 7.7). As the tip scans the surface of the sample, the tip deflects and the laser beam is bounced off the cantilever. Depending on the interaction between the tip and the sample,

there will be a difference in the intensities of the reflected light. This difference is measured by the photodetector and the signal is sent off to the controller feedback loop. The feedback loop will attempt to keep the cantilever deflection constant by maintaining a constant distance between the cantilever and the sample. This can be done by moving the scanner (by applying a voltage) in the Z direction at each point. The voltage is then converted to a cantilever deflection.^[16]

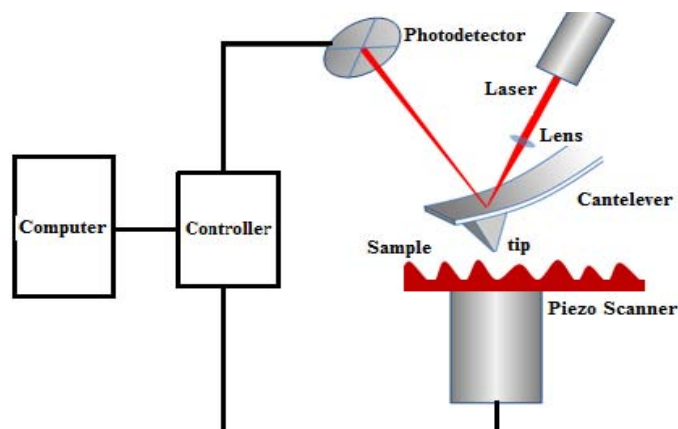


Figure 7.7: Principle of an atomic force microscope.

Based on the sample surface-tip interaction, there are three operation modes: contact mode, non-contact mode and tapping mode. In contact mode, the tip constantly touches the sample surface and scans across the surface. The contact mode microscopy can give an accurate image with high resolution, but both the sample and tip may be damaged due to the direct contact. Such damage can be avoided by using non-contact mode; however, the resolution is decreased. Hence, the tapping mode, a combination of contact and non-contact mode, appears to be a solution to this problem. In tapping mode, the tip is alternatively placed in contact with the surface to provide high resolution and then lifting the tip off the surface to avoid dragging the tip across the surface. The cantilever oscillates close to or at the resonant frequency with an amplitude between 20 nm and 100 nm.^[20]

In this work, tapping mode SFM (*Multimode and Dimension Icon 3100, DI-Veeco*) operated in air at room temperature was used. Commercial silicon cantilevers with typical force constants of 32.0-54.4 N.m⁻¹ (Nano-sensors) were used. The measurements were carried out at a specific position of the sample with 2 μm scan sizes. Each scanned micrograph consisted of 512 lines. Images were taken

continuously with a scan rate of 1.0 Hz. All the observed films were performed on the active layers of the actual devices in order to ensure that the observed morphologies were typical.

7.4.3. Transmission Electron Microscopy

TEM operates on the same basic principle as optical microscopy but uses electrons instead of light. Thus, TEM is capable of imaging at a significantly higher resolution than light microscopy. An electron source at the top of the microscopy emits the electrons that travel through vacuum in the column of the microscopy. Instead of glass lenses used for focusing the light in optical microscopy, TEM uses electromagnetic lenses to focus the electrons into a very thin beam. The electron beam then travels through the specimen under study. Depending on the nature of the material (density or thickness), some of the electrons are scattered. At the bottom of the microscope, an image is formed from the interaction of the electrons transmitted through the specimen; the image is then magnified and focused onto an imaging device, such as a fluorescent screen (or on a layer of photographic film) to be detected by a sensor such as a CCD camera. The contrast in TEM image is dependent on the thickness of the film, composition and electron density of the materials.^[21]

Following SFM observations, the active layer films were collected from the devices for further TEM observations. The P3HT:PCBM thin film were immersed into deionized water to dissolve the PEDOT:PSS layer and allow the blend film to float. It was then collected and placed on a 400 square-mesh copper TEM grid (*Agar Sci., Inc.*). TEM images were recorded using a *Hitachi H-7650* transmission electron microscope operated at 80 kV. In the TEM image, P3HT region is bright relative to a PCBM region because of the lower mass density (mass density, 1.1 g/cm³) of P3HT compared to that of PCBM (1.5 g/cm³). Thus, the bright and dark regions are attributed to P3HT-rich domains and PCBM-rich domains, respectively.^[22, 23] For crystalline materials and those with very little electron-density, the contrast is brought by the mass density difference.

7.4.4. UV-vis Absorption Measurement

Each molecule has an internal energy which can be considered as the sum of the energy of its electrons, the energy of vibration between its constituent atoms and the energy associated with the rotation of the molecule. For the case of electronic transitions, high energy photons far and near UV, as well in the visible region are required to bring about transitional changes. For example, the electronic energy levels of simple molecules are widely separated and usually only the absorption of a high energy photon (*i.e.*, one of very short wavelength) can excite the electron of a molecule from one level to another. In complex molecules, the energy levels are more closely spaced and photons of near ultraviolet and visible light can effect the electronic transition. These substances, therefore, will absorb light in some areas of the near ultraviolet and visible regions.

The ultraviolet-visible absorption spectroscopy is used for the detection and quantitative measurements that undergoes electronic transitions between different energy levels of the ground and excited states upon photon absorption. When sample molecules are exposed to light having an energy that matches a possible electronic transition within the molecule, some of the light energy will be absorbed as the electron is promoted to a higher energy orbital. An optical spectrometer records the wavelengths at which absorption occurs, together with the degree of absorption at each wavelength. The only molecular moieties containing chromophores likely to absorb light in the UV-vis region (200 to 800 nm) are the π -electron functions ($\pi \rightarrow \pi^*$) and hetero atoms having non-bonding valence-shell (lone) electron pairs ($n \rightarrow \pi^*$) (Figure 7.8).^[24] For conjugated systems, the most energetically favorable excitation or electronic transitions occur during the absorption of ultraviolet and visible light is from the HOMO to the LUMO level of the π -orbital ($\pi \rightarrow \pi^*$). The resulting spectrum is presented as a graph of absorbance versus wavelength. In the spectrum of conjugated systems, there is a possibility to show several absorption peaks or shoulders. It indicates the electronic transitions between the different vibrational energy levels possible for each electronic state. It also reflects the formation of fine structures and the different conformations the systems may assume.

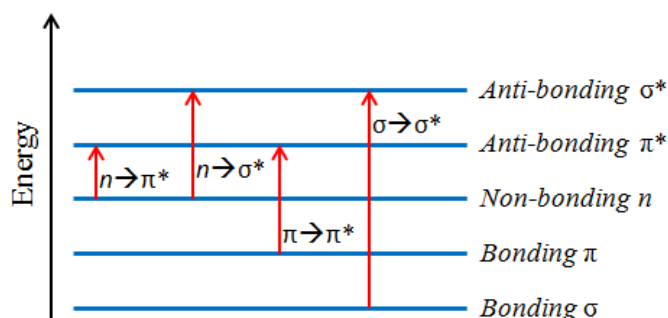


Figure 7.8: The various kinds of electronic excitation that may occur in conjugated organic molecules.

The amount of light absorbed is expressed as either transmittance or absorbance. Absorbance is directly proportional to the path length (thickness), L , and the concentration, c (mol.L^{-1}), of the absorbing species. It is expressed by using the Beer-Lambert law: $A = -\log(I_0/I) = \alpha cL$; where, I_0 is the incident radiation, I is the transmitted radiation, A is the measured absorbance (Figure 7.9). For each species and wavelength, α is the absorption coefficient or the molar absorptivity, which is a fundamental molecular property in units of $\text{L.mol}^{-1}.\text{cm}^{-1}$ and it is defined as: $\alpha = 4\pi k/\lambda$; where k is the extinction coefficient and λ is the wavelength. In this study, UV-vis spectra were recorded using a SAFAS UVMC² over the spectral range 300–800 nm.

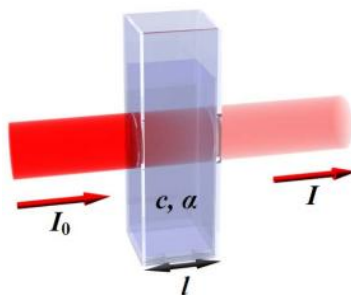


Figure 7.9: The change of light intensity through absorbance or transmittance.

7.4.5. X-ray Diffraction and Neutron Reflectometry

X-ray diffraction (XRD) is a versatile, non-destructive technique that reveals detailed information about the chemical composition and crystallographic structure of materials. The principle of X-ray diffraction is; when a monochromatic X-ray beam with wavelength λ is projected onto a crystalline material at an angle θ , diffraction occurs only when the distance traveled by the rays

reflected from successive planes differs by a complete number n of wavelengths (i.e. Bragg's Law conditions). Plotting the angular positions and intensities of the resultant diffracted peaks of radiation produces a pattern, which is characteristic of the sample (i.e. its structural, physical and chemical information). For example, a polymer can be considered partly crystalline and partly amorphous. The crystallinity parts give sharp narrow diffraction peaks and the amorphous component gives a very broad peak. The ratio between these intensities can be used to calculate the amount of crystallinity (degree of crystallinity) in the material. From the diffraction peaks, it is also possible to estimate the crystal size and orientation of domains.

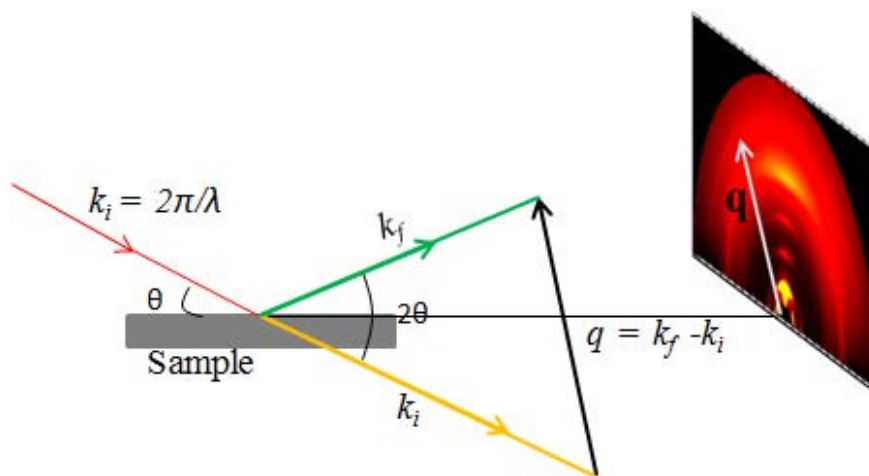


Figure 7.10: Schematic representations of X-ray diffraction measurements.

The scattering intensity, $I(q)$, is measured as a function of the angle between the incoming beam and the scattered beam, 2θ , and the resulting patterns are typically represented as scattered intensity as a function of the magnitude of the wave vector transfer, q . The scattering vector q is defined with respect to the center of the incident beam and has a magnitude of $q = (4\pi/\lambda)\sin\theta$, where 2θ is the scattering angle and λ is the wavelength of the X-ray or neutron beams.

GIXD experiments were performed on the Dutch-Belgian Beamline (DUBBLE CRG), station BM26B, at the European Synchrotron Radiation Facility (ESRF), Grenoble, France. The energy of the X-rays was 12 keV and the angle of incidence was set at 0.15° . The diffracted intensity was recorded by a *Frelon* CCD camera and it was normalized by the incident photon flux and the acquisition time.

We have already shown that crystallinity, crystallite size and domain orientation are not the only structural features in the active layers that affects the performance of organic solar cells. The distribution of components through the bulk has also greater importance in determining the PV characteristics. As we have already shown in our studies, Neutron reflectometry (NR) was employed to investigate the distribution of P3HT and PCBM components along the normal. Since they are uncharged, they can penetrate deeply into most materials, suitable to probe bulk properties. It determines the profile of the atomic composition along the surface normal for single or multilayered thin film structures with thicknesses usually in the range of 1 to 100 nm at nanometer resolutions.^[25]

In its simplest form, NR technique measures the intensity of a specularly (angle of incidence = angle of reflection) reflected neutron beam as a function of wavelength and/or angle. If the thin film surface constitutes the (x, y) plane and the z axis is normal to the surface, then for specular reflectivity, momentum transfer q_x and q_y are zero and q_z is given by: $q_z = (4\pi/\lambda)\sin\theta$, where λ is the wavelength of the neutron and θ the reflection angle. The absolute reflectivity, $R(q_z)$, is a function of the depth-dependent scattering potential of the thin film sample, which is commonly expressed in terms of the scattering length density profile, $\rho(z)$, z being the out-of-plane axis of the film:^[26]

$$R(q) = \frac{16\pi^2}{q^2} \left| \int \rho(z) e^{-iq_z z} dz \right|^2 \quad (7.12)$$

$$\rho(z) = \left[\frac{\sum_i b_i(z)}{V_m} \right] = \frac{\sum_i b_i(z) * D * N_A}{M} \quad (7.13)$$

Where the summation is over each type of isotope in the sample, b is the nuclear scattering length (a known quantity characteristic of a given isotope), and V_m is the molecular volume i.e. the molecular weight (atomic mass) divided by the mass density (D) and Avogadro's number (N_A). Equation (6.12) tells us that the reflectivity depends on the gradient of the average scattering length density perpendicular to the surface (i.e., in the z direction). If we have a layered material, this gradient will

have spikes at the interfaces between layers and one may use to deduce the thickness of a layer close to the interfaces using reflectivity measurements.

NR measurement was performed on the EROS G3 bis neutron beamline at the, CEA-Saclay, France. The EROS G3 bis reflectometer has a distribution of neutron wavelengths from 3 to 23 Å and a time-of-flight detection system. Two different incident angles ($\theta = 0.93^\circ$ and 1.6°) were used to obtain the reflectivity as a function of the momentum transfer perpendicular to the sample plane, q_z , where the scattering vector \mathbf{q} has been defined previously (in XRD section). The NR measurements were carried out on samples containing the PEDOT:PSS layer, prepared under similar procedures in the PV devices. Silicon wafer with diameter ~ 50.0 mm and thickness 4.0 mm (SILTRONIX SAS) were used as a substrate.

References

- [1] R.S. Loewe, S.M. Khersonsky, R.D. McCullough, *Advanced Materials* **1999**, *11*, 250–253.
- [2] M. Jeffries-EL, G. Sauvé, R.D. McCullough, *Advanced Materials* **2004**, *16*, 1017–1019.
- [3] A. Yokoyama, R. Miyakoshi, Y. Tsutomu, *Macromolecules* **2004**, *37*, 1169–1171.
- [4] Y.R. Fetters, L. J.; Luston, J.; Quirk, R. P.; Vass, F.; N., *Anionic Polymerization*, **1984**.
- [5] M. Urien, H. Erothu, E. Cloutet, R.C. Hiorns, L. Vignau, H. Cramail, *Macromolecules* **2008**, *41*, 7033–7040.
- [6] S.-J. Mougner, C. Brochon, E. Cloutet, S. Magnet, C. Navarro, G. Hadziioannou, *Journal of Polymer Science Part A: Polymer Chemistry* **2012**, *50*, 2463–2470.
- [7] M. Burgos, M. Langlet, *J. Sol-gel Science and Technology* **1999**, *16*, 267–276.
- [8] C.J. Brabec, N.S. Sariciftci, J.C. Hummelen, *Advanced Functional Materials* **2001**, *11*, 15–26.
- [9] S.E. Shaheen, C.J. Brabec, N.S. Sariciftci, F. Padinger, T. Fromherz, J.C. Hummelen, *Applied Physics Letters* **2001**, *78*, 841.
- [10] H. Hoppe, N.S. Sariciftci, *Journal of Materials Chemistry* **2006**, *16*, 45.
- [11] B.F. Padinger, R.S. Rittberger, N.S. Sariciftci, *Advanced Functional Materials* **2003**, *13*, 85–88.
- [12] P. Destruel, H. Bock, I. Séguy, P. Jolinat, M. Oukachmih, E. Bedel-Pereira, *Polymer International* **2006**, *55*, 601–607.

- [13] N. Grossiord, J.M. Kroon, R. Andriessen, P.W.M. Blom, *Organic Electronics* **2012**, *13*, 432–456.
- [14] S.M. Sze, *Physics of Semiconductor Devices*, John Wiley & Sons, Inc. **1981**.
- [15] B.P. Rand, D.P. Burk, S.R. Forrest, *Physical Review B* **2007**, *75*, 115327.
- [16] [Http://afmhelp.com](http://afmhelp.com), Accessed on February **2013**.
- [17] B. Fillon, A. Thierry, B. Lotz, J.C. Wittmann, *Journal of Thermal Analysis*, **1994**, *42*, 721–731.
- [18] a. J. Müller, V. Balsamo, M.L. Arnal, T. Jakob, H. Schmalz, V. Abetz, *Macromolecules* **2002**, *35*, 3048–3058.
- [19] A.T. Lorenzo, M.L. Arnal, J.J. Sanchez, A.J. Muller, *Journal of Polymer Science Part B: Polymer Physics* **2006**, *44*, 1738–1750.
- [20] <http://www.cnst.nist.gov/nanofab/pdf/AFM-DI-3100.pdf>, Accessed on February **2013**.
- [21] [Http://www.nobelprize.org/educational/physics/microscopes/tem/index.html](http://www.nobelprize.org/educational/physics/microscopes/tem/index.html), Accessed on February **2013**.
- [22] J.S. Moon, J.K. Lee, S. Cho, J. Byun, A.J. Heeger, *Nano Letters* **2009**, *9*, 230–234.
- [23] W. Ma, J.Y. Kim, K. Lee, A.J. Heeger, *Macromolecular Rapid Communications* **2007**, *28*, 1776–1780.
- [24] [Http://teaching.shu.ac.uk/hwb/chemistry/tutorials/molspec/uvvisab1.htm](http://teaching.shu.ac.uk/hwb/chemistry/tutorials/molspec/uvvisab1.htm), Accessed on February **2013**.
- [25] C.F. Majkrzak, *Acta Physica Polonica A* **1999**, *96*, 81–99.
- [26] J.W. Kiel, M.E. Mackay, B.J. Kirby, B.B. Maranville, C.F. Majkrzak, *Journal of Chemical Physics* **2010**, *133*, 074902.

About the Author

About the Author:

Dargie Hailu DERIBEW was born in Ethiopia (Alamata) on 23th May, 1980. He obtained his B.Sc degree in Engineering in 2004 from Bahir Dar University (Ethiopia) and he then obtained his double Master of Science diploma in Functionalized Advanced Materials Science and Engineering in July 2009 from Grenoble Institute of Technology (France) and Université Catholique de Louvain (Belgium), under the Erasmus Mundus Master Course Frame Work. In March 2010, he started his Ph.D. research at the Laboratoire de Chimie des Polymères Organiques (LCPO) and Laboratoire de l'Intégration du Matériau au Système (IMS) of University of Bordeaux -1.

List of Patents:

- 1) **C. Nicolet, D. Deribew, C. Renaud, G. Fleury, C. Brochon, E. Cloutet, L. Vignau, G. Hadziioannou:** Composition d'une Cellule Photovoltaïque Organique d'un Module Photovoltaïque. ARKEMA FRANCE Nov, 30 2012: FR2975831 A1.
- 2) **S-J. Mougner, C. Brochon, G. Hadziioannou, G. Fleury, E. Cloutet, C. Nicolet, D. Deribew, C. Renaud, L. Vignau:** Composition d'une Cellule Photovoltaïque Organique d'un Module Photovoltaïque. ARKEMA FRANCE Nov, 30 2012: FR2975832 A1.
- 3) **C. Nicolet, D. Deribew, C. Renaud, G. Fleury, C. Brochon, E. Cloutet, L. Vignau, S-J. Mougner, G. Hadziioannou:** Composition of an Organic Photovoltaic Cell in a Photovoltaic Model/ Composition d'une Cellule Photovoltaïque Organique d'un Module Photovoltaïque. ARKEMA FRANCE Dec, 6 2012: WO 2012/164194.

List of publications in international peer reviewed journals:

- 1) **D. Deribew, C. Renaud, G. Fleury, L. Vignau, G. Hadziioannou:** **Effects of long-term light illumination on Device lifetime of P3HT:PCBM photovoltaic Devices – The Block Copolymer Approach.** Article in preparation.

- 2) *D. Deribew, E. Pavlopoulou, G. Fleury, C. Nicolet, C. Renaud, S-J. Mougner, L. Vignau, E. Cloutet, C. Brochon, F. Cousin, G. Portale, M. Geoghegan, G. Hadziioannou: **Crystallization-driven Enhancement in Organic Photovoltaic Performance through Rod-coil Block Copolymer Incorporation into P3HT:PCBM Blends.** Macromolecules **2013**, 46, 3015–3024.*
- 3) *E. Pavlopoulou, G. Fleury, D. Deribew, F. Cousin, M. Geoghegan, G. Hadziioannou: **Phase Separation-Driven Stratification in Conventional and Inverted P3HT:PCBM Organic Solar Cells.** Organic Electronics, **2013**, 14, 1249–1254.*
- 4) *C. Renaud, S-J. Mougner, E. Pavlopoulou, C. Brochon, G. Fleury, D. Deribew, G. Portale, E. Cloutet, S. Chambon, L. Vignau, G. Hadziioannou: **Block copolymer as nano-structuring agent for high-efficiency and annealing-free bulk hetero-junction organic solar cells.** Adv. Mater. **2012**, 24, 2196–2201*
- 5) *C. Nicolet, D. Deribew, C. Renaud, G. Fleury, C. Brochon, E. Cloutet, L. Vignau, G. Wantz, H. Cramail, M. Geoghegan, G. Hadziioannou: **Optimization of the Bulk Heterojunction Composition for Enhanced Photovoltaic Properties: Correlation between the Molecular Weight of the Semi-Conducting Polymer and Device Performance.** J. Phys. Chem. B, **2011**, 115(44), 12717–12727*

Oral and Poster Presentations in National and International Conference:

a) International

- ❖ *Dargie Deribew, C. Nicolet, C. Renaud, G. Fleury, E. Pavlopoulou, S.J. Mougner, C. Brochon, E. Cloutet, L. Vignau, G. Hadziioannou. **Rod-Coil Block Copolymer for Enhanced Photovoltaic Performance and Device Stability in Bulk Heterojunction Organic Solar Cells; Gordom Research Conference (GRC) on « Electronic Processes in Organic Materials”, 3 – 8 June 2012, Renaissance Tuscany II, Cioccu Resort, Lucca (Braga), Italy.***
- ❖ *D. Deribew, C. Nicolet, C. Renaud, G. Fleury, L. Vignau, E. Cloutet, C. Brochon, G. Hadziioannou. **Optimization of the Bulk Heterojunction Composition for enhanced Photovoltaic***

Properties: Correlation between Phase Behavior and Photovoltaic Performance; 4th International Symposium on Flexible Organic Electronics (ISFOE11) 10-13, July 2011, "Ioannis Vellidis" Congress Center, Thessaloniki, Greece.

- ❖ D. Deribew, C. Nicolet, C. Renaud, C. Brochon, G. Fleury, E. Cloutet, L. Vignau, G. Wantz, H. Cramail, G. Hadziioannou. **Correlation between macromolecular design, morphology and performances on the use of block copolymers as additives in P3HT:PCBM blend for OPV cells;** 3rd International Symposium on Flexible Organic Electronics (ISFOE), Halkidiki, Greece (July 10-14 2010) CA.

b) National

- ❖ D. Deribew, C. Nicolet, C. Renaud, G. Fleury, L. Vignau, E. Cloutet, C. Brochon, G. Hadziioannou. **Rod-Coil Block Copolymers for Enhanced Photovoltaic Performance and Device Stability in Bulk Heterojunction Organic Solar Cells.** *Materiaux et Nanostructures π -Conjugés, MNPC-11*, 03-07 Oct 2011 – Obernai, France.